Optimization of Hydrogenated Amorphous Silicon Thin Films and Fabrication of Solar Cells on Flexible Substrates at Low Temperature

A thesis submitted

by

Ramakrishna Madaka
Roll No: 11612109

In partial fulfillment of the requirement for the award of the degree of Doctor of Philosophy

Department of Physics
Indian Institute of Technology, Guwahati
Guwahati – 781 039, Assam, India

April 2018

DECLARATION

The work contained in this thesis entitled **"Optimization of Hydrogenated Amorphous Silicon Thin Films and Fabrication of Solar Cells on Flexible Substrates at Low Temperature"** has been carried out by me under the supervision of Dr. Pratima Agarwal, Professor, Department of Physics, Indian Institute of Technology, Guwahati, Assam, India. This thesis does not contain any materials previously submitted for the award of any degree or diploma.

Date: April 12th , 2018

Ramakrishna Madaka
Roll No: 11612109
Department of Physics
Indian Institute of Technology Guwahati
Guwahati-781039, Assam, India

Certificate

Dedicated

to

my parents (late)

&

My wife and daughter

Acknowledgements

First and foremost, I wish to express my sincere thanks to my thesis supervisor, Prof. Pratima Agarwal, for taking me as a PhD student and providing me the opportunity to work in a well-established experimental lab to conduct my doctoral research. She has been very helpful throughout my research work. She assisted me in learning basic knowledge of physics to material science and designing experiments through discussions and consistent support. I feel very fortunate that she provided me with so many learning opportunities, which helped me in the successful culmination of the present endeavor. She not only helped in academics but also in financial support.

I am grateful to my doctoral committee members Prof. Saurabh Basu (Chairman), Dr. Ashwini Kumar Sharma and Prof. Roy Paily Palathinkal for regular review of my research work and their constructive suggestions and fruitful discussions at various stages of my research work. I express my sincere thanks to the present and former Head of the Department of Physics for their encouragement and allowing me to use departmental facilities throughout my research work. I am also thankful to all other faculty members of the Physics department.

The RF-PECVD multi-chamber system used for deposition of Si films and solar cells is supported by the funds received from Department of Science and Technology (DST) and Defence Research and Development Organization (DRDO), New Delhi, India.

My special thanks to Mr. Basab Bijoy Purkayastha for his help in automation of external quantum efficiency measurement setup.

I am grateful to Prof. S. C. Agarwal, visiting faculty in the Department of Physics for valuable discussions in different area of research.

I would like to acknowledge my former lab mates Dr. Himanshu S. Jha, Dr. Mukesh Singh and Dr. Lalhriatzuala, and my colleagues Ms. Asha Yadav, Mr. Venkanna Kanneboina, Mr. Pilik Basumatary, Ms. Juhi kumari, Mr. Manvendra Singh Gangwar, Mr. Vivek Ghritlahre, Ms. Shubhangi Bhardwaj, Ms. Jai Shree Bharadwaj, Ms. Niharika Gogoi and Mr. Suman Sarkar for providing an ambient atmosphere and helped me in different stages of my research work.

I would like to thank CIF, IIT Guwahati for using CIF facilities. I am also thankful to technical officers Mr. Chandan Borgohain, Mr. Madhurjya Borah and Mr. Kh. Kesho Singh.

I would like to thank Prof. P. K. Iyer, Department of Chemistry, for allowing me to do some measurements in his lab.

My special thanks to Dr. Himanshu S. Jha and Mr. Raghuram Chinta for their continuous financial support.

My special thanks to Mr. Subash Pai (M/s Excel Instruments, Mumbai) for fabricating the multi-chamber RF-PECVD system as per our design and requirement. I would like to thank Mr. Pramod, service engineer M/s Excel Instruments and Mr. Ranjan, Pfeiffer vacuum for their immediate response and technical support whenever there is an issue/ problem with our instruments.

I would like thank Mr. Venkanna Kanneboina for spectroscopic ellipsometry measurements.

I am very fortunate to have friends Dr. Subbarao V.V. Nimmakayala, Dr. Murali Gedda, Dr. Mahesh Peddigari, Dr. Ranganath Gopal Rao, Dr. Partha, Dr. Chandra Sekhar Murapaka, Dr. Suresh Vasimella, Dr. Bheem Raj, Dr. Ramesh, Mr. Amit Singh, Mr. Ravi Kumar Patta, Mrs. Madhu, Mr. Harikrishna Veldandi, Mr. Ravichandra Chilaka, Mr. Rajendra, Mr. Shiva Kumar Gorli, who supported me during my research work.

I am thankful to all the research scholars of Department of Physics for their help and wonderful time shared with me.

Since my mother and father passed away, my brothers had taken the whole responsibilities of the family at home. I would like to thank my brothers Mr. Ch. S. Naidu, Mr. Krishnam Naidu, Mr. Gowru Naidu and Mr. Trinadha for their moral support for all these years. I would like thank my mother-in-law Mrs. Simhachalamma and brother-in-laws Mr. Harikrishna and Mr. Aneel for their constant support in my life.

Last but not the least I thank my wife Gowri and daughter Sudhiksha. My wife stood behind me throughout my struggle. She inspired and motivated me throughout my doctoral work. When my daughter came into this world, my life was forever changed. One look at her

beautiful face, I felt overjoyed and free from all the problems and struggle. Finally I thank God for all his blessings.

Ramakrishna Madaka
IIT Guwahati

PREFACE

In recent years, the use of flexible substrate is becoming a great interest in various applications *viz*. transistors, sensors, solar cells. The flexible substrates have additional advantages such as bendable, less weight, non-breakable, low cost and compatibility with roll-to-roll printing process along with the ease of handling and transportation etc. A few commonly used flexible substrates are polyethylene terephthalate (PET), polyethylene naphthalene (PEN), polyimide (PI), polytetrafluoro-ethylene *(PTFE)*, stainless steel (SS) and paper etc. These substrates need a low deposition temperature (T_s) due to its low deformation temperature and high coefficient of thermal expansion (CTE) limiting the efficiency of solar cells based on materials such as CdTe, CIGS, perovskite and Si. In *a-Si:H* based thin films deposited at low T_s can exhibit poor optoelectronic properties due to voids formation and other effects. In order to improve the *a-Si:H* film quality deposition parameters such as hydrogen dilution, process pressure and rf power etc. are to be optimized.

The main motivation of the present thesis work had been to fabricate *a-Si:H* based solar cells on low cost flexible substrates such as PI, PET and photo paper at low processing temperature (<200^{o}C). Based on this motivation, the objective of the present thesis work had been:

- Deposition of device quality *a-Si:H* films (both intrinsic and doped) at low substrate temperature on flexible substrates by tuning the other deposition parameters such as rf power, hydrogen dilution and substrate temperature in the range of 70-150 ^{o}C.
- Direct fabrication of *n-i-p* solar cells on both glass and flexible substrates at low temperature (≤150 ^{o}C).
- Improvement of overall solar cell efficiency using back reflector, H_2 plasma treatment at interfaces and amorphous silicon carbide as a window layer.

The present thesis consists of seven (07) chapters. Chapter 1 is the Introduction chapter. Chapter 2 gives the brief description of RF-PECVD system which has been used for the deposition of *a-Si:H* single layers and fabrication of solar cells. This chapter also contains a brief description of different characterization techniques used for the study of different properties of single layer thin films and solar cells. Chapter 3 presents the detail studies on the influence of deposition parameters on structural and optoelectronics properties of intrinsic hydrogenated amorphous silicon thin films. Three different series of films were prepared varying one deposition parameter at a time while keeping all the other parameter fixed;

Series (I): Variation of Substrate temperature (T_s) in the temperature range 70-200°C. **Series (II)**: Variation of H_2 flow rate (HFR) during SiH_4 plasma at T_s = 150°C. **Series (III)**: Variation of rf power during silane plasma at T_s = 110°C. Chapter 4 deals with studies on the structural and optoelectronics properties of doped films. Two different series of boron doped and one series of phosphine doped amorphous silicon films were prepared by RF-PECVD technique. **Series (I)**, rf power variation of *a-Si:H*(*p*) thin films at low substrate temperature T_s (=110°C). **Series (II)**, Methane CH_4 flow rate (*MFR*) variation of *a-Si:H*(*p*) thin films at low T_s (T_s=110°C). **Series (III),** Substrate temperature (T_s=90-150°C) variation of *a-Si:H*(*n*) thin films. Chapter 5 describes the studies on structural and optoelectronic properties of indium-tin-oxide (ITO) thin films. Two different series of ITO films are prepared T_s at 100°C by rf-sputtering technique. **Series (I)**: Variation of process pressure and **Series (II)**: Variation of Ar flow rate during deposition of ITO films. Chapter 6 presents the direct fabrication of amorphous silicon solar cells (*n-i-p*) on flexible substrates. The influence of intrinsic layer thickness, back reflector, hydrogen plasma treatment (*HPT*) at *n/i* and *i/p* interface and *a-SiC:H* (*p*) as a window layer on solar cell parameters viz. short circuit current density (J_{sc}), open circuit voltage (V_{oc}), fill factor (*FF*), and efficiency (η(%)) is presented in this chapter. Chapter 7 is the final chapter of the thesis, which summarizes the contents of each chapter and gives the final conclusion based on the work reported in this thesis. The thesis work is concluded with the scope for future work from the present investigation.

LIST OF ABBREVIATIONS AND SYMBOLS

a-Si	Amorphous silicon
a-Si:H	Hydrogenated amorphous silicon
AFM	Atomic force microscope
Ag	Silver
BFR	Boron flow rate
CB	Conduction band
CCD	Charge coupled device
CTE	Coefficient of thermal expansion
EQE	External quantum efficiency
FESEM	Field emissin scanning electron microscopy
FTIR	Fourier transform infrared microscopy
FWHM	Full width at half maxima
HFR	Hydrogen flow rate
HPT	Hydrogen plasma treatment
ITO	Indium tin oxide
MRF	Methane flow rate
MRO	Medium range order
PET	Polyethylene terephthalate
PFR	Phosphine flow rate
PI	Polyimide
PP	Photo paper
RF-PECVD	Radio frequency plasma enhanced chemical vapor deposition
sccm	Standard cubic centimeters per minute
SE	Spectroscopic ellipsometry
SFR	Silane flow rate
SRO	Short range order
SS	Stainless steel
TCO	Transparent conducting oxide
T_s	Substrate temperature
UV-Vis-NIR	Ultraviolet visible near infrared
VB	Valance band
XRD	X-Ray diffraction

TA	Transverse acoustic
LA	Longitudinal acoustic
LO	Longitudinal optical
TO	Transverse optical
J_{sc}	Current density
V_{oc}	Open circuit voltage
FF	Fill factor
η	Efficiency
R_s	Series resistance
R_{sh}	Shunt resistance
$\Delta\theta_B$	rms deviation of tetrahedral angle
Γ	Full width at half maxima of TO mode
B_1	Broadening due to crystallite size
ρ	Resistivity or reflection ratio
$<\varepsilon>$	Pseudo-dielectric function
$<\varepsilon_1>$	Real part of seudo-dielectric function
$<\varepsilon_2>$	Imaginary part of pseudo-dielectric function
A	Amplitude factor
C	Broadening parrameter
E_0	Resonance energy
E	Photon energy
E_g	Optical bandgap
E_a	Activation energy
l	Wavelength
h	Planks constant
υ	frequency
ω	wavenumber
σ	Conductivity
t	thickness of the film
K	Boltzmann constant
T	Temperature in kelvin

TABLE OF CONTENT

LIST OF FIGURES

LIST OF TABLES

Chapter 1

Introduction

Solar energy is one of the alternatives for renewable energy generation. It is extracted directly in the form of electrical energy from solar radiation using photovoltaic (*PV*) solar cells. The *PV* market is dominated by crystalline-silicon based solar cells. However, thin-film solar cells are becoming increasingly important, because these are deposited at relatively low temperatures and as such offer the possibility to produce flexible and light-weight solar panels. The later can be applied, for instance on the roofs of buildings. An important new application area for solar cells is building-integrated photovoltaics (*BIPV*), allowing for individual buildings to generate their own solar power. In *BIPV*, installation cost is reduced greatly since flexible *PV* laminates can be directly bonded to roofing materials and hence no land is required for installation [1]. In recent years, the use of flexible substrate is becoming a great interest in various electronic applications. The flexible substrates have additional advantages such as bendable, less weight, non-breakable, low cost and compatibility with roll-to-roll printing process along with the ease of handling and transportation etc. A few commonly used flexible substrates are polyethylene terephthalate (PET), polyethylene naphthalene (PEN), polyimide (PI), polytetrafluoro-ethylene *(*PTFE), stainless steel (SS) and paper etc. Various types of devices like thin film transistors (TFT) [2, 3], light emitting diode (LED) [4, 5], photo detectors [6], humidity sensors [7] etc. are being made on flexible substrates. Photo paper (PP) also belongs to this category; it is also inexpensive, biodegradable, recyclable etc. In the recent years, a number of devices are fabricated on different type of papers as a substrate like TFT [8-11], humidity sensors [12], batteries [13, 14], LED [15-18] and solar cells [19-22] etc.

A major fraction of solar cells being fabricated worldwide use c-Si wafers which are very expensive. As an effective strategy to reduce the cost of solar cell is to use inexpensive substrates such as glass sheets, metal foils and plastic films for the fabrication of solar cells [23-28]. By using these substrates and a thin layer of silicon, it is possible to significantly reduce the fabrication costs. A number of new materials and technologies like dye synthesized solar cell (DSSC) [29, 30], organic photovoltaic (OPV) [31, 32], perovskite [33,

34], based solar cells are being explored as a cheaper alternative to c-Si based solar cells with relatively high efficiencies. The main bottleneck in commercializing these technologies are, its very short life time (2-3 hours to about one week), low area (<1 cm^2) and more than 2 or 3 different layer processing. The a-Si based solar cells thus hold the promise as a cheaper alternative for different applications because of its very long life time (~25 years). Other thin film solar cells like Cadmium telluride [35, 36] and Copper Indium Gallium Selenide (CIGS) [37] solar cells have inherent difficulties like toxic nature of Cd and scarcity of Indium to make these technologies widely acceptable.

1.1 Issues with flexible substrates

For a number of applications, for example power driven toys, etc. where the life of products itself is not very long (~ 1year), use of solar cells on eco-friendly low cost flexible substrate is desired as these may not contribute much to the waste generated and its subsequent management. Among the flexible substrates, there are several challenges in fabricating thin film solar cells on low cost flexible substrates. These substrates need a low deposition temperature (T_s) due to its low deformation temperature and high coefficient of thermal expansion (CTE); low deformation temperature limiting the T_s for high efficiency solar cells based on materials such as CdTe, CIGS, perovskite and Si [38]. Flexible substrates with high CTE may develop stress and strain in the deposited thin films thus leading to poor device performance or failure of device. However, PI and PET have advantage over other substrates such as lower CTE, low water absorption and are less affected from humidity changes. It is important to point out that plastic substrates face certain other issues that need to be addressed for this to be a commercial success. These include stress in the film that causes curling of the substrate and cracking the film [39, 40]. In addition to that, ion bombardment during plasma deposition and sputtering during TCO deposition also cause stress in a-Si film. In addition, a-Si based thin films deposited at low T_s can exhibit poor optoelectronic properties due to voids formation and other effects. In order to improve the *a-Si:H* film quality deposition parameters such as hydrogen dilution, process pressure and rf power etc. are to be optimized.

1.2 Hydrogenated amorphous silicon

In crystalline silicon (*c-Si*) structure, each silicon atom is covalently bonded to four neighbour atoms. The symmetrical atomic arrangement in *c-Si* structure leads to a long-range order and the bond lengths and band angles between the bonds are equal. In amorphous

silicon (*a-Si*), there is no regular atomic arrangement over a long range due to deviations in coordination number, bond lengths and bond angles between neighbour atoms. As a result this material often considered having a short range ordered structure [41]. The fluctuations in bond angles and bond lengths between the neighboring atoms in *a-Si* result in weak bonds and a small thermal energy can easily break these weak bonds. This process leads to the formation of coordination defects in the atomic network. The coordination defects in *a-Si* are mainly due to Si atoms with threefold coordinated bond, where a Si atom is covalently bonded to only three neighboring atoms leaving behind an unpaired electron. These unpaired electrons are called dangling bonds [42]. In *a-Si*, the concentration of these dangling bonds is the order of 10^{21} cm^{-3}, which results in poor optoelectronic properties to fabricate any device. However, with incorporation of hydrogen (H_2) gas into the amorphous silicon atomic network during deposition, the dangling bonds are passivated with atomic hydrogen. In this process, the concentration of dangling bonds is reduced to $\leq 10^{16} cm^{-3}$. The material is usually named as hydrogenated amorphous silicon (*a-Si:H*). This *a-Si:H* material show good optoelectronic properties to fabricate devices. The main difference between *a-Si:H* and *c-Si* is the density of states. The schematic diagram of density of states versus energy for *c-Si* and *a-Si:H* is shown in Figure 1.1.

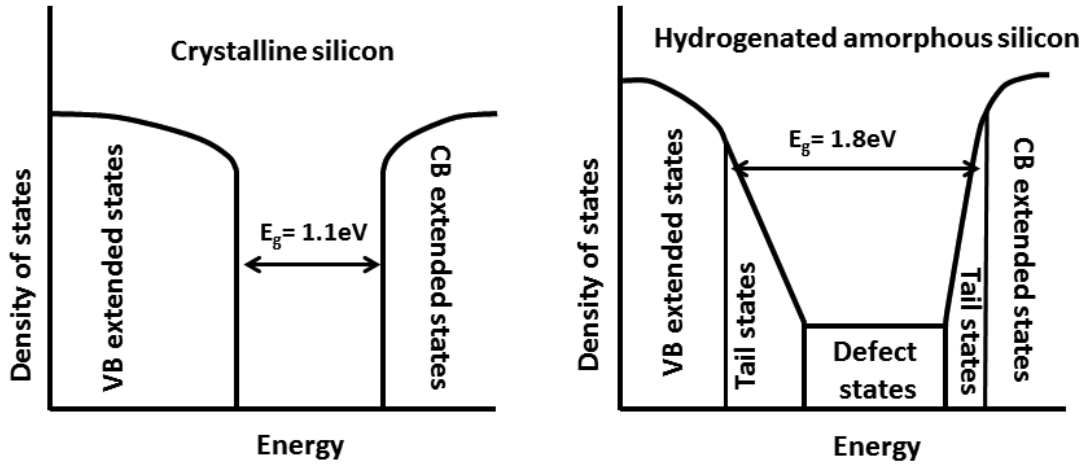

Figure 1.1*: Schematic diagram of density of states vs energy plot for c-Si and a-Si:H* [41, 42].

In *c-Si*, optical band gap (E_g) is well defined due to the long-range order of the atomic structure. It is defined as the energy difference between the maximum of the valence band (*VB*) and minimum of the conduction band (*CB*). But in case of *a-Si:H*, the bonding disorder in the material causes spreading of the *VB* and *CB* states into the E_g. This forms regions of localized states that are called as band tails. In addition to these band tails, coordination

defects create some deep energy states between the *VB* and *CB* edges. Due to the localized nature of these states, the charge carrier mobility in these energy regions is much smaller than that in the extended states beyond the *VB* and *CB* edges. Consequently, the threshold energy levels which characterize this mobility difference is used to define the optical band gap (E_g) with a typical value of 1.7-1.9 eV in *a-Si:H* [41].

Several deposition techniques have been established to prepare amorphous silicon films including Sputtering [43], Pulsed laser deposition (PLD) [44], Remote plasma CVD (RP-CVD) [45], Microwave plasma enhanced chemical vapour deposition (MW-PECVD) [46], Photo CVD [47], Very high frequency plasma enhanced CVD (VHF-PECVD) [39], Hot wire CVD (HWCVD) [48] and Radio frequency plasma enhanced CVD (RF-PECVD) [49]. Among them, RF-PECVD is the promising and widely used deposition technique for the preparation of amorphous silicon films as well as other alloys of silicon. The scientific community has adapted a standard frequency of 13.56 MHz for this technique which is used for industrial applications also [50-52]. The advantage of this technique is that high quality films are deposited uniformly over a large area at low substrate temperature. The technique thus has a potential for industrial applications.

The *a-Si:H* films consist of different silicon phases (polymorphous, nanocrystalline and microcrystalline, etc.) [53]. The growth of different phases depends upon the deposition parameters which control the structural and optoelectronic properties of these films. Hydrogen dilution improves the material quality by passivating dangling bonds; however deposition rates are drastically reduced [54]. Heavy hydrogen dilution may result in change of phase of films from pure amorphous to microcrystalline. The silicon films prepared in the regime of amorphous to microcrystalline transition have attracted a great deal of attention because solar cells with stable performance can be prepared at a hydrogen dilution ratio just below the onset of microcrystallinity [55]. A specific phase of amorphous silicon, in which nanocrystallites are embedded in amorphous matrix, also called as polymorphous hydrogenated amorphous silicon (*pm-Si:H*) or proto type hydrogenated amorphous silicon, exhibits lower density of states in the gap in comparison to amorphous silicon film [56, 57]. Presence of nanocrystallites in the amorphous matrix results in improvement in short and medium range order and thus these films have superior optoelectronic transport and structural properties and also a dense homogeneous amorphous network as compared to pure *a-Si:H* [58]. Figure 1.2 shows the phase diagram for the growth of silicon film with the dilution ratio

and thickness [59]. The phase transition is also possible with dilution with gases like Argon [60]. The optoelectronic properties of these nanocrystallites embedded films are less influenced by Staebler-Wronski (S-W) effect [61] (optoelectronic properties of *a-Si:H* films are changed when exposed to the light for a long time. During this process, weak Si-Si bonds break as a result the defect density in the film increases). In order to optimize the preparation conditions to make device quality films the correlation between the preparation conditions and the structure of the material, the hydrogen configuration and optoelectronic properties as well as stability of the material need to be studied carefully.

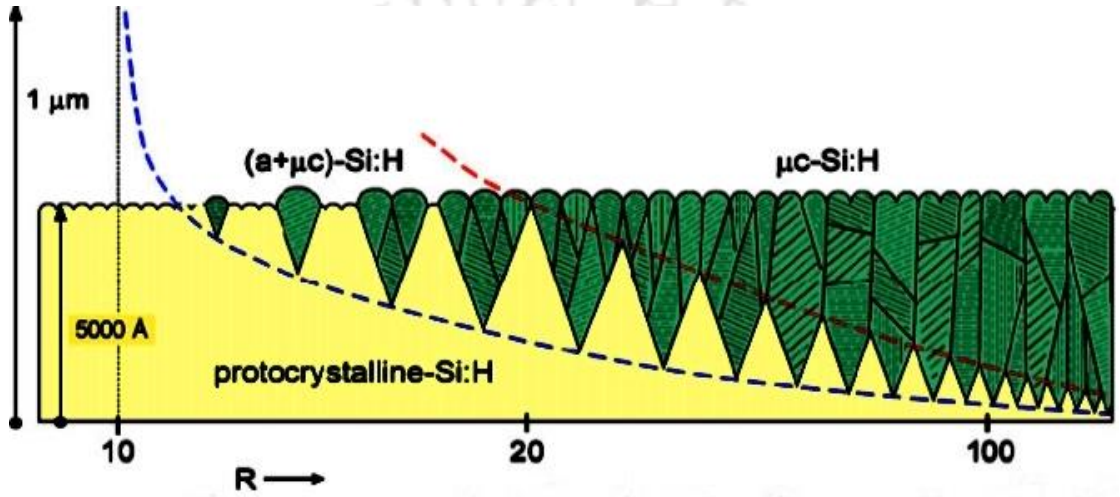

***Figure 1.2**: phase diagram of a-Si:H film with hydrogen dilution* [59].

Thin films deposited at low T_s are often porous and more disordered and exhibit poor optoelectronic properties though the quality of the films deposited at low T_s can be improved by changing the deposition parameters such as rf power and hydrogen dilution in SiH_4 by RF-PECVD technique. It is believed that SiH_3 radical is the main precursor responsible for the growth of *a-Si:H* and *µc-Si:H* films however the exact microstructure depends upon the relative concentration of short lived species like SiH, SiH_2, Si and long lived SiH_3 radical plasma during growth [62, 63]. The concentration of different radical in the plasma depends upon the growth parameters like SiH_4 flow rate, rf power and process pressure. In addition, density of atomic hydrogen in plasma, which primarily depends upon the H_2/SiH_4 ratio also controls the growth of *a-Si:H*/*nc-Si:H* phases [62]. The atomic hydrogen arriving at the surface of growing films breaks the weak Si-Si bonds through etching and replaces it with strong Si-Si bonds. Atomic hydrogen can also diffuse into the film and rearrange the bonding thus favors the growth of more ordered *a-Si:H* films and also *nc-Si:H* films[62]. The rate of impingement and diffusion of incoming species and their desorption determine the overall

microstructure and thus the optoelectronic properties of the films [64]. In addition to hydrogen dilution, rf power mainly control, the rate of dissociation of the gas and also the deposition rate. Verkeek *et al* [65] reported that total ion energy carried to growing silicon film was strongly reduced when the deposition temperature was lowered from 200°C to 39°C at a constant silane concentration. Long *et al* [66] reported that plasma density and ion energy both increase with increasing applied rf power. At low rf powers, most of ions lose their energy through ion-neutral collisions, whereas at high rf powers some of the ions, after colliding with neutrals, are energetic even after collision. The strong sheath field accelerates these ions towards substrate leading to strong ion bombardment. Increase of high rf power also leads to generation of higher silane radicals and powder formation. In order to provide a device graded *a-Si:H* thin film, an optimum rf power is required. Film properties also depend upon choice of substrate.

A number of models have been proposed to understand the growth of amorphous silicon films with different phases by depositing films under different deposition conditions [64, 67, 68]. It is difficult to experimentally probe growing surface on nanoscopic level and observe the physio-chemical process that take place during deposition, especially in RF-PECVD process where a number of species impinge on the growing surface and the flux of these species depends upon the deposition conditions and film properties may vary significantly [62]. The growth of *a-Si:H* and *μc-Si:H*/*nc-Si:H* films has also been studied using molecular dynamics (MD) simulations and by correlating the microstructure and optoelectronic properties of these films deposited under different deposition conditions [69, 70]. These models predict that when SiH_3 is the sole precursor, the films are much smooth and exhibit superior optoelectronic properties.

1.3 Thin film silicon solar cell structure

Solar cell, also called as photovoltaic cell generates electricity directly from visible light by means of the photovoltaic effect. In principle, solar cell consists of a junction between *p*- type and *n*- type semiconductors. In hydrogenated amorphous silicon solar cells, doping of amorphous material creates a large concentration of defects and reduces the diffusion length of minority carriers. Due to short diffusion length of photo-generated carriers, they would recombine in the doped layers before reaching the depletion region at *p-n* junction. Addition of intrinsic layer between *p*- and *n*- layers can resolve the above mentioned problem. In *n-i-p* or *p-i-n* structure, the intrinsic layer acts as an absorber layer. The thin doped layers build upon internal electric field across the absorber layer. In these configurations, electron-hole

pairs are mainly generated in the intrinsic layer and encounter the internal electric field, which facilitate separation of electrons and holes and, thus, avoids their recombination. The field assisted travel distance is given by the drift length. The separated electrons and holes move towards the doped layers and are collected by the respective electrode.

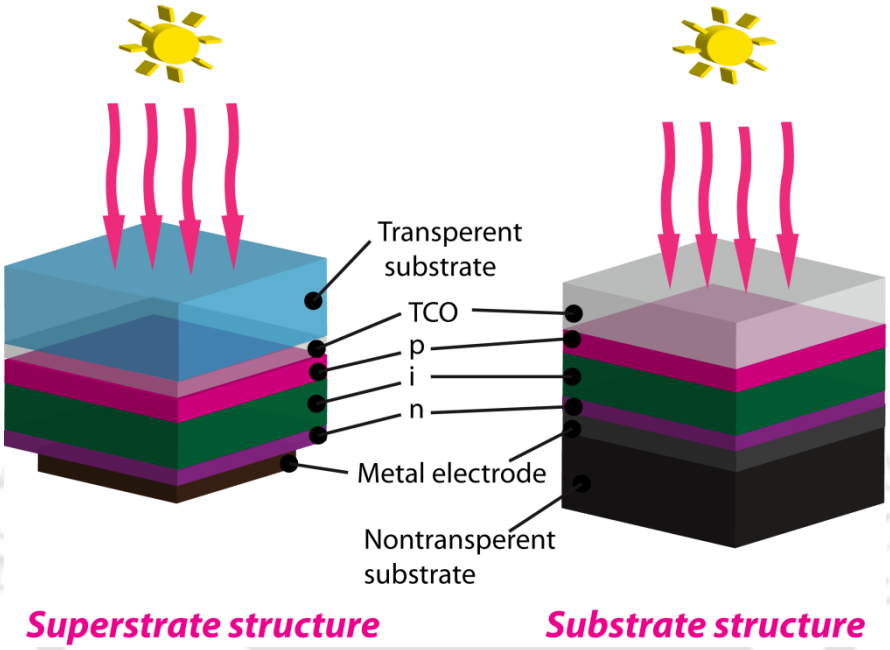

***Figure 1.3**: Schematic diagram of superstrate (p-i-n) and substrate (n-i-p) structure of solar cell.*

The structure of solar cells is defined on the basis of sequence of doped and undoped layers. In silicon based solar cells two different structures are possible; (1) *p-i-n* structure (superstrate structure), (2) *n-i-p* structure (substrate structure). The schematic diagram of *p-i-n* and *n-i-p* structures is shown in Figure 1.3 (Superstrate and substrate).

In *p-i-n* structure, the *p-i-n* layers are sequentially deposited on transparent conducting oxide (TCO) coated substrate. In this structure, front contact and substrate should be transparent. In the case of *n-i-p* structure, the sequence of *n-i-p* layers is grown on the opaque substrate. In both structures, *i-* layer is the main absorber layer which is inserted between *p-* and *n-* layer for optimum utilization of incident light. The electric field must extend through the entire cell thickness. The typical thickness of each layer in both configuration is; *p-* layer ~20-30 nm, *i-* layer ~ 300-400 nm, *n-* layer ~ 20-25 nm, *TCO* ~ 250 nm and *Ag* ~ 100 nm for contacts [71-74]. The doping levels of *p-* and *n-* layers should be high enough to ensure ohmic contacts and high electric fields. The optimization of *p-* layer is very challenging step, because sun light enters through *p*-layer, which serves as a window layer. This window layer allows transmission of the maximum portion of photons incident on it to reach the absorber layer to

generate charge carriers. If *p*- layer thickness is too less, it may not be possible to sustain electric field over the intrinsic region of the solar cell. In this case, collection of generated carriers will be reduced. At higher thickness, high defect density has determinable effect on the incoming light. Photon absorption in doped layers leads to photo-generated carriers which cannot be collected. The short wavelength generated carriers recombine in with the *p*- layer. As a result, people try to minimize the thickness of these layers and make them as transparent as possible to the incoming photons.

Another essential layer in solar cell is transparent conducting oxide (*TCO*) layer. Solar cells require a wide bandgap transparent conductor as window electrode for efficient light transmission as well as extraction of photocurrent. The *TCO*s have good electrical conductivity and high transmission (>90%) in the visible spectrum. The most commonly used *TCO*s for front electrode are zinc oxide (*ZnO*) [75], Aluminum doped zinc oxide (*ZnO:Al*), tin dioxide (SnO_2) [76] and indium tin oxide (*ITO*). Different methods are used for *ITO* thin film deposition including spray pyrolysis [77], chemical vapor deposition [78], radio frequency (RF) sputtering [79], direct current (DC) sputtering [80], etc. In case of thin film solar cells RF sputtering method shows better uniformity and better adhesion to the substrates as compared to other deposition methods [81].

1.4 Technology overview

Fabrication of thin film *a-Si:H* based solar cells on flexible substrates started in early 1980s and gaining significant importance now a days. Table 1.1 provides overview of solar cells fabricated on different flexible substrates. Okaniwa *et al* [82] has reported the first fabrication of *n-i-p a-Si:H* solar cells on PI (Kapton ®) substrates in 1982. They achieved a low short-circuit current density due to the surface defects of PI films. To solve this problem, M. Yano *et al* [83] suggested using PET instead of PI films, as the PET substrates had a much smoother surface than PI films. Finally, they succeeded in fabrication of solar cells with efficiency of 5.5%. Until 2002, researchers have employed amorphous silicon as the active layer in their solar cells. Generally, due to the light-induced degradation effects, the efficiency of amorphous silicon solar cells is low (5-7%). Microcrystalline silicon has a much moderate form of light induced degradation. Moreover, due to the lower bandgap of this material compared to the amorphous silicon, it has a high capacity for absorption in the near infrared region. Mase *et al*. [40] employed this new material to fabricate a single junction *n-i-p* solar cell on Ethylene-Tetracyclododecene (E/TD) copolymer and they achieved an

efficiency of 6% with thick (~1μm) microcrystalline silicon absorbing layer order. By using proper light management techniques such as substrate texturing, one can increase the effective optical path within the solar cell. Using this method, T. Takeda *et al*. [84] obtained an efficiency of 8.1% and a high short-circuit current of 25.8 mA/cm^2 in a single junction *n-i-p* structure.

Table 1.1*: Substrate, solar cell structure, substrate temperature and parameters of thin film silicon solar cells on flexible substrates*

Substrate	structure	T_s (°C)	*i*- layer	J_{sc} (mA/cm^2)	V_{oc} (mV)	*FF*	η (%)	Ref.
PI	*p-i-n*	300	*a-Si*	10.42	898	0.62	6.38	[82]
PI	*p-i-n*	180	*a-Si*	8.50	823	0.62	4.30	[85]
PI	*n-i-p*	240	*a-Si*	15.10	906	0.64	8.70	[86]
PI	*n-i-p*	N/A	*a-Si/a-SiGe*	7.06	2097	N/A	9.86	[87]
PI	*n-i-p*	150	*a-Si*	17.20	397	0.33	2.20	[88]
PI	*n-i-p*	N/A	*µc-Si*	23.10	475	0.68	7.50	[89]
PI	*n-i-p*	150	*a-Si*	10.40	850	0.52	4.63	[73]
PEN	*n-i-p*	100	*a-Si*	10.40	920	0.58	5.52	[39]
PEN	*n-i-p*	<200	*a-Si*	14.40	895	0.67	8.70	[24]
PEN	*n-i-p*	150	*nc-Si*	12.50	900	0.57	6.30	[90]
PET	*p-i-n*	N/A	*a-Si*	15.30	880	0.67	9.00	[83]
PET	*n-i-p*	N/A	*a-Si*	12.50	877	0.69	7.62	[91]
PET	*n-i-p*	N/A	*µc-Si*	17.90	501	0.72	6.46	[91]
PET	*n-i-p*	N/A	*a-Si/ µc-Si*	9.4/12.1	1330	0.68	8.30	[91]
PET	*n-i-p*	N/A	*µc-Si*	12.50	850	0.54	5.80	[92]
PET	*p-i-n*	110	*a-Si*	8.80	908	0.61	4.90	[38]
PET	*n-i-p*	150	*µc-Si*	23.10	512	0.73	8.70	[93]
PET	*p-i-n*	125	*a-Si*	6.82	980	0.69	4.60	[94]
PET	*n-i-p*	100	*a-Si*	11.13	910	0.55	5.56	[39]
SS	*n-i-p*	N/A	*µc-Si*	20.23	459	0.59	5.50	[95]
SS	*n-i-p*	N/A	*µc-Si*	20.22	503	0.59	6.01	[95]
SS	*n-i-p*	100	*µc-Si*	11.20	840	0.52	5.30	[96]

Recently a process has been developed for texturization on polyimide (PI) substrates [97]. In this process, textured SnO_2*:F/glass* from Asahi-U has been used as the template. A 100 nm SiO_x buffer layer was coated onto a textured template and then the PI film was coated over the textured SiO_x buffer layer surface using a slot/blade coating technique. After curing, PI film of 40 nm thick was peeled off from the template and then pasted onto a glass substrate. The initial efficiency of 6.74% was reported for cells, which are fabricated on textured PI substrate. Yukimi Ichikawa *et al*.[98] have reported efficiency of 4.9% single junction cells on untextured PET substrate at 110^{o}C. Later the same group has reported stabilized efficiency of 8.1% in *a-Si:H/a-Si:H* tandem cells, while for multijunction cells an initial efficiency between 13 and 15% has been reported. Karen Wilken *et al*. [99] have reported 6 % efficiency with nanoimprint on PET substrate. Rath *et al*. [39] have reported 5.9 % and 7.7 % efficiencies of *a-Si:H* based single junction solar cells fabricated directly on polymer substrate as well as by transfer process using Helianthos concept respectively. In transfer process, solar cells were first fabricated on temporary substrate at high temperature and then transferred to a permanent polymer substrate. The transfer of the cell from a temporary to permanent substrate is a sophisticated and critical issue here.

1.5 Motivation and content of the present thesis

As mentioned above fabrication of solar cells on flexible substrates is challenging because flexible substrates have low glass transition temperature. At low T_s, amorphous silicon film exhibit poor optoelectronic properties. In this sense, RF-PECVD technique has finite advantage to deposit amorphous silicon layers at low T_s with good opto-electronic properties as well as fabrication of solar cells. Though a few reports are available on direct fabrication of *a-Si:H* based solar cells on flexible substrate by RF-PECVD technique. The main motivation of the present thesis work had been to fabricate *a-Si:H* based solar cells on low cost flexible substrates such as PI, PET and photo paper at low processing temperature (<200^{o}C). Based on this motivation, the objective of the present Ph.D. thesis work had been:

- Deposition of device quality *a-Si:H* films (both intrinsic and doped) at low substrate temperature on flexible substrates by tuning the other deposition parameters such as rf power, hydrogen dilution and substrate temperature in the range of 70-150 ^{o}C.
- Direct fabrication of *n-i-p* solar cells on both glass and flexible substrates at low temperature (≤150 ^{o}C).

- Improvement of overall solar cell efficiency using back reflector, H_2 plasma treatment at interfaces and amorphous silicon carbide as a window layer.

The present thesis consists of seven (07) chapters. Chapter 1 is the Introduction chapter. Chapter 2 gives the brief description of RF-PECVD system which has been used for the deposition of *a-Si:H* single layers and fabrication of solar cells. This chapter also contains a brief description of different characterization techniques used for the study of different properties of single layer thin films and solar cells.

Chapter 3 presents the detail studies on the influence of deposition parameters on structural and optoelectronics properties of intrinsic hydrogenated amorphous silicon thin films. Three different series of films were prepared varying one deposition parameter at a time while keeping all the other parameter fixed; **Series (I)**: Variation of Substrate temperature (T_s) in the temperature range 70-200°C. **Series (II)**: Variation of H_2 flow rate (HFR) during SiH_4 plasma at T_s = 150°C. **Series (III)**: Variation of rf power during silane plasma at T_s = 110°C.

Chapter 4 deals with studies on the structural and optoelectronics properties of doped films. Two different series of boron doped and one series of phosphine doped amorphous silicon films were prepared by RF-PECVD technique. **Series (I)**, rf power variation of *a-Si:H*(*p*) thin films at low substrate temperature T_s (=110°C). **Series (II)**, Methane CH_4 flow rate (*MFR*) variation of *a-Si:H*(*p*) thin films at low T_s (T_s=110°C). **Series (III),** Substrate temperature (T_s=90-150°C) variation of *a-Si:H*(*n*) thin films.

Chapter 5 describes the studies on structural and optoelectronic properties of indium-tin-oxide (*ITO*) thin films. Two different series of ITO films are prepared T_s at 100°C by rf-sputtering technique. **Series (I)**: Variation of process pressure and **Series (II)**: Variation of Ar flow rate during deposition of *ITO* films.

Chapter 6 presents the direct fabrication of amorphous silicon solar cells (*n-i-p*) on flexible substrates. The influence of intrinsic layer thickness, back reflector, hydrogen plasma treatment (*HPT*) at *n/i* and *i/p* interface and *a-SiC:H* (*p*) as a window layer on solar cell parameters viz. short circuit current density (J_{sc}), open circuit voltage (V_{oc}), fill factor (*FF*), and efficiency (η(%)) is presented in this chapter.

Chapter 7 is the final chapter of the thesis, which summarizes the contents of each chapter and gives the final conclusion based on the work reported in this thesis. The thesis work is concluded with the scope for future work from the present investigation.

1.6 References

[1] E. Biyik, M. Araz, A. Hepbasli, M. Shahrestani, R. Yao, L. Shao, E. Essah, A.C. Oliveira, T. del Caño, E. Rico, J.L. Lechón, L. Andrade, A. Mendes, Y.B. Atlı, A key review of building integrated photovoltaic (BIPV) systems, *Engineering Science and Technology*, **20** (2017) 833-858.

[2] C.M. Chou, C.W. Chang, K.H. Wen, V.K.S. Hsiao, Plasma-enhanced chemical vapor-deposited organic dielectric layer for low voltage, flexible organic thin-film transistor, *Surface and Coatings Technology*, **320** (2017) 554-558.

[3] Y.H. Lee, M. Jang, M.Y. Lee, O.Y. Kweon, J.H. Oh, Flexible Field-Effect Transistor-Type Sensors Based on Conjugated Molecules, *Chem*, **3** (2017) 724-763.

[4] K.M. Lee, R. Fardel, L. Zhao, C.B. Arnold, B.P. Rand, Enhanced outcoupling in flexible organic light-emitting diodes on scattering polyimide substrates, *Organic Electronics*, **51** (2017) 471-476.

[5] K.A. Knauer, E. Najafabadi, W. Haske, M.P. Gaj, K.C. Davis, C. Fuentes-Hernandez, U. Carrasco, B. Kippelen, Stacked inverted top-emitting green electrophosphorescent organic light-emitting diodes on glass and flexible glass substrates, *Organic Electronics*, **14** (2013) 2418-2423.

[6] M. Xi, X. Wang, Y. Zhao, Q. Feng, F. Zheng, Z. Zhu, H. Fong, Mechanically flexible hybrid mat consisting of TiO2 and SiO2 nanofibers electrospun via dual spinnerets for photo-detector, *Materials Letters*, **120** (2014) 219-223.

[7] C.Z. Thomas Kinkeldei, Niko Münzenriederand Gerhard Tröster, Influence of flexible substrate materials on the performance of polymer composite gas sensors, *The 14th International Meeting on Chemical Sensors*, DOI 10.5162/imcs2012/6.2.4(2012) 537-540.

[8] J.-H. Seo, T.-H. Chang, J. Lee, R. Sabo, W. Zhou, Z. Cai, S. Gong, Z. Ma, Microwave flexible transistors on cellulose nanofibrillated fiber substrates, *Applied Physics Letters*, **106** (2015) 262101.

[9] N. Liu, K.N. Yun, H.-Y. Yu, J.H. Shim, C.J. Lee, High-performance carbon nanotube thin-film transistors on flexible paper substrates, *Applied Physics Letters*, **106** (2015) 103106.

[10] M. Trifunovic, T. Shimoda, R. Ishihara, Solution-processed polycrystalline silicon on paper, *Applied Physics Letters*, **106** (2015) 163502.

[11] T. Shimoda, Y. Matsuki, M. Furusawa, T. Aoki, I. Yudasaka, H. Tanaka, H. Iwasawa, D. Wang, M. Miyasaka, Y. Takeuchi, Solution-processed silicon films and transistors, *Nature*, **440** (2006) 783-786.

[12] C. Steffens, A. Manzoli, R.T. Paschoalin, L. Tiggemann, J. Steffens, E. Teixeira, P.S.d.P. Herrmann, Tracing paper substrate used for development of interdigitated graphite electrode and its application as humidity sensor, *Synthetic Metals*, **183** (2013) 36-39.

[13] K. Sun, D.A. Juarez, H. Huang, E. Jung, S.J. Dillon, Aqueous lithium ion batteries on paper substrates, *Journal of Power Sources*, **248** (2014) 582-587.

[14] L. Hu, N. Liu, M. Eskilsson, G. Zheng, J. McDonough, L. Wågberg, Y. Cui, Silicon-conductive nanopaper for Li-ion batteries, *Nano Energy*, **2** (2013) 138-145.

[15] H. Zhu, Z. Fang, Z. Wang, J. Dai, Y. Yao, F. Shen, C. Preston, W. Wu, P. Peng, N. Jang, Q. Yu, Z. Yu, L. Hu, Extreme Light Management in Mesoporous Wood Cellulose Paper for Optoelectronics, *ACS Nano*, **10** (2016) 1369-1377.

[16] H. Zhu, Z. Xiao, D. Liu, Y. Li, N.J. Weadock, Z. Fang, J. Huang, L. Hu, Biodegradable transparent substrates for flexible organic-light-emitting diodes, *Energy & Environmental Science*, **6** (2013) 2105.

[17] D.-Y. Yoon, D.-G. Moon, Bright flexible organic light-emitting devices on copy paper substrates, *Current Applied Physics*, **12** (2012) e29-e32.

[18] D.-Y. Yoon, T.-Y. Kim, D.-G. Moon, Flexible top emission organic light-emitting devices using sputter-deposited Ni films on copy paper substrates, *Current Applied Physics*, **10** (2010) 135-138.

[19] L. Leonat, M.S. White, E.D. Głowacki, M.C. Scharber, T. Zillger, J. Rühling, A. Hübler, N.S. Sariciftci, 4% Efficient Polymer Solar Cells on Paper Substrates, *The Journal of Physical Chemistry C*, **118** (2014) 16813-16817.

[20] Y. Zhou, C. Fuentes-Hernandez, T.M. Khan, J.C. Liu, J. Hsu, J.W. Shim, A. Dindar, J.P. Youngblood, R.J. Moon, B. Kippelen, Recyclable organic solar cells on cellulose nanocrystal substrates, *Scientific reports*, **3** (2013) 1536.

[21] T. Masuda, N. Sotani, H. Hamada, Y. Matsuki, T. Shimoda, Fabrication of solution-processed hydrogenated amorphous silicon single-junction solar cells, *Applied Physics Letters*, **100** (2012) 253908.

[22] B. Wang, L.L. Kerr, Dye sensitized solar cells on paper substrates, *Solar Energy Materials and Solar Cells*, **95** (2011) 2531-2535.

[23] K. Beernink, A. Banerjee, J. Yang, K. Lord, F. Liu, G. DeMaggio, G. Pietka, C. Worrel, S. Guha, Flexible, Lightweight, Amorphous Silicon Based Solar Cells on Polymer Substrate for Space and Near-Space Applications, *MRS Proceedings*, **1321** (2011).

[24] T. Soderstrom, F.J. Haug, V. Terrazzoni-Daudrix, C. Ballif, Optimization of amorphous silicon thin film solar cells for flexible photovoltaics, *Journal of Applied Physics*, **103** (2008).

[25] J. Fang, B. Yan, T. Li, C. Wei, D. Zhang, B. Li, Q. Huang, X. Chen, G. Hou, G. Wang, Y. Zhao, X. Zhang, Substrate effect on ultra-thin hydrogenated amorphous silicon solar cells, *Solar Energy Materials and Solar Cells*, **171** (2017) 222-227.

[26] Y. Zhou, F. Zhang, K. Tvingstedt, W. Tian, O. Inganäs, Multifolded polymer solar cells on flexible substrates, *Applied Physics Letters*, **93** (2008) 033302.

[27] R. Biron, S. Hänni, M. Boccard, C. Pahud, K. Söderström, M. Duchamp, R. Dunin-Borkowski, G. Bugnon, L. Ding, S. Nicolay, G. Parascandolo, F. Meillaud, M. Despeisse, F.-J. Haug, C. Ballif, New progress in the fabrication of n–i–p micromorph solar cells for opaque substrates, *Solar Energy Materials and Solar Cells*, **114** (2013) 147-155.

[28] K. Tao, D. Zhang, L. Wang, J. Zhao, H. Cai, Y. Sui, Z. Qiao, Q. He, Y. Zhang, Y. Sun, Development of textured back reflector for n–i–p flexible silicon thin film solar cells, *Solar Energy Materials and Solar Cells*, **94** (2010) 709-714.

[29] R. Bashir, A.R. Makhdoom, M.K. Bilal, M. Ahmad Badar, Comparative study of the photovoltaic behavior of ruthenium and the other organic and inorganic Dye-Sensitized Solar Cells (DSSC), *Optik*, **157** (2018) 11-15.

[30] M.S. Su'ait, M.Y.A. Rahman, A. Ahmad, Review on polymer electrolyte in dye-sensitized solar cells (DSSCs), *Solar Energy*, **115** (2015) 452-470.

[31] Z. Ding, V. Stoichkov, M. Horie, E. Brousseau, J. Kettle, Spray coated silver nanowires as transparent electrodes in OPVs for Building Integrated Photovoltaics applications, *Solar Energy Materials and Solar Cells*, **157** (2016) 305-311.

[32] J.E. Carlé, F.C. Krebs, Technological status of organic photovoltaics (OPV), *Solar Energy Materials and Solar Cells*, **119** (2013) 309-310.

[33] M.K. Assadi, S. Bakhoda, R. Saidur, H. Hanaei, Recent progress in perovskite solar cells, *Renewable and Sustainable Energy Reviews*, **81** (2018) 2812-2822.

[34] M. Azam, S. Yue, K. Liu, Y. Sun, J. Liu, K. Ren, Z. Wang, S. Qu, Z. Wang, Insights on the correlation of precursor solution, morphology of the active layer and performance of the pervoskite solar cells, *Journal of Alloys and Compounds*, **731** (2018) 375-380.

[35] J.-K. Sim, S. Kang, R. Nandi, J.-Y. Jo, K.-U. Jeong, C.-R. Lee, Implementation of graphene as hole transport electrode in flexible CIGS solar cells fabricated on Cu foil, *Solar Energy*, **162** (2018) 357-363.

[36] A. Romeo, E. Artegiani, D. Menossi, Low substrate temperature CdTe solar cells: A review, *Solar Energy*, DOI: https://doi.org/10.1016/j.solener.2018.02.038(2018).

[37] R.L. Garris, S. Johnston, J.V. Li, H.L. Guthrey, K. Ramanathan, L.M. Mansfield, Electrical characterization and comparison of CIGS solar cells made with different structures and fabrication techniques, *Solar Energy Materials and Solar Cells*, **174** (2018) 77-83.

[38] Y. Ishikawa, M.B. Schubert, Flexible protocrystalline silicon solar cells with amorphous buffer layer, *Japanese Journal of Applied Physics*, **45** (2006) 6812-6822.

[39] J.K. Rath, M. Brinza, Y. Liu, A. Borreman, R.E.I. Schropp, Fabrication of thin film silicon solar cells on plastic substrate by very high frequency PECVD, *Solar Energy Materials and Solar Cells*, **94** (2010) 1534-1541.

[40] H. Mase, M. Kondo, A. Matsuda, Microcrystalline silicon solar cells fabricated on polymer substrate, *Solar Energy Materials and Solar Cells*, **74** (2002) 547-552.

[41] R.A. Street, *Hydrogenated Amorphous Silicon*, Cambridge University Press1992.

[42] A. Shah, *Thin-Film Silicon Solar Cells*, EPFL Press, 2010.

[43] G. Morell, R.S. Katiyar, S.Z. Weisz, H. Jia, J. Shinar, I. Balberg, Raman study of the network disorder in sputtered and glow discharge a-Si:H films, *Journal of Applied Physics*, **78** (1995) 5120-5125.

[44] R. Ayouchi, R. Schwarz, L.V. Melo, R. Ramalho, E. Alves, C.P. Marques, L. Santos, R. Almeida, O. Conde, Morphological and optical properties of silicon thin films by PLD, *Applied Surface Science*, **255** (2009) 5299-5302.

[45] S.C. Kim, M.H. Jung, J. Jang, Growth of microcrystal silicon by remote plasma chemical vapor deposition, *Applied Physics Letters*, **58** (1991) 281-283.

[46] H. Jia, H. Kuraseko, H. Fujiwara, M. Kondo, Ultrafast deposition of microcrystalline silicon films using high-density microwave plasma, *Solar Energy Materials and Solar Cells*, **93** (2009) 812-815.

[47] R.E. Rocheleau, S.S. Hegedus, W.A. Buchanan, S.C. Jackson, Novel photochemical vapor deposition reactor for amorphous silicon solar cell deposition, *Applied Physics Letters*, **51** (1987) 133-135.

[48] P. Gogoi, H.S. Jha, P. Agarwal, Variation of microstructure and transport properties with filament temperature of HWCVD prepared silicon thin films, *Thin Solid Films*, **519** (2011) 4506-4510.

[49] J. He, C. Wang, W. Li, K.C. Qi, Y.D. Jiang, Effect of gas temperature on the structural and optoelectronic properties of a-Si:H thin films deposited by PECVD, *Surface Coating Technology*, **214** (2013) 131-137.

[50] W. Liu, L. Zhang, S. Cong, R. Chen, Z. Wu, F. Meng, Q. Shi, Z. Liu, Controllable a-Si:H/c-Si interface passivation by residual SiH_4 molecules in H_2 plasma, *Solar Energy Materials and Solar Cells*, **174** (2018) 233-239.

[51] J. Fang, Z. Chen, G. Hou, F. Wang, X. Chen, C. Wei, G. Wang, J. Sun, D. Zhang, Y. Zhao, X. Zhang, High-quality hydrogenated intrinsic amorphous silicon oxide layers treated by H2 plasma used as the p/i buffer layers in hydrogenated amorphous silicon solar cells, *Solar Energy Materials and Solar Cells*, **136** (2015) 172-176.

[52] J. Ma, J. Ni, J. Zhang, Q. Liu, G. Hou, X. Chen, X. Zhang, X. Geng, Y. Zhao, The influence of perpendicular transport behavior on the properties of n-i-p type amorphous silicon solar cells, *Solar Energy Materials and Solar Cells*, **120** (2014) 635-641.

[53] A. Fontcuberta i Morral, P. Roca i Cabarrocas, C. Clerc, Structure and hydrogen content of polymorphous silicon thin films studied by spectroscopic ellipsometry and nuclear measurements, *Physical Review B*, **69** (2004).

[54] A. Remolina, B.M. Monroy, M.F. Garcia-Sanchez, A. Ponce, M. Bizarro, J.C. Alonso, A. Ortiz, G. Santana, Polymorphous silicon thin films obtained by plasma-enhanced chemical vapor deposition using dichlorosilane as silicon precursor, *Nanotechnology*, **20** (2009) 245604.

[55] Y.M. Soro, A. Abramov, M.E. Gueunier-Farret, E. Johnson, C. Longeaud, P.R.I. Cabarrocas, J.P. Kleider, Device grade hydrogenated polymorphous silicon deposited at high rates, *Journal of Non-Crystalline Solids*, **354** (2008) 2092-2095.

[56] P.R.I. Cabarrocas, A. Fontcuberta i Morral, Y. Poissant, Growth and optoelectronic properties of polymorphous silicon thin films, *Thin Solid Films*, **403-404** (2002) 39-46.

[57] P.R.I. Cabarrocas, N. Chaâbane, A.V. Kharchenko, S. Tchakarov, Polymorphous silicon thin films produced in dusty plasmas: application to solar cells, *Plasma Physics and Controlled Fusion*, **46** (2004) B235-B243.

[58] P.R.I. Cabarrocas, Plasma enhanced chemical vapor deposition of amorphous, polymorphous and microcrystalline silicon films, *Journal of Non-Crystalline Solids*, **266** (2000) 31-37.

[59] C.R. Wronski, J.M. Pearce, J. Deng, V. Vlahos, R.W. Collins, Intrinsic and light induced gap states in a-Si:H materials and solar cells effects of microstructure, *Thin Solid Films*, **451-452** (2004) 470-475.

[60] P. Gogoi, P.N. Dixit, P. Agarwal, Amorphous silicon films with high deposition rate prepared using argon and hydrogen diluted silane for stable solar cells, *Solar Energy Materials and Solar Cells*, **91** (2007) 1253-1257.

[61] D.L. Staebler, C.R. Wronski, Reversible conductivity changes in discharge-produced amorphous Si, *Applied Physics Letters*, **31** (1977) 292-294.

[62] A. Matsuda, Microcrystalline silicon. Growth and device application, *Journal of Non-Crystalline Solids*, **338-340** (2004) 1-12.

[63] J. Robertson, Deposition mechanism of hydrogenated amorphous silicon, *Journal of Applied Physics*, **87** (2000) 2608-2617.

[64] J. Ramanujam, A. Verma, Photovoltaic Properties of a-Si:H Films Grown by Plasma Enhanced Chemical Vapor Deposition: A Review, *Materials Express*, **2** (2012) 177-196.

[65] A.D. Verkerk, M.M. de Jong, J.K. Rath, M. Brinza, R.E.I. Schropp, W.J. Goedheer, V.V. Krzhizhanovskaya, Y.E. Gorbachev, K.E. Orlov, E.M. Khilkevitch, A.S. Smirnov, Compensation of decreased ion energy by increased hydrogen dilution in plasma deposition of thin film silicon solar cells at low substrate temperatures, *Materials Science and Engineering: B*, **159-160** (2009) 53-56.

[66] J. Long, Y. Yin, S.Y.R. Sian, Z. Ren, J. Wang, P. Vayalakkara, S. Venkataraj, A.G. Aberle, Doped Microcrystalline Silicon Layers for Solar Cells by 13.56MHz Plasma-enhanced Chemical Vapour Deposition, *Energy Procedia*, **15** (2012) 240-247.

[67] T. Kuwahara, H. Ito, K. Kawaguchi, Y. Higuchi, N. Ozawa, M. Kubo, The reason why thin-film silicon grows layer by layer in plasma-enhanced chemical vapor deposition, *Scientific reports*, **5** (2015) 9052.

[68] A.H.M.S. W.M.M. Kessels, D.C. Marra, E.S. Aydil, D.C. Schram, M.C.M. van de Sanden, On the growth mechanism of a-Si:H, *Thin Solid Films*, **383** (2001) 154-160.

[69] T. Karabacak, Y.P. Zhao, G.C. Wang, T.M. Lu, Growth front roughening in silicon nitride films by plasma-enhanced chemical vapor deposition, *Physical Review B*, **66** (2002).

[70] J.T. Drotar, Y.P. Zhao, T.M. Lu, G.C. Wang, Mechanisms for plasma and reactive ion etch-front roughening, *Physical Review B*, **61** (2000) 3012-3021.

[71] A. Rawat, M. Sharma, D. Chaudhary, S. Sudhakar, S. Kumar, Numerical simulations for high efficiency HIT solar cells using microcrystalline silicon as emitter and back surface field (BSF) layers, *Solar Energy*, **110** (2014) 691-703.

[72] M. Sharma, S. Kumar, N. Dwivedi, S. Juneja, A.K. Gupta, S. Sudhakar, K. Patel, Optimization of band gap, thickness and carrier concentrations for the development of efficient microcrystalline silicon solar cells: A theoretical approach, *Solar Energy*, **97** (2013) 176-185.

[73] J. Wang, K. Tao, H. Cai, D. Zhang, G. Li, A study of the i/p interface for flexible n–i–p a-Si:H thin film solar cells, *Materials Science in Semiconductor Processing*, **25** (2014) 186-189.

[74] S. Singh, S. Kumar, N. Dwivedi, Band gap optimization of p–i–n layers of a-Si:H by computer aided simulation for development of efficient solar cell, *Solar Energy*, **86** (2012) 1470-1476.

[75] Meriem Chadel, Michel Aillerie, Mohammed Moustafa Bouzaki, Boumediene Benyouce, A. Chade, Thickness optimization of the ZnO based TCO layer in a CZTSSe solar cell. Evolution of its performance with thickness when external temperature changes, *Journal of Physics: Conference Series*, **879** (2017) 012006.

[76] Ü. Dagkaldiran, A. Gordijn, F. Finger, H.M. Yates, P. Evans, D.W. Sheel, Z. Remes, M. Vanecek, Amorphous silicon solar cells made with SnO2:F TCO films deposited by atmospheric pressure CVD, *Materials Science and Engineering: B*, **159-160** (2009) 6-9.

[77] V. Vasu, A. Subrahmanyam, Reaction kinetics of the formation of indium tin oxide films grown by spray pyrolysis, *Thin Solid Films*, **193-194** (1990) 696-703.

[78] M. Toshiro, T. Kenji, Indium-Tin Oxide Thin Films Prepared by Chemical Vapor Deposition from Metal Acetates, *Japanese Journal of Applied Physics*, **29** (1990) L355.

[79] O. Tuna, Y. Selamet, G. Aygun, L. Ozyuzer, High quality ITO thin films grown by dc and RF sputtering without oxygen, *Journal of Physics D: Applied Physics*, **43** (2010) 055402.

[80] V. Teixeira, H.N. Cui, L.J. Meng, E. Fortunato, R. Martins, Amorphous ITO thin films prepared by DC sputtering for electrochromic applications, *Thin Solid Films*, **420** (2002) 70-75.

[81] M. M. Aliyu, S. Hossain, J. Husna, N. Dhar, M. Q. Huda, K. Sopian, N. Amin, High Quality Indium Tin Oxide (ITO) Film Growth by Controlling Pressure in RF Magnetron Sputtering, *IEEE Journal*, (2011) 002009-002013.

[82] O. Hiroshi, N. Kenji, Y. Mitsuaki, A. Mitsuo, S. Kazutomi, Preparation and Properties of a-Si: H Solar Cells on Organic Polymer Film Substrate, *Japanese Journal of Applied Physics*, **21** (1982) 239.

[83] M. Yano, K. Suzuki, K. Nakatani, H. Okaniwa, Roll-to-roll preparation of a hydrogenated amorphous silicon solar cell on a polymer film substrate, *Thin Solid Films*, **146** (1987) 75-81.

[84] T. Takeda, M. Kondo, A. Matsuda, Thin film silicon solar cells on liquid crystal polymer substrate, *Proceeding of the 3rd World Conference on Photovoltaic Energy Conversion*, (2003) 1580-1583.

[85] K. Yasuo, I. Hiroshi, M. Kenji, K. Shinichi, M. Masashi, S. Hisashi, N. Hidenori, K. Yukinori, A New Type of Ultralight Flexible a-Si Solar Cell, *Japanese Journal of Applied Physics*, **31** (1992) 12.

[86] P. Pernet, R. Felder, M. Goetz, H. Keppner, D. Fischer, A. Shah, Optimization of amorphous silicon solar cells on polymer film substrates, *Proceedings of the 14th EC Photovoltaic Solar Energy Conference*, (1997) 2339-2342.

[87] A. Vijh, X. Yang, W. Du, X. Deng, Triple-junction amorphous silicon-based flexible solar minimodule with integrated interconnects, *Solar Energy Materials and Solar Cells*, **90** (2006) 2657-2664.

[88] S.A. Filonovich, P. Alpuim, L. Rebouta, J.E. Bourée, Y.M. Soro, Hydrogenated amorphous and nanocrystalline silicon solar cells deposited by HWCVD and RF-PECVD on plastic substrates at 150°C, *Journal Non-Crystalline Solids*, **354** (2008) 2376-2380.

[89] J. Hotovy, J. Hüpkes, W. Böttler, E. Marins, L. Spiess, T. Kups, V. Smirnov, I. Hotovy, J. Kováč, Sputtered ITO for application in thin-film silicon solar cells: Relationship between structural and electrical properties, *Applied Surface Science*, **269** (2013) 81-87.

[90] K. Tao, J. Wang, H. Cai, D. Zhang, Y. Sui, Y. Zhang, Y. Sun, Low-temperature preparation of flexible a-Si:H solar cells with hydrogenated nanocrystalline silicon p layer, *Vacuum*, **86** (2012) 1477-1481.

[91] J. Bailat, V. Terrazzoni-Daudrix, J. Guillet, F. Freitas, X. Niquille, A. Shah, C. Ballif, T. Scharf, R.Morf, A. Hansen, D. Fischer, Y. Ziegler, A. Closset, Recent development of solar

cells on low cost plastic substrates, *Proceedings of the 20th EU Photovoltaic Solar Energy Conference*, (2005) 1529-1532.

[92] V. Terrazzoni-Daudrix, J. Guillet, X. Niquille, L. Feitknecht, F. Freitas, P. Winkler, A. Shah, R. Morf, O. Parriaux, D. Fischer, Enhanced light trapping in thin film silicon solar cells deposited on PET and glass, 3*rd World Conference on Photovoltaic Energy Conversion*, 2003, pp. 1596-1600.

[93] F.J. Haug, T. Söderström, M. Python, V. Terrazzoni-Daudrix, X. Niquille, C. Ballif, Development of micromorph tandem solar cells on flexible low-cost plastic substrates, *Solar Energy Materials and Solar Cells*, **93** (2009) 884-887.

[94] J. Ni, J. Zhang, Y. Cao, X. Wang, X. Chen, X. Geng, Y. Zhao, Low temperature deposition of high open-circuit voltage (>1.0V) p–i–n type amorphous silicon solar cells, *Solar Energy Materials and Solar Cells*, **95** (2011) 1922-1926.

[95] B. Yan, G. Yue, J. Yang, A. Banerjee, S. Guha, Hydrogenated microcrystalline silicon single junction and multi junction solar cells, *MRS Proceding*, **762** (2003) A41.41-A44.41.12.

[96] M. Brinza, J.K. Rath, R.E.I. Schropp, Thin film silicon n–i–p solar cells deposited by VHF PECVD at 100°C substrate temperature, *Solar Energy Materials and Solar Cells*, **93** (2009) 680-683.

[97] C.H. Yang, C.Y. Hsueh, D.J. Yeh, C.I. Ho, C.M. Leu, Y.H. Yeh, S.C. Lee, Hydrogenated Amorphous Silicon Solar Cells on Textured Flexible Substrate Copied From a Textured Glass Substrate Template, *IEEE Electron Device Letters*, **32** (2011) 1254-1256.

[98] Y. Ichikawa, T. Yoshida, T. Hama, H. Sakai, K. Harashima, Production technology for amorphous silicon-based flexible solar cells, *Solar Energy Materials and Solar Cells*, **66** (2001) 107-115.

[99] K. Wilken, U.W. Paetzold, M. Meier, G.M. Ablayev, E.I. Terukov, N. Prager, M. Fahland, F. Finger, V. Smirnov, Light management in flexible thin-film solar cells on transparent plastic substrates, *physica status solidi (a)*, **213** (2016) 1955-1963.

Chapter 2

Experimental Details and Characterization Techniques

In this chapter, we describe the detailed deposition techniques used for the deposition of undoped and doped hydrogenated amorphous silicon (*a-Si:H*) and indium tin oxide (*ITO*) films followed by the characterization of these films. Different characterization techniques used for the analysis of properties of films and characterization of solar cells are also described in this chapter.

2.1 Film preparation and solar cell fabrication

Intrinsic *a-Si:H* and doped (boron and phosphine) films were prepared in three different chambers using radio frequency plasma enhanced chemical vapour deposition (RF-PECVD) multi-chamber system. Indium-Tin-Oxide films and silver contacts were deposited by RF-sputtering system. These methods are briefly described below.

2.1.1 Radio frequency plasma enhanced chemical vapour deposition (RF PECVD)

The RF-PECVD technique is most commonly used deposition method to produce device quality hydrogenated amorphous silicon (*a-Si:H*) thin films[1-3]. The role of the plasma in this technique is to provide a source of energy to dissociate silane (SiH_4) molecules. SiH_4 is dissociated into SiH_n ($n \leq 3$) as well as H_2 and H [4]. Hydrogen molecules are also decomposed into atomic hydrogen. Excitation of the ground state electron to the vacuum state gives rise to ionization events, generating new electrons and ions to maintain the plasma. The plasma is confined between two parallel plates, one of which holds the substrate. Different radicals formed in dissociation of source gas silane, with the help of plasma are SiH, SiH_2, SiH_3, SiH_x^+, SiH_x^-H, H_2 etc. The radicals so formed undergo secondary gas phase reactions, mostly with parent SiH_4 and H_2 as mentioned below in Equation 2.1 [5-7].

$$\left.\begin{array}{ll}
\text{Ion exchange} & : SiH_x^+ + SiH_4 \rightarrow SiH_x + SiH_x^+ \\
\text{Ion} - \text{molecule} & : SiH_x^+ + SiH_4 \rightarrow SiH_3^+ + SiH_3 \\
\text{Neutral} - \text{molecule} & : SiH + SiH_4 \rightarrow Si_2H_5 \\
\text{Disproportionation} & : Si + SiH_4 \rightarrow SiH_3 + SiH \\
\text{Insertion} & : SiH_2 + SiH_4 \rightarrow Si_2H_6 \\
\text{Recombination} & : SiH_2 + H_2 \rightarrow SiH_4 \\
\text{Abstraction} & : SiH_3 + SiH_4 \rightarrow SiH_4 + SiH_3 \\
 & \quad H + SiH_4 \rightarrow H_2 + SiH_3 \\
\text{Ion} - \text{radical} & : \text{less probable} \\
\text{Radical} - \text{radical} & : \text{less probable}
\end{array}\right\} \qquad (2.1)$$

The radicals formed in secondary gas phase reactions and then get deposited on the substrate, yielding the film. As SiH_3 is the least reactive species, its number density becomes much higher than the other radicals. Hence the main film-forming radical in PECVD method is SiH_3 [6, 8]. Radio frequency plasma enhanced chemical vapour deposition (RF-PECVD) (13.56 MHz) multi-chamber system (EXCEL instruments, Mumbai, India) has been used for the deposition of silicon thin films and fabrication of solar cells. Figure 2.1 (a) shows the schematic diagram of the RF-PECVD multi-chamber system and Figure 2.1 (b) show the real image of RF-PECVD multi-chamber. The system consists of four cylindrical chambers made of stainless steel (SS304 grade), three (PECVD) chambers and a central load lock cum hot wire chemical vapour deposition (HWCVD) chamber. Out of the three PECVD chambers, one is used for the deposition of intrinsic (undoped) amorphous silicon films, whereas other two are used to deposit *n*- type *a-Si:H* (phosphine as dopant gas) and *p*- type *a-Si:H* (diborane as dopant gas) in separate chambers respectively. All the three PECVD chambers are separated from load lock chamber (i.e. HWCVD) using CF100 gate valve. The substrate can be transferred from one PECVD chamber to other PECVD chamber through load-lock without breaking the vacuum. This prevents contamination of other chambers. All the process chambers are individually connected to a turbo-molecular pump (TMP) (Pfieffer, HIPAC 300) with a gate valve between them. The TMP is backed by a two-stage rotary pump (Pfieffer, PASCAL 2020SD). Exhaust line of each rotary pump is connected to the burn box. During deposition, burn box temperature is kept at 700 ^oC and these burnt gases were dissolved in the soap water before going to atmosphere. Cold water is supplied to the TMP and burn box and one fan was attached to each TMP to keep it

cool. Pirani and penning gauges are used to monitor the pressure inside the chambers. Separate gas lines are used to feed the reactant gases in these chambers.

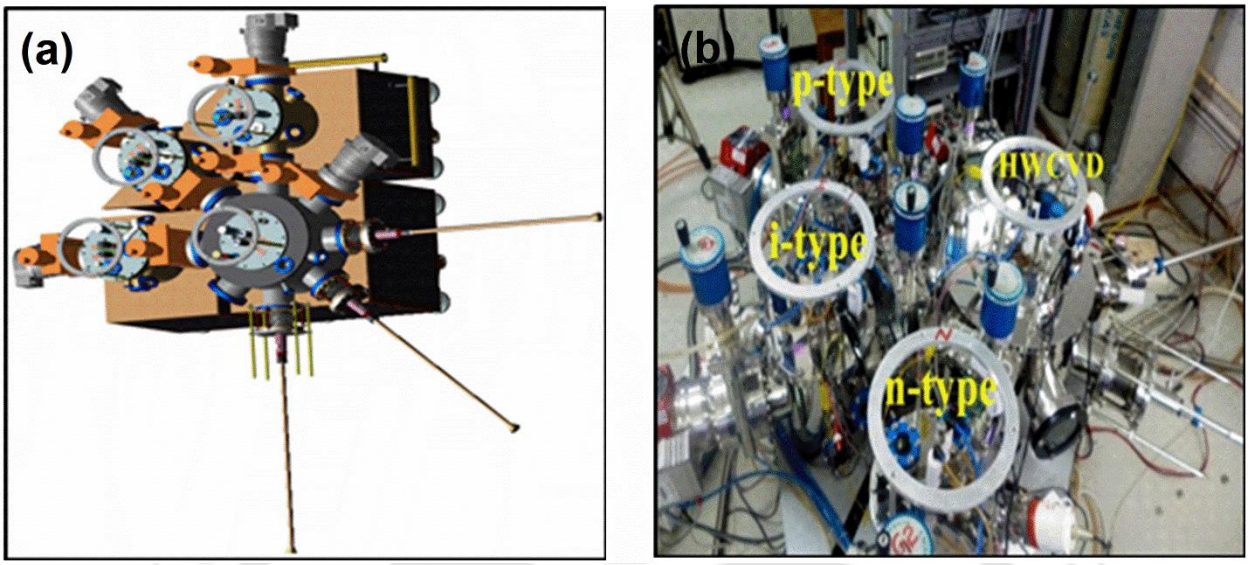

Figure 2.1: *(a) Schematic diagram of RF- PECVD multi-chamber system (b) real image of RF-PECVD multi-chamber*

2.1.2 RF sputtering

In this thesis, indium-tin-oxide (ITO) and silver (Ag) materials have been chosen to make transparent conducting layer and electrical contacts respectively in the device fabrication [9, 10]. These layers were deposited by using RF sputtering. Sputtering is a physical vapor deposition (PVD) technique, basically the physical ejection of atoms from a solid source "target" due to energetic gas ions bombardment. Prior to the sputtering process, base pressure of ~10^{-7} mbar is created inside the chamber. Once the chamber reaches to its base pressure, the controlled flow of inert gas Ar is introduced into the deposition chamber. A high voltage between the electrodes (target/cathode, substrate/anode), leads to the ionization of Ar gas. The ionized gas is then accelerated towards the cathode. The energetic ions strike the target surface and sputter the target atoms. The ejected atoms are then moved towards the grounded anode and these stick onto the substrate in the form of a thin film.

2.2 Characterization techniques

The thin films prepared using above-mentioned methods were characterized for studying its structural, optical and electrical properties using different experimental techniques described below.

2.2.1 Amorphous silicon film characterization

2.2.1.1 Raman Scattering Spectroscopy

Raman spectroscopy is one of the non-destructive and very powerful tools to study vibrational modes of a material for understanding the crystal structure and many other fundamental properties. Raman scattering is an inelastic scattering phenomena of photons by the fluctuations such as atomic vibrations, charge density and spin density and so on in the material. Positions of the peaks are related to the inter-atomic forces and distances, to their masses and chemical environments. Raman studies reported in this thesis were performed using HORIBA Jobin-Yvon LabRam HR Raman spectroscopy equipped with Ar-ion laser at a wavelength of 488 nm. The spot size of the laser beam was 1 μm in diameter and the incident laser power on the sample was less than 1 mW. These studies were carried out at room temperature (*RT*) in the backscattering geometry. Raman mapping was recorded for an area of 17×22 μm^2 on the sample surface. The image of the surface (Raman Mapping) was recorded with the charge coupled device (CCD) attached to the Raman spectrophotometer to identify different phases on the surface. The resolution and the recorded spectral range of Raman shifts are 1 cm^{-1} and 100–800 cm^{-1}, respectively. The main Raman-active peaks observed in our films, i.e., *a-Si:H* film, correspond to several vibrational modes such as transverse acoustic (TA), longitudinal acoustic (LA), longitudinal optical (LO), transverse optic (TO) modes at ~ 150 cm^{-1}, ~300-320 cm^{-1}, ~ 410-440 cm^{-1}, ~ 470-520 cm^{-1}, respectively [11-13]. The TO mode peak centered near ~480 cm^{-1} is the characteristic feature of amorphous silicon whereas peaks at 490-500 cm^{-1}, ~510 cm^{-1}, 520 cm^{-1} correspond to grain boundaries, nanocrystalline silicon and crystalline silicon phase respectively [14, 15].

The TO mode is sensitive to short-range order (SRO) which is a measure of rms deviation in the tetrahedral bond angle ($\Delta\theta_B$) and it can be obtained from the FWHM of amorphous TO mode. Lower deviation signifies better order in the film. As the bond angle deviation increases the material becomes more disordered with a broadening of the amorphous TO peak. The $\Delta\theta_B$ is calculated using linear equation 2.2 given below [16].

$$\Gamma = 15 + 6\Delta\theta_B \tag{2.2}$$

where Γ is full-width at half maxima (FWHM) of amorphous TO mode and $\Delta\theta_B$ is the rms deviation in the tetrahedral bond angle.

The medium range order (MRO) is given by the intensity ratio between the amorphous TA peak to the TO peak [17, 18]. A lower ratio corresponds to improved MRO.

$$MRO = \frac{I_{TA}}{I_{TO}} \tag{2.3}$$

In case of nanocrystallites embedded amorphous films the crystalline peak shifts from 520 cm^{-1} towards lower value due to the size limitation of the crystallites, smaller the crystallite size, larger is the shift. Hence the crystallite size can be calculated from the shift of crystalline peak from 520 cm^{-1}. The crystallite size and crystalline fraction are estimated from the deconvoluted spectra corresponding to the nanocrystallite embedded phase. The crystallite size d_{Raman} is calculated using Equation 2.4 [19].

$$d_{Raman} = 2\pi\sqrt{\frac{B}{\Delta w}} \tag{2.4}$$

where Δw is the shift in the nanocrystalline Raman peak with respect to c-Si and B is 2 cm^{-1} nm^2. The total crystalline volume fraction is calculated using Equation 2.5 [19, 20].

$$X_c(\%) = \frac{I_{nc} + I_{gb}}{I_{nc} + I_{gb} + I_{am}} \times 100 \tag{2.5}$$

where I_{nc}, I_{gb} and I_{am} are integrated intensities of TO phonon peaks corresponding to nanocry-crystalline (~510 cm^{-1}), grain boundary (~490-500 cm^{-1}) and amorphous phases (~ 480 cm^{-1}) respectively.

2.2.1.2 Spectroscopic Ellipsometry

Spectroscopic ellipsometry (SE) is a nondestructive optical analysis technique to extract optical constants of the material**.** In SE, the variation in ellipsoidal shape between the incident and reflected lights is determined by relative reflection ratio (ρ) expressed in the following Equation 2.6 [21].

$$\rho = \frac{r_p}{r_s} = \tan\psi e^{i\Delta} \tag{2.6}$$

where *r* is the complex reflection coefficient, *p* and *s* represent *p*- polarized light and *s*- polarized light respectively, tanψ corresponds to relative amplitude ratio of *p*- polarized light to *s*-polarized light, and Δ represents relative phase difference between *p*- polarized light and *s*- polarized light.

The experimental ellipsometry data ψ and Δ are converted into the pseudo-dielectric function <ε> using relation as defined in Equation 2.7 for a single interface [22]. The pseudo-dielectric function characterized by the whole system, i.e., substrate + film, reflects the light and reduces to the dielectric function (ε) of the material when the reflecting sample has an infinite thickness and a smooth surface and Φ is an incident angle.

$$\langle \varepsilon \rangle = \sin^2 \Phi \left(1 + \left(\frac{1-\rho}{1+\rho} \right)^2 tan^2 \Phi \right) \tag{2.7}$$

One of the well-established and widely used dispersion models to describe the optical properties of the amorphous materials is the Tauc-Lorentz model. To derive optical parameters, experiential data is fitted with Tauc-Lorentz model by constructing a two-layer model consisting of an *ambient/rough surface layer/bulk a-Si:H layer/substrate*. The Tauc-Lorentz model expression for $<\varepsilon_1>$ and $<\varepsilon_2>$ is given in Equation 2.8 & 2.9 [23].

$$\langle \varepsilon_2 \rangle = \begin{cases} \dfrac{A.E_0.C\left(E-E_g\right)^2}{\left(E^2-E_0\right)^2 + C^2.E^2} . \dfrac{1}{E} & for\ (E > E_g) \\ 0 & for\ (E \le E_g) \end{cases} \tag{2.8}$$

$$\langle \varepsilon_1 \rangle = \varepsilon_1(\infty) + \frac{2}{\Pi} P \int_{E_g}^{\infty} \frac{u \varepsilon_2(u)}{u^2 - E^2} du \tag{2.9}$$

where E_0 is peak transition energy or resonance energy, E_g is an optical band gap, C is oscillator broadening parameter and A is amplitude factor, $\varepsilon_1(\infty)$ is energy independent contribution to $\varepsilon_1(E)$ at infinite energy. $\varepsilon_1(\infty)$ represents contribution of the optical transitions at higher energies and appears as an additional fitting parameter. P stands for the Cauchy principle part of the integral.

In the present thesis spectroscopic ellipsometey (SE) measurements were performed using SOPRA GES5 spectroscopic ellipsometer in reflection mode film on Corning, polyimide (PI) and photo paper (PP) substrates. SE spectra were recorded at room temperature in the range of 2

- 5 *eV* photon energy on *a-Si:H* films on corning, PI and PP substrates. In the SE measurements, angle of incidence was fixed at 70^o for films on corning, PI substrates whereas 72^o for films on PP substrate. The size of the elliptical spot falling on the sample is 2 x 5 mm. In order to fit the raw data, we have used corning substrate refractive index and extinction coefficient (*n-k*) file in SE analyzer software (SEA 1.5.26). However, *n-k* file of PI and PP substrates are not listed in the SEA 1.5.26. Therefore, we recorded SE spectra on bare PI and PP substrates and determined corresponding *n-k* using SEA software. This *n-k* file has been used to determine the optical constants of deposited silicon films. To derive optical parameters of films, experimental data was fitted with *T-L* model by constructing a two-layer model consisting of *ambient/rough surface layer/bulk a-Si:H layer/substrate*. The expression for imaginary ($<\varepsilon_2>$) and real ($<\varepsilon_1>$) part of dielectric constant in *T-L* model is given in equation 2.8, 2.9 respectively.

2.2.1.3 UV-Vis-NIR Spectroscopy

Ultraviolet-Visible-Near Infrared (UV-Vis-NIR) spectrometry is very important characterization technique to measure the transmittance/absorbance of the films when the films are exposed to UV-Vis-NIR light. The transmission mode is used in the region of UV-Vis-NIR for the films deposited on corning 1737 glass with respect to air. These measurements are performed using Shimadzu UV 3101 PC in the range of 200-2500 nm. For a uniform thin film, the thickness of these films is estimated from the interference fringes in the transmission spectrum using Swanepoel method [24]. According to Swanepoel's method, which is based on the idea of creating the envelopes of interference maxima and minima as a first approximation, the refractive index (n_{film}) of the films in the regions of medium and weak absorption can be estimated using the expression 2.10

$$n_{film} = \left[N_{film} + \left(N_{film}^2 - s^2 \right)^{1/2} \right]^{1/2} \tag{2.10}$$

where

$$N_{film} = 2s \times \frac{T_M - T_m}{T_M T_m} + \frac{s^2 + 1}{2} \tag{2.11}$$

And s, T_M and T_m are the substrate refractive index, transmission maximum and the corresponding minimum at a certain wavelength (λ).

The thickness of film was calculated using following relation

$$d = \frac{\lambda_1 \times \lambda_2}{2\left(\lambda_1 n_{film2} - \lambda_2 n_{film1}\right)} \tag{2.12}$$

Where n_{film2} and n_{film1} are the refractive indices at two adjacent maxima or minima corresponding to λ_2 and λ_1 respectively

The optical band gap (E_g) of the film is calculated using Tauc's relation [25, 26]

$$\alpha h\upsilon = B\left(h\upsilon - E_g\right)^n \tag{2.13}$$

Where hυ is the incident photo energy, E_g is optical band gap and B is proportionality constant. The values of exponent n are 2 and ½ for indirect and direct gap transition respectively.

2.2.1.4 Surface profilometer

A Surface profilometer is used to measure the thickness of deposited films. It is capable to scan area of tens of millimeters with a vertical range starting from hundreds of microns to a few nanometers. In the present thesis, measurements were carried out using Veeco-Dektak 150 stylus profilometer. Thickness measurement was performed for each film on corning 1737 glass at three different mask locations and those values were averaged to determine the thickness. These values are verified with thickness calculated using UV-Vis-NIR and spectroscopic ellipsometry measurements.

2.2.1.5 Fourier transform infrared spectroscopy

Fourier transform infrared (FTIR) spectroscopy is a non-destructive technique which can identify the bond configuration in the material. This instrument works based on the fact that each molecular bond has its own distinct quantized vibrational levels whose frequency lie usually in the mid-infrared region of 200 – 4000 cm^{-1}. Once the frequency of an incident infrared radiation matches with the frequency of molecular vibration modes, radiation is absorbed by the molecules. A single beam 'Perkin Elmer BX' FTIR spectrometer is used to record the IR transmission spectra for all prepared samples. The films are deposited on IR transparent substrate such as both sides polished undoped monocrystalline Si (100) wafer. The spectrometer is operated using normal incidence with step size of 1 cm^{-1} and resolution of 4 cm^{-1} with average of sixty-four scans for each sample. In order to remove the absorption of a substrate, background correction was done with bare c-Si wafer. The *a-Si:H* film absorbs the IR radiation due to different modes of bond vibration at the positions listed in the Table 2.1 [3, 27].

The total hydrogen content in the film can be estimated from the following Equation 2.14 [28].

$$C_H(at.\%) = \frac{A_{630}}{N_{Si}} \int_{\omega} \frac{\alpha(\omega)}{\omega} d\omega \tag{2.14}$$

Here the proportionality constant A_{630}= 1.6 x 10^{19} cm^{-2} and atomic density of Si, N_{Si} = 5.4×10^{22} cm^{-3} [29]. In order to find the C_H (%), FTIR data between 520-760 cm^{-1} was selected. In amorphous silicon, hydrogen is bonded to Si as Si-H, SiH_2, Si-H_n etc. Though the vibrational frequency for stretching modes are different for different bonds, the rocking.bending mode frequency for the all the bonds is same as 630 cm^{-1}. Absorption band near 630 cm^{-1} is thus better choice to estimate total hydrogen content in the films [30].

Table 2.1*: Different modes of silicon hydrogen bond vibration and the corresponding peak positions*

Bonding Configuration	Vibrational Mode	Peak Position (cm^{-1})
Si-H	Wagging	630
	Stretching	2000
Si-H_2	Rocking	630
	Twist	820
	Wagging	850
	Scissor Bending	880
	Stretching	2100
Si-H_3	Wagging	630
	Symmetric Deformation	862
	Degenerate Deformation	907
	Stretching	2140

The bonded hydrogen in stretching mode has absorption band around 2000-2100 cm^{-1} and is deconvoluted into peaks near 2000 and 2100 cm^{-1} corresponding to Si-H and Si-H_2 stretching bonding configurations respectively [31]. Microstructure factor (*R**) can be defined as the fraction of integrated intensity of Si-H_2 (I_{2100}) to sum of integrated intensities of Si-H and Si-H_2 (I_{2000}+I_{2100}). The microstructure factor *R** is given by Equation 2.15 [32].

$$R^* = \frac{I_{2100}}{I_{2000} + I_{2100}} \tag{2.15}$$

where I_{2000} and I_{2100} are the integrated intensities under the deconvoluted absorption bands at 2000 and 2100 cm^{-1} respectively.

2.2.1.6 Atomic force microscopy

Atomic force microscopy (AFM) is one of the useful tool to observe surface topography of the films. AFM consists of a microscale cantilever with a sharp tip at its end that is used to scan the surface of the film. Cantilever is generally made with Silicon or silicon nitride. When the tip is brought close to the film surface, the force between film and tip leads to a deflection of the cantilever. The deflection is measured using a laser spot reflected from the top surface of the cantilever into an array of photodiodes. In this thesis, the measurements were performed with AFM (model Agilent, 5500 series) in tapping mode using silicon nitride cantilever with force constant 33 N/m and a resonance frequency of 304 KHz. The root mean square (RMS) roughness of films is calculated using "WSxM'' software for the selected area of 2 μm x 2 μm.

2.2.1.7 Field emission scanning electron microscopy (FESEM)

Surface morphology of the films and cross sectional image of solar cells were recorded by field emission scanning electron microscopy (FESEM, model: ΣIGMA ZEISS). In this technique, a field emission cathode provides narrow electron beam of high energy which is focused on the sample and result in improvement of resolution of the image. FESEM was operated with an accelerating voltage of 2 to 4 KeV and films were coated with a very thin gold layer with the plasma to avoid charging effect during measurement.

2.2.1.8 Conductivity measurements

Conductivity of *a-Si:H* films were measured using two probe method in coplanar geometry. Silver paint was used as electrodes for conductivity measurements. In coplanar geometry, if l is the length of electrodes, d is the separation between them, t is the thickness of the film, V is the applied voltage and I is the measured current then the conductivity is given by the following Equation 2.16

$$\sigma = \frac{I \times d}{V \times l \times t} \tag{2.16}$$

A 100 Watt halogen lamp was used for to illuminate the films during photoconductivity measurements. Photoconductivity was calculated from the photocurrent using the Equation 2.16. To measure temperature dependent conductivity, chamber was first evacuated to high vacuum of

the order of 10^{-5} mbar. The films were heated from room temperature to deposition temperature of the films under high vacuum.

The dark conductivity activation energy (E_a) was determined from temperature dependent dark conductivity data using Arrhenius plot (Equation 2.17). The relation between the dark conductivity σ_d and activation energy E_a is given by [33]

$$\sigma_d = \sigma_0 \exp\left(-\frac{E_a}{kT}\right) \tag{2.17}$$

where σ_d is the dark conductivity prefactor, k is Boltzmann constant and T is the absolute temperature (in Kelvin).

2.2.2 Indium tin oxide (*ITO*) thin films characterization

2.2.2.1 X-Ray Diffraction (XRD)

X-ray diffractometer, Rigaku TTRAX III, 18 kW with CuK_α radiation of 1.54 Å, was used for microstructure investigations of Indium-Tin-Oxide (*ITO*) thin films. XRD study was performed on the films deposited on Corning 1737 glass. The measurements were performed in 2θ thin film mode at a grazing angle of incidence of 3°. The films were scanned in the range of 10-70° with a step of 0.05°. The crystallite size in the film was calculated using Scherrer's formula [34] (Equation 2.18) as follows

$$d_{XRD} = \frac{0.9\lambda}{B_1 Cos\theta_{hkl}} \tag{2.18}$$

where d_{XRD} is the crystallite size, λ is the wavelength of X-ray, B_1 is the broadening due to crystallite size and θ_{hkl} is the peak position corresponding to the (hkl) plane.

2.2.2.2 Four probe measurement

Resistivity of *ITO* thin films was determined using four-point probe technique. Schematic diagram of four-probe measurement setup is shown in Figure 2.2. The four-point probe set up consists of four equally spaced tungsten metal strips with a finite radius. Two outer the probes are used to supply current (probe 1 and 4) and the other two probes (probe 2 and 3) are used to measure voltage difference. Four probe technique eliminates measurement errors due to the probe resistance, the spreading resistance of each probe, and the contact resistance between each metal probe and the semiconductor material.

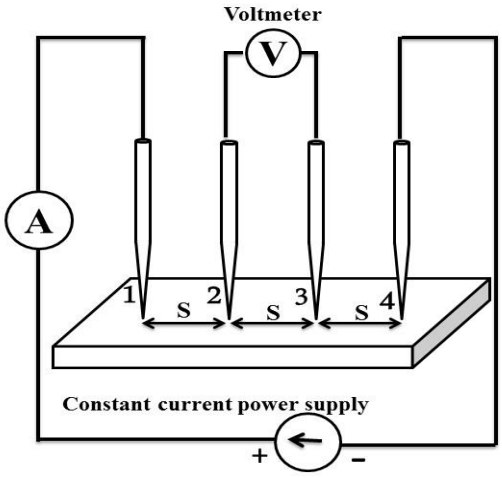

Figure 2.2: *Schematic diagram of four probe method of measuring resistivity of a sample*

We assume that the metal tip is infinitesimal and samples are semi infinitesimal in lateral dimensions. For bulk samples where the sample thickness, t>>s the expression for resistivity is $\rho = 2\pi s\left(\frac{V}{I}\right)$. For thin films, where the sample thickness t << s, $\rho = \frac{\pi t}{\ln 2}\left(\frac{V}{I}\right)$ [35]. This expression is independent of the probe spacing. Furthermore, this later expression is frequently used for characterization of semiconductor layers. In general, the sheet resistivity $R_s = \rho / t$ can be expressed as $R_s = k\left(\frac{V}{I}\right)$ where the factor *k* is a geometric factor. In the case of a semi-infinite thin sheet, *k* = 4.53. The factor *k* is different for non-ideal samples.

2.3 Solar cell characterization

2.3.1 Current density (*J*) – Voltage (*V*) measurement

Electrical performance of a solar cell was determined from the current density-voltage (*J*-*V*) curve obtained by illuminating the solar cell with halogen lamp of 100W power. Intensity of light beam falling on the sample was about 100 mW/cm^2. A Keithley 2450 Source meter controlled by a computer is used to provide voltage sweeps and record the corresponding current. Current density-voltage characteristic of solar cell is illustrated in Figure 2.3.

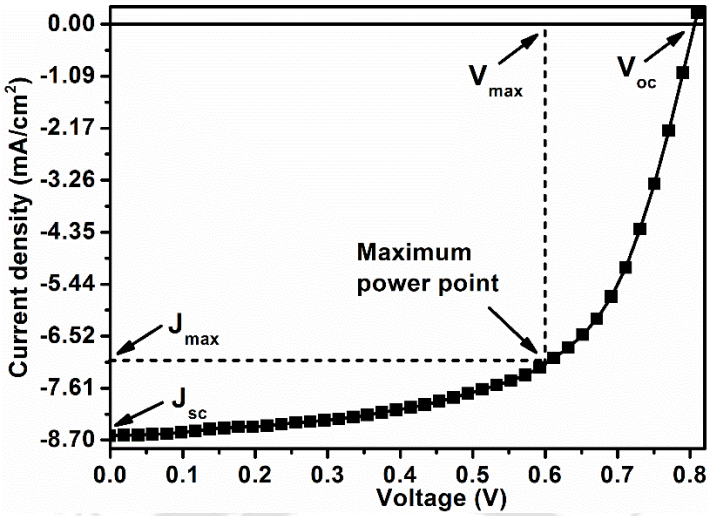

Figure 2.3: *Current density (J) – voltage (V) characteristics of solar cell*

From the *J-V* curve, short-circuit current density (J_{sc}), open-circuit voltage (V_{oc}) and fill factor (*FF*) are obtained. The solar cell efficiency (η) is defined as the ratio of maximum electrical energy output to the incident solar energy on the cell. The η (%) is determined by the following Equation 2.19 [36].

$$\eta\,(\%) = \frac{J_{sc} \times V_{oc} \times FF}{P_{in}} \times 100 \qquad (2.19)$$

$$\text{where} \quad FF = \frac{J_{\max} \times V_{\max}}{J_{sc} \times V_{oc}}$$

where J_{sc}, V_{oc}, *FF* and P_{in} are short-circuit current density, open-circuit voltage, fill factor and input power. The V_{oc} is the voltage at which no current flows through the external circuit; that is at $J = 0$. On the other hand, J_{sc} is current density at which voltage drop is zero across the solar cell. The *FF* is the ratio of the maximum power that can be obtained from the cell to the product of J_{sc} and V_{oc}. It is a measure of 'squareness' of the *J-V* curve and describes the operating point at which the solar cell gives maximum power to the attached load. In order to estimate the series (R_s) and parallel (R_p) resistances of the solar cells, slope of J-V curve near short circuit and open circuit points were calculated using following Equations 2.20 & 2.21 .

$$R_s = \frac{1}{\left(\frac{dJ}{dV}\right)_{J=0}} \qquad (2.20)$$

$$R_p = \frac{1}{\left(\frac{dJ}{dV}\right)_{V=0}} \tag{2.21}$$

2.3.2 External quantum efficiency (*EQE*)

External quantum efficiency (*EQE*) measurements were performed at *RT* using an in-house built dual beam set up. Figure 2.4 shows the schematic diagram of the quantum efficiency measurement setup. The first part of the system, light source for the *EQE* measurements was a xenon lamp, which was fed into a monochromator (Horiba Jovin Yvon-Triax). The lamp was turned on at least half an hour before recording any measurements. This was found to be sufficient to produce a stable current output from an *a-Si: H* solar cell.

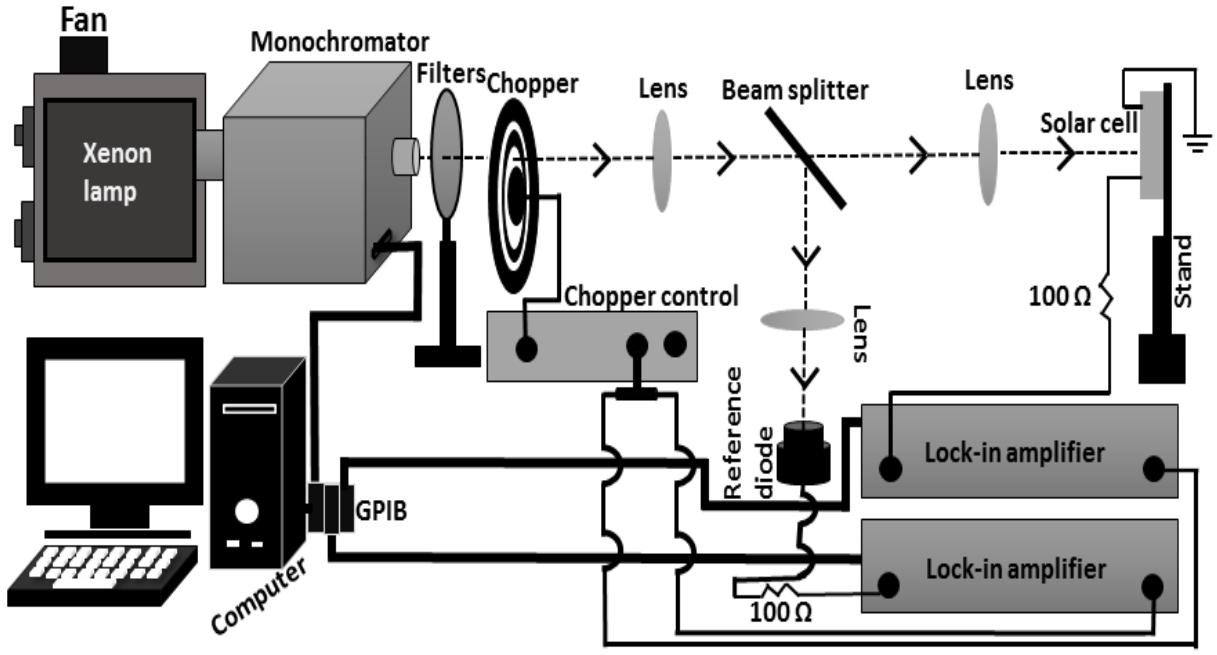

Figure 2.4: *Schematic diagram of quantum efficiency measurement setup*

Beam splitter was used to split the incident beam into two beams; one beam for reference calibrated diode and other beam for solar cell. During measurements, optical lens were used to focus the light from the monochromator onto the reference photodiode and solar cell to ensure optimum positioning. The slit width was kept at 3 mm diameter. Second order filters of 400 nm and 610 nm cut off wavelengths were used to block second harmonics of light when the sample was exposed to the light at longer wavelengths. Optical chopper (Stanford Research Systems Model SR540) was used for periodically interrupting the light beam. The controller uses a phase

locked loop motor speed control design to precisely maintain the chopping speed and phase relative to the reference signal. In our experiments, a chopper was placed in front of the monochromator entrance slit. We used 6 slots blade set and chopper frequency was fixed at 17 Hz. The optical chopper outputs were connected to two lock-in amplifiers (Stanford Research Systems Model SR-810). One lock-in amplifier was connected to the reference photodiode and another was connected to the solar cell. Lock-in amplifier measures a single output, the component of the signal at a specific reference frequency. Noise signals, at frequencies other than the reference frequency, are rejected and do not affect the measurements. LabVIEW program was used to control the monochromator, two lock-in amplifiers through general purpose interface bus (GPIB) card and cables and the output signals were collected from reference diode and solar cell in terms of volts.

External quantum efficiency can be obtained from Equation 2.22 [37, 38]

$$EQE\ (\%) = \frac{h \times c}{q \times \lambda} \times SR_{cell} \times 100 \tag{2.22}$$

where h,c,q,λ and SR_{cell} are planks constant, velocity of light, charge of electron, wave length of light and spectral response of the measured solar cell respecively.

Spectral response of the measured solar cell can be obtained from the following Equation 2.23

$$SR_{cell} = SR_{ref} \times \left(\frac{V_{cell}}{V_{std}} \right) \times \left(\frac{V_{ref/std}}{V_{ref/cell}} \right) \tag{2.23}$$

where SR_{ref}, V_{cell}, V_{std}, $V_{ref/std}$ and $V_{ref/cell}$ are respectively the spectral response of standard diode, voltage of the test cell, voltage of a standard diode, reference diode voltage when standard diode voltage was measured and reference diode voltage when test cell voltage respectively.

2.4 References

[1] W. Chen, R. Cariou, G. Hamon, R. Léal, J.-L. Maurice, P.R.I. Cabarrocas, Influence of deposition rate on the structural properties of plasma-enhanced CVD epitaxial silicon, *Scientic Reports*, **7** (2017) 43968.

[2] J. He, C. Wang, W. Li, K.C. Qi, Y.D. Jiang, Effect of gas temperature on the structural and optoelectronic properties of a-Si:H thin films deposited by PECVD, *Surface Coating Technology*, **214** (2013) 131-137.

[3] T. Anutgan, S. Uysal, Low temperature plasma production of hydrogenated nanocrystalline silicon thin films, *Current Applied Physics*, **13** (2013) 181-188.

[4] J. Ramanujam, A. Verma, Photovoltaic Properties of a-Si:H Films Grown by Plasma Enhanced Chemical Vapor Deposition: A Review, *Material Express*, **2** (2012) 177-196.

[5] A. Matsuda, Microcrystalline silicon. Growth and device application, *Journal of Non-Crystalline Solids*, **338-340** (2004) 1-12.

[6] A. Matsuda, Thin-Film Silicon Growth Process and Solar Cell Application, *Japanese Journal of Applied Physics*, **43** (2004) 7909-7920.

[7] S. Sriraman, E.S. Aydil, D. Maroudas, Atomic-scale analysis of deposition and characterization of a-Si:H thin films grown from SiH radical precursor, *Journal of Applied Physics*, **92** (2002) 842-852.

[8] A.H.M.S. W.M.M. Kessels, D.C. Marra, E.S. Aydil, D.C. Schram, M.C.M. van de Sanden, On the growth mechanism of a-Si:H, *Thin Solid Films*, **383** (2001) 154□160.

[9] A. Rayerfrancis, P.B. Bhargav, N. Ahmed, S. Bhattacharya, B. Chandra, S. Dhara, Sputtered AZO Thin Films for TCO and Back Reflector Applications in Improving the Efficiency of Thin Film a-Si:H Solar Cells, *Silicon*, **9** (2015) 31-38.

[10] Y. Wang, C. Zhang, J. Li, G. Ding, L. Duan, Fabrication and characterization of ITO thin film resistance temperature detector, *Vacuum*, **140** (2017) 121-125.

[11] V.A. Volodin, D.I. Koshelev, Quantitative analysis of hydrogen in amorphous silicon using Raman scattering spectroscopy, *Journal of Raman Spectroscopy*, **44** (2013) 1760-1764.

[12] N.M. Liao, W. Li, Y.D. Jiang, Y.J. Kuang, K.C. Qi, Z.M. Wu, S.B. Li, Raman study of a-Si : H films deposited by PECVD at various silane temperatures before glow-discharge, *Applied Physics a-Mater*, **91** (2008) 349-352.

[13] A.M. Ali, S. Hasegawa, Effect of hydrogen dilution on the growth of nanocrystalline silicon films at high temperature by using plasma-enhanced chemical vapor deposition, *Thin Solid Films*, **437** (2003) 68-73.

[14] V. Vavrunkova, J. Mullerova, R. Srnanek, P. Sutta, Structural changes studies of a-Si:H films deposited by PECVD under different hydrogen dilutions using various experimental techniques, *Vacuum*, **84** (2009) 123-125.

[15] D. Chaudhary, M. Sharma, S. Sudhakar, S. Kumar, Effect of Pressure on Bonding Environment and Carrier Transport of a-Si:H Thin Films Deposited Using 27.12 MHz Assisted PECVD Process, *Silicon*, **10** (2016) 91-97.

[16] D. Beeman, R. Tsu, M. Thorpe, Structural information from the Raman spectrum of amorphous silicon, *Phys Rev B*, **32** (1985) 874-878.

[17] I. Manabu, K. Michio, Systematic Study of Photodegradation of Tailored Nanostructure Si Solar Cells by Controlling Their Medium Range Order, *Japanese Journal of Applied Physics*, **45** (2006) L230.

[18] G. Morell, R.S. Katiyar, S.Z. Weisz, H. Jia, J. Shinar, I. Balberg, Raman study of the network disorder in sputtered and glow discharge a-Si:H films, *Journal of Applied Physics*, **78** (1995) 5120-5125.

[19] P. Alpuim, V. Chu, J.P. Conde, Amorphous and microcrystalline silicon films grown at low temperatures by radio-frequency and hot-wire chemical vapor deposition, *Journal of Applied Physics*, **86** (1999) 3812-3821.

[20] P. Gogoi, P. Agarwal, Structural and optical studies on hot wire chemical vapour deposited hydrogenated silicon films at low substrate temperature, *Solar Energy Materials and Solar Cells*, **93** (2009) 199-205.

[21] H. Fujiwara, *Spectroscopic Ellipsometry Principles and Applications*, 1 ed., John Wiley & Sons Ltd, **2007**.

[22] Y. Bouizem, C. Abbes, J.D. Sib, D. Benlakehal, R. Baghdad, L. Chahed, K. Zellama, S. Charvet, Ellipsometric and Raman spectroscopic study of nanocrystalline silicon thin films prepared by a rf magnetron sputtering technique, *Journal of Physics: Condensed Matter*, **20** (2008) 445221.

[23] S.Y. Lee, J.H. Shim, D.J. You, S.W. Ahn, H.M. Lee, The novel usage of spectroscopic ellipsometry for the development of amorphous Si solar cells, *Solar Energy Materials and Solar Cells*, **95** (2011) 142-145.

[24] R. Swanepoel, Determination of the thickness and optical constants of amorphous silicon, *J. Phys. E: Sci. Instrum.*, **16** (1983) 1214.

[25] Gogoi P, Jha H. S, A. P., High band gap nanocrystallite embedded amorphous silicon prepared by hotwire chemical vapour deposition, *Thin Solid Films*, **518** (2010) 6818-6828.

[26] G.R. Tauc J, Vancu A, Optical properties and electronic structure of amorphous germanium, *Phys Status Solidi*, **15** (1966) 627.

[27] A.M. Funde, N.A. Bakr, D.K. Kamble, R.R. Hawaldar, D.P. Amalnerkar, S.R. Jadkar, Influence of hydrogen dilution on structural, electrical and optical properties of hydrogenated nanocrystalline silicon (nc-Si:H) thin films prepared by plasma enhanced chemical vapour deposition (PE-CVD), *Solar Energy Materials and Solar Cells*, **92** (2008) 1217-1223.

[28] C. Shin, J. Park, J. Jung, S. Bong, S. Kim, Y.J. Lee, J. Yi, Control of micro void fraction and optical band gap in intrinsic amorphous silicon thin films (VHF-PECVD) for thin film solar cell application, *Materials Research Bulletin*, **60** (2014) 895-899.

[29] C.J. Fang, K.J. Gruntz, L. Ley, M. Cardona, The hydrogen content of a-Ge:H and a-Si:H as determined by IR spectroscopy, gas evolution and nuclear reaction techniques, *Journal of Non-Crystalline Solids*, **35 & 36** (1980) 255-260.

[30] R.A. Street, Hydrogenated Amorphous Silicon, Cambridge University Press1992.

[31] D.M. Goldie, S.K. Persheyev, Quantitative hydrogen measurements in PECVD and HWCVD a-Si:H using FTIR spectroscopy, *Journal of Material Science*, **41** (2006) 5287-5291.

[32] P. Gogoi, H.S. Jha, P. Agarwal, Variation of microstructure and transport properties with filament temperature of HWCVD prepared silicon thin films, *Thin Solid Films*, **519** (2011) 4506-4510.

[33] W. Du, X. Yang, H. Povolny, X. Liao, X. Deng, Impact of hydrogen dilution on microstructure and optoelectronic properties of silicon films deposited using trisilane, *Journal of Physics D: Applied Physics*, **38** (2005) 838-842.

[34] B. D. Cullity, *Elements of X-ray Diffraction*, 1st ed., Pearson Publishers, **1956**.

[35] D.K. Schroder, *Semiconductor Material and Device Characterization*, 2nd edition, John Wiley & Sons Inc.**1998**.

[36] A. Belfar, Simulation study of the a-Si:H/nc-Si:H solar cells performance sensitivity to the TCO work function, the band gap and the thickness of i-a-Si:H absorber layer, *Solar Energy*, **114** (2015) 408-417.

[37] Y.R. Chen, Z.Q. Li, X.H. Chen, C. Liu, X.J. Ye, Z.B. Wang, Z. Sun, S.M. Huang, Improved performance of flexible amorphous silicon solar cells with silver nanowires, *Journal of Applied Physics*, **112** (2012) 124320.

[38] Subhash Chander, A. Purohit, Anshu Nehra, S.P. Nehra, M.S. Dhaka, A Study on Spectral Response and External Quantum Efficiency of Mono-Crystalline Silicon Solar Cell, *International journal of renewable energy*, **5** (2015) 41-44.

Chapter 3

Optimization of Intrinsic *a-Si:H* Thin Films at Low Substrate Temperature

In *a-Si:H* based *n-i-p* or *p-i-n* solar cells, intrinsic layer is the main photon absorber layer. The performance of the solar cells depends upon the optolectronic properties of this layer. Since, the deposition parameters have a significant influence on the structural and optoelectronic properties of the *a-Si:H* layer, therefore, before fabricating the solar cells, it is necessary to optimize the deposition parameters of intrinsic layer to get the best quality films. In silicon based solar cells, the device grade silicon layers are generally deposited in temperature range ≥ 200-350 ^{o}C [1-3]. At the same time, the lower substrate temperature (T_s) is economically beneficial as this reduces the energy required to manufacture the devices as well as use of low cost flexible substrates is possible if fabrication temperature is lowered. Flexible substrates need a low deposition temperature due to its low deformation temperature and high coefficient of thermal expansion (CTE) [4]. The amorphous Si films deposited at low T_s are often porous, more disordered and exhibit poor optoelectronic properties limiting the performance of solar cells. The quality of the films deposited at low T_s can be improved by changing the deposition parameters such as rf power and hydrogen dilution in SiH_4 etc. by RF-PECVD technique. The influence of deposition parameters on quality of *a-Si:H* films using RF-PECVD technique are still not clearly understood. With this motivation, three series of intrinsic *a-Si:H* thin films were prepared, by varying different deposition parameters, one deposition parameter at a time while keeping all the other parameters fixed. The chapter presents the systematic study of structural and optoelectronic properties of these films.

The deposited films were characterized by Raman spectroscopy, spectroscopic ellipsometry (SE), atomic force microscopy (AFM), field emission scanning electron microscopy (FESEM), UV-Vis-NIR, profilometer, Fourier transform infrared spectroscopy (FTIR) and electrical transport measurements. The details of the characterization techniques used in the present study are mentioned in Chapter 2.

3.1 Deposition parameters for intrinsic *a-Si:H* film

The intrinsic hydrogenated amorphous silicon (*a-Si:H* (*i*)) thin films were deposited by RF-PECVD (13.56 MHz) in a multi-chamber system on Corning 1737 glass (Corning), polyimide (PI) (Kapton type, HN grade), photo paper (PP) (Kodak company, high gloss, white color, thickness 230 micrometer) and undoped *c-Si* substrates. Three different series of intrinsic films were prepared by varying one deposition parameter at a time while keeping all the other parameter fixed; **Series (I)**: Variation of substrate temperature (T_s) in the range 70-200°C. **Series (II)**: Variation of H_2 flow rate (HFR) during SiH_4 plasma at T_s = 150°C. **Series (III)**: Variation of rf power during silane plasma at T_s = 110°C. The deposition parameters for each series of films are listed in Table 3.1

Table 3.1: *Deposition parameters for intrinsic a-Si:H thin films by RF-PECVD technique*

Deposition parameters	**T_s series**	**HFR series**	**rf power series**
rf power (Watt)	40	40	**40-70***
H_2 (sccm)	60	**50-90***	60
SiH_4 (sccm)	5	5	5
Process pressure (mbar)	0.72	0.72	0.72
Substrate temperature (^oC)	**70-200***	150	110
Deposition time (minute)	60	60	60

*variable parameters

3.2 Results and discussion

3.2.1 Series (I): Variation of substrate temperature (T_s) in the temperature range 70-200°C

In this study, intrinsic *a-Si:H* thin films were deposited by varying the substrate temperature (T_s) in the range of 70 – 200 ^oC on Corning 1737 glass (Corning) and c-Si substrates, whereas on photo paper (PP) and polyimide (PI) substrates, T_s was varied in the range of 70 – 150 ^oC. The deposition parameters for this study are listed in Table 3.1.

3.2.1.1 Raman scattering

Raman scattering is a nondestructive technique used to estimate the evolution of network structure due to its sensitivity to the structural disorder in solids. Raman spectra were recorded at several different positions on the surface of the films on Corning, PI and PP substrates. It was observed that for films deposited at low T_s (≤110^oC), Raman spectra

corresponded to amorphous phase at all the locations probed, whereas when the substrate temperature was increased (≥130^{o}C), Raman spectra showed amorphous phase at some places and nanocrystalline phase at other places. In order to understand the change in Raman spectra with position, image of the surface (Raman mapping) of the films were recorded to identify the different phases on the surface. Figure 3.1, Figure 3.2 and Figure 3.3 show Raman mapping of the films deposited at different T_s on Corning, PI and PP substrates respectively.

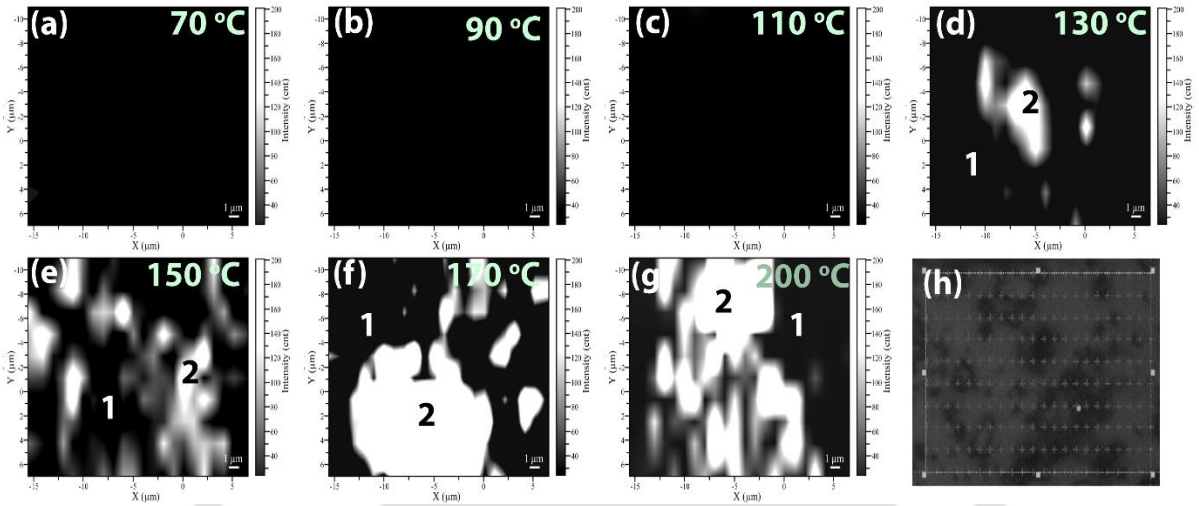

***Figure 3.1**: (a-g) Raman mapping of intrinsic a-Si:H films prepared at different T_s on Corning substrate (h) optical image of film prepared T_s at 150^{o}C on Corning.*

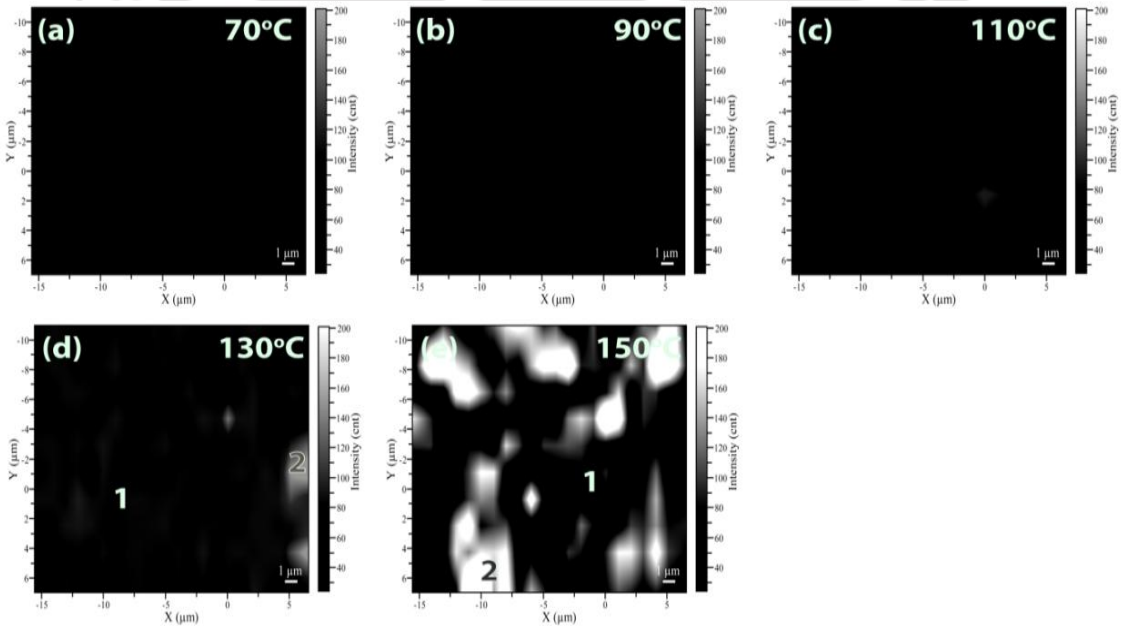

***Figure 3.2**: (a - e) Raman mapping of intrinsic a-Si:H films prepared at different T_s on polyimide substrate.*

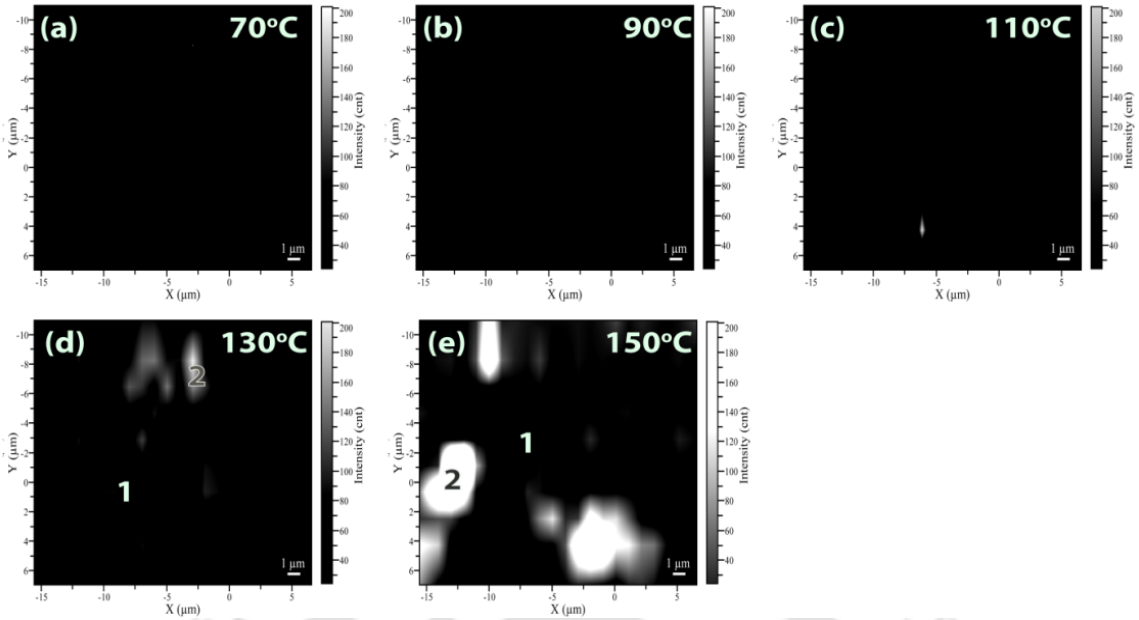

***Figure 3.3**: (a - e) Raman mapping of intrinsic a-Si:H films prepared at different T_s on photo paper substrate.*

The black color in the Raman mapped image corresponds to the amorphous region whereas white color represents nanocrystallites embedded region in amorphous matrix. Films prepared at $T_s \leq 110^oC$ are completely amorphous in nature. The presence of white spots in Raman mapping of the sample prepared at $T_s \geq 130^oC$ for Corning, PI and PP substrates (Figure 1 (d-g), Figure 2(d, e) and Figure 3(d, e)) indicates that formation of nanocrystallites in the amorphous matrix at these temperatures. The formation of nanocrystallites started in the amorphous film around 130^oC and density of these nanocrystallites increased with further increase in T_s. The percentage area covered by nanocrystallites in films at T_s = 130, 150, 170 and 200^oC is 9, 30, 53 and 55% respectively on Corning substrate whereas on PI and PP substrates T_s=130 & 150^oC it is found to be 3 & 18% and 4 & 10% respectively. Figure 3.1(h) shows microscopic image of film deposited at T_s = 150^oC on Corning substrate. In this image, nanocrystallites are appearing in black color where as these are shown in white color in the Raman image Figure 3.1(e). Raman spectra were recorded by focusing the laser beam on the regions marked as 1(amorphous phase) and 2 (nanocrystalline phase) in Figure 3.1(d-*g*), Figure 3.2 (d, e) and Figure 3.3 (d, e). The corresponding Raman spectra of amorphous and nanocrystalline phase are shown in Figure 3.4 (a-*g*), Figure 3.5 (a-e) and Figure 3.6 (a-e) respectively. Raman spectra of these films in different regions, dark and bright regions, (in Figure 3.1, Figure 3.2 and Figure 3.3) consists of peaks corresponding to several vibrational modes; transverse acoustic (TA), longitudinal acoustic (LA), longitudinal optical (LO), transverse optic (TO) modes of Si at~ 150 cm^{-1}, ~300-320 cm^{-1}, ~ 410-440 cm^{-1}, ~ 470-520

cm^{-1} respectively [5-7]. The TO mode peak centered near ~480 cm^{-1} is the characteristic feature of amorphous silicon structure whereas peaks centered near ~490-500 cm^{-1}, ~510 cm^{-1} and 520 cm^{-1} correspond to grain boundaries, nanocrystalline silicon and crystalline silicon phase respectively [8, 9].

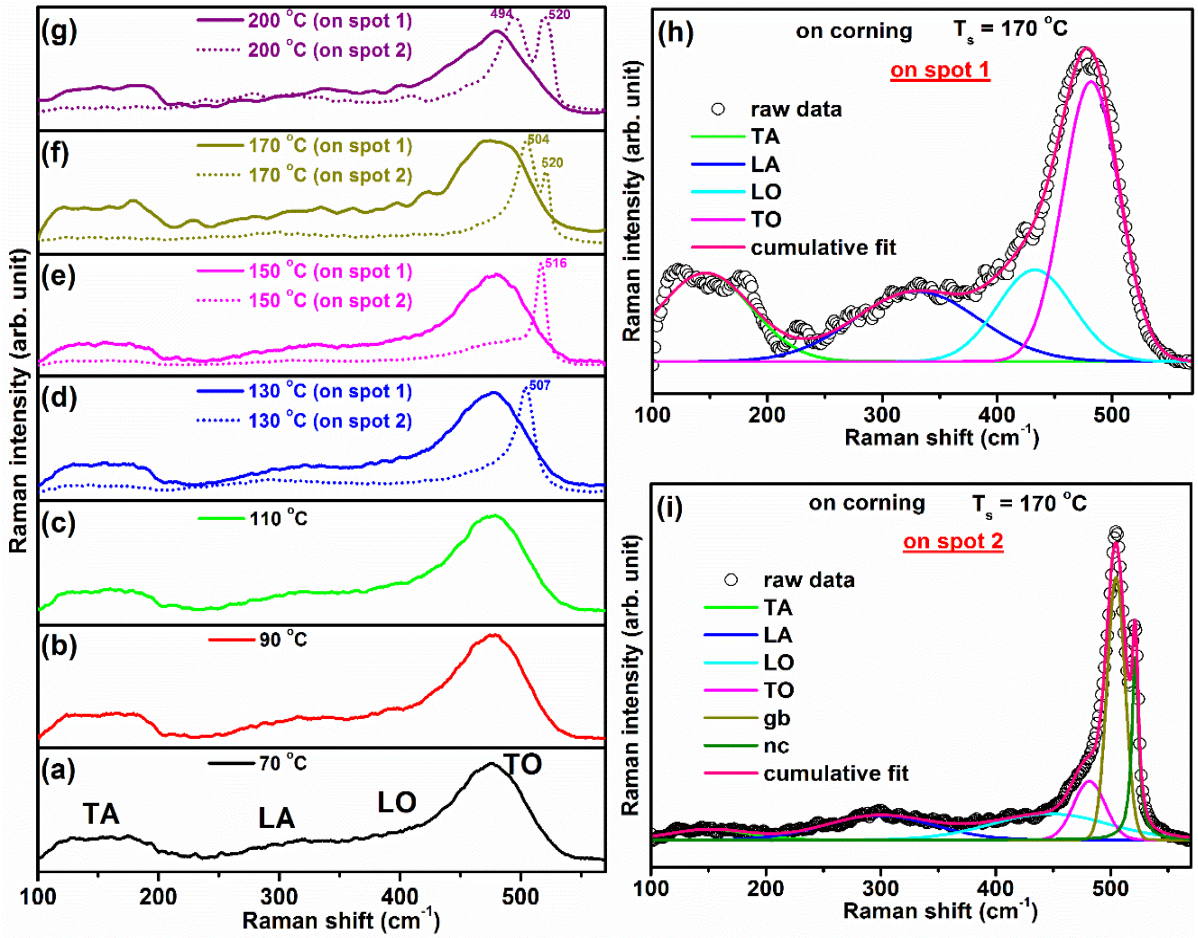

***Figure 3.4**: (a-g) Raman spectra of intrinsic a-Si:H films prepared at different T_s on Corning substrate. Deconvoluted Raman spectra of a-Si:H film deposited at T_s= 170 °C on Corning (h) amorphous phase (on spot 1) (i) nanocrystalline phase (on spot 2).*

In order to find the different parameters like total crystalline fraction (X_c), crystallite size (d_{Raman}), rms deviation of tetrahedral angle ($\Delta\theta_B$) and medium range order (*MRO*) each Raman spectra were deconvoluted in the range 100-570 cm^{-1} into different components. The detailed calculation procedure is mentioned in Chapter 2.

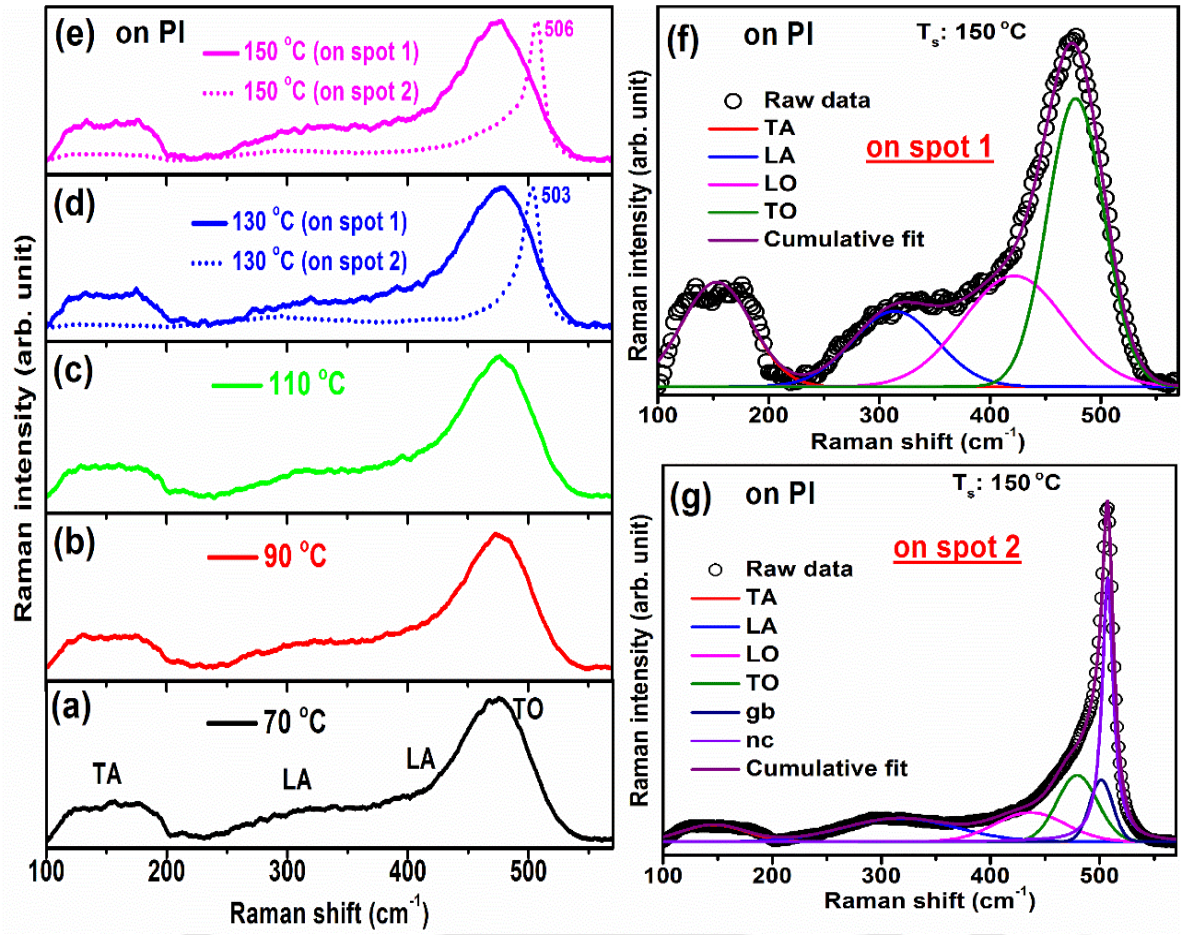

***Figure 3.5**: (a-e) Raman spectra of intrinsic a-Si:H films at different T_s on polyimide substrate. Deconvoluted Raman spectra of a-Si:H film deposited at T_s= 150 °C on Corning (f) amorphous phase (on spot 1) (g) nanocrystalline phase (on spot 2).*

The deconvoluted Raman spectra of amorphous and nanocrystalline phase of films on Corning, PI and PP substrates are shown in Figure 3.4 (h, i), Figure 3.5 (f, g) and Figure 3.6 (f, g) respectively. The TO mode is sensitive to short-range order (*SRO*) which is measure of rms deviation in the tetrahedral bond angle ($\Delta\theta_B$) and it can be obtained from the full width at half maxima (*FWHM*) of amorphous TO mode.

The *FWHM* is deduced from deconvoluted spectra for each sample and $\Delta\theta_B$ is calculated for all the samples. The values of *FWHM* and the corresponding $\Delta\theta_B$ are listed in Table 3.2. In the Table *–am* and *–nc* indicate that amorphous and crystalline phases respectively. A decrease in $\Delta\theta_B$ from 7.38 to 6.73° on Corning, 7.27 to 6.68° on PI and 7.31 to 6.84° on PP with increase in T_s indicates an improvement in structural ordering of amorphous network irrespective of substrate. As I_{TA}/ I_{TO} is a measure of dihedral angle variation, lower value indicates better medium range order (*MRO*). The I_{TA}/ I_{TO} values are found to be low for

amorphous network for films on Corning compared to films on PI and PP. In nanocrystalline phases also, low values of I_{TA}/I_{TO} are observed indicating an improvement of medium range order. It is further observed that size of the nanocrystallites (d_{Raman}) and total crystalline fraction (Xc(%)) increases with increase in T_s. The calculated *FWHM* of TO mode, $\Delta\theta_B$, I_{TA}/I_{TO}, d_{Raman} and X_c (%) [10-13] for each sample are listed in Table 3.2.

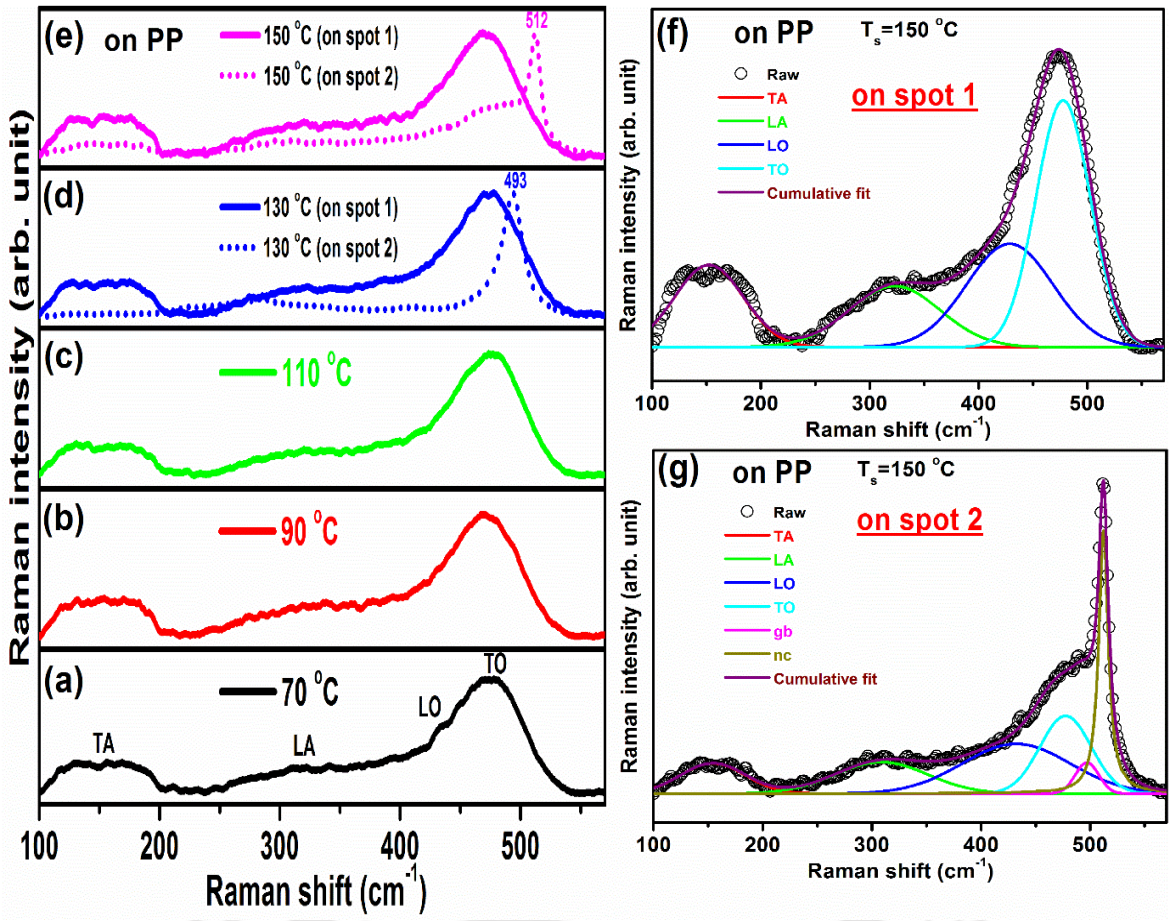

***Figure 3.6**: (a-e) Raman spectra of intrinsic a-Si:H films at different T_s on photo paper substrate. Deconvoluted Raman spectrum of a-Si:H film deposited at T_s= 150 °C on Corning (f) amorphous phase (on spot 1) (g) nanocrystalline phase (on spot 2).*

***Table 3.2**: Estimated values of full width at half maxima (FWHM) of TO mode, rms bond angle deviation $\Delta\theta_B$ (^{o}), crystallite size and total crystalline fraction X_c (%) from Raman spectra of the films on Corning, PI and PP substrates at different T_s. In the table –am and –nc indicate that amorphous and nanocrystalline phase respectively.*

Ts (^{o}C)	*FWHM* of TO mode (cm^{-1})			$\Delta\theta_B$ (^{o})			I_{TA}/I_{TO}			Crystallite size (nm)			Total crystalline fraction X_c (%)		
	Corning	PI	PP	Corning	PI	PP	Corning	PI	PP	Corning	PI	PP	Corning	PI	PP
70-am	59.28	58.62	58.86	7.38	7.27	7.31	0.39	0.42	0.40	-	-	-	-	-	-
90-am	57.85	58.32	61.02	7.14	7.22	7.67	0.40	0.37	0.45	-	-	-	-	-	-
110-am	56.72	58.38	57.77	6.95	7.20	7.13	0.32	0.39	0.42	-	-	-	-	-	-
130-am	56.50	56.46	57.72	6.92	6.91	7.12	0.35	0.36	0.40	-	-	-	-	-	-
150-am	55.53	55.08	55.09	6.76	6.68	6.68	0.33	0.43	0.46	-	-	-	-	-	-
170-am	55.49	-	-	6.75	-	-	0.42	-	-	-	-	-	-	-	-
200-am	55.38	-	-	6.73	-	-	0.42	-	-	-	-	-	-	-	-
130-nc	50.17	50.28	48.03	5.86	5.88	5.51	0.29	0.35	0.44	2.37	2.09	1.68	44	49	48
150-nc	48.98	43.74	50.16	5.66	4.79	5.86	0.23	0.32	0.48	3.97	2.29	2.96	68	67	52
170-nc	39.88	-	-	4.15	-	-	0.30	-	-	8.88	-	-	74	-	-
200-nc	35.12	-	-	3.35	-	-	0.37	-	-	8.88	-	-	71	-	-

3.2.1.2 Spectroscopic ellipsometry (SE)

Spectroscopic ellipsometry (SE) is a nondestructive optical technique used to extract optical constants of the material**.** Figure 3.7 (a-f) show the experimental (open) and fitted (solid line) data of real $<\varepsilon_1>$ and imaginary $<\varepsilon_2>$ parts of the pseudo dielectric function of *a-Si:H* thin films deposited at different T_s on Corning, PI and PP substrates.

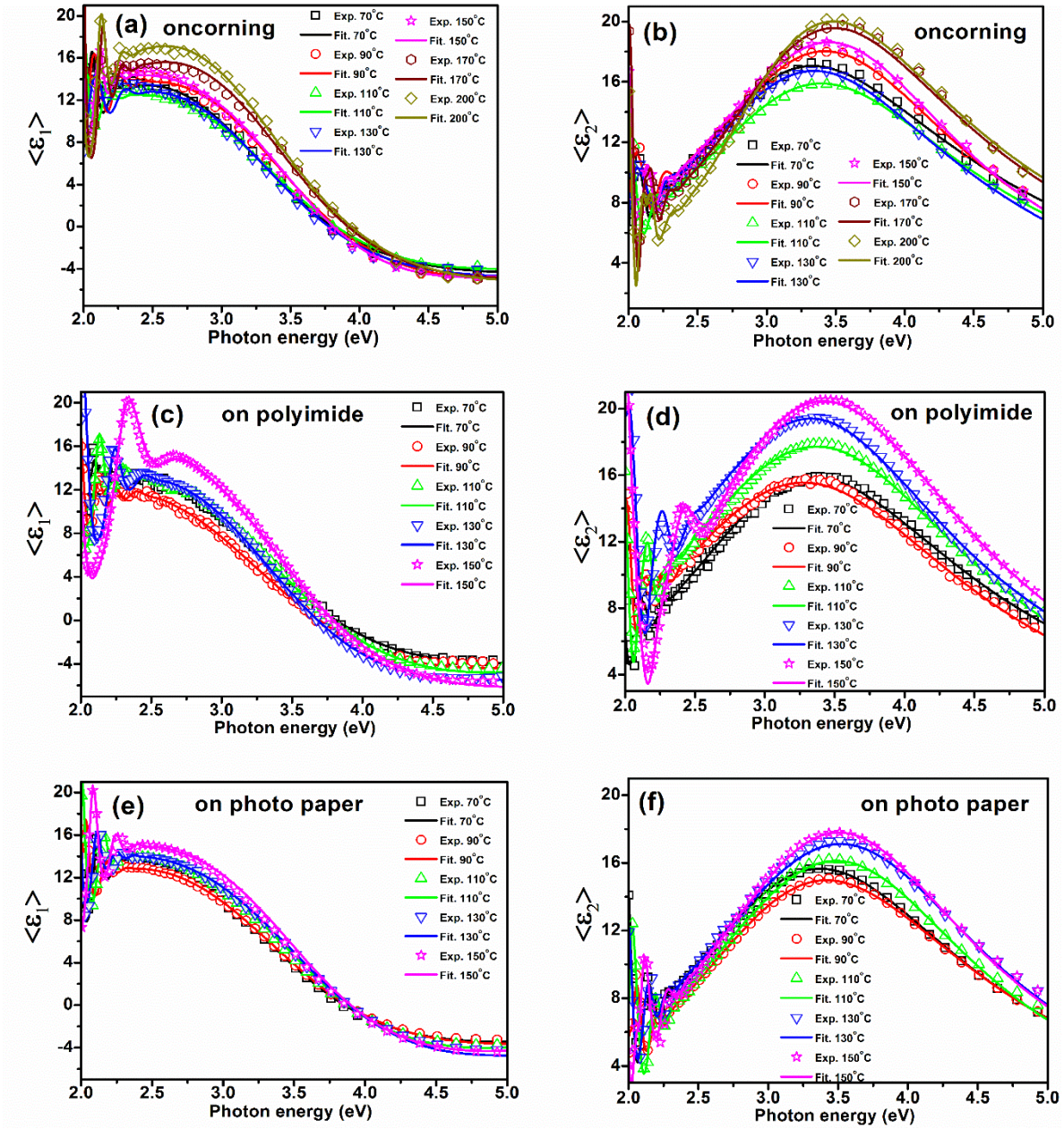

Figure 3.7*: The experimental (open) and fitted (solid line) data of (a, c, e) the pseudo dielectric function of real $<\varepsilon_1>$ and (b, d, f) imaginary $<\varepsilon_2>$ of intrinsic a-Si:H thin films deposited at different T_s on Corning, PI and PP substrates.*

In order to fit experimental data, we have used Tauc-Lorentz model [14-17], one of the widely used dispersion model to describe the optical properties of the amorphous materials, by constructing a two-layer structure consisting of *ambient/rough surface layer/bulk a-Si:H layer/substrate*. The expressions for imaginary ($<\varepsilon_2>$) and real ($<\varepsilon_1>$) part of dielectric functions in *T-L* model are discussed in Chapter 2.

Figure 3.7 show the experimental (open) and fitted (solid line) data of real $<\varepsilon_1>$ and imaginary $<\varepsilon_2>$ parts of pseudo dielectric function of *a-Si:H* thin films deposited at different T_s on Corning, PI and PP substrates. The *T-L* model fitted parameters (rough surface layer, amplitude (*A*), resonance energy (E_0), broadening (*C*)) are shown in Figure 3.7 for films on Corning, PI and PP substrates respectively. A broad peak around ~3.5 eV in $<\varepsilon_2>$ versus photon energy plot is characteristic feature of the direct optical transition in amorphous silicon structure [18, 19]. In *SE* spectra, amplitude factor (*A*) is proportional to the maximum height of $<\varepsilon_2>$ and is related to the density of the film [20]. It can be seen that amplitude of the peak increases with increase in T_s, which indicates that denser film formation takes place at higher T_s. It is observed that position of maximum $<\varepsilon_2>$ ($<\varepsilon_2>_{max}$) remains at around 3.5 *eV* for films up to 130 ^oC and for T_s > 130^oC, $<\varepsilon_2>_{max}$ is shifted towards higher energy side (Figure 3.7 (b, d, f)). The shift in the $<\varepsilon_2>_{max}$ is due to presence of a few nano meter sized crystallites in the film [21].This is in good agreement with results obtained from Raman measurements. However, it is observed that amplitude factor is smaller in case of 110 and 130 ^oC films on Corning and 90 ^oC films on PI and PP substrate as compared to that for films deposited at other T_s. This could be due to higher porosity in these films, which causes decrease in $<\varepsilon_2>_{max}$ without any significant shift in its peak energy position. Oscillator broadening parameter (*C*) is another parameter, which is directly related to Si-H_2 fractions in the film. Higher fraction of Si-H_2 bonds in the film signifies higher disorder in the material [15]. Decrease in the broadening of $<\varepsilon_2>$ peak with increase in T_s indicates a decrease in fraction of Si-H_2 bonds in the films on Corning, PI and PP substrates. It is observed that films on PI and PP substrates have slightly higher broadening compared to film on Corning. The thickness of rough surface layer for the films on PI and PP are similar to those for films on Corning substrate. The variation in thickness of rough surface layer is ~ ±1 nm. The results suggest that the growth kinetics is similar in all the cases, though there is a difference in physical properties of the substrates.

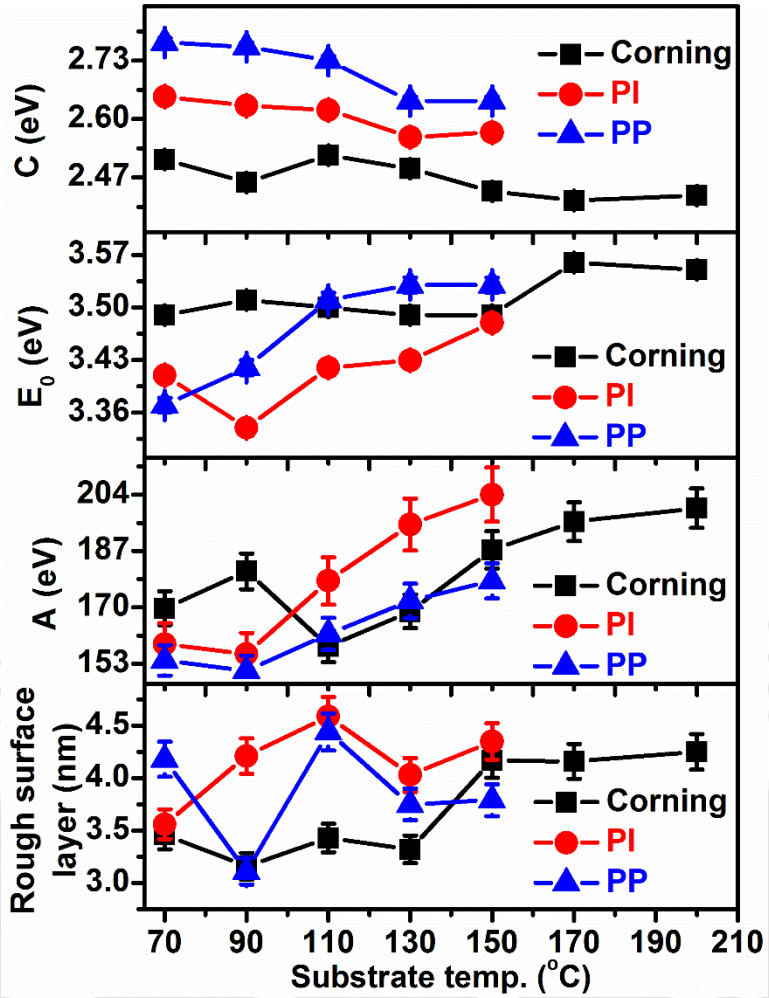

***Figure 3.8**: T-L model fitting parameters of intrinsic a-Si:H films deposited at different T_s on Corning, PI and PP substrates*

3.2.1.3 UV-Vis-NIR

Figure 3.9(a) shows UV-Vis-NIR transmission spectra of intrinsic *a-Si:H* films recorded on Corning substrate. The presence of large number of interference fringes indicate that the films are sufficiently thick and are of uniform thickness. Thickness of the film was calculated from Swanepoel's method [22] using interference fringes. The optical band gap (E_g) was calculated using Tauc's relation by plotting $(\alpha h\upsilon)^{1/2}$ versus $h\upsilon$ [23]. Figure 3.9 (b) shows the Tauc's plot of sample prepared at different T_s. The intercept of the fitted line (in red colour) on the energy axis gives the E_g of the film. Since PI and PP are not transparent substrates, thickness and E_g of these films were estimated from SE measurements only. The calculated thickness and E_g of the films from different measurements are shown in Figure 3.9 (c, d)

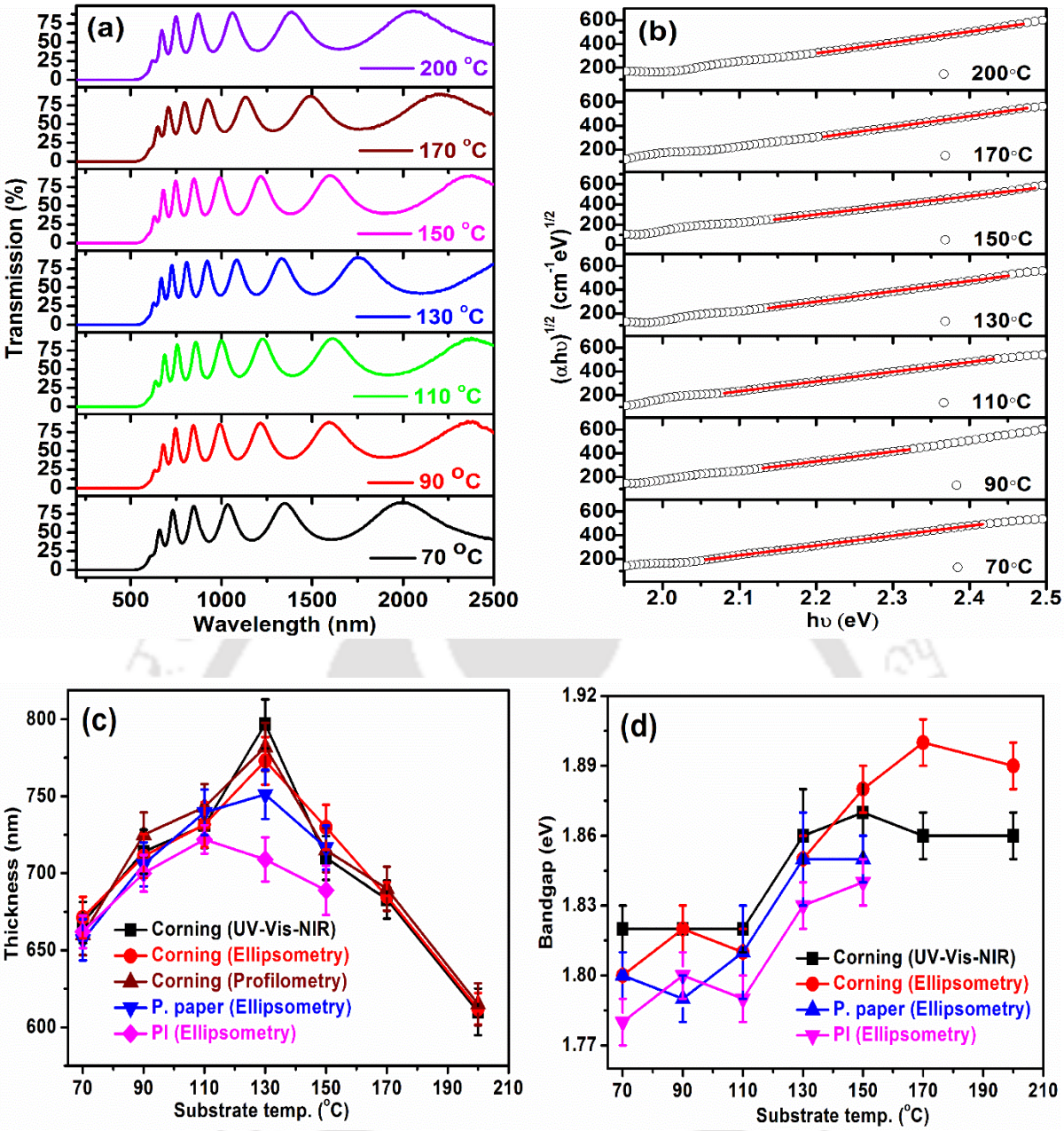

***Figure 3.9**: (a) UV-Vis-NIR transmission spectra of a-Si:H thin films with different T_s. (b) Plot of $(\alpha h\upsilon)^{1/2}$ versus $h\upsilon$ for samples prepared at different T_s on Corning. (c) estimated thickness and (d) band gap from different measurements.*

The error bars in Figure 3.9 (c, d) indicate the uncertainty in the calculated thickness and E_g. The thickness is found to be in the range of 610±15–794±15 nm (70-200°C), 662±10–722±9 nm and 656±13–751±15 nm (70-150°C) corresponding to film on Corning, PI and PP substrates respectively. At T_s<130 °C, thickness of the films increases with increase in T_s since the increase in the sticking probability of precursor radicals adsorbed on the growing surface of a-Si:H is more in comparison with rate of surface recombination reactions [24].

When T_s is high (≥ 130 ^oC), more hydrogen radicals in plasma participate in selective etching of loosely bonded Si or strained Si atoms in the amorphous material leaving behind nanocrystalline silicon film, which results in a decrease in thickness of the films [25]. The E_g increases at higher T_s due to narrowing of band tail width as a result of improved crystallinity in the samples. The thickness and band gap (E_g) energy values estimated from SE measurement are in agreement with UV-Vis-NIR measurement data.

3.2.1.4 Fourier Transform Infrared Spectroscopy (FTIR)

The FTIR transmission spectra of films deposited at different T_s on c-Si substrate are shown in Figure 3.10(a). It can be seen that the spectra have dips at ~630 cm^{-1}, ~2000 cm^{-1}, and ~2100 cm^{-1} corresponding to Si-H wagging or rocking mode and stretching modes of Si-H and Si-H_2 respectively [26, 27]. The hydrogen content (C_H (%)) in the film was calculated from the total IR absorption intensity under the peak corresponding to wagging mode of silicon hydrogen bond, whereas microstructure factor (R*) is calculated from the fraction of Si-H_2 bond density to (Si-H + Si-H_2) bond density [28, 29]. The calculation details of C_H (%) and R* have been discussed in chapter 2.

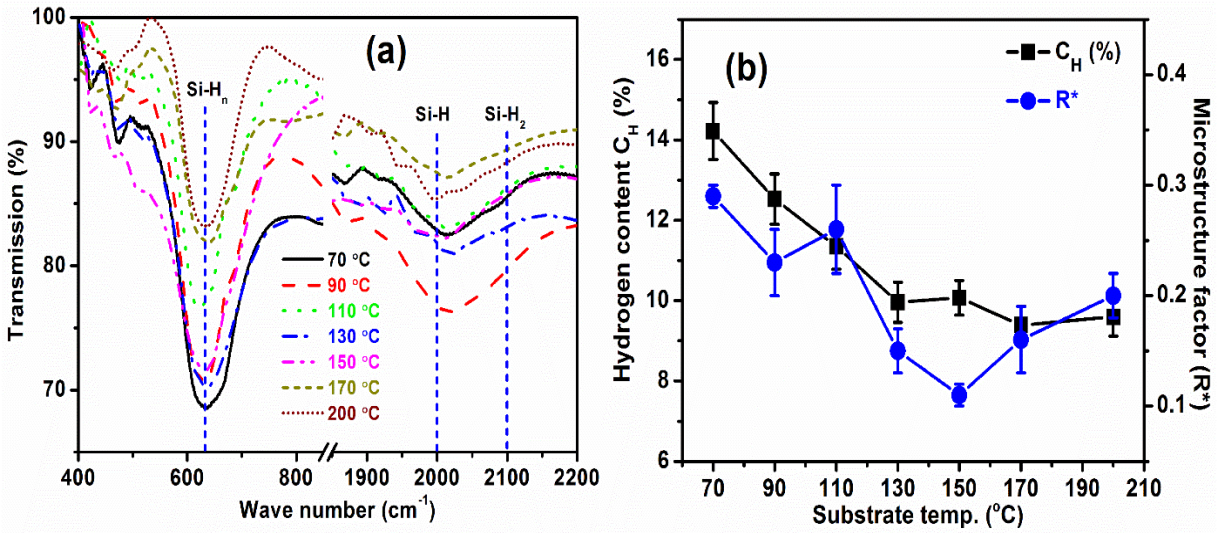

***Figure 3.10**: (a) FTIR transmission spectra of the films deposited at different T_s on c-Si substrates, (b) Bonded hydrogen content and microstructural factor as a function of T_s.*

Figure 3.10 (b) shows variation of C_H (%) and R* for film deposited at different T_s. The values of C_H (%) are found to be in the range of 8.65±0.43-14.22±0.71. The results show that the total hydrogen concentration, as estimated from the dip near ~630 cm^{-1}, gradually decreases with increase in T_s. From the Figure 3.10(a), it is also observed that dip near 2000

cm^{-1}, corresponding to absorption in stretching mode, systematically shifts toward lower wavenumber. This indicates that hydrogen bonding in the amorphous network gradually shifts from $(Si\text{-}H_2)_n$ or $Si\text{-}H_2$ to Si-H with increase in T_s. The R^* has been used to characterize the structural inhomogeneity of *a-Si:H* films. It is known that there is a close correlation between the infrared absorption at about 2100 cm^{-1} and disordered domains or microvoid structure; the absorption in this region is due to hydrogen bonded as $(Si\text{-}H_2)_n$ or $Si\text{-}H_2$ configuration [30]. A continuous decrease of R^* is observed with increasing T_s as shown in Figure 3.10 (b). The decrease of R^* suggests that, the density of disordered domains is reduced in the amorphous network value with increasing T_s. During thin film deposition, the silicon atoms arriving at growing surface undergo surface diffusion and adsorption reaction [24]. The increase in T_s improves the surface mobility of silicon atoms allowing them to achieve a low energy site easily to form Si-Si bond. Consequently, the surface disorder of amorphous network reduces. In addition, the inhomogeneous regions could be decreased further as the strained Si-Si bonds are etched by the incident hydrogen atoms, the probability of which increases with the increase of T_s [24, 31]. Accompanying these processes, the total concentration of adsorbed hydrogen atoms on film surface is also decreased because the hydrogen desorption process is enhanced at higher T_s. From the *SE* measurements also, a decrease in broadening parameter C was observed at higher T_s. The broadening of $<\varepsilon_2>$ peak is directly related to $Si\text{-}H_2$ bond fractions in the film. The *SE* results are well consistent with results obtained from FTIR measurements. These values of $C_H(\%)$ and R^* are in good agreement with literature values for amorphous and mixed phase films deposited by RF-PECVD films [8, 32-35].

3.2.1.5 Atomic force microscopy (AFM)

Surface topography of intrinsic *a-Si:H* films on Corning, PI and PP substrates was recorded using AFM in tapping mode. The area of scan size over the film was 2×2 μm^2. Figure 3.11 (a-g), Figure 3.12 (a-e) and Figure 3.13 (a-e) show the surface topographic images of intrinsic *a-Si:H* films on Corning, PI and PP substrates at different T_s respectively.

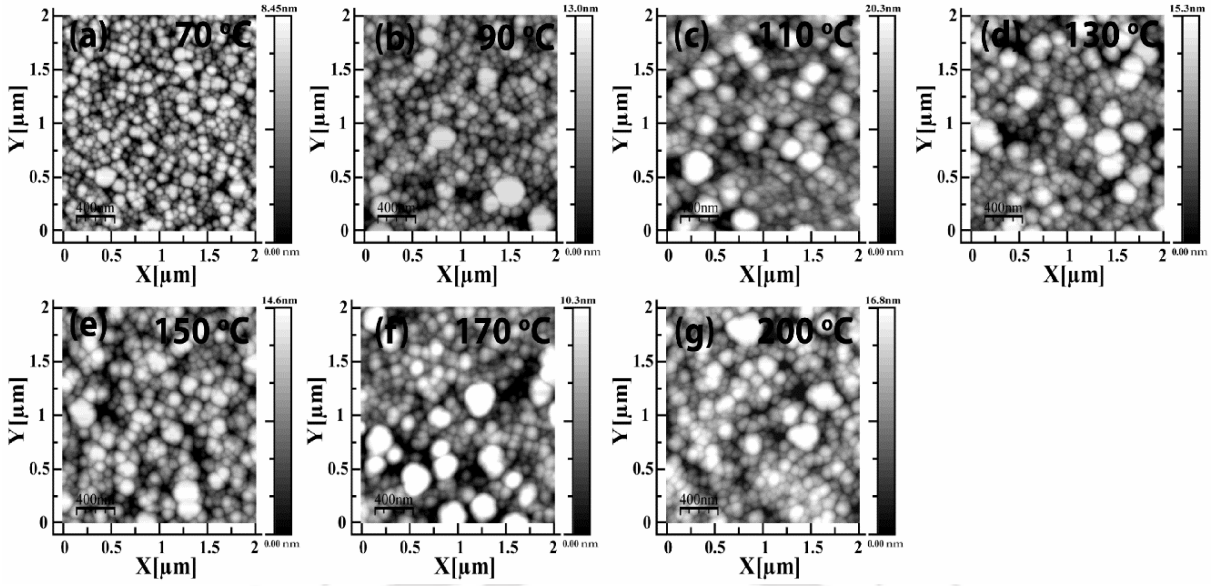

***Figure 3.11**: 2D surface morphologies of AFM images on Corning at different T_s (a) 70 °C (b) 90 °C (c) 110 °C (d) 130 °C (e) 150 °C (f) 750 °C and (g) 200 °C.*

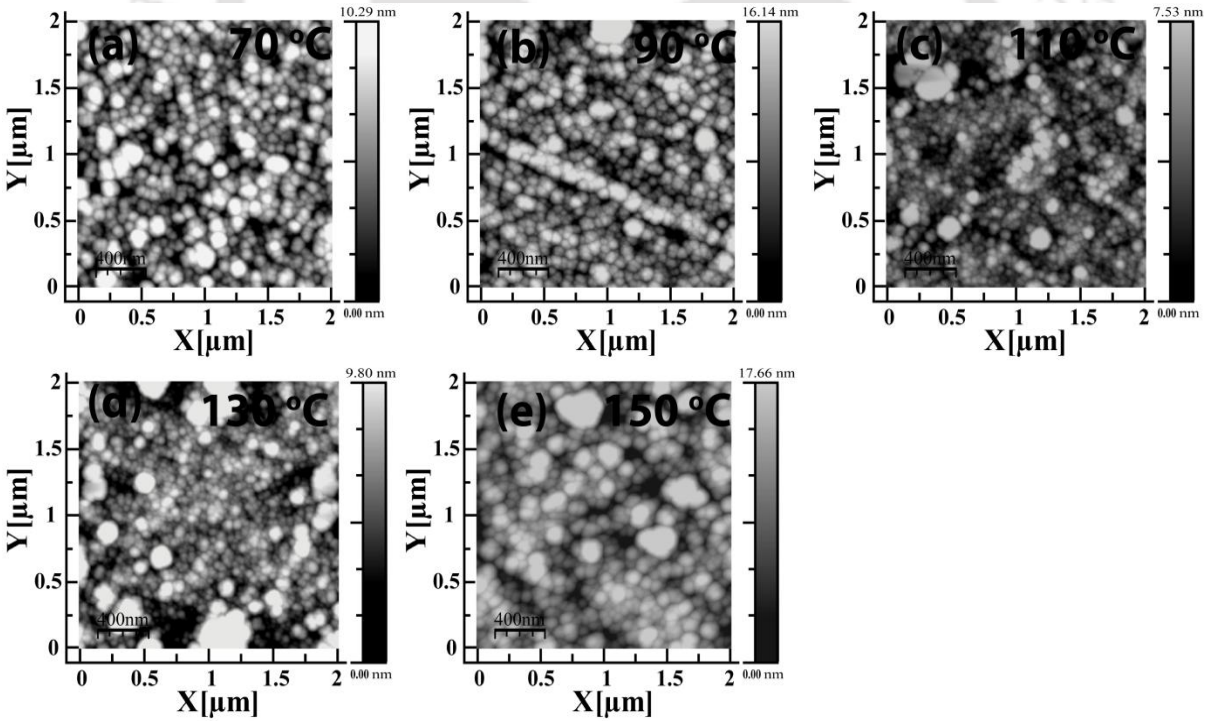

***Figure 3.12**: 2D surface morphologies of AFM images on polyimide at different T_s (a) 70 °C (b) 90 °C (c) 110 °C (d) 130 °C and (e) 150 °C.*

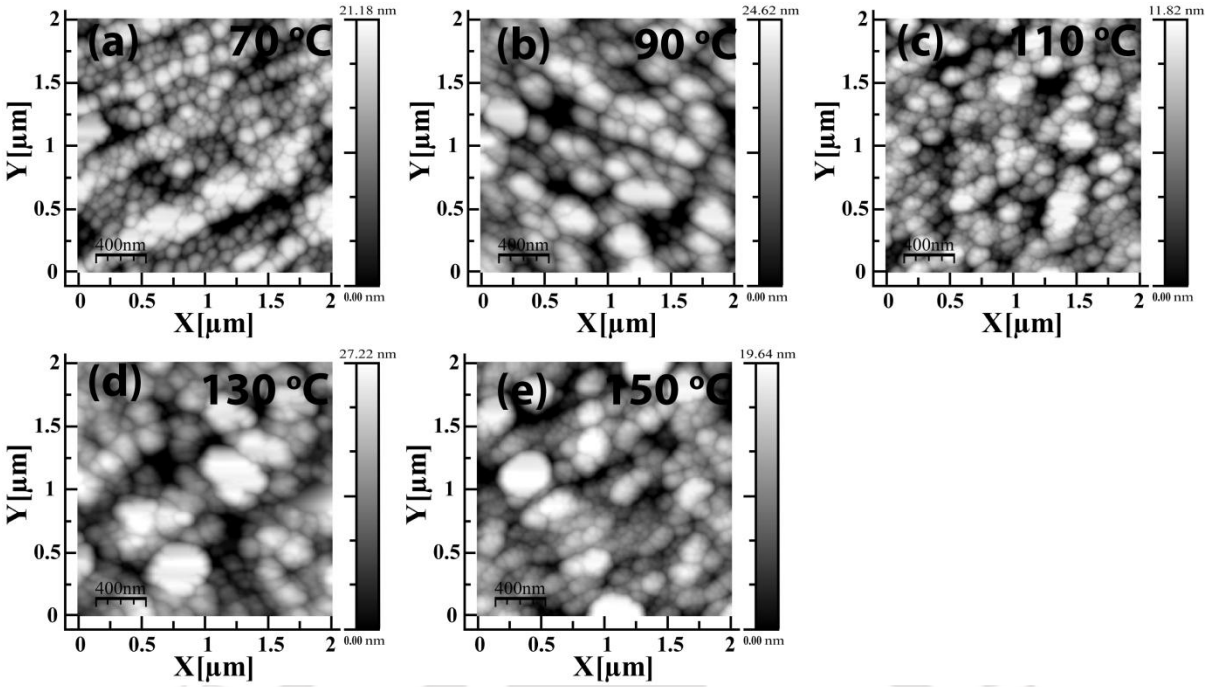

***Figure 3.13**: 2D surface morphologies of AFM images on photo paper at different T_s (a) 70 °C (b) 90 °C (c) 110 °C (d) 130 °C and (e) 150 °C.*

The root mean square (RMS) roughness of intrinsic films deposited T_s at 70, 90, 110, 130, 150, 170 and 200°C on Corning substrates are 2.07±0.06, 3.17±0.19, 4.09±0.11, 4.74±0.36, 4.11±0.13, 4.12±0.05 and 4.52±0.09 nm respectively whereas on PI and PP substrate the corresponding values at T_s of 70, 90, 110, 130 and 150 are 2.45±0.11, 3.92±0.13, 1.76±0.23, 2.35±0.31, 4.27±0.15 and 5.18±0.34, 5.97±0.12, 3.84±0.16, 6.70±0.36, 4.83±0.11 nm respectively. The RMS roughness of the bare Corning, PI and PP substrates are 0.36, 0.53 and 6.56 nm respectively. The RMS roughness values of the films on PI and PP substrates are comparable with the films on Corning substrate. The RMS roughness values are also consistent with the rough surface layer thickness values obtained from *SE* results.

3.2.1.6 Conductivity

In order to study electronic transport properties of the films, dark (σ_d) and photo conductivity (σ_{ph}) measurements were performed at room temperature. Figure 3.14 (a) shows the variation of room temperature σ_d and σ_{ph} as a function of T_s. The σ_d values of all the films are found to be quite low, comparable with that reported for device quality films deposited at higher temperature on conventional rigid substrates [11, 36]. Slightly higher value of σ_d for the films on PP substrate compared to that on rigid Corning substrate could be due to higher surface roughness of bare PP. The σ_d changes slightly from 10^{-11} - 10^{-10} $\Omega^{-1}cm^{-1}$ with increasing T_s.

On the other hand, σ_{ph} increases with T_s up to 150 ^oC and after which it saturates and remain more or less constant for films deposited on Corning. The σ_{ph} of the films changes from 10^{-8} - 10^{-6} $\Omega^{-1}cm^{-1}$. Photo sensitivity (σ_{ph}/σ_d) observed is ~ 4 orders of magnitude up to T_s = 130 ^oC and ~ 6 orders of magnitude above this T_s. The higher σ_{ph}/σ_d at higher T_s is due to presence of nanocrystallites and improvement in short range order, which also result in less broadening of peak in $<\varepsilon_2>$ spectra as compared to the films with pure amorphous phase. Temperature dependence of the conductivity was studied for films deposited at T_s = 150 ^oC. Figure 3.14(b) shows temperature dependence of dark and photo conductivity of films on Corning, PI and PP substrates. To deduce activation energy, the dark conductivity curve is fitted with Arrhenius equation. The activation (E_a) energy was found to be 0.95 eV, 0.98 eV and 0.91 eV for films deposited on Corning, PI and PP respectively. The E_a is approximately half of band gap energy. The high photosensitivity and purely intrinsic behavior as observed from the activation energy indicate that the films deposited at T_s = 150 ^oC are more or less defects free and suitable for photovoltaic and other device applications.

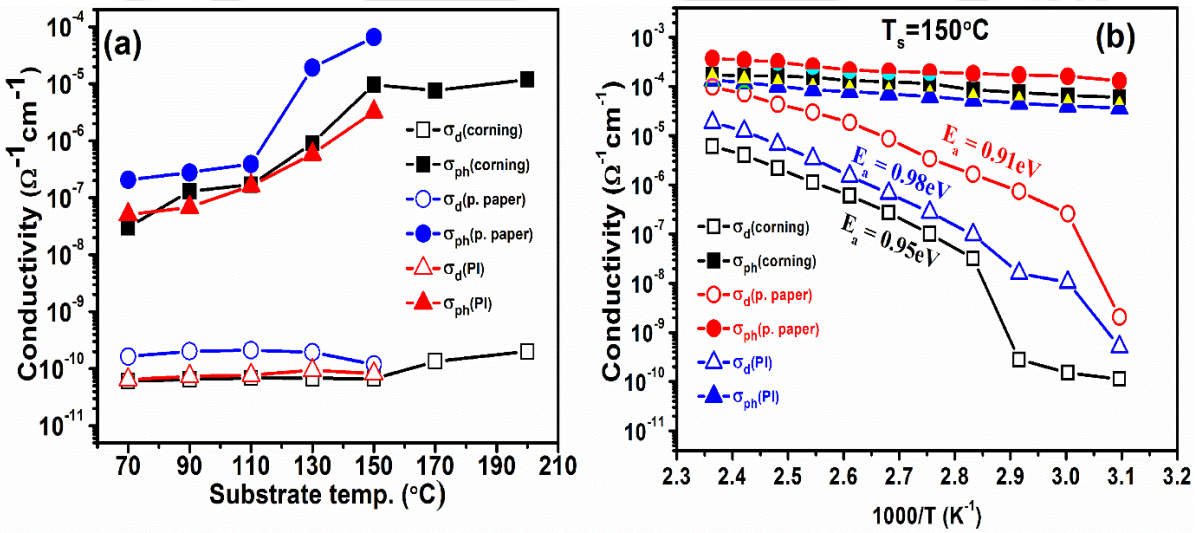

***Figure 3.14**: (a) Room temperature dark and photo conductivities of films prepared at different T_s. (b) Temperature dependent conductivity of sample prepared at T_s = 150 ^oC on Corning, PI and PP.*

3.2.2 Series (II): Variation of H_2 flow rate (HFR) during SiH_4 plasma at T_s = 150°C

In earlier substrate temperature variation series (section 3.2.1), it is observed that high photo sensitivity, improvement in short range order, less broadening of peak in $<\varepsilon_2>$ for films deposited at T_s =150^oC are due to presence of few nanometer sized nanocrystallites embedded in amorphous matrix. In order to study the microstructural and optoelectronic properties with hydrogen dilution on these films, we kept T_s at 150°C and varied hydrogen

flow rate (HFR) from 50- 90 sccm. The other deposition parameters were kept constant. The films were deposited on three different substrates, viz. Corning 1737 glass (Corning), photo paper (PP) and c-Si. The deposition parameters for this series are listed in 3.1.

3.2.2.1 Raman scattering

Like in previous T_s series (section 3.2.1), Raman spectra were recorded at several different positions on the surface of the films on Corning and PP substrates. A variation in Raman spectra corresponding to pure amorphous phase and nanocrystalline silicon embedded amorphous phase was observed at different positions on the film surface. To identify the different phases on the surface of the film, the image of the surface was recorded through Raman Mapping. Figure 3.15 (a-e) and Figure 3.16 (a-e) show the Raman mapping of the films deposited at different HFR on Corning and PP substrates respectively.

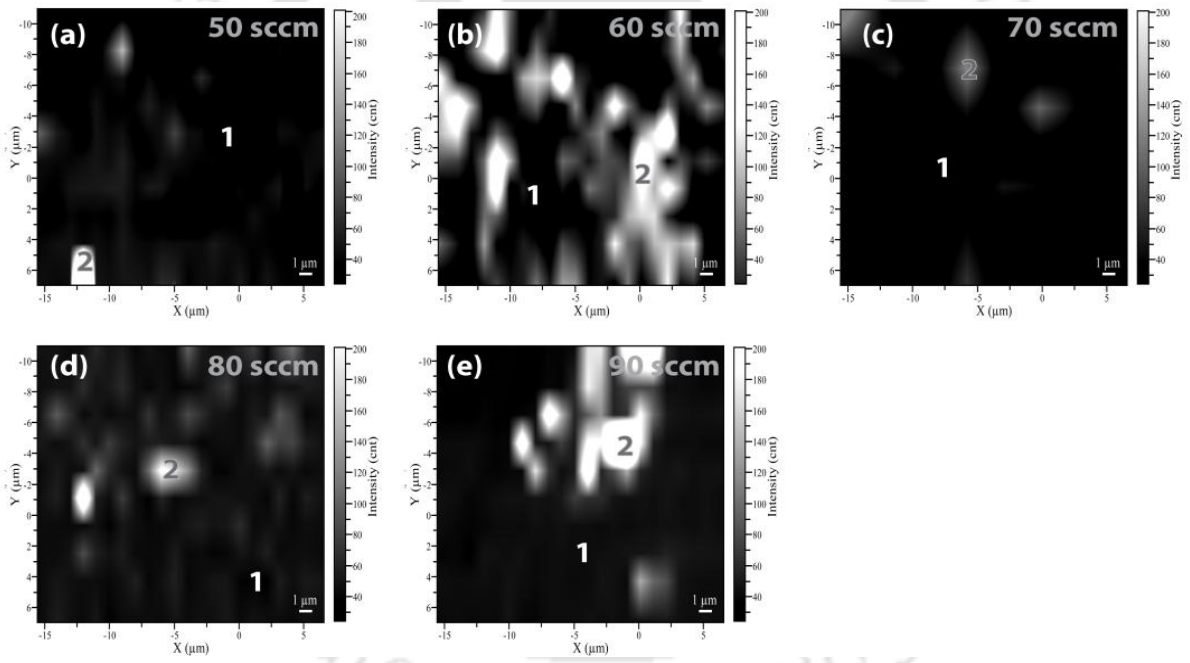

***Figure 3.15**: (a - e) Raman mapping of samples prepared at different hydrogen flow rates on Corning substrate.*

The black color in the image represents the amorphous phase whereas white color represents the region where nanocrystallites are embedded in amorphous matrix. The percentage area of the nanocrystallites embedded region for films deposited at HFR = 50, 60, 70, 80 and 90 sccm are 7.27, 30.23, 7.18, 27.45 and 18.61 % respectively for films on Corning substrates whereas FOR film on PP, it was found to be 7, 10, 5, 25 and 23% respectively. Raman spectra were recorded on these films by focusing the laser beam at amorphous region

(marked as spot 1) and nanocrystallites embedded region (marked as spot 2). The corresponding to amorphous and nanocrystalline phases Raman spectra are shown in Figure 3.17 (a) and 3.17 (b) for films on Corning and PP substrates respectively.

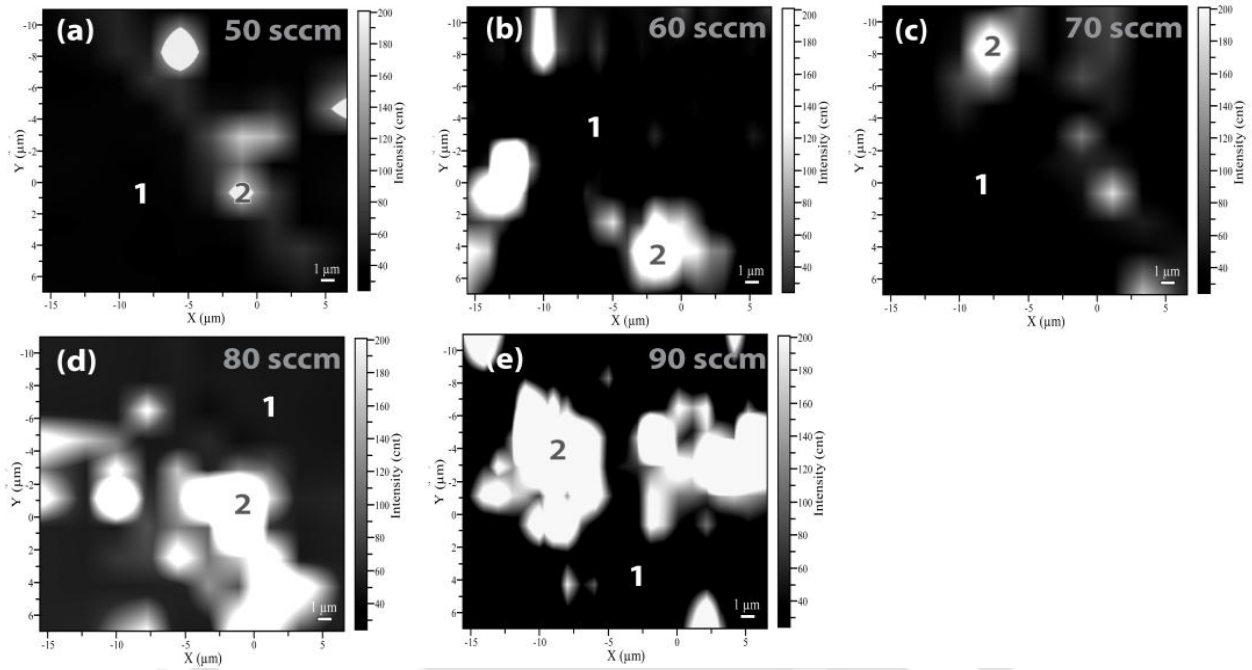

***Figure 3.16**: (a - e) Raman mapping of samples prepared at different hydrogen flow rates on PP substrate.*

Figure 3.17 (a-b) shows the Raman spectra of films prepared at different HFR on Corning and PP. For the quantitative estimation of different parameters like rms deviation of tetrahedral angle ($\Delta\theta_B$), total crystalline fraction (X_c (%)), crystallite size (d_{Raman}), the Raman spectra are deconvoluted in the range 100-570 cm^{-1} into different components similarly as described in earlier section 3.2.1. The deconvoluted Raman spectra of amorphous and nanocrystallites embedded phase of films prepared at HFR=80 sccm on Corning and PP substrates are shown in Figure 3.18 (a & c) and Figure 3.18(b & d) respectively.

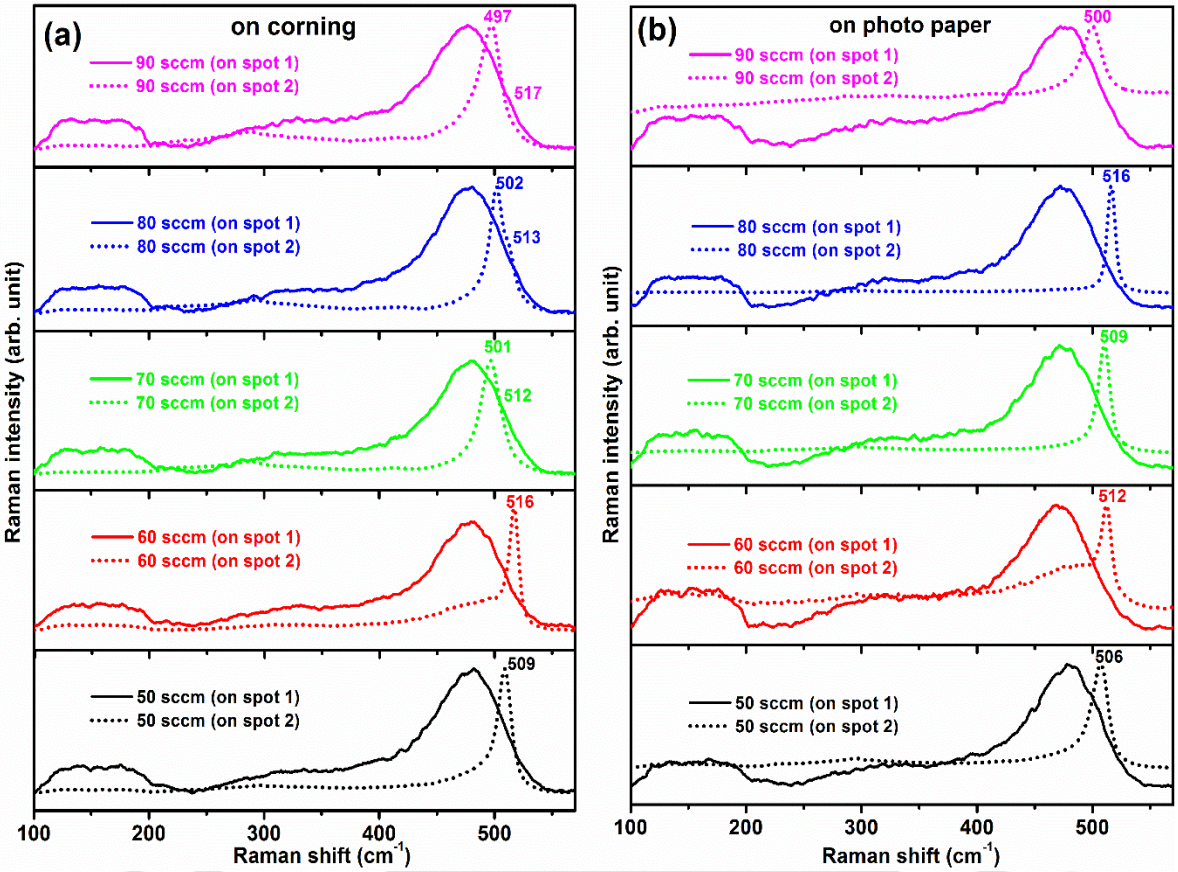

***Figure 3.17**: Raman spectra of films prepared at different hydrogen dilution prepared on (a) Corning and (b) photo paper substrates*

The values of crystallite size under present studies are found to be in the range of 2.56 - 4.44 nm for films on Corning and 2.46 - 6.28 nm for films on PP substrate respectively. It is observed that the crystallite size increases with increasing HFR on Corning and PP substrates. At high HFR, higher concentration of hydrogen in plasma helps in the full surface coverage and thus facilitates the surface diffusion of the film forming precursors like SiH_3, SiH_2, SiH and Si. Hence the adsorbed radicals find energetically favorable sites leading to improvement in order and also lead to the formation and growth of crystallites [24]. The atomic hydrogen also acts as etchant and breaks the weak Si-Si bonds on the growing film surface and thus helps in the creation of strong Si-Si bonds [37]. The atomic hydrogen not only acts on the top surface layer but it can also penetrate into few layers below the film surface where it helps in the formation of ordered structure by compensation of dangling bonds, breaking of weak bonds as well as reconstruction of strong bonds and the strain relaxation [38, 39]. Thus higher hydrogen flow rate results in increase in crystallite size.

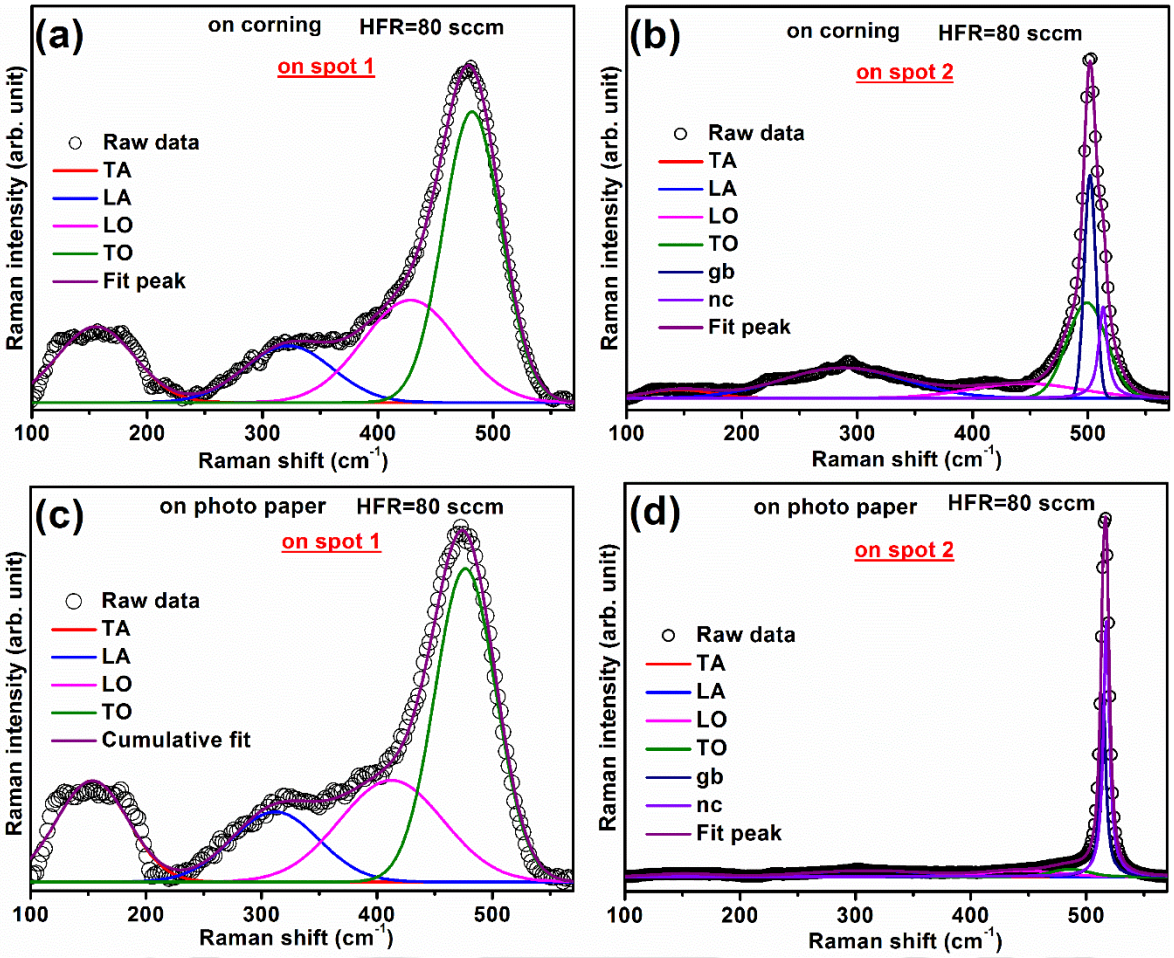

***Figure 3.18**: Deconvoluted Raman spectra of a-Si:H film deposited at HFR at 80 sccm on Corning and photo paper substrates (a, c) amorphous (spot 1)and (b, d) nanocrystallite embeded phase (spot 2).*

The rms bond angle deviations ($\Delta\theta_B$) is calculated for all the films using *FWHM* of amorphous TO mode deduced from deconvoluted spectra. The *FWHM* and the corresponding $\Delta\theta_B$ values are listed in Table 3.3. It is observed that, $\Delta\theta_B$ values for amorphous phase is in the range of 6.76- 7.69° on Coning substrate whereas on PP substrate it is around 6.22-8.09°. The $\Delta\theta_B$ values are nearly independent of HFR. The low value of $\Delta\theta_B$ on Corning and PP suggest better *SRO* even in amorphous phase. The calculated $\Delta\theta_B$ values for nanocrystalline phase are also listed in Table. 3.3, which are very good numbers for nc-Si:H and a-Si:H films. The total crystalline volume fractions of the films on Corning and PP substrates with different HFR are listed in Table 3.3.

***Table 3.3**: Estimated values of full width at half maxima (FWHM) of TO mode, rms bond angle deviation $\Delta\theta_B$ (^{o}), I_{TA}/I_{TO}, crystallite size and total crystalline fraction from Raman spectra of the films on Corning and PP substrates at different HFR. In the table –am and –nc indicate that amorphous and nanocrystalline phase respectively.*

H_2 flow rate (sccm)	*FWHM* of TO mode (cm^{-1})		$\Delta\theta_B$ (^{o})		I_{TA}/I_{TO}		Crystallite size (nm)		Total crystalline fraction X_c (%)	
	Corning	PP	Corning	PP	Corning	PP	Corning	PP	Corning	PP
50-*am*	59.21	52.32	7.37	6.22	0.33	0.34	-	-	-	-
60-*am*	55.53	55.08	6.76	6.68	0.33	0.46	-	-	-	-
70-*am*	58.53	63.51	7.26	8.09	0.33	0.40	-	-	-	-
80-*am*	60.59	62.25	7.60	7.88	0.30	0.36	-	-	-	-
90-*am*	61.16	61.17	7.69	7.70	0.33	0.39	-	-	-	-
50-*nc*	45.13	50.56	5.02	5.93	0.29	0.47	2.56	2.46	85	80
60-*nc*	48.98	50.16	5.66	5.86	0.23	0.48	3.97	2.96	68	52
70-*nc*	44.36	38.65	4.89	3.94	0.32	0.27	2.96	2.67	73	84
80-*nc*	44.02	35.23	4.84	3.37	0.31	0.21	3.14	3.97	49	86
90-*nc*	43.52	47.93	4.75	5.49	0.30	0.23	4.44	6.28	59	63

3.2.2.2 Spectroscopic ellipsometry

The optical parameters of intrinsic *a-Si:H* films were derived using spectroscopic ellipsometry (*SE*). The experiential data of $<\varepsilon_1>$ and $<\varepsilon_2>$ are fitted with *T-L* model by constructing two-layer model. The *T-L* model is discussed in in Chapter 2. Figure 3.19 show the experimental (open) and fitted (solid line) data real $<\varepsilon_1>$ part real (Figure 3.19 (a, c)) and imaginary $<\varepsilon_2>$ (Figure 3.19 (b, d)) part of pseudo dielectric function of *a-Si:H*(*i*) thin films deposited at different HFR (50-90 sccm) on Corning and PP substrates respectively. The *T-L* model fitted parameters (Thickness of bulk and rough surface layer, *A*, E_0, *C* and E_g) are listed in Table 3.4 and 3.5, respectively, for films on Corning and PP substrates.

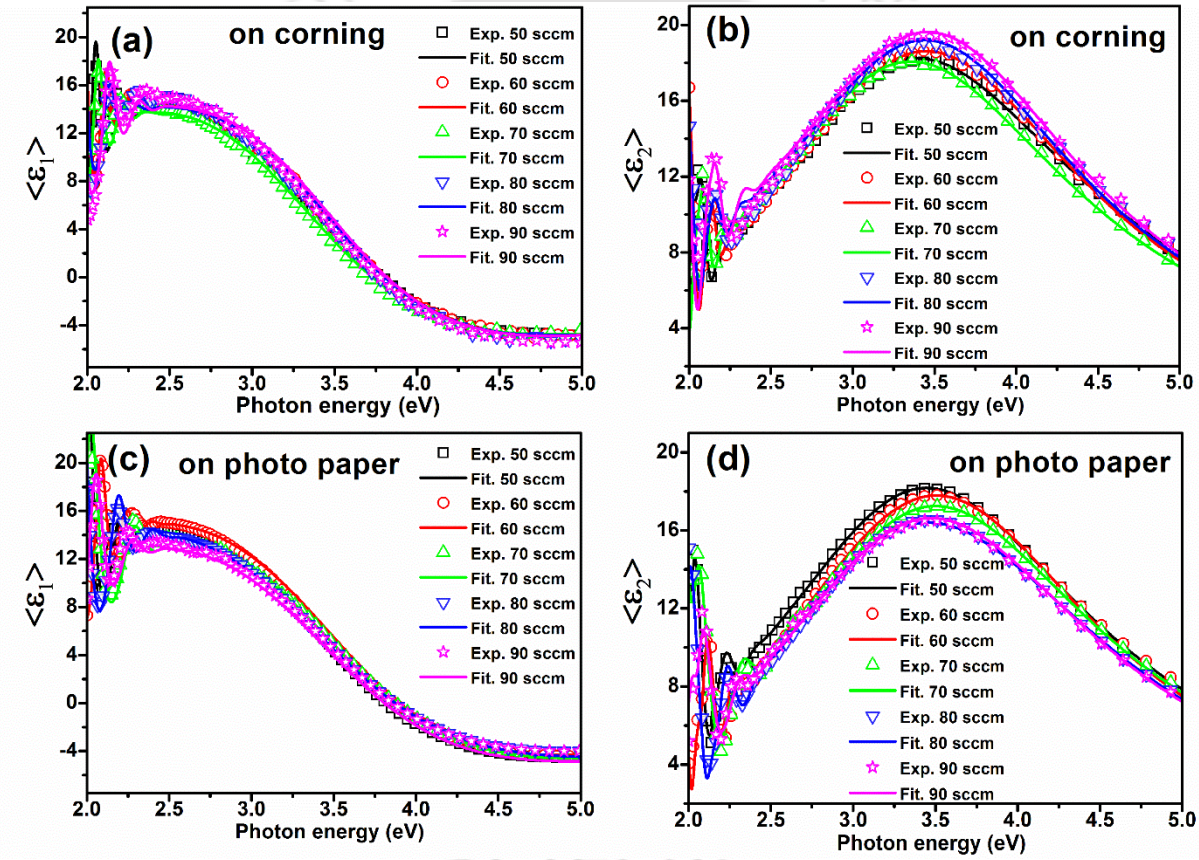

***Figure 3.19**: (a & c) Plot of experimental (open) and fitted (solid line) data of real dielectric function $<\varepsilon_1>$ against photon energy, (b & d) Plot of imaginary dielectric function $<\varepsilon_2>$ against photon energy at different H_2 flow rate on Corning and photo paper.*

The Amplitude factor (*A*) is proportional to the maximum height of $<\varepsilon_2>$ and is related to the density of the film. From the Figure 3.19 (b) we can observe that, the amplitude of $<\varepsilon_2>$ peak increases with increase in HFR on Corning substrate, which indicates that denser film formation takes place at higher HFR. On the other hand the amplitude of $<\varepsilon_2>$ peak decreases

with increase in HFR for films on PP substrate (Figure 3.19 (d)), which indicates film density decreases with increase in HFR for films on PP. Earlier for T_s variation series we have observed that, the film growth kinetics was not much influenced by the substrate. However this seems to be not true in the present case. Rao *et al* [40] reported that, the subsurface decomposition of radicals depend on the nature of the substrate. It has also been reported that the probability of incoming particle sticking to the substrate surface and particle distribution are different on rough surface and smooth surface.

***Table 3.4**: Estimated values of rough surface layer thickness (nm), thickness of bulk layer (nm), amplitude factor A (eV), resonance energy E_0 (eV), broadening parameter C (eV), optical bandgap E_g (eV) and constant $\varepsilon_1(\infty)$ from ellipsometry on Corning.*

H_2 flow rate (sccm)	Thickness of rough surface layer (nm)	Thickness of bulk layer (nm)	*A* (eV)	E_0 (eV)	*C* (eV)	E_g (eV)	$\varepsilon_1(\infty)$
50	4.56±0.01	744±05	182±03	3.51±0.01	2.52±0.01	1.85±0.01	0.43
60	4.17±0.01	729±14	187±06	3.49±0.01	2.44±0.01	1.88±0.01	0.31
70	5.77±0.01	747±09	178±02	3.45±0.01	2.53±0.01	1.87±0.01	1.05
80	4.88±0.01	658±05	196±05	3.50±0.01	2.51±0.01	1.88±0.01	0.67
90	5.28±0.01	616±08	207±03	3.52±0.01	2.54±0.01	1.89±0.01	1.23

***Table 3.5**: Estimated values of rough surface layer thickness (nm), thickness of bulk layer (nm), amplitude factor A (eV), resonance energy E_0 (eV), broadening parameter C (eV), optical bandgap E_g (eV) and constant $\varepsilon_1(\infty)$ from ellipsometry on PP.*

H_2 flow rate (sccm)	Thickness of rough surface layer (nm)	Thickness of bulk layer (nm)	*A* (eV)	E_0 (eV)	*C* (eV)	E_g (eV)	$\varepsilon_1(\infty)$
50	4.41±0.01	700±10	183±03	3.43±0.01	2.51±0.01	1.82±0.01	1.13
60	3.79±0.01	716±08	178±02	3.53±0.01	2.64±0.01	1.85±0.01	0.43
70	4.43±0.01	714±06	171±03	3.50±0.01	2.73±0.01	1.83±0.01	1.26
80	6.33±0.01	664±09	165±05	3.49±0.01	2.71±0.01	1.81±0.01	0.82
90	4.86±0.01	580±11	176±06	3.50±0.01	2.75±0.01	1.80±0.01	1.62

The position of maximum in $<\varepsilon_2>$ spectra ($<\varepsilon_2>_{max}$) is shifted towards higher energy side on both Corning and PP substrates with increase in HFR. The shift in position of $<\varepsilon_2>_{max}$ towards higher energy side indicates the presence of small nanometer sized crystallites embedded in the film. The similar feature was also observed by Bouizem *et al* [20], Losurdo *et al* [21] and S-B Li *et al* [41] for *a-Si:H* films. The *SE* results presented in this study are in

good agreement with Raman spectroscopy results. The E_0 values are found to be nearly independent of HFR on Corning and PP substrate. Broadening parameter (C) of $<\varepsilon_2>$ peak does not change much for films on Corning whereas for films on PP, it increases with HFR. Higher broadening of the $<\varepsilon_2>$ peak is related to higher fraction of Si-H_2 bonds in these films.

3.2.2.3 UV-Vis-NIR

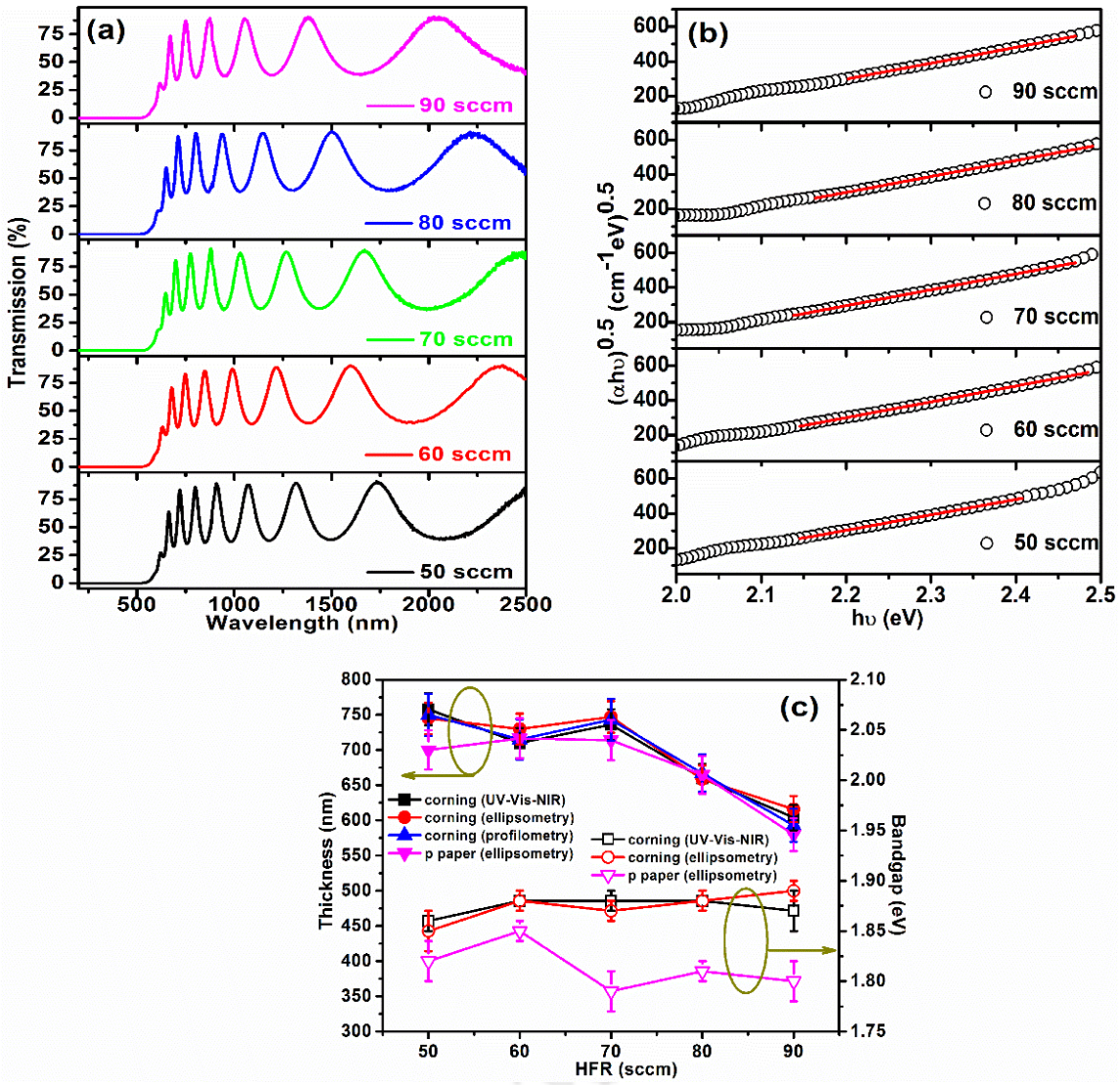

***Figure 3.20**: (a) UV-Vis-NIR transmission spectra of intrinsic a-Si:H thin films Corning with different HFR. (b) Plot of $(\alpha h\upsilon)^{1/2}$ versus $h\upsilon$ for samples prepared at different HFR on Corning (c) Estimated thickness and E_g from different measure measurements*

Figure 3.20 (a) show the UV-Vis-NIR transmission spectra of films, deposited on Corning substrate, as a function of HFR. The thickness of the films is calculated from interference fringes following Swanepoel's [22] method and E_g is calculated from Tauc's plot [23]. The $(\alpha h\upsilon)^{0.5}$ versus $h\upsilon$ plots for films deposited under different HFR are shown in Figure 3.20

(b). The calculated thickness and E_g of these films plotted as a function of HFR are shown in Figure. 3. 20 (c).

The thickness and E_g values calculated from *SE* results match well with those estimated from UV-Vis-NIR transmission spectra. A decrease in thickness with increasing hydrogen dilution of silane can be attributed to the presence of atomic H in plasma, which leads to excessive etching and breaking of weak Si–Si bonds [42-44]. Moreover, the increase in HFR increases the hydrogen partial pressure in the deposition chamber, which increases the gas phase polymerization. This leads to increase in concentration of higher silicon hydride species with lower sticking coefficients, which further increases the etching probability. Therefore, the overall thickness decreases with increase in hydrogen dilution in silane. Hydrogen dilution does not effect the band gap of the films [11, 36]. The band gap of the films on PP is slightly (~0.1eV) less than that of films on Corning substrate.

3.2.2.4 Fourier Transform Infrared Spectroscopy (FTIR)

Figure 3.21 (a) show FTIR transmission spectra for films under present study. The dips in the transmission spectra near 630 cm^{-1} corresponds to the wagging mode of all types of silicon hydrogen bond vibration i.e., SiH, SiH_2, SiH_3 etc. whereas dips at ~2000 and 2100 cm^{-1} correspond to stretching mode of Si-H and Si-H_2 respectively . The absorption coefficients in the wagging mode and stretching mode are shown in Figure 3.21 (b, c) respectively. From Figure 3.21 (b) one can see that the shape of wagging mode (~630 cm^{-1}) is losing its symmetry with increase in HFR and extra hump is observed at 665 cm^{-1} due to development of nanocrystallites in the amorphous film. Zhang *et al* and Halindintwali *et al* [45, 46] also observed the similar behavior with high H_2 dilution in silane. This development of crystallinity in the film is in good agreement with Raman results discussed previously. The total hydrogen content C_H (%) in the films is almost same up to HFR=70 sccm and decreases with further increase in HFR as shown in Figure 3.22 (a). The decrease in C_H (%) at higher HFR is due to high concentration of hydrogen in the plasma resulting strong hydrogen etching in the growing film. These values of C_H (%) are comparable with the reported values for hydrogen diluted amorphous films [8, 11, 47-49].

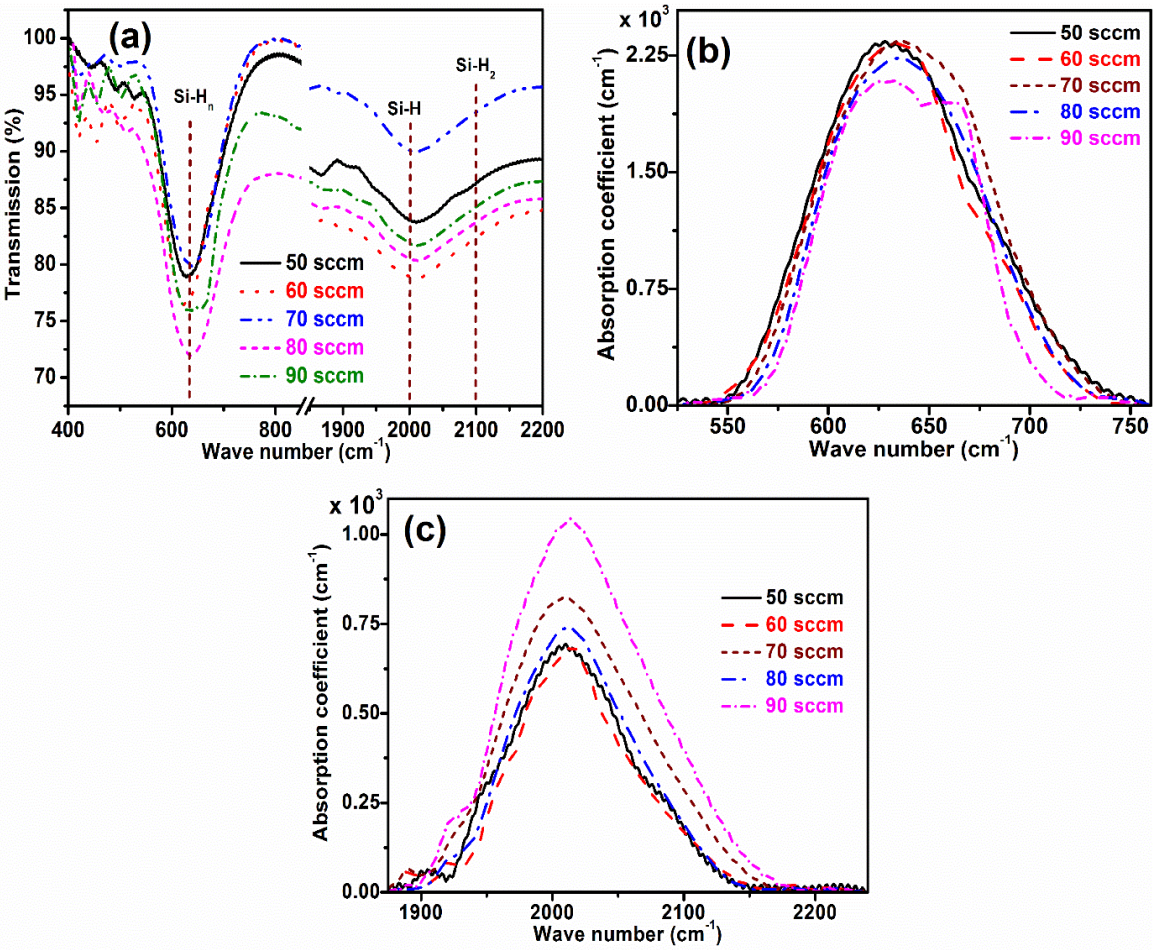

***Figure 3.21**: (a) FTIR transmittance spectra for the films at different HFR, (b) & (c) absorption coefficients due to the wagging mode and stretching mode of silicon hydrogen bond vibration derived from the FTIR transmittance spectra respectively.*

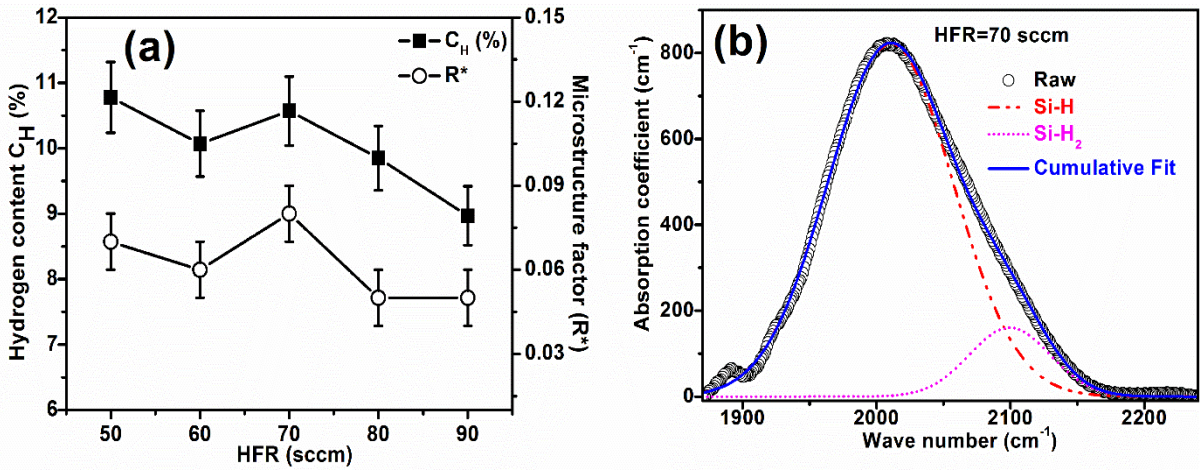

***Figure 3.22**: (a) Bonded hydrogen content C_H(%) and microstructural factor (R*) at different HFR (b) Deconvoluted absorption peak around 2000 cm^{-1} and 2100 cm^{-1} for film HFR=70 sccm*

In order to find the microstructural factor (*R**), absorption coefficient spectra was selected in the range 1870-2240 cm^{-1} and deconvoluted into two peaks centered at 2000 and 2100 cm^{-1}, corresponding to Si-H and Si-H_2 stretching modes, respectively. Figure 3.22(b) show the de-convoluted absorption spectra of film deposited at HFR =70 sccm. The *R** is in the range of 0.06±0.01-0.08±0.01 for different HFR films. It is indicating that, most of the hydrogen atoms in these films are bonded as strong Si-H bonds.

3.2.2.5 Atomic force microscopy (AFM)

Figure 3.23 (a-e) and Figure 3.24 (a-e) show 2-D surface topography images (AFM) of intrinsic *a-Si:H* thin films at different HFR deposited on Corning and PP substrates, respectively. The RMS roughness values of intrinsic films deposited at HFR = 50, 60, 70, 80 and 90 sccm on Corning substrates are 2.02±0.10, 4.11±0.13, 3.65±0.22, 4.13±0.12, and 5.28±0.13 nm respectively, whereas for films deposited on PP substrate, the corresponding values are 3.02±0.23, 4.83±0.11, 3.41±0.31, 7.21±0.18 and 3.81±0.11 nm respectively.

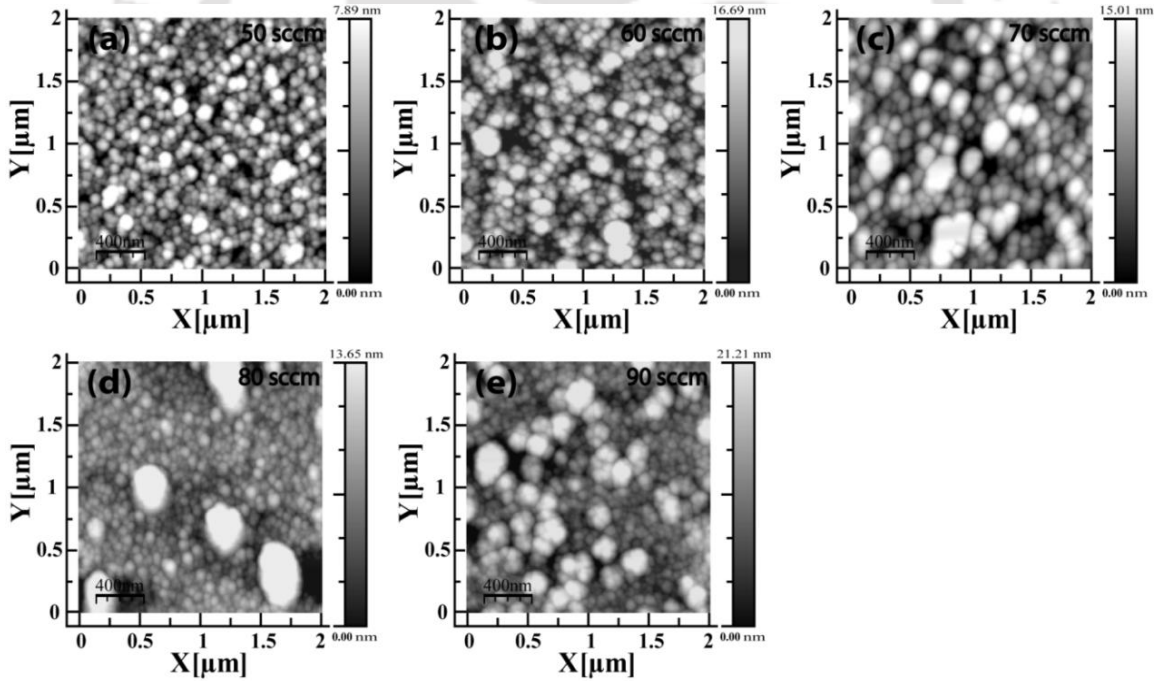

***Figure 3.23**: Two dimensional surface morphologies of AFM images of intrinsic a-Si:H films on Corning at different HFR (a) 50 sccm (b) 60 sccm (c) 70 sccm and (d) 80 sccm and (e) 90 sccm respectively.*

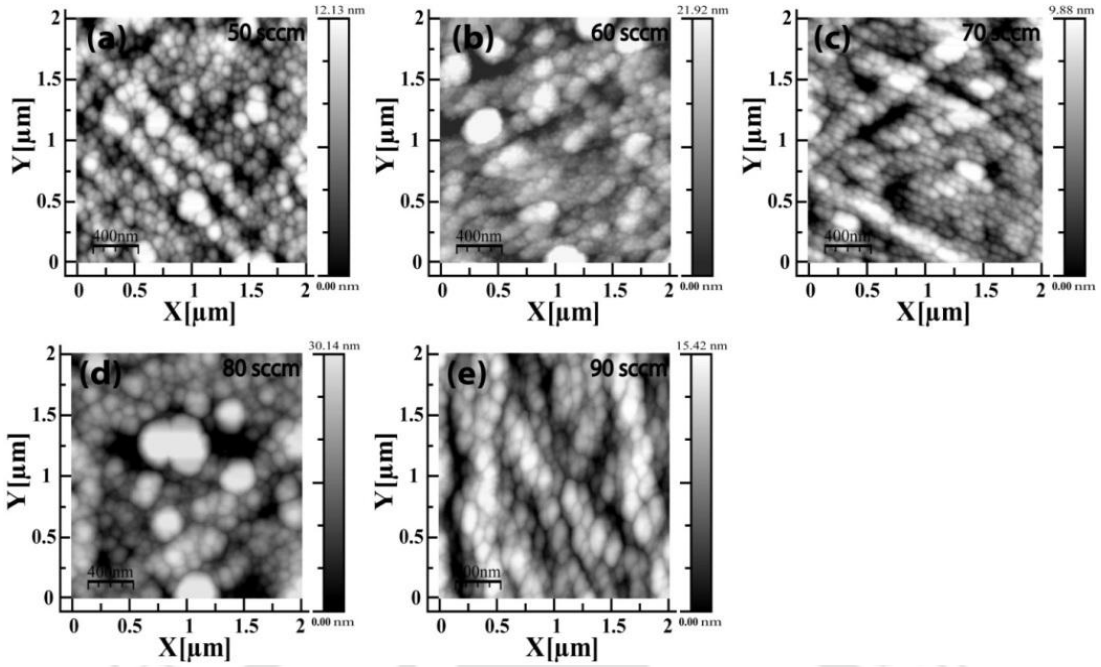

***Figure 3.24**: Two dimensional surface morphologies of AFM images of intrinsic a-Si:H films on photo paper at different HFR (a) 50 sccm (b) 60 sccm (c) 70 sccm and (d) 80 sccm and (e) 90 sccm respectively.*

The thickness of rough surface layer estimated from SE (Table 3.4, 3.5) is nearly comparable with the RMS roughness estimated from AFM measurement. It is observed from AFM surface image that the films deposited on Corning are densely packed. Whereas for films deposited on PP substrate, scattered clusters are seen suggesting a decrease in density of the films. These observations are in agreement with *SE* results, where a decrease in amplitude of $<\varepsilon_2>$ peak for films on PP substrate with increase in HFR was observed; the amplitude of $<\varepsilon_2>$ peak is directly related to the density of the films.

3.2.2.6 Conductivity

In order to study electronic transport properties of the films, dark (σ_d) and photo conductivity (σ_{ph}) measurements, in coplanar geometry, were performed at room temperature. Figure 3.25 shows the variation of σ_d and σ_{ph} of the films as a function of HFR on Corning and PP substrate. For the films on Corning and PP, the σ_d changes slightly from 10^{-11} - 10^{-10} $\Omega^{-1}cm^{-1}$ and σ_{ph} remains almost constant ~ 10^{-5} $\Omega^{-1}cm^{-1}$ with increase in HFR. The films on PP substrate show higher σ_d compared to that of films on Corning due to higher substrate roughness. The photosensitivity (σ_{ph}/σ_d) of films on PP is nearly ~5- 6 orders of magnitude, similar to that of films on Corning substrate. Higher σ_{ph}/σ_d ~5-6 order is due to presence of few nanometer sized crystallites distributed through out film and improvement in *SRO* in

amorphous phase [50]. These conductivity properties are well correlated with Raman and *SE* results obtained in this study.

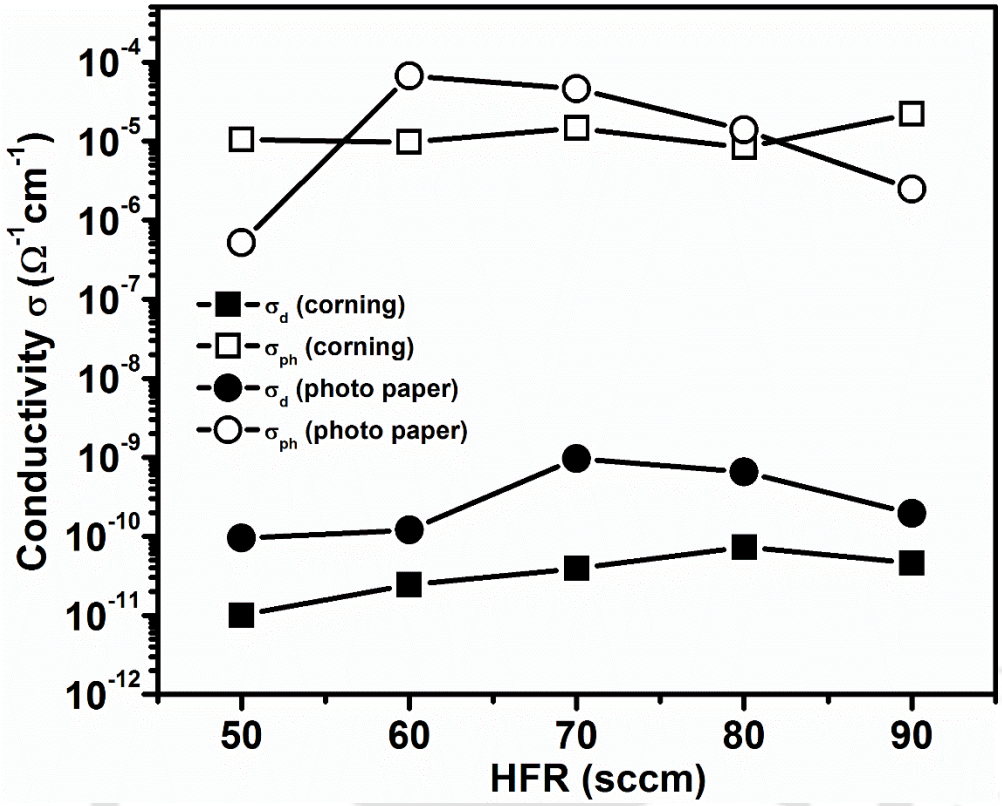

Figure 3.25: *Room temperature dark (σ_d) and (σ_{ph}) as a function of HFR on Corning and PP substrate*

3.2.3 Series (III): Variation of rf power during silane plasma at T_s = 110°C

In this series, intrinsic *a-Si:H* thin films were deposited at 110°C substrate temperature with variation in rf power (40-70W) using RF-PECVD (13.56 MHz) on Corning, PP and c-Si substrates. The deposition parameters for this series are listed in Table 3.1.

3.2.3.1 Raman scattering

Raman spectra of films deposited on Corning and PP substrates are shown in Figure 3.26 (a). The spectra were identified having TA, LA, LO and TO modes of *a-Si:H* [7]. For this series of films, we did not observe any TO mode peak ~510 cm^{-1} (for *nc-Si:H*). All films show TO mode peak at ~480 cm^{-1}, which indicates that these films are pure amorphous irrespective of the variation in rf power.

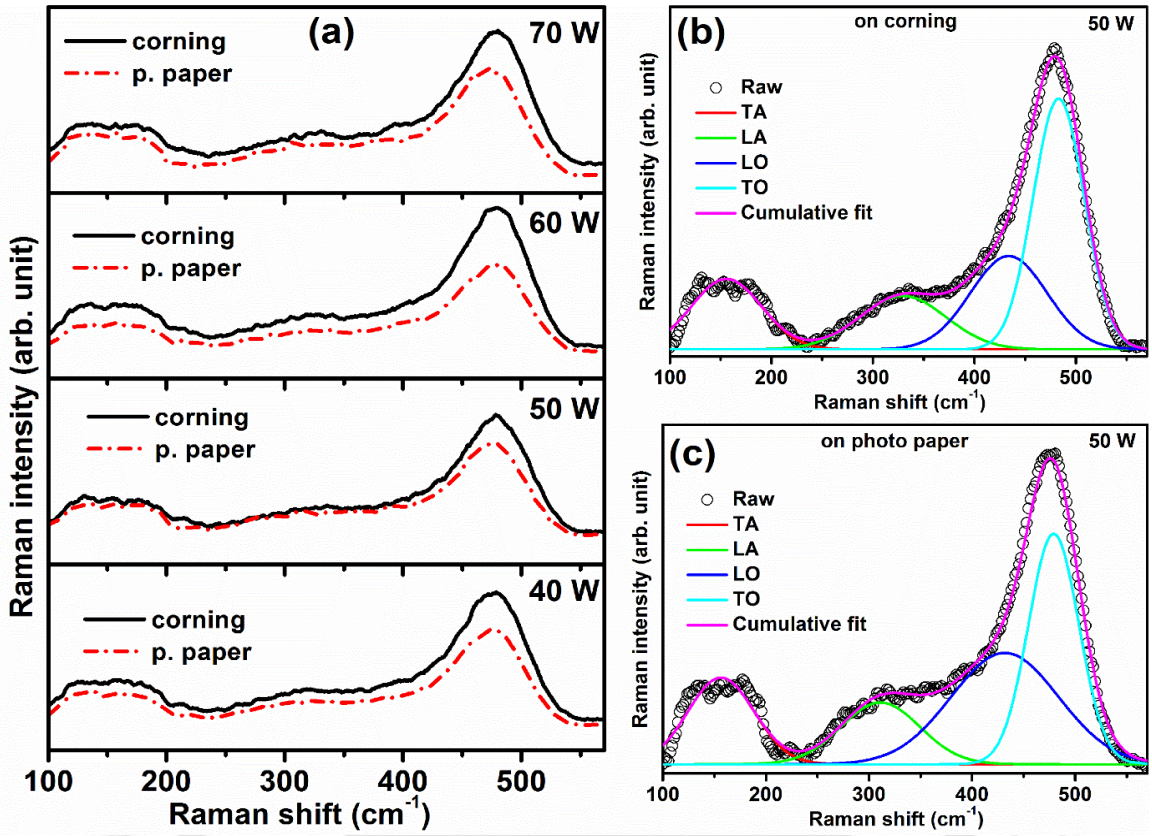

***Figure 3.26**: (a) Raman spectra of a-Si: H thin films deposited at different rf powers on Corning and photo paper. (b & c) Deconvoluted Raman spectra of films at rf power of 50 W.*

In order to find the TO mode peak position and its *FWHM*, each Raman spectra was de-convoluted into four Gaussian peaks. The deconvoluted Raman spectra of films deposited at 50 W rf power on Corning and PP substrates are shown in Figure 3.26 (b & c). The calculation of $\Delta\theta_B$ is mentioned in Chapter 2. The TO mode peak position and its *FWHM*, $\Delta\theta_B$ and I_{TA}/I_{TO} for all the films are listed in Table 3.6.

One can see that there is not much variation in TO mode peak position with variation in rf power for films on both substrates. The $\Delta\theta_B$ values are found to be in the range of 6.22 ± 0.12° to 7.09 ± 0.14° on Corning whereas on PP substrates it varies from 7.13 ± 0.14° to 7.21 ± 0.15°. For films grown on Corning substrate, $\Delta\theta_B$ is smallest when rf power is 50 W, which also shows low value of I_{TA}/I_{TO}. On the other hand, not much variation in *FWHM* and $\Delta\theta_B$ is observed with variation in rf power for films on PP. The low value of $\Delta\theta_B$ indicates less disorder in these films.

***Table 3.6**: The TO mode peak position, FWHM and $\Delta\theta_B$ values of intrinsic a-Si:H thin films on Corning and photo paper for different RF power.*

RF power (W)	on Corning				on photo paper			
	TO peak position (cm^{-1})	*FWHM* (cm^{-1})	$\Delta\theta_B$ (^{o})	I_{TA}/I_{TO}	TO peak position (cm^{-1})	*FWHM* (cm^{-1})	$\Delta\theta_B$ (^{o})	I_{TA}/I_{TO}
40	479	56.72	6.95	0.37	478	57.77	7.13	0.42
50	482	52.35	6.22	0.32	479	58.23	7.21	0.48
60	482	56.03	6.83	0.41	480	57.85	7.14	0.45
70	481	57.55	7.09	0.38	476	59.14	7.18	0.52

3.2.3.2 Spectroscopic ellipsometry (SE)

Figure 3.27 show the experimental (open) and fitted (solid line) data of real $<\varepsilon_1>$ (Figure 3.27 (a, c)) and imaginary $<\varepsilon_2>$ (Figure 3.27 (b, d)) parts of pseudo dielectric function of intrinsic *a-Si:H* thin films obtained from *SE* measurement. To deduce optical parameters, experiential data is fitted with *T-L* [51] model by considering a two-layered model. The *T-L* model details have been discussed in Chapter 2.

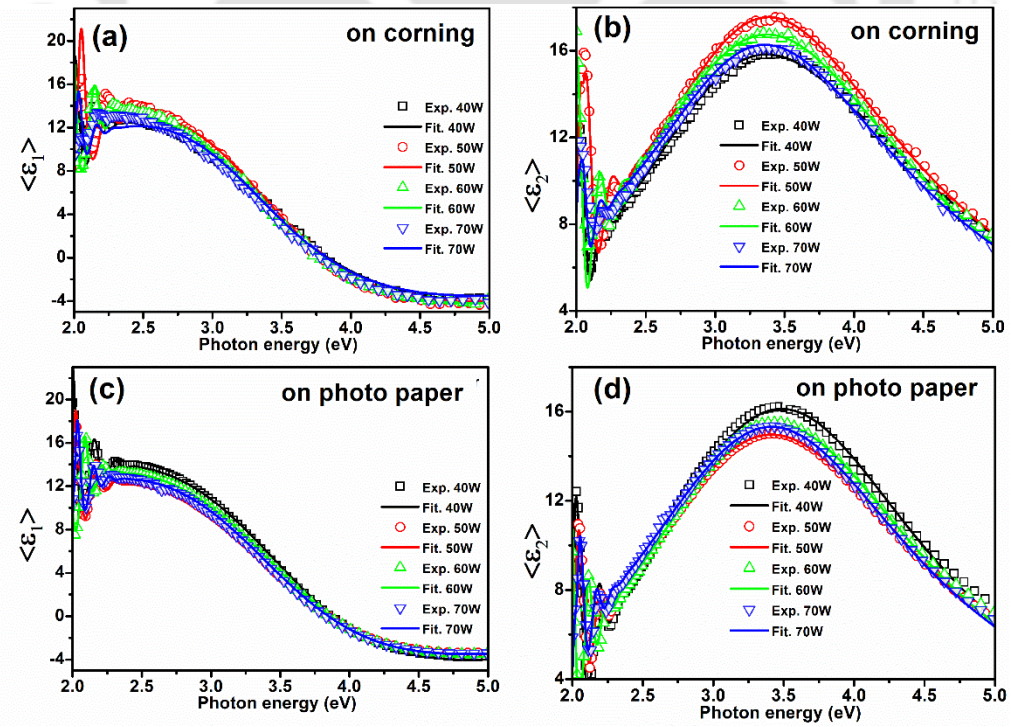

***Figure 3.27**: (a & c) Plot of experimental (open) and fitted (solid line) data of real dielectric function $<\varepsilon_1>$ and (b & d) imaginary dielectric function $<\varepsilon_2>$against photon energy.*

Figure 3.28 shows the *SE* fitting parameters for *a-Si:H* films on Corning and PP substrates deposited at different rf-power. In $<\varepsilon_2>$ spectra, position of maxima ($<\varepsilon_2>_{max}$) at around 3.5 eV and 4.2 eV are often attributed to amorphous and nanocrystalline silicon structure respectively [18]. In Fig 3.27, no shoulder peak around 4.2 eV is observed even with variation in rf power. This suggests that these films have pure amorphous structure, which is consistent with the results obtained in Raman spectra. It is observed that increase in rf power leads to a decrease in the magnitude of $<\varepsilon_2>$ without any significant shift in the position of peak ($<\varepsilon_2>_{max}$) on both Corning and PP substrates. The amplitude factor (*A*), which is related to the height/magnitude of the $<\varepsilon_2>$, is directly proportional to the density of the film [20]. The decrease in *A* with increase in rf power, indicates a decrease in the Si-Si bond density or alternatively an increase in the fraction of voids or vacancies in the film deposited at higher rf power.

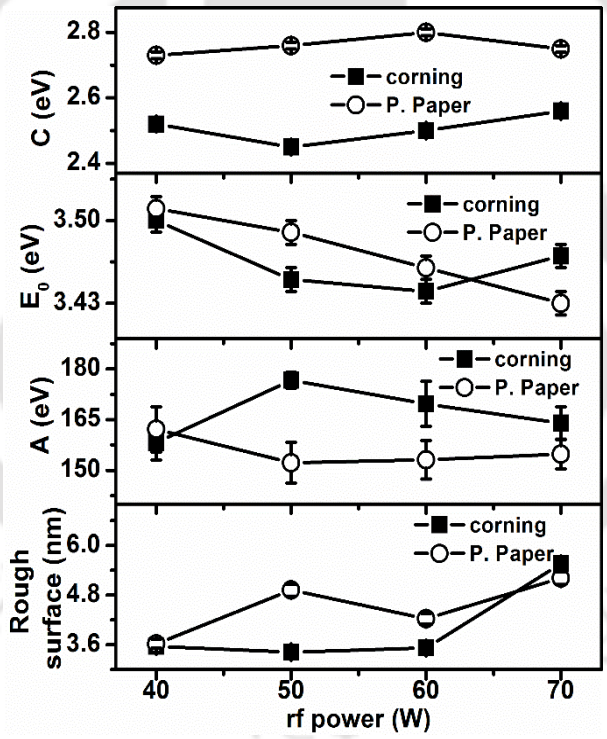

***Figure 3.28**: Fitting parameters of rough surface layer thickness (nm), amplitude factor (A), resonance energy (E_0), broadening (C) obtained from Tauc-Lorentz model for intrinsic a-Si:H films at different rf powers on Corning and PP substrates.*

The broadening parameter (*C*) in $<\varepsilon_2>$ is directly related to Si-H_2 bonds configurations within the film; higher broadening indicates higher fraction of Si-H_2 bonds in the film. Broadening of $<\varepsilon_2>$ peak increases with increase in rf power. The films on PP show higher broadening compared to films on Corning indicating higher fraction of Si-H_2 bonds in the films deposited

on PP. The films deposited at rf power of 50 W and 40 W on Corning and PP respectively show higher amplitude factor and lesser broadening in comparison to other films. Band gap of films on Corning slightly increases whereas a small decrease in band gap is observed for films on PP with increase in rf power.

3.2.3.3 UV-Vis-NIR

Figure 3.29 (a) show the UV-Vis-NIR transmission spectra of films deposited on Corning substrate at different rf-power. Transmission spectra of intrinsic *a-Si:H* films were used to determine its thickness by Swanepoel's [22] method using interference fringes.

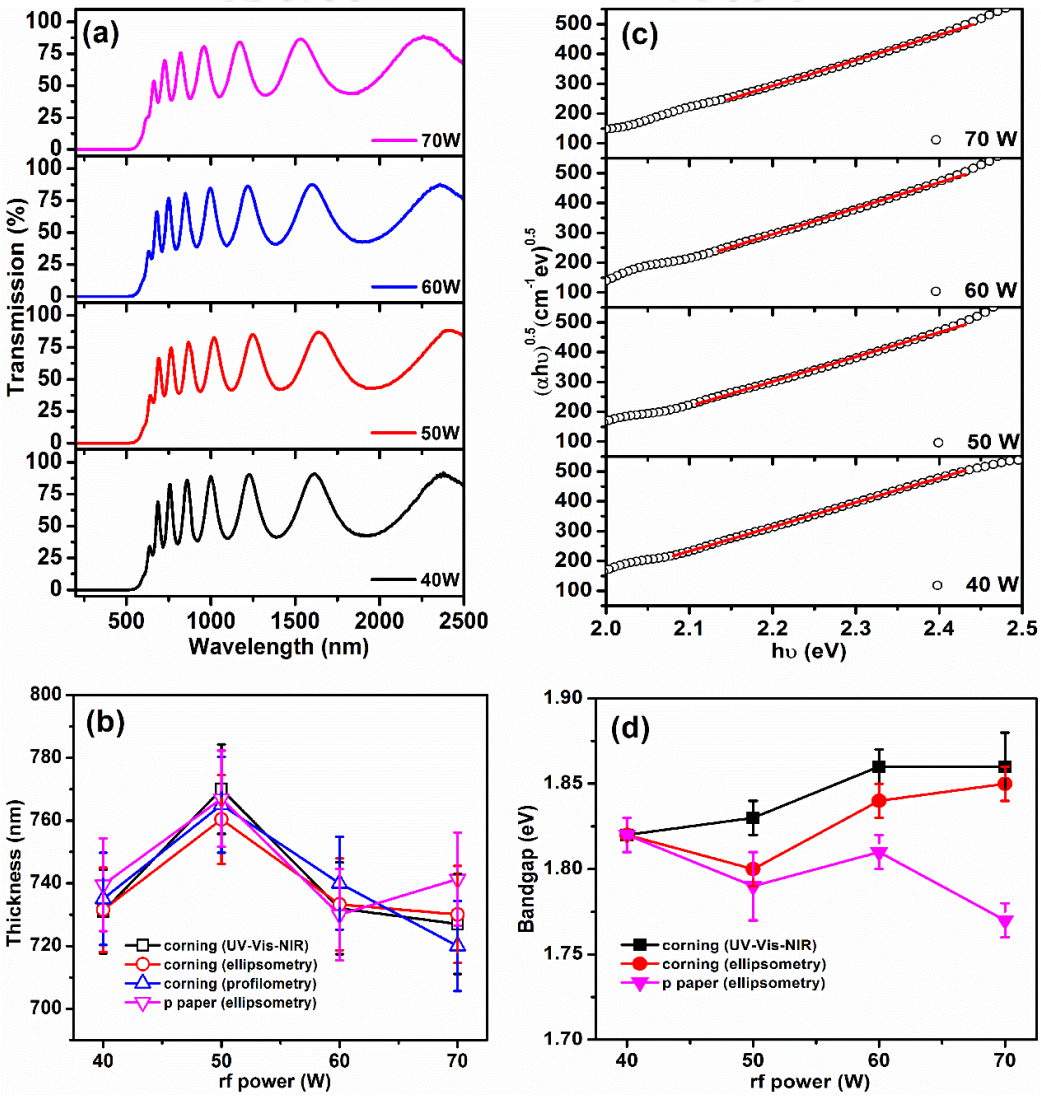

***Figure 3.29**: (a) UV-Vis-NIR transmittance spectra of different rf powers on Corning substrate (b) Estimated thickness from different measurements (c) Plot of $(\alpha h\upsilon)^{0.5}$ versus $h\upsilon$ for films prepared at different rf power (d) Estimated band gap for films at different rf power on Corning and PP substrates.*

The thickness of these films is found to be in the range of 730±10 to 770±15 nm. The film thickness obtained from surface profilometer, UV-Vis-NIR transmission spectra and SE are plotted together as a function of rf power as shown in Figure. 3.29 (b). With the increase in rf power from 40 W to 50 W, thickness of the films increases by about 40 nm. The lower thickness at 40 W rf power is related to the lower density of growth precursors in the deposition chamber due to unsaturated decomposition of SiH_4. Increasing the rf power to 50 W leads to enhancement of dissociation of SiH_4 molecules as well as H_2 molecules, thus resulting in higher density of precursors available for the growth [52]. With further increase in rf power to 60 W and above, high energy ions etch the loosely bonded Si-Si bonds resulting in decrease in thickness. Figure 3.29(c) shows the plot of $(\alpha h\upsilon)^{0.5}$ versus $h\upsilon$ for films prepared at different rf power. The optical band gap (E_g) determined from Tauc's plot [23] and *SE*, as a function of rf power, is shown in Figure 3.29 (d). Band gap of these films is in the range 1.82±0.02 eV on Corning whereas on PP it is in the range of 1.80±0.02eV. The E_g of 70 W film on PP is slightly low (1.76 eV) as compared to other films. At high rf power, high energetic ions break weak Si-Si bonds on the growing surface resulting in more disorder in the film on PP. The E_g may also depend on the nature of substrate as the incoming particle distribution and its diffusion on surface is different for smooth and rough surface [53]. The error bars in Figure 3.29 (b, d) indicate uncertainties in the calculated thickness and E_g.

3.2.3.4 Fourier Transform Infrared Spectroscopy (FTIR)

To estimate total hydrogen content C_H (%) and hydrogen bonding configuration in the film, FTIR spectroscopy was performed. The FTIR transmission spectra of films deposited on c-Si substrate at different rf power (40-70W) are shown in Figure 3.30(a). It can be seen that the spectra have dips at ~640 cm^{-1}, ~880 cm^{-1}, ~1950 cm^{-1}, ~2000 cm^{-1}, and ~2100 cm^{-1} which correspond to Si-H wagging or rocking mode, Si-H_2 bending mode, $(Si\text{-}H_2)_n$ wagging mode, stretching mode of isolated Si-H and Si-H_2 respectively [54]. In order to find the C_H (%), FTIR spectra between 520-760 cm^{-1} were analysed. The hydrogen content in the films is estimated to be about 11±1 at%.

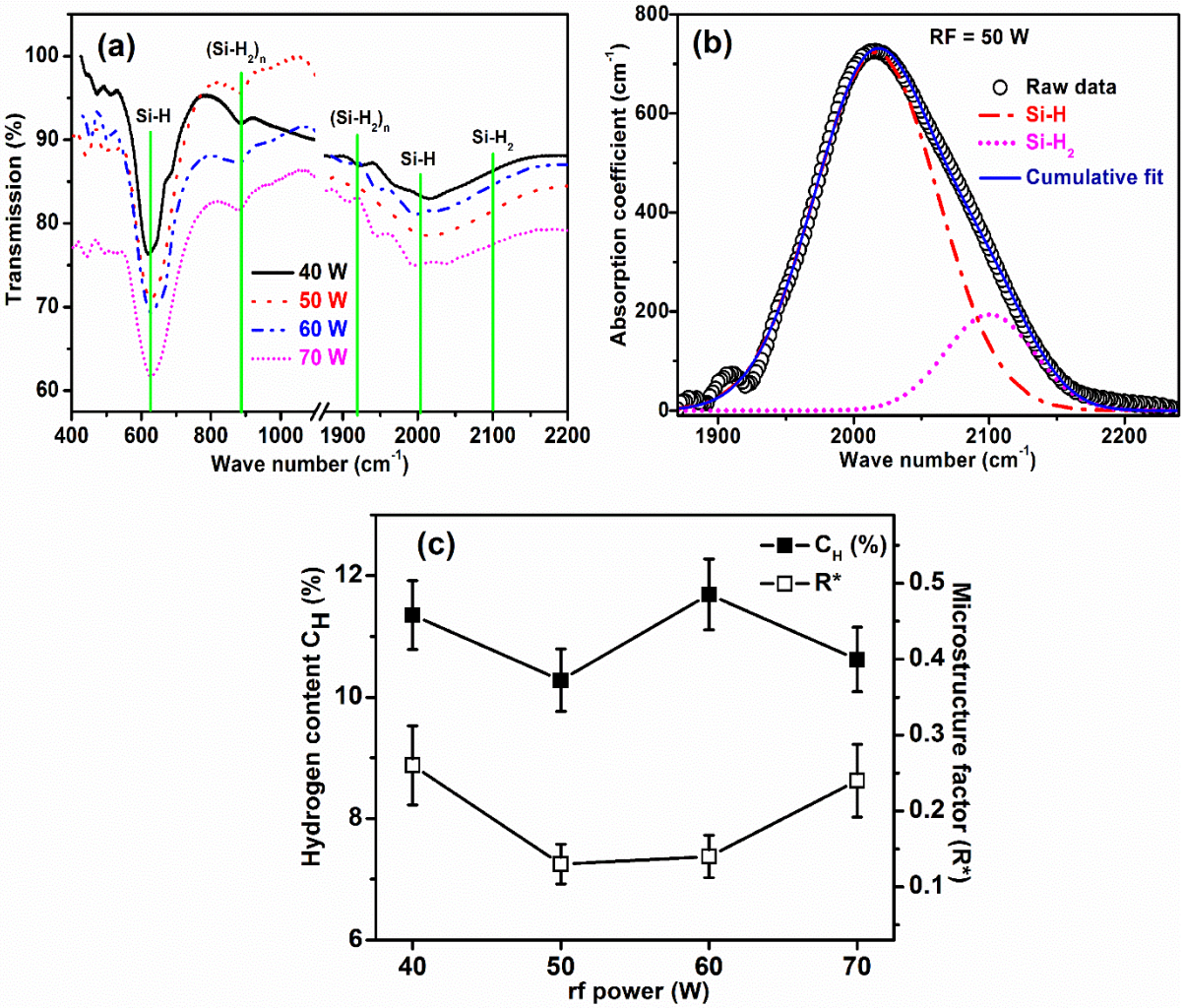

***Figure 3.30**: (a) FTIR transmittance spectra of intrinsic a-Si:H films deposited at different rf power on c-Si (b) Deconvoluted FTIR absorption spectra for 50 W film on c-Si substrate (c) Hydrogen content C_H(%) and microstructure factor (R*) against rf power.*

In order to estimate *R**, absorption coefficient spectra in the range 1870-2240 cm^{-1} was de-convoluted into two peaks centered at ~ 2000 and 2100 cm^{-1} corresponding to Si-H and Si-H_2 stretching modes, respectively. The absorption coefficient spectra of deconvoluted mono-hydride (Si-H) and di-hydride (Si-H_2) components are shown in Figure 3.30(b). The calculated C_H (%) and *R** are plotted against rf power in Figure 3.30 (c). It is observed that C_H (%) in these films is nearly independent of rf power, whereas intensity of mono hydride Si-H vibrational mode at ~2000 cm^{-1} increases with increasing rf power from 40 W to 50 W resulting in a decrease in *R**. However, when rf power is further increased, an increase in intensity of Si-H_2 vibration mode is observed, resulting in an increase in *R**. This trend in *R** with rf power is consistent with the variation in amplitude factor *A* and broadening parameter *C* in *SE* measurements on films on Corning substrates, which also suggest a decrease in

density and increase in void density of the films when rf power is increased beyond 50W. These results can be understood in terms of the gas phase reactions in plasma during the film deposition. At high rf power, the probability of radical-radical reactions and the collision of the radicals with ambient SiH_4 is enhanced due to increase in ion energy. Thus, higher silane radicals are developed through insertion reactions of SiH_2 radicals [55, 56]. When these high silane radicals are incorporated in the film, these create more pores in films which results in increase in *R**. It is believed that films containing high fraction of Si-H_2 and poly hydrides exhibit poor electrical properties as these lead to the formation of micro voids in the films.

3.2.3.5 Atomic force microscopy (AFM)

Surface topography (2D image) of intrinsic *a-Si:H* films were recorded using AFM in tapping mode. Scan size of each film surface was 2 x 2 μm^2. Figure 3.31 (a-d) and Figure 3.32 (a-d) show two dimensional surface topography images of intrinsic *a-Si:H* thin films deposited at different rf power (40-70W) on Corning and PP substrates, respectively.

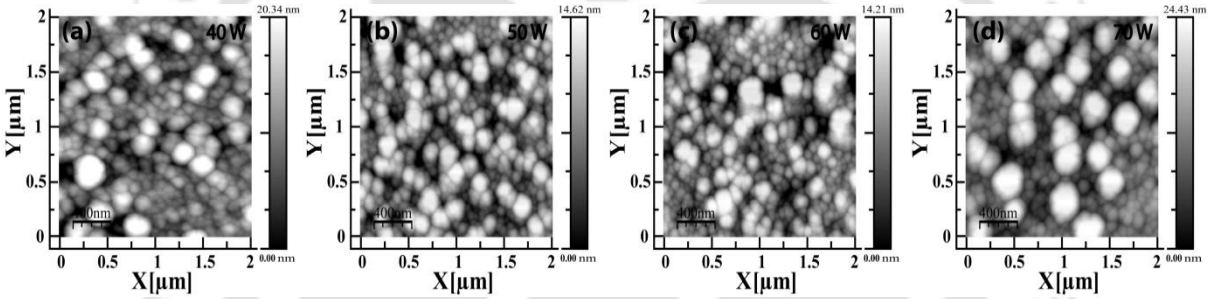

Figure 3.31*: Two dimensional surface morphologies of AFM images of intrinsic a-Si:H films on Corning at rf powers of (a) 40W (b) 50W (c) 60W and (d) 70W respectively.*

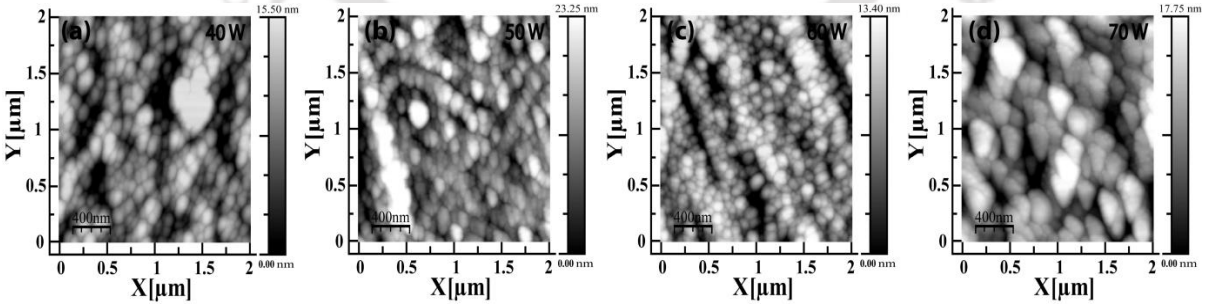

Figure 3.32*: Two dimensional surface morphologies of AFM images of intrinsic a-Si:H films on photo paper at rf powers of (a) 40W (b) 50W (c) 60W and (d) 70W respectively.*

The rms roughness values of intrinsic films deposited at 40, 50, 60 and 70 W on Corning substrates are 4.09±0.11, 3.63±0.16, 3.48±0.15, and 6.09±0.19 nm, respectively whereas for the films deposited on PP substrate, the corresponding values are 3.84±0.16, 5.69±0.20,

3.26±0.11, and 4.77±0.23 nm respectively. The bare substrate RMS roughness of Corning and PP are 0.37 and 6.56 nm respectively. From the surface topography, we can observe that films deposited at low rf power have grains with small sizes whereas at higher rf powers, small grains are aggregated and form large grains. These large grains create voids in the film and deteriorate optoelectronic properties of the films. RMS roughness of the films on Corning and PP is not very different and also not much influenced by rf power. Though, it has been reported that the probability of incoming particle sticking to the substrate surface and particle distribution is different on rough surface and smooth surface [53]. More studies are still underway to understand the underlying mechanism of such dependency of growth morphology and microstructure on different substrates.

3.2.3.6 Field emission scanning electron microscopy (FESEM)

Figure 3.33 (a, b) shows FESEM images of bare Corning and photo paper substrates. Figure 3.33 (c, d) show the images after deposition of the *a-Si:H* thin film (50W) on respective substrates. It can be clearly seen that the unlike the Corning surface, PP surface is not smooth. Further after deposition of the *a-Si:H* films also, a rough microstructure is seen for films on PP, whereas on Corning, the FESEM images seems to be very smooth.

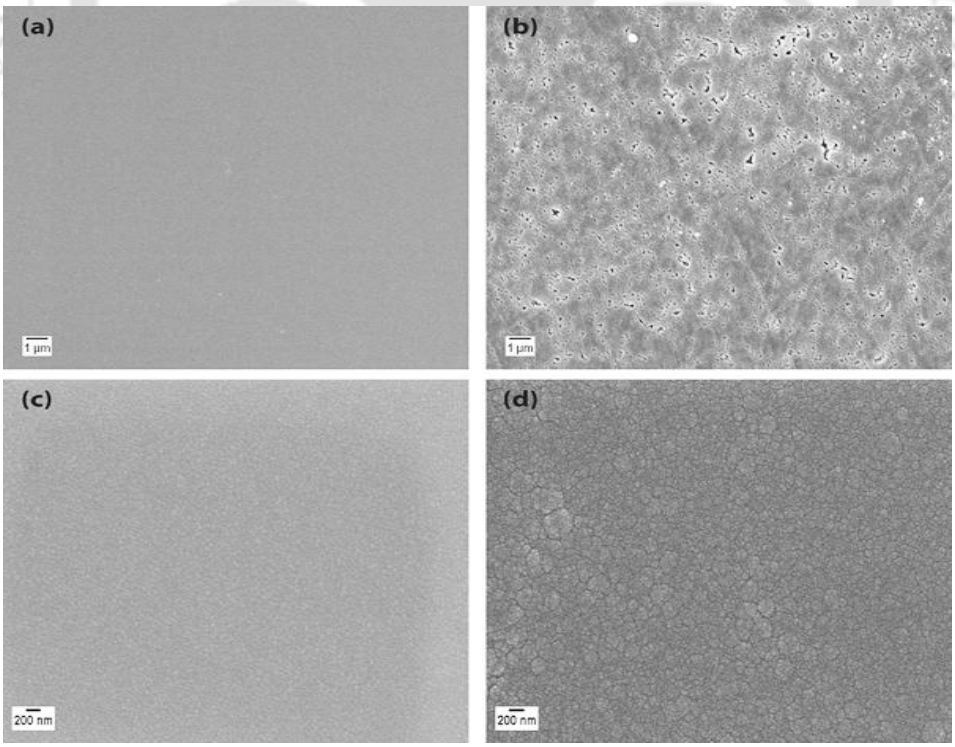

Figure 3.33*: FESEM surface morphologies of (a, b) bare Corning and photo paper substrates (c, d) a-Si:H film (rf power at 50 W) on Corning and photo paper substrates respectively.*

3.2.3.7 Conductivity

To determine the electronic transport properties of *a-Si:H* thin films, dark (σ_d) and photoconductivity (σ_{ph}) measurements were performed at room temperature (*RT*). Figure 3.34 shows the variation of σ_d and σ_{ph} as a function of rf power at *RT* on Corning and PP substrates. For films on Corning, σ_d is ~ 10^{-10} $\Omega^{-1}cm^{-1}$ with small increase with increasing rf power, however, σ_{ph} remains almost constant *at* ~ 10^{-6} $\Omega^{-1}cm^{-1}$. The films on PP show higher σ_d as compared to that for films on Corning due to higher substrate roughness. Higher photosensitivity (σ_{ph}/σ_d) ~ 4 orders of magnitude is observed for films deposited at 50 W on Corning and 40 W on PP, due to improvement in *SRO* and less disorder in these films. These films also show less broadening and higher amplitude in $<\varepsilon_2>$ spectra. The small variation in conductivity is well correlated with Raman and *SE* measurements.

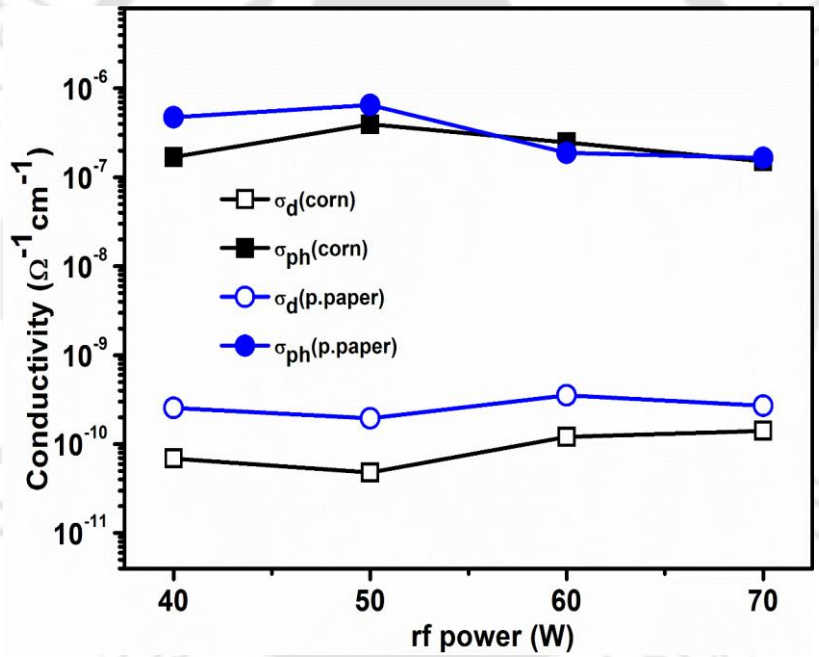

Figure 3.34*: Room temperature dark (σ_d) and photo (σ_{ph}) conductivity of samples prepared at different rf powers on Corning and photo paper substrate.*

3.3 Conclusion: In this chapter, effect of substrate temperature, hydrogen flow rate and rf power on microstructure and opto-electronic properties of intrinsic *a-Si:H* films is reported. The observations for different series are summarized below:

Series (I): Variation of substrate temperature (T_s) in the temperature range 70-200°C: In this series, the effect of T_s on microstructure and optoelectronic properties of the intrinsic *a-Si:H* films deposited on rigid Corning, flexible PI and PP substrates is studied. It was

observed that, nanocrystallites formation started in amorphous matrix at around T_s=130 ^oC and it was further increased with increase in T_s irrespective of the substrate. With increase in T_s, an improvement in the *SRO* and less broadening in $<\varepsilon_2>$ were observed from Raman and ellipsometry measurements. The band gap E_g and hydrogen content for these films are ~1.89 ± 0.01 eV and ~ 9.6±0.48 atomic % respectively. The films deposited at high T_s (≥ 150 ^oC) exhibit a high photosensitivity (~ 6 orders of magnitude) at room temperature. The results indicate that films prepared at T_s of 150 ^oC are nearly defect free and suitable for fabrication of devices on Corning, PI and PP substrate.

Series (II): **Variation of H_2 flow rate (HFR) during SiH_4 plasma at T_s = 150°C:** In this series, influence of variation of H_2 flow rate during SiH_4 plasma on microstructure and optoelectronic properties of the intrinsic *a-Si:H* films, deposited on Corning, and PP substrates at T_s = 150^oC, is studied. It was observed that the formation of nanocrystallites took place in the amorphous film on both the substrates irrespective of HFR. The crystallite size calculated from Raman spectroscopy was found to increase with increase in HFR. *SE* studies showed that, $<\varepsilon_2>_{max}$ shifted towards high energy side with increase in HFR due to presence of nanocrystallites in the film. The thickness of the film has decreased at higher HFR as atomic H lead to excessive etching and breaking of weak Si–Si bonds. FTIR studies showed the hydrogen content is in the range of ~ 8.97±0.44-10.78±0.53 atomic %. These films are found to possess good photo sensitivity (~6 orders of magnitude).

Series (III): **Variation of rf power during silane plasma at T_s = 110°C:** In this series, influence of variation of rf power during silane plasma on microstructure and optoelectronic properties of the intrinsic *a-Si:H* films, deposited on Corning, and PP substrates at T_s = 110 ^oC, are studied. Raman and spectroscopic ellipsometry show that films are purely amorphous irrespective of rf power. In FESEM images, a rough microstructure is seen for films on PP, whereas film on Corning seems to be very smooth. The films deposited at rf power of 50 W on Corning, and 40 W on PP possess device grade quality; improvement in the *SRO*, less broadening in $<\varepsilon_2>$, lesser Si-H_2 fraction and good photosensitivity (σ_{ph}/σ_d) ~ 4 orders of magnitude in these films.

3.4 References

[1] J. Fang, Z. Chen, G. Hou, F. Wang, X. Chen, C. Wei, G. Wang, J. Sun, D. Zhang, Y. Zhao, X. Zhang, High-quality hydrogenated intrinsic amorphous silicon oxide layers treated

by H_2 plasma used as the p/i buffer layers in hydrogenated amorphous silicon solar cells, *Solar Energy Materials and Solar Cells*, **136** (2015) 172-176.

[2] W. Yu, L.H. Meng, J. Yuan, H.J. Lu, S.J. Wu, G.S. Fu, Influence of substrate temperature on growth of a-Si:H films by reactive facing target sputtering deposition, *Sci China Phys Mech*, **53** (2010) 807-811.

[3] W. Chen, R. Cariou, G. Hamon, R. Léal, J.-L. Maurice, P.R.i. Cabarrocas, Influence of deposition rate on the structural properties of plasma-enhanced CVD epitaxial silicon, *Scientific Reports*, **7** (2017) 43968.

[4] G.H. Wang, C.Y. Shi, L. Zhao, H.W. Diao, W.J. Wang, Fabrication of flexible silicon thin film solar modules by substrate transfer technology, *Vacuum*, **102** (2014) 72-74.

[5] N. Liao, W. Li, Y. Kuang, Y. Jiang, S. Li, Z. Wu, K. Qi, Raman and ellipsometric characterization of hydrogenated amorphous silicon thin films, *Sci China Ser E*, **52** (2009) 339-343.

[6] N.M. Liao, W. Li, Y.D. Jiang, Y.J. Kuang, K.C. Qi, Z.M. Wu, S.B. Li, Raman study of a-Si : H films deposited by PECVD at various silane temperatures before glow-discharge, *Appl Phys a-Mater*, **91** (2008) 349-352.

[7] V.A. Volodin, D.I. Koshelev, Quantitative analysis of hydrogen in amorphous silicon using Raman scattering spectroscopy, *Journal of Raman Spectroscopy*, **44** (2013) 1760-1764.

[8] V. Vavrunkova, J. Mullerova, R. Srnanek, P. Sutta, Structural changes studies of a-Si:H films deposited by PECVD under different hydrogen dilutions using various experimental techniques, *Vacuum*, **84** (2009) 123-125.

[9] Gogoi P, Jha H. S, A. P., High band gap nanocrystallite embedded amorphous silicon prepared by hotwire chemical vapour deposition, *Thin Solid Films*, **518** (2010) 6818-6828.

[10] P. Gogoi, P. Agarwal, Structural and optical studies on hot wire chemical vapour deposited hydrogenated silicon films at low substrate temperature, *Solar Energy Materials and Solar Cells*, **93** (2009) 199-205.

[11] P. Alpuim, V. Chu, J.P. Conde, Amorphous and microcrystalline silicon films grown at low temperatures by radio-frequency and hot-wire chemical vapor deposition, *Journal of Applied Physics*, **86** (1999) 3812-3821.

[12] D. Beeman, R. Tsu, M. Thorpe, Structural information from the Raman spectrum of amorphous silicon, *Physical Review B*, **32** (1985) 874-878.

[13] I. Manabu, K. Michio, Systematic Study of Photodegradation of Tailored Nanostructure Si Solar Cells by Controlling Their Medium Range Order, *Japanese Journal of Applied Physics*, **45** (2006) L230.

[14] D. Saha, R.S. Ajimsha, K. Rajiv, C. Mukherjee, M. Gupta, P. Misra, L.M. Kukreja, Spectroscopic ellipsometry characterization of amorphous and crystalline TiO2 thin films grown by atomic layer deposition at different temperatures, *Applied Surface Science*, **315** (2014) 116-123.

[15] S.Y. Lee, J.H. Shim, D.J. You, S.W. Ahn, H.M. Lee, The novel usage of spectroscopic ellipsometry for the development of amorphous Si solar cells, *Solar Energy Materials and Solar Cells*, **95** (2011) 142-145.

[16] A. Fontcuberta i Morral, P. Roca i Cabarrocas, C. Clerc, Structure and hydrogen content of polymorphous silicon thin films studied by spectroscopic ellipsometry and nuclear measurements, *Physical Review B*, **69** (2004).

[17] S. Kageyama, M. Akagawa, H. Fujiwara, Dielectric function ofa-Si:H based on local network structures, *Physical Review B*, **83** (2011).

[18] R.W. Collins, A.S. Ferlauto, G.M. Ferreira, C. Chen, J. Koh, R.J. Koval, Y. Lee, J.M. Pearce, C.R. Wronski, Evolution of microstructure and phase in amorphous, protocrystalline, and microcrystalline silicon studied by real time spectroscopic ellipsometry, *Solar Energy Materials and Solar Cells*, **78** (2003) 143-180.

[19] V. Kanneboina, R. Madaka, P. Agarwal, Spectroscopic ellipsometry studies on microstructure evolution of a-Si:H to nc-Si:H films by H2 plasma exposure, *Materials Today Communications*, **15** (2018) 18-29.

[20] Y. Bouizem, C. Abbes, J.D. Sib, D. Benlakehal, R. Baghdad, L. Chahed, K. Zellama, S. Charvet, Ellipsometric and Raman spectroscopic study of nanocrystalline silicon thin films prepared by a rf magnetron sputtering technique, *Journal of Physics: Condensed Matter*, **20** (2008) 445221.

[21] M. Losurdo, M.M. Giangregorio, P. Capezzuto, G. Bruno, M.F. Cerqueira, E. Alves, M. Stepikhova, Dielectric function of nanocrystalline silicon with few nanometers (<3 nm) grain size, *Applied Physics Letters*, **82** (2003) 2993-2995.

[22] R. Swanepoel, Determination of the thickness and optical constants of amorphous silicon, *J. Phys. E: Sci. Instrum.*, **16** (1983) 1214.

[23] G.R. Tauc J, Vancu A, Optical properties and electronic structure of amorphous germanium, *Phys Status Solidi*, **15** (1966) 627.

[24] A. Matsuda, Microcrystalline silicon. Growth and device application, *Journal of Non-Crystalline Solids*, **338-340** (2004) 1-12.

[25] A. Matsuda, Thin-film silicon - Growth process and solar cell application, *Jpn J Appl Phys* **43** (2004) 7909-7920.

[26] S.R. Jadkar, J.V. Sali, S.T. Kshrisagar, M.G. Takwale, Deposition of hydrogenated amorphous silicon (a-Si : H) films by hot wire chemical vapor deposition: role of filament temperature, *Thin Solid Films*, **437** (2003) 18-24.

[27] S.T. Hwang, D.J. You, S.H. Kim, S. Lee, H.M. Lee, Large area Si thin film solar module applying n-mu c-SiOx:H intermediate layer with low refractive index, *Solar Energy Materials and Solar Cells*, **113** (2013) 79-84.

[28] G. Ambrosone, U. Coscia, R. Murri, N. Pinto, M. Ficcadenti, L. Morresi, Structural, optical and electrical characterizations of μc-Si:H films deposited by PECVD, *Solar Energy Materials and Solar Cells*, **87** (2005) 375-386.

[29] C. Shin, J. Park, J. Jung, S. Bong, S. Kim, Y.-J. Lee, J. Yi, Control of micro void fraction and optical band gap in intrinsic amorphous silicon thin films (VHF-PECVD) for thin film solar cell application, *Materials Research Bulletin*, **60** (2014) 895-899.

[30] F. Wang, X. Zhang, L. Wang, Y. Jiang, C. Wei, S. Xu, Y. Zhao, Improved amorphous/crystalline silicon interface passivation for heterojunction solar cells by low-temperature chemical vapor deposition and post-annealing treatment, *Physical chemistry chemical physics : PCCP*, **16** (2014) 20202-20208.

[31] P.R. Cabarrocas, Y. Bouizem, M.L. Theye, Defect density and hydrogen bonding in hydrogenated amorphous silicon as functions of substrate temperature and deposition rate, *Philosophical Magazine B*, **65** (2006) 1025-1040.

[32] J. Mouro, A. Gualdino, V. Chu, J.P. Conde, Microstructure factor and mechanical and electronic properties of hydrogenated amorphous and nanocrystalline silicon thin-films for microelectromechanical systems applications, *Journal of Applied Physics*, **114** (2013) 184905.

[33] A. H. Mahan, J. Yang, S. Guha, D.L. Williamson, Structural changes in a-Si:H film crystallinity with high H dilution, *Physical Review B*, **60** (2004) 1677-1679.

[34] A. Fontcuberta i Morral, H. Hofmeister, P.R.I. Cabarrocas, Structure of plasma-deposited polymorphous silicon, *Journal of Non-Crystalline Solids*, **299-302** (2002) 284-289.

[35] P.R.I. Cabarrocas, S. Hamma, S.N. Sharma, G. Viera, E. Bertran, J. Costa, Nanoparticle formation in low-pressure silane plasmas: bridging the gap between a-Si:H and μc-Si films, *Journal of Non-Crystalline Solids*, **227** (1998) 871-875.

[36] P. Gogoi, P.N. Dixit, P. Agarwal, Amorphous silicon films with high deposition rate prepared using argon and hydrogen diluted silane for stable solar cells, *Solar Energy Materials and Solar Cells*, **91** (2007) 1253-1257.

[37] A. Fontcuberta i Morral, P. Roca i Cabarrocas, Role of hydrogen diffusion on the growth of polymorphous and microcrystalline silicon thin films, *The European Physical Journal Applied Physics*, **35** (2006) 165-172.

[38] P.R.i. Cabarrocas, N. Chaâbane, A.V. Kharchenko, S. Tchakarov, Polymorphous silicon thin films produced in dusty plasmas: application to solar cells, *Plasma Physics and Controlled Fusion*, **46** (2004) 235-243.

[39] M. Akihisa, Thin-Film Silicon –Growth Process and Solar Cell Application–, Japanese *Journal of Applied Physics*, **43** (2004) 7909.

[40] R. Rao, F. Kail, P. Roca i Cabarrocas, Effect of substrate on hydrogen in and out diffusion from a-Si:H thin films, *Journal of Materials Science: Materials in Electronics*, **18** (2007) 1051-1056.

[41] S.-B. Li, Z.-M. Wu, Y.-D. Jiang, J.-S. Yu, W. Li, N.-M. Liao, Growth mechanism of microcrystalline and polymorphous silicon film with pure silane source gas, *Journal of Physics D: Applied Physics*, **41** (2008) 105207.

[42] A. Matsuda, Thin-Film Silicon –Growth Process and Solar Cell Application–, Japanese *Journal of Applied Physics*, **43** (2004) 7909-7920.

[43] S. Sriraman, E.S. Aydil, D. Maroudas, Atomic-scale analysis of deposition and characterization of a-Si:H thin films grown from SiH radical precursor, *Journal of Applied Physics*, **92** (2002) 842-852.

[44] W.M.M. Kessels, J.P.M. Hoefnagels, P.J. van den Oever, Y. Barrell, M.C.M. van de Sanden, Temperature dependence of the surface reactivity of SiH3 radicals and the surface silicon hydride composition during amorphous silicon growth, *Surface Science*, **547** (2003) 865-870.

[45] S. Zhang, X. Liao, L. Raniero, E. Fortunato, Y. Xu, G. Kong, H. Águas, I. Ferreira, R. Martins, Silicon thin films prepared in the transition region and their use in solar cells, *Solar Energy Materials and Solar Cells*, **90** (2006) 3001-3008.

[46] S. Halindintwali, D. Knoesen, R. Swanepoel, B.A. Julies, C. Arendse, T. Muller, C.C. Theron, A. Gordijn, P.C.P. Bronsveld, J.K. Rath, R.E.I. Schropp, Improved stability of intrinsic nanocrystalline Si thin films deposited by hot-wire chemical vapour deposition technique, *Thin Solid Films*, **515** (2007) 8040-8044.

[47] A.H. Mahan, W. Beyer, D.L. Williamson, J. Yang, S. Guha, An explanation for the low-temperature H evolution peak in hydrogenated amorphous silicon films deposited 'on the edge of crystallinity, *Philosophical Magazine Letters*, **80** (2000) 647-652.

[48] J.Y. Ahn, K.H. Jun, K.S. Lim, M. Konagai, Stable protocrystalline silicon and unstable microcrystalline silicon at the onset of a microcrystalline regime, *Applied Physics Letters*, **82** (2003) 1718-1720.

[49] M. Zeman, G. van Elzakker, F.D. Tichelaar, P. Sutta, Structural properties of amorphous silicon prepared from hydrogen-diluted silane, *Philosophical Magazine*, **89** (2009) 2435-2448.

[50] S.A. Filonovich, P. Alpuim, L. Rebouta, J.E. Bourée, Y.M. Soro, Hydrogenated amorphous and nanocrystalline silicon solar cells deposited by HWCVD and RF-PECVD on plastic substrates at 150°C, *Journal of Non-Crystalline Solids*, **354** (2008) 2376-2380.

[51] S. Kageyama, M. Akagawa, H. Fujiwara, Dielectric function of a-Si:H based on local network structures, *Physical Review B*, **83** (2011) 195205.

[52] J. L. Andujar, J. Kasaneva, J Serra, A. Canlllas, C. Roth, J. L. Morenza, E. Bertran, Effects of r.f. power on optical and electrical properties of plasma-deposited hydrogenated amorphous silicon thin films, *Sensors and Actuators A*, **37-38** (1993) 733-736.

[53] H.J. Qi, J.D. Shao, D.P. Zhang, K. Yi, Z.X. Fan, Simulation of growth process of thin film on non-planar substrate, *Applied Surface Science*, **249** (2005) 85-90.

[54] T. Anutgan, S. Uysal, Low temperature plasma production of hydrogenated nanocrystalline silicon thin films, *Current Applied Physics*, **13** (2013) 181-188.

[55] B. Kalache, A.I. Kosarev, R. Vanderhaghen, P.R.I. Cabarrocas, Ion bombardment effects on microcrystalline silicon growth mechanisms and on the film properties, *Journal of Applied Physics*, **93** (2003) 1262-1273.

[55] E. Bertran, J. Costa, G. Sardin, J. Campmany, J.L. Andujar, A. Canillas, Effects of plasma processing on the microstructural properties of silicon powders, *Plasma Sources Science and Technology*, **3** (1994) 348.

Chapter 4

Optimization of Doped *a-Si:H* Thin Films

This chapter describes the details of preparation and characterization of boron and phosphorus doped hydrogenated amorphous silicon thin films prepared by radio frequency plasma enhanced chemical vapour deposition (RF-PECVD) technique. In the *n-i-p* or *p-i-n* solar cell, an electric field is developed between the *p*- and *n*- layers that stretches across the middle intrinsic resistive region. Light reaches the intrinsic layer generating free electrons and holes, which are then separated by the electric field. The main objective of doping *a-Si:H* is to modify its electrical conductivity in order to establish an electrical field necessary to extract the electrons and holes that are generated in the intrinsic layer of solar cell. Concerning the *p*- layer, the optimum conductivity is generally achieved by mixing the silicon source gas silane (SiH_4) with diborane (B_2H_6) [1]. However, boron tends to alloy with *a-Si:H* leading to a strong reduction in the band gap and this drawback can be resolved by adding carbon (as CH_4) to the lattice [2]. The determination of the opto-electronic properties and the band gap energy (E_g) of doped layers, is crucial to estimate the behaviour and final efficiency of the *a-Si:H* based solar cells [3]. The microstructure and optoelectronic properties of doped film can be changed by changing the deposition parameters like rf power, process pressure, etc., using RF-PECVD technique. With this motivation we have prepared two series of boron doped films and one series of phosphine doped films. The deposited parameters for each series are listed in Table 4.1. The deposited films were characterized by various characterization tools. These studies have been presented in this chapter.

4.1 Experimental details

The doped *a-Si:H* thin films were prepared on Corning 1737 glass (Corning) and c-Si substrates (Each substrate size is 4 cm^2 and discharge electrode size is 21.2 cm^2) using RF-PECVD (13.56 MHz) multi-chamber system. Two different series of boron doped (*a-Si:H*(*p*)) and one series of phosphorus doped (*a-Si:H*(*n*)) films were prepared: **Series (I)**, rf power variation of *a-Si:H*(*p*) thin films at low substrate temperature T_s (=110°C); **Series (II)**, Methane CH_4 flow rate (MFR) variation of *a-Si:H*(*p*) thin films at low T_s (T_s=110°C); **Series**

(III), Substrate temperature (T_s=90-150°C) variation of *a-Si:H*(*n*) thin films. The deposition parameters for each series of films are listed in Table 4.1

Table 4.1: *Deposition parameters for doped a-Si:H thin films by rf-PECVD technique*

Deposition parameters	**rf power series**	***MFR* series**	**T_s series**
rf power (Watt)	**40-70***	60	20
H_2 (sccm)	100	100	50
SiH_4 (sccm)	5	5	5
B_2H_6 (sccm)	5	5	-
PH_3 (sccm)	-	-	5
CH_4 (sccm)	-	**1-4***	-
Process pressure (mbar)	0.61	0.61	0.82
Substrate temperature (^oC)	110	110	**90-150***
Deposition time (minute)	10	10	10

*variable parameters

4.2 Results and Discussion:

4.2.1 Series (I): rf power variation of *a-Si:H*(*p*) thin films at low substrate temperature T_s (=110°C)

In this series, boron doped *a-Si:H* films were deposited at 110°C substrate temperature by varying rf power (40-70W) on Corning and c-Si substrates. The detailed deposition parameters are listed in Table 4.1

4.2.1.1 Raman scattering

The Raman spectra of *a-Si:H*(*p*) thin films deposited at different rf-power on Corning are shown in Figure 4.1(a). The spectra were identified having TA, LA, LO and TO phonon vibrational modes of Si-Si bonds in amorphous structure [4] as discussed in Chapter 2. A broad TO mode peak around 480 cm^{-1} is observed for all films, while there was no signature of a peak near ~ 510 cm^{-1}(peak position for *nc-Si*) [4]. This indicates that all deposited films have pure amorphous structure irrespective of rf power.

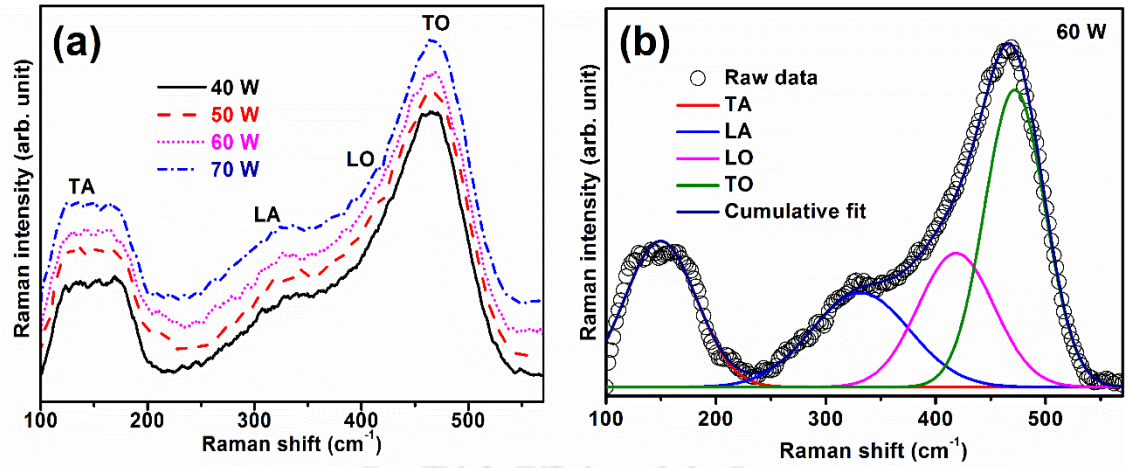

***Figure 4.1**: (a) Raman spectra of a-Si:H(p) films at different rf powers (b) Deconvoluted Raman spectra of a-Si:H(p) film at rf power 60W.*

In order to find the TO mode peak position, rms tetrahedral bond angle deviation ($\Delta\theta_B$) and I_{TA}/I_{TO} [4, 5], each Raman spectra was deconvoluted into peaks corresponding to different vibrational modes of Si-Si bonds. One of the deconvoluted Raman spectra for film deposited at 60W rf power is shown in Figure 4.1 (b). From Table 4.2, one can see that, the TO mode position is not much influenced by the variation in rf power. The calculated full width at half maxima (*FWHM*) of TO mode, $\Delta\theta_B$ and I_{TA}/I_{TO} values of *a-Si:H(p)* films at different rf power are also listed in Table 4.2.

***Table 4.2**: TO mode peak position, FWHM of TO mode, rms deviation in the tetrahedral bond angle ($\Delta\theta_B$) and I_{TA}/I_{TO} values of a-Si:H(p) thin films deposited at different rf powers on Corning 1737 glass substrate.*

rf power (W)	TO mode peak position(cm^{-1})	TO mode *FWHM* (cm^{-1})	$\Delta\theta_B$ (°)	I_{TA}/I_{TO}
40	475	63.11	8.02	0.53
50	474	63.06	8.01	0.68
60	476	61.34	7.72	0.50
70	474	64.48	8.25	0.53

The $\Delta\theta_B$ values are found to be in the range of 7.22 ° to 8.25° at different rf power. The $\Delta\theta_B$ and I_{TA}/I_{TO} values are also not much affected by rf power. Lowest value of $\Delta\theta_B$= 7.72 ° and I_{TA}/I_{TO} = 0.50 indicate better *SRO* and *MRO* for 60 W film.

4.2.1.2 Spectroscopic ellipsometry (SE)

Figure 4.2 (a & b) show the experimental (open) and fitted (solid line) data of real $<\varepsilon_1>$ and imaginary $<\varepsilon_2>$ dielectric function of *a-Si:H(p)* thin films at different rf power. The

experimental data was fitted with *T-L* model by constructing two layer model [6]. The details of *T-L* model and two layer model are discussed in Chapter 2.

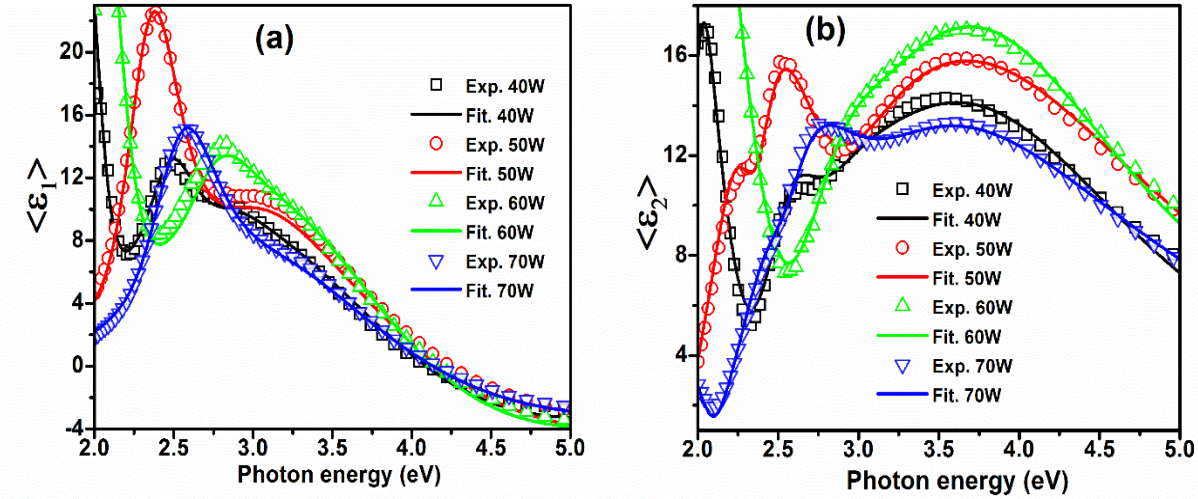

***Figure 4.2**: Plot of experimental and fitted (solid line) data of (a) real dielectric function $<\varepsilon_1>$ and (b) imaginary dielectric function $<\varepsilon_2>$ against photon energy for boron doped amorphous silicon films prepared at different rf powers on Corning and substrates.*

The fitting parameters of *T-L* model for *a-Si:H*(*p*) films are listed in table 4.3. It was observed that the thickness of rough surface layer had increased with increase in rf power. The amplitude factor (*A*) of $<\varepsilon_2>$ peak was also increased with increase in rf power from 40W to 60W. These observations indicate the films are getting denser with increase in rf power up to 60W. However, in case of film at 70W, *A* was found to be smaller compared to other films suggesting a lower density of this film. In *SE* spectra of *a-Si:H* films, the position of maximum $<\varepsilon_2>$ ($<\varepsilon_2>_{max}$) at around 3.5 eV and 4.2 eV are often attributed to amorphous and nanocrystalline phases of Si respectively [7]. The rf power did not affect the $<\varepsilon_2>_{max}$; $<\varepsilon_2>_{max}$ was observed at ~ 3.62 eV for all films. No shoulder peak around 4.2 eV, a characteristic feature of *nc-Si* phase, was observed with variation in rf power confirming that these films are purely amorphous. Basa *et al*. [8] also observed the similar behaviour with $<\varepsilon_2>_{max}$ at ~3.7 eV for amorphous *a-Si:H*(*p*) films. The SE results are well consistent with the results obtained from Raman measurements. Another fitting parameter, broadening parameter (*C*) of $<\varepsilon_2>$ peak was found to be in the range of 2.62±0.01–2.73 ±0.01eV for different rf power and was hardly affected by rf power variation. The lowest broadening of 2.62±0.01 eV was observed for film deposited at 60 W.

***Table 4.3**: The T-L model fitted parameters: rough surface layer thickness (nm), thickness of bulk layer (nm), amplitude factor A (eV), resonance energy E_0 (eV), broadening parameter C (eV), optical band gap E_g (eV) and constant $\varepsilon_1(\infty)$ from ellipsometry for different rf power.*

MFR (sccm)	Thickness of rough surface layer (nm)	bulk layer thickness (nm)	*A* (eV)	E_0 (eV)	*C* (eV)	E_g (eV)	$\varepsilon_1(\infty)$
40	1.23±0.04	103±2.32	139.88±5.33	3.72±0.01	2.65±0.01	1.75±0.01	1.88
50	1.56±0.06	87±4.98	154.51±4.12	3.68±0.01	2.64±0.01	1.78±0.01	0.49
60	2.34±0.09	72±3.36	173.21±4.35	3.65±0.01	2.62±0.01	1.82±0.01	0.63
70	4.93±0.27	70±6.32	129.63±4.48	3.70±0.01	2.73±0.01	1.80±0.01	1.58

4.2.1.3 UV-Vis-NIR

Figure 4.3(a) show the UV-Vis-NIR transmission spectra of *a-Si:H(p)* films at different rf power on Corning substrate. In the transmission spectra, there were not sufficient interference fringes to apply Swanepoel's [9] method for the determination of film thickness. Hence, the thicknesses of these films were estimated using surface profilometer. Band gap (E_g) was calculated from UV-Vis-NIR spectra using Tauc's plot [10]. Figure 4.3(b) show the $(\alpha h\upsilon)^{0.5}$ versus $h\upsilon$ of these films at different rf power. The thickness and E_g of the films were also estimated from spectroscopic ellipsometry measurement. The values of thickness and E_g obtained from different measurements are shown in Figure 4.4.

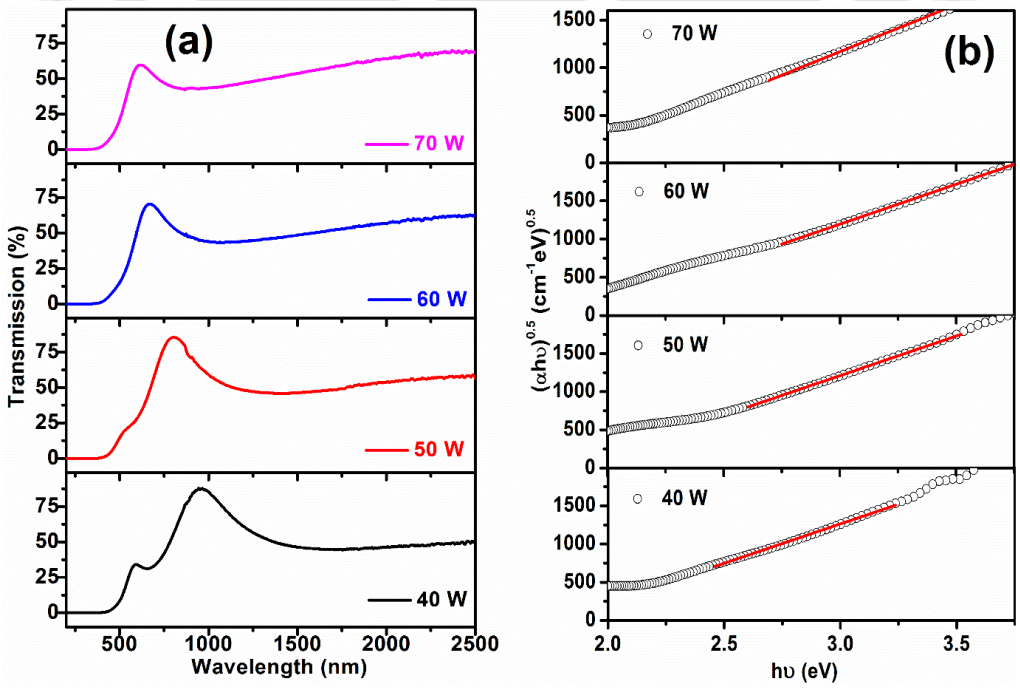

***Figure 4.3**: (a) UV-Vis-NIR transmission spectra of a-SiH(p) films at different rf power. (b) Plot of $(\alpha h\upsilon)^{0.5}$ versus $h\upsilon$ for a-Si:H(p) films at different rf powers.*

The thickness of *a-Si:H*(*p*) film is in the range of 110±5 to 75±4 nm at different rf power as shown in Figure 4.4. The thickness of the film is found to be gradually decreasing from ~ 110±4nm to 75±5nm with increasing rf power from 40 W to 70W. The decrease in thickness at higher rf power is due to the enhancement of dissociation of SiH_4 molecules as well as H_2 molecules as rf power is increased. This results in an increase in density of precursors with higher average energy available for the growth. These high-energy ions then etch the loosely bonded Si-Si bonds resulting in decrease in film thickness [11]. The band gap is in the range of 1.78±0.01-1.86±0.01 eV at different rf power. The band gap of the films slightly changes by ~ ±0.1 eV with rf power.

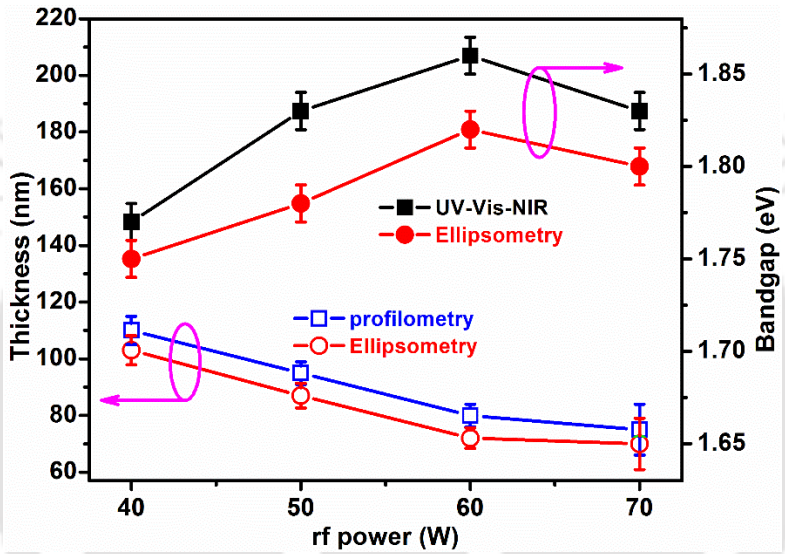

***Figure 4.4**: Estimated thickness (from ellipsometry and profilometer) and bandgap (from UV-Vis-NIR and ellipsometry) of boron doped films prepared at different rf powers on Corning substrates.*

4.2.1.4 Fourier Transform Infrared Spectroscopy (FTIR)

Figure 4.5(a) show the FTIR transmission spectra of *a-Si:H*(*p*) films deposited on c-Si substrate at different rf power. The spectra show the wagging and stretching vibrational modes of silicon hydrogen bonds near 630 and 2000-2100 cm^{-1} respectively [12, 13]. The hydrogen content, (C_H (%)) [14] and microstructure factor *R** [15] were calculated from absorption coefficient spectra as discussed in the Chapter 2. Figure 4.5(b) show C_H (%) and *R** at different rf power. The *R** value is found to be not affected by variation in rf power, however the total C_H (%) in the film is found to decrease with increase in rf power due to etching of the loosely bonded Si-Si bonds by high energy ions. The hydrogen content in these *a-Si:H* (*p*) films, deposited at low temperature, is comparable with that reported in literature [15-17].

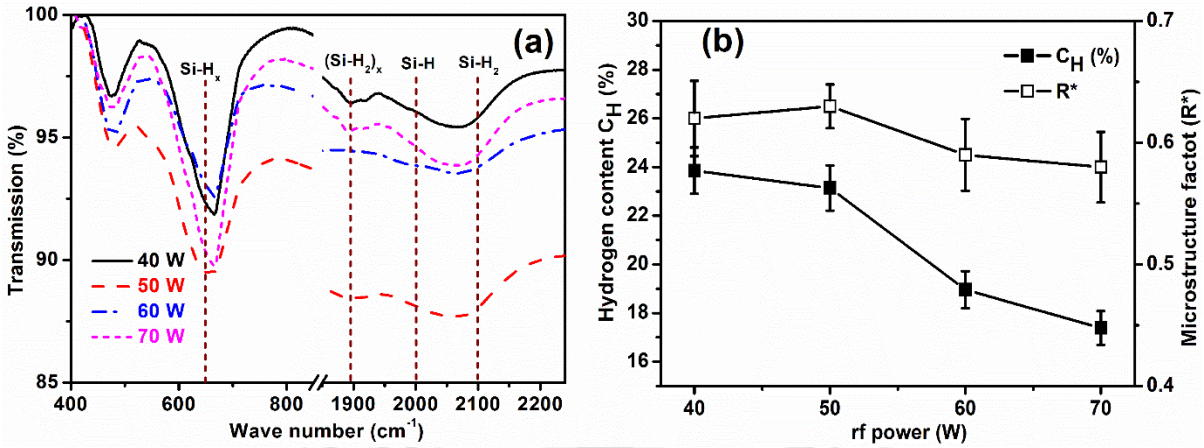

***Figure 4.5**: (a) FTIR transmission spectra of a-Si:H(p) thin films on c-Si at different rf power (b) Hydrogen content C_H(%) and microstructure factor (R*) against different rf power.*

4.2.1.5 Conductivity

In order to study electronic transport properties of the films, dark (σ_d) and photo (σ_{ph}) conductivity measurements in coplanar geometry were performed at room temperature.

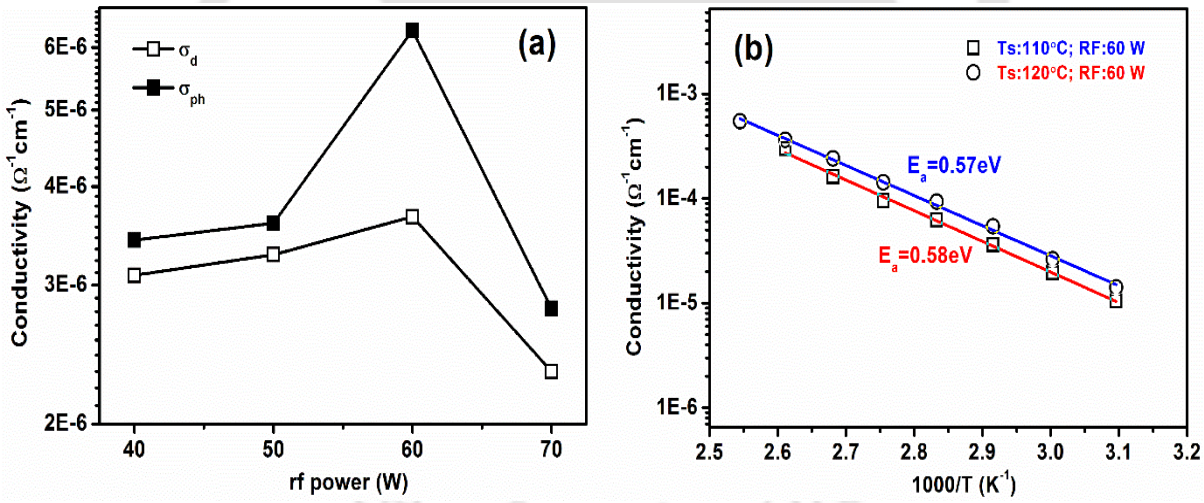

***Figure 4.6**: (a) Room temperature dark (σ_d) and photo (σ_{ph}) conductivity of a-Si:H(p) films prepared at different rf power (b) Temperature dependent conductivity of a-Si:H(p) films (T_s=110 and 120°C) at rf power 60 W.*

Figure 4.6(a) show the variation of σ_d and σ_{ph} for films deposited at different rf powers. The σ_d of *a-Si:H*(*p*) films is found to be more than 4 orders of magnitude higher than intrinsic *a-Si:H* films (chapter 3, section 3.2.3.7). These results suggest that films are doped efficiently by adding diborane during deposition. In addition to this series, one more film was prepared at slightly higher T_s=120°C with rf power 60 W. The room temperature σ_d and σ_{ph} of film

deposited at T_s=120°C are found to be 4.45×10-6 $\Omega^{-1}cm^{-1}$ and 5.73×10-6 $\Omega^{-1}cm^{-1}$ respectively. Figure 4.6 (b) show the temperature dependent conductivity of *a-Si:H*(*p*) film at 60 W. The activation energy is found to be 0.57 eV and 0.58 eV for films deposited at 110°C and 120°C respectively, indicating that Fermi level is closer to valance band. The dark conductivity and activation energy values are comparable with other reports [18-20].

4.2.2 Series (II): Methane (*CH_4*) flow rate (*MFR*) variation of *a-Si:H*(*p*) thin films at low T_s (T_s=110°C)

In case of *a-Si:H* based solar cells, the light enters through the *p*- layer. The efficiency of the solar cells depends upon the absorption of photons in this layer and hence the band gap. Adding Methane during Silane plasma can increase the bandgap of *a-Si:H*(*p*) films by adding carbon atoms to silicon network [2, 21]. In order to study the influence of methane (*CH_4*) dilution during plasma on microstructural and optoelectronic properties of these films, a series of films were deposited by varying *CH_4* flow rate (*MFR*) from 1-4 sccm. In earlier series, it was observed that *a-Si:H*(*p*) films deposited at 60 W exhibited better structural and optoelectronic properties. Hence for this series of films, the rf power was fixed at 60W and other deposition parameters were kept same as in Series I. The deposition parameters for this series are listed in Table 4.1.

4.2.2.1 Raman scattering

In order to find the microstructural properties of *a-SiC:H*(*p*) films, Raman measurements have been carried out in the range of 100-2000 cm^{-1}. Figure 4.7 (a) shows the Raman spectra of different MFR films. Raman spectra consist of LA, TA, LO and TO of phonon vibrational modes of Si-Si bonds [4] as discussed in Chapter 2. In addition to these Si-Si modes, extra phonon modes are observed at ~890 cm^{-1} and ~1300-1500 cm^{-1} corresponding to LO and overlapping of acoustic (TA+LA) phonon modes of Si-C and C-C respectively in 3C-SiC [22-24]. These extra modes in the Raman spectra indicate presence of carbon atoms in the films. All films show broad TO mode peak at ~480 cm^{-1}, which indicate that these films are pure amorphous irrespective of variation in *MFR* [25]. From Figure 4.7(a) one can see that, as the CH_4 concentration increases, the intensity of the peak at ~1300-1500 cm^{-1} increases, indicating that, the phonon modes of *C-C* increase at higher *MFR*.

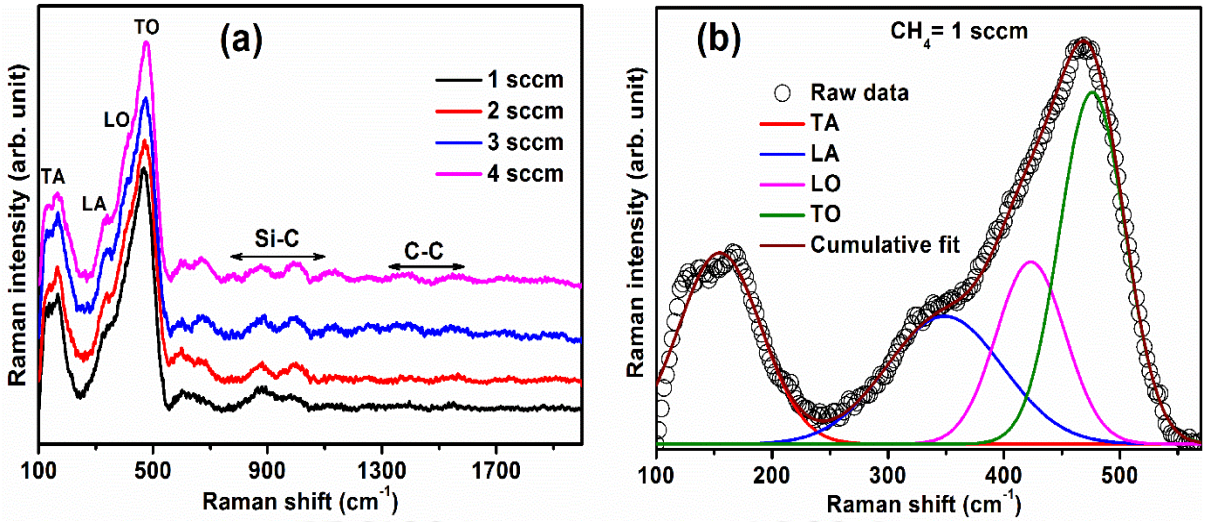

***Figure 4.7**: (a) Raman spectra of different CH_4 flow rate of a-SiC:H(p) films (b) Deconvoluted Raman spectrum of CH_4 flow rate at 1sccm.*

In order to find the amorphous silicon TO mode peak position, $\Delta\theta_B$ [5] and I_{TA}/I_{TO} [4] each Raman spectra was deconvoluted into four Gaussian peaks in the range of 100-570 cm^{-1}. One of the deconvoluted Raman spectrum corresponding to the film deposited at *MFR* = 1 sccm is shown in Figure 4.7(b). The TO mode peak position of Si, *FWHM* of TO mode, $\Delta\theta_B$ and I_{TA}/I_{TO} values of *a-SiC:H*(*p*) films at different *MFR* are listed in Table 4.4.

***Table 4.4**: FWHM and SRO values of a-SiC:H(p) thin films on Corning 1737 glass for different CH_4 flow rate.*

MFR (sccm)	TO mode peak position of Si (cm^{-1})	*FWHM* (cm^{-1})	$\Delta\theta_B$ (^{o})	I_{TA}/I_{TO}
1	478	66.10±1.26	8.52 ± 0.73	0.66
2	478	68.47±1.25	8.91 ± 0.74	0.65
3	474	72.87±1.09	9.65 ± 0.89	0.70
4	475	73.77±1.24	9.80 ± 0.75	0.72

From table 4.4, it is worth noting that the *MFR* does not have much influence on the TO mode peak position of a-Si. However, the *FWHM* of this TO mode, $\Delta\theta_B$ and I_{TA}/I_{TO} slightly increase with increase in *MFR* due to incorporation of additional carbon atoms bonded with Si, which increases the bond angle deviation. These *FWHM* and $\Delta\theta_B$ values are comparable with other reported works in literature [4].

4.2.2.2 Spectroscopic ellipsometry (SE)

In order to deduce optical parameters of *a-SiC:H*(*p*) films, experiential data is fitted with Tauc-Lorentz (*T-L*) model by constructing a two-layer model [6, 26]. The *T-L* model is discussed in Chapter 2.

Figure 4.8 (a and b) show experimental (open) and fitted (solid line) data of real $<\varepsilon_1>$ and imaginary $<\varepsilon_2>$ dielectric function versus photon energy (*E*) for *a-SiC:H*(*p*) thin films at different *MFR*. In $<\varepsilon_2>$ spectra, position of maxima ($<\varepsilon_2>_{max}$) at around 3.5 eV and 4.2 eV are often attributed to amorphous and nanocrystalline silicon structures respectively [7, 27]. In Figure 4.8(b), no shoulder peak around 4.2 eV is observed even with variation in *MFR* confirming that these films are pure amorphous, which is well consistent with the results obtained in Raman measurements. The fitting parameters of *T-L* model are listed in Table 4.5. From the Table 4.5, one can clearly notice that amplitude factor (*A*) of $<\varepsilon_2>$ decreases with increase in *MFR*. This suggests that the mass density of film decreases with increase in the carbon content which can be attributed to increase in void density at higher *MFR*. The decrease in height of $<\varepsilon_2>$ peak is in agreement with the experimental results of others [8, 28, 29].

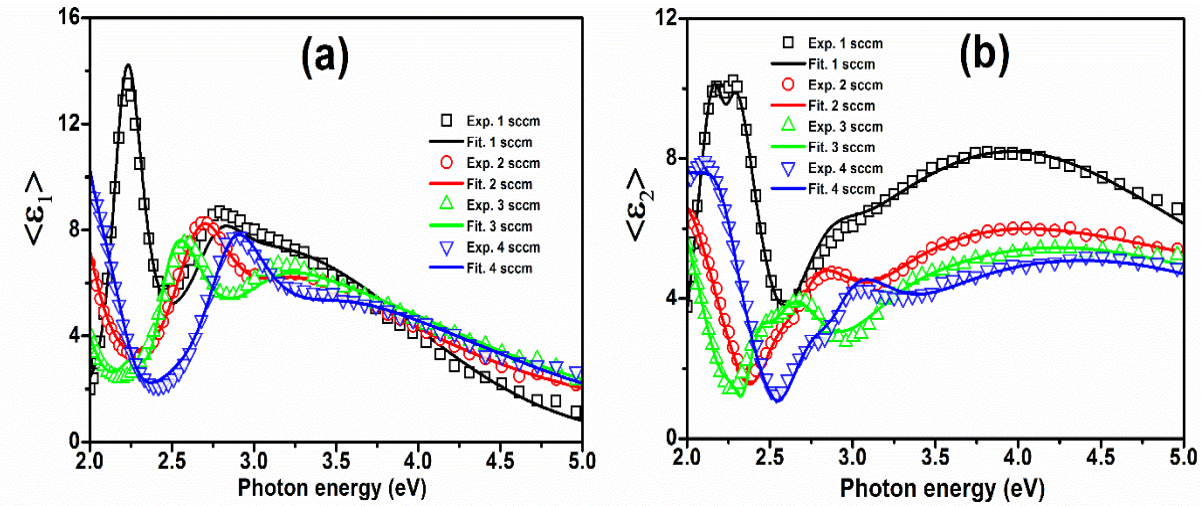

***Figure 4.8**: The experimental (open) and fitted (solid line) data of real $<\varepsilon_1>$ and imaginary $<\varepsilon_2>$ dielectric function of a-SiC:H(p) thin films at different CH_4 flow rate.*

The broadening parameter (*C*) increases with increase in *MFR* indicating an increase in Si-H_2 bond density in the film. Another fitting parameter, band gap energy (E_g) increases with increase in *MFR* and this can be attributed to the replacement of weaker Si–Si bonds by stronger Si–C bonds as well as C–H bonds [30].

***Table 4.5**: The T-L model fitted parameters: rough surface layer thickness (nm), thickness of bulk layer (nm), amplitude factor A (eV), resonance energy E_0 (eV), broadening parameter C (eV), optical band gap E_g (eV) and constant $\varepsilon_1(\infty)$ from ellipsometry for different MFR.*

MFR (sccm)	Thickness of rough surface layer (nm)	bulk layer thickness (nm)	*A* (eV)	E_0 (eV)	*C* (eV)	E_g (eV)	$\varepsilon_1(\infty)$
1	0.59±0.06	279±5	115.62±6.99	3.67±0.01	2.69±0.01	1.85±0.01	1.82
2	1.05±0.07	231±4	71.27±7.72	3.75±0.01	2.75±0.01	2.05±0.01	1.35
3	1.56±0.11	207±3	68.56±8.66	3.81±0.01	2.81±0.01	2.11±0.01	2.43
4	3.89±0.36	175±9	56.44±6.48	3.90±0.01	2.86±0.01	2.08±0.01	2.01

4.2.2.3 UV-Vis-NIR

Figure 4.9(a) shows UV-Vis-NIR transmission spectra of *a-SiC:H(p)* films on Corning substrate at different *MFR*. All films are highly transparent and maximum % transmission is close to that of bare Corning glass substrate. The blank Corning substrate transmission is also included in Figure 4.9(a). The thickness data obtained from surface profilometer and *SE* along with E_g from Tauc's plot [10] and *SE* are plotted together against different *MFR* as shown in Figure 4.9(b). The error bars in Figure 4.9(b) indicate uncertainties in the calculated thickness and E_g.

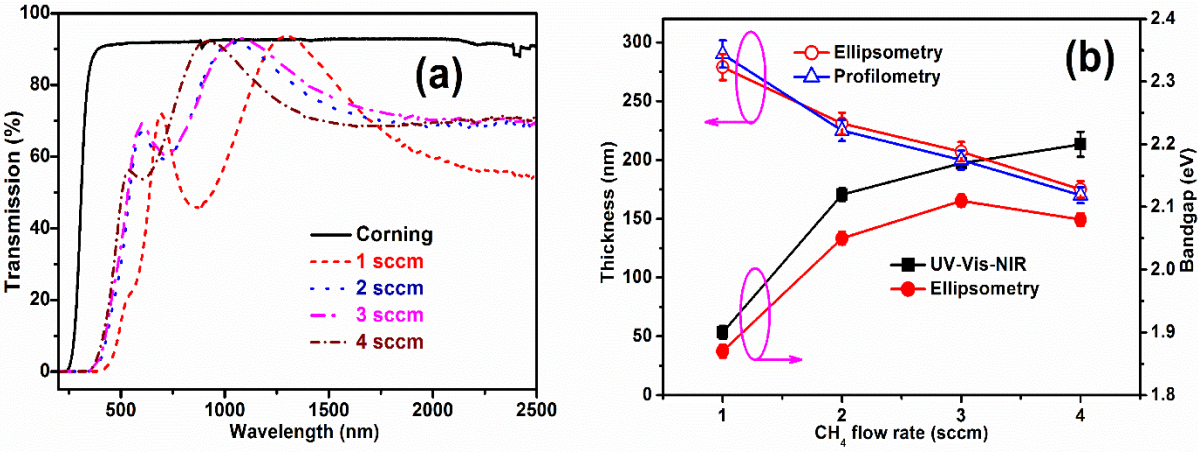

***Figure 4.9**: (a)UV-Vis-NIR transmission spectra of a-SiC:H(p) films at different MFR. (b) Estimated thickness and band gap from different measurements at different MFR.*

From Figure 4.9(b), one can see that the thickness of the film decreases with increase in *MFR*, which is due to etching of weakly or loosely bonded hydrogen atoms from the surface of the film by CH_n radicals. During this growth process, unsaturated bonds or vacancy are created on the growing surface, these unsaturated bonds are then filled by carbon atoms. Due

to these excess carbon atoms incorporated in the film, the E_g increases with increasing *MFR* [8].

4.2.2.4 Fourier Transform Infrared Spectroscopy (FTIR)

To examine the local bonding configurations in the films, FTIR transmission spectra were used. Figure 4.10(a) shows the FTIR transmission spectra of *a-SiC:H*(*p*) films simultaneously deposited on c-Si substrate. The dips in the transmission spectra correspond to absorption by the different vibrational modes of the bonds between Si, H, and C. The absorption peaks at : ~ 640 cm^{-1}, 740-800 cm^{-1}, ~900 cm^{-1}, 960-1000 cm^{-1}, 2000-2100 cm^{-1} and 2800-3000 cm^{-1} are associated with Si-H rocking or waging mode, Si-C stretching mode, Si-O, C-H_n waging or bending modes, vibration of Si-H_n stretching and stretching vibrations of C-H_n, respectively [12, 31-33]. From Figure 4.10 (a) one can clearly identify an increase in the density of Si-C and C-H_n bonds (~740 and 1000 cm^{-1}) at higher *MFR*.

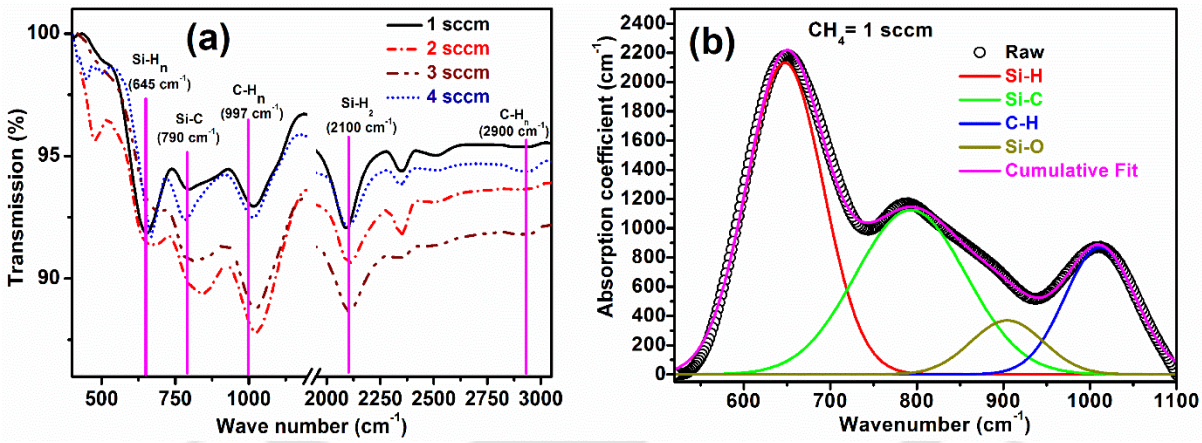

***Figure 4.10**: (a) FTIR transmittance spectra of a-SiC:H(p) films with different MFR on c-Si substrate (b) The deconvoluted absorption coefficient spectra of CH_4=1 sccm.*

The bond density of Si-H (N_{Si-H}), Si-C (N_{Si-C}) and C-H (N_{C-H}) in the films has been calculated using the equation 4.1, after deconvoluting the FTIR absorption spectra in to bands corresponding to Si-H, Si-C, Si-O and C-H bonds.

$$N = A_{\omega} \int \frac{\alpha(\omega)}{\omega} d\omega \qquad (4.1)$$

Where the oscillator strength A_{ω} has a value of 1.6×10^{19} cm^{-2} for Si-H [12], 2.13×10^{19} cm^{-2} for Si-C [22] and 1.35×10^{21} cm^{-2} for C-H [31] respectively. One of the deconvoluted spectra corresponding to film deposited at MFR=1sccm is shown in Figure 4.10(b).

Figure 4.11 demonstrates the effect of variation in *MFR* on the densities (*N*) of Si-H, Si-C and C-H bonds present in the thin film. The Si-H bond density (N_{Si-H}) has the highest value at CH_4 flow rate of 1 sccm and then decreases gradually with the increase in CH_4 flow rate.

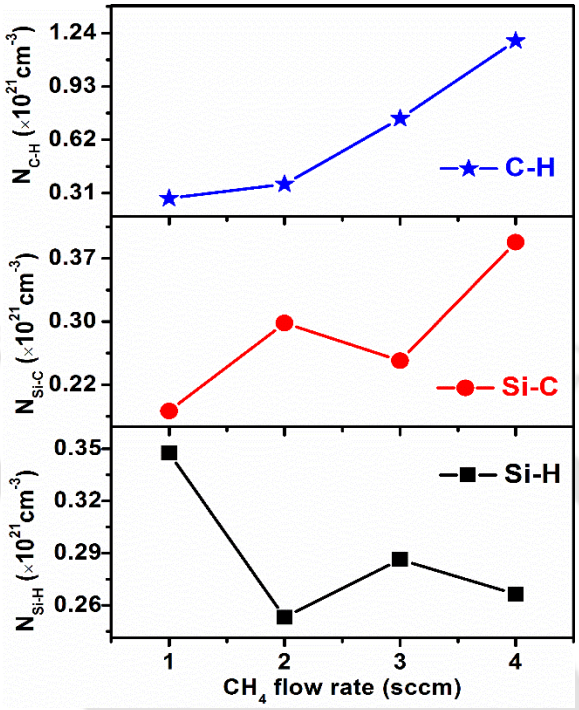

***Figure 4.11**: Content of Si-H, Si-C and C-H bonds for different MFR.*

Furthermore, the bond densities of Si-C and C-H (N_{Si-C} and N_{C-H}) bonds, increase steadily with the increase in CH_4 flow rate. The results obtained for N_{Si-C} and N_{C-H} suggest that at higher *MFR*, more number of carbon radicals are attached with Si and H [34]. The total hydrogen content C_H (%) [14] and microstructure factor (R^*) [15] in the film was calculated using rocking-wagging mode of Si-H and stretching modes of Si-H and $Si-H_2$ respectively. The complete procedure is mentioned in Chapter 2. The calculated C_H (%) and *R** at different *MFR* are listed in Table 4.6. From the Table 4.6, it is observed that C_H (%) in the film found to be not affected in these films and the intensity of mono hydride Si-H vibrational mode at ~2000 cm^{-1} decreases at higher *MFR*, the *R** is found to be lowest for *MFR* at 1sccm.

***Table 4.6**: Total hydrogen content at ~640 cm^{-1} and microstructure factor R* at different MFR*

MFR (sccm)	Hydrogen content in Si-H mode C_H (%)	Microstructure factor (R^*)
1	6.4±0.32	0.64±0.02
2	4.7±0.24	0.82±0.03
3	5.3±0.27	0.73±0.03
4	4.9±0.25	0.84±0.03

4.2.2.5 Conductivity

The dark (σ_d) and photo (σ_{ph}) conductivity measurements were carried out at room temperature (*RT*) in coplanar geometry. Figure 4.12 shows the variation of σ_d and σ_{ph} for films deposited at different *MFR*. The σ_d of films is found to be more than 4 orders of magnitude higher than intrinsic *a-Si:H* deposited at the same temperature (Chapter 3, section 3.4.7). However a gradual fall in conductivity with increase in *MFR* may be attributed to increase in the void density due to increase in structural disorder in films deposited at higher *MFR*.

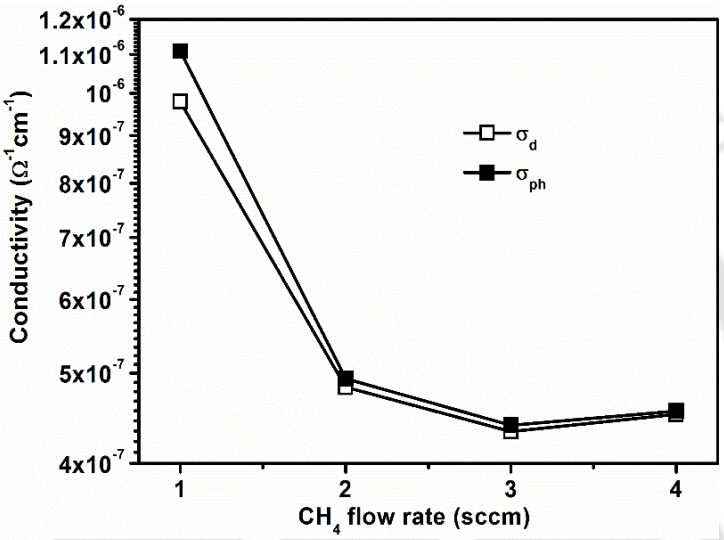

***Figure 4.12**: Room temperature dark (σ_d) and photo (σ_{ph}) conductivity of a-Si:H(p) films deposited at different MFR.*

4.2.3 Series (III): Substrate temperature (T_s=90-150°C) variation of *a-Si:H*(*n*) thin films

In this series, phosphine doped amorphous silicon (*a-Si:H*(*n*)) thin films were deposited on Corning substrate by varying the substrate temperature in the range of 90 – 150 ^oC, keeping other deposition parameters constant. The deposition parameters are listed in Table 4.1

4.2.3.1 Raman scattering

Figure 4.13(a) show Raman spectra of *a-Si:H*(*n*) films, deposited at different substrate temperature (T_s). The Raman spectra has been identified having TA, LA, LO and TO modes of a-Si:H [4]. We did not observe any TO mode peak ~510 cm^{-1} (for *nc-Si:H*) with variation in T_s. All films show broad TO mode peak at ~480 cm^{-1}, which indicates that these films are pure amorphous [30] irrespective of T_s. In order to find short and medium range order (*SRO* and *MRO*), the Raman spectra were deconvoluted into different components as mentioned in

Chapter 2. One of the deconvoluted Raman spectrum corresponding to T_s at 150°C is shown in Figures 4.13(b). The TO mode peak position, *FWHM* of TO mode, $\Delta\theta_B$ and I_{TA}/I_{TO} values for these films are listed in the Table 4.7.

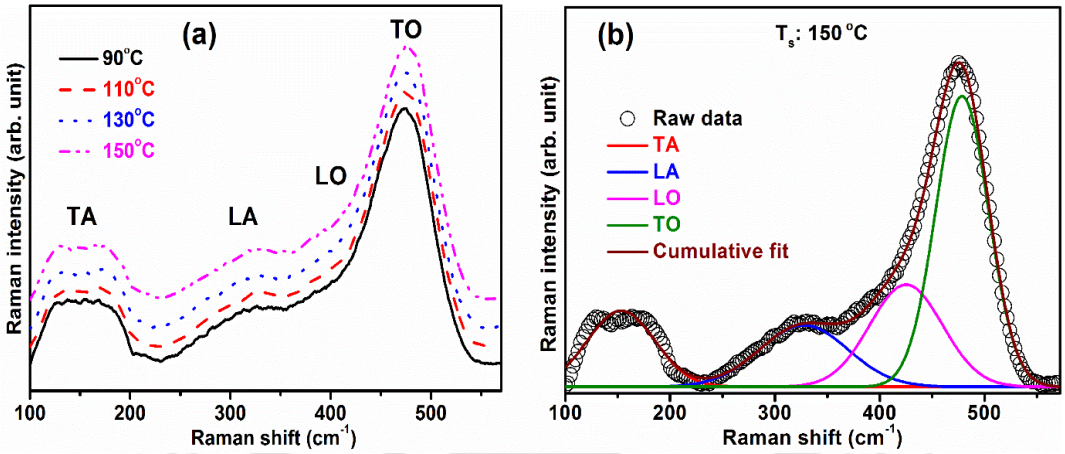

***Figure 4.13**: (a) Raman spectra for the films prepared with varying T_s. (b) Deconvoluted Raman spectra for T_s = 150°C.*

It was observed that, TO mode peak position did not vary much with variation in T_s. The $\Delta\theta_B$ (°) values of *a-Si:H*(*n*) films at different T_s were found to be in the range of 7.43 ± 1.62° to 7.68± 1.74°. The substrate temperature had not much effect on the TO mode peak position, $\Delta\theta_B$ and I_{TA}/I_{TO} values of *a-Si:H*(*n*) films. However, film deposited at *Ts* 150°C showed lower $\Delta\theta_B$ =7.43° and I_{TA}/I_{TO} =0.31 indicating an improvement in *SRO* and *MRO* at higher T_s.

***Table 4.7**: The TO mode peak position, FWHM of TO mode, $\Delta\theta_B$ (°) and I_{TA}/I_{TO} values of a-Si:H(n) thin films deposited at different T_s on corning 1737 glass substrate.*

Substrate temperature (°C)	TO mode peak Position (cm^{-1})	*FWHM* (cm^{-1})	$\Delta\theta_B$ (°)	I_{TA}/I_{TO}
90	476	60.56	7.59	0.39
110	477	61.08	7.68	0.32
130	477	61.09	7.68	0.32
150	478	59.59	7.43	0.31

4.2.3.2 Spectroscopic ellipsometry (SE)

Figure 4.14 (a and b) show the *SE* experimental (open) and fitted (solid line) data of the pseudo dielectric function of real $\langle\varepsilon_1\rangle$ and imaginary $\langle\varepsilon_2\rangle$ of *a-Si:H*(*n*) thin films deposited at different T_s. To deduce optical parameters, experiential data is fitted with *T-L* model by constructing a two-layer model [6]. The *T-L* model details have been discussed in Chapter 2.

In $<\varepsilon_2>$ spectra, $<\varepsilon_2>_{max}$ is observed around ~3.5 eV, which is a characteristic feature of the direct optical transition in amorphous silicon structure [6].

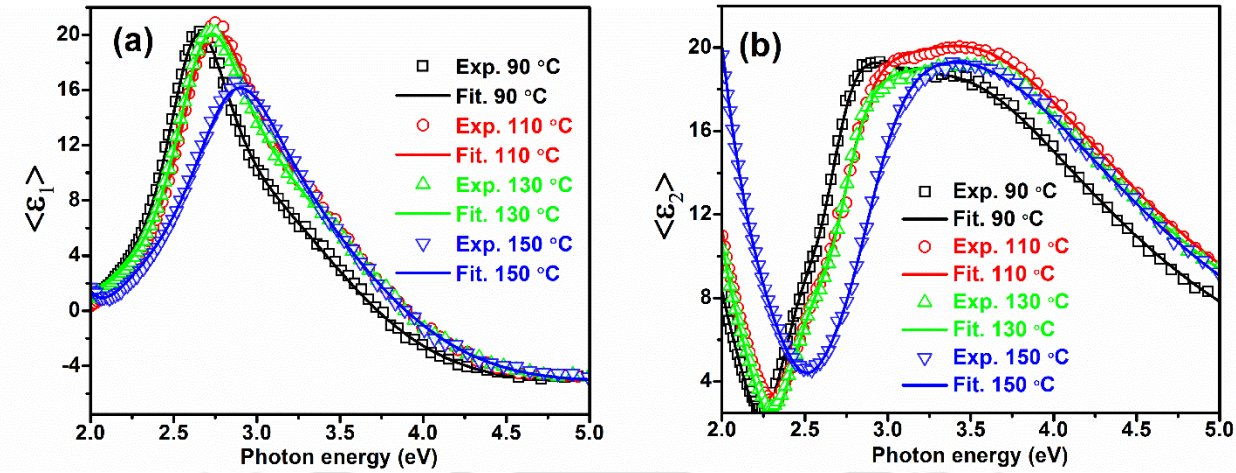

***Figure 4.14**: Plot of experimental (open) and fitted (solid line) data of (a) real dielectric function $<\varepsilon_1>$ and (b) imaginary dielectric function $<\varepsilon_2>$against photon energy at different T_s.*

The fitted parameters of *T-L* model for *a-Si:H*(*n*) at different T_s are listed in Table 4.8. The thickness of rough surface layer is slightly increased with substrate temperature. It can be seen that amplitude factor (*A*) has also slightly increased with increase in T_s, which indicates that denser film formation takes place at higher T_s. The broadening parameter (*C*) did not change much with increase in T_s. However, slightly lower *C* value was observed at T_s=150^{o}C indicating that these films have less fraction of Si-H_2 bonds.

***Table 4.8**: The T-L model fitted parameters: rough surface layer thickness (nm), thickness of bulk layer (nm), amplitude factor A (eV), resonance energy E_0 (eV), broadening parameter C (eV), optical band gap E_g (eV) and constant $\varepsilon_1(\infty)$ from ellipsometry for a-Si:H(n) films at different T_s.*

Ts (^{o})	Thickness of rough surface layer (nm)	bulk layer thickness (nm)	*A* (eV)	E_0 (eV)	*C* (eV)	E_g (eV)	$\varepsilon_1(\infty)$
90	0.86±0.04	65±4	185.21±2.15	3.53±0.01	2.69±0.01	1.78±0.01	1.32
110	1.03±0.07	73±6	192.85±1.02	3.51±0.01	2.66±0.01	1.78±0.01	1.38
130	1.56±0.11	86±2	192.03±2.54	3.47±0.01	2.66±0.01	1.80±0.01	1.14
150	1.82±0.26	102±7	198.54±7.26	3.45±0.01	2.62±0.01	1.81±0.01	0.89

4.2.3.3 UV-Vis-NIR

Figure 4.15(a) show the UV-Vis-NIR transmission spectra of *a-Si:H*(*n*) films at different T_s. In the transmission spectra, there were not sufficient interference fringes to apply

Swanepoel's method for the determination of film thickness [9]. Hence, the thicknesses of these films were estimated using surface profilometer. Figure 4.15(b) show the thickness of *a-Si:H*(*n*) at different T_s.

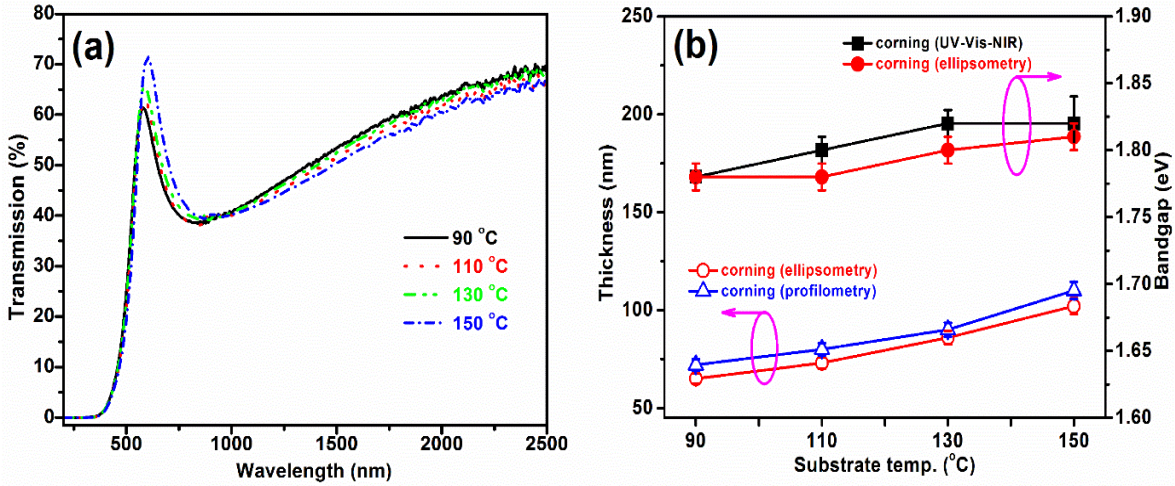

***Figure 4.15**: (a) UV-Vis-NIR transmission spectra of a-Si:H(n) films at different T_s (b) Thickness and band gap of a-Si:H(n) films estimated from different measurements at different T_s.*

It was observed that the thickness of the films is in the range of 63±05-110±06 nm. Thickness of the films increases with increase in T_s since the increase in the sticking probability of precursor radicals adsorbed on the growing surface of a-Si:H is more in comparison with that of rate of surface recombination reactions [35]. The E_g of the films was calculated from Tauc's plot [10]. The E_g of the films at different T_s is in the range of 1.78±0.01-1.82±0.01 eV. The E_g was slightly higher (0.1 eV) at high T_s. The thickness values estimated from profilometry and and E_g values estimated from Tauc plot are in good agreement with *SE* results.

4.2.3.4 Conductivity

In order to study electronic transport properties of *a-Si:H*(*n*) films, dark (σ_d) and photo conductivity (σ_{ph}) measurements were performed in coplanar geometry at room temperature. Figure 4.16(a) shows the variation of σ_d and σ_{ph} at different T_s. The σ_d of *a-Si:H*(*n*) films are found to be more than 6 orders of magnitude higher than intrinsic *a-Si:H* films (chapter 3, section 3.2.1.6). These results suggest that films are doped efficiently by adding phosphine during deposition. Figure 4.16(b) shows the temperature dependence conductivity of film deposited at T_s = 150 °C. The activation energy is found to be 0.33 eV, indicating that Fermi level is closer to the conduction band. The dark conductivity and activation energy values are comparable with other reports [36, 37].

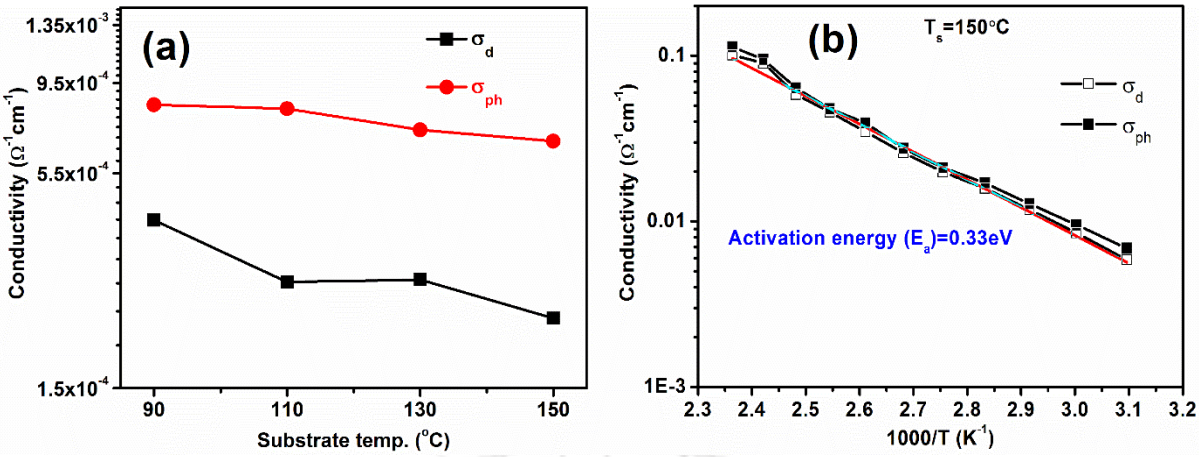

***Figure 4.16**: (a) Room temperature dark (σ_d) and photo (σ_{ph}) conductivity of a-Si:H(n) films at different T_s. (b) Temperature dependent conductivity of a-Si:H(n) film at T_s=150°C.*

4.3 Conclusion

In this chapter, microstructural and opto-electronic properties of *a-Si:H*(*p*) films have been reported with variation in rf power and CH_4 dilution. In addition, the microstructural and opto-electronic properties of phosphorus doped films with variation in T_s have also been studied. The observations for different series are summarized below:

Series (I), rf power variation of *a-Si:H*(*p*) thin films at low substrate temperature T_s (=110°C): In this series, influence of rf power on microstructure and optoelectronic properties of the *a-Si:H*(*p*) films deposited at T_s = 110 °C, is studied. Raman and spectroscopic ellipsometry results show that films are purely amorphous irrespective of rf power. The films deposited at rf power of 60 W possess device grade quality; improvement in the *SRO*, less broadening in $<\varepsilon_2>$, lesser Si-H_2 fraction. The dark conductivity of *a-Si:H*(*p*) films show more than 4 orders of magnitude increase from that of intrinsic a-Si:H films. These results suggest that films are doped efficiently by adding diborane during deposition.

Series (II), Methane CH_4 flow rate (MFR) variation of *a-Si:H*(*p*) thin films at low T_s (T_s=110°C): In this series, we have performed a systematic study on the effect of *MFR* on structural and optoelectronic properties of *a-SiC:H*(*p*) films. Thin films deposited at different *MFR* are amorphous in nature as confirmed by Raman spectroscopy measurements and also supported by the SE measurements. The mass density of film decreases with increase in the carbon content due to increase in void density at higher *MFR*. The FTIR results show hydrogen bonded to Si decreases due to etching of hydrogen atoms and replacement of weak Si-H bonds with Si-C. The bond densities Si-C and C-H (N_{Si-C} and N_{C-H}), increase steadily

with the increase in CH_4 flow rate. Films deposited at *MFR*=1 sccm was found to be suitable for solar cell fabrication due to its less broadening in $<\varepsilon_2>$, low *SRO*, *MRO* and lower densities of Si-C and C-H bonds.

Series (III), Substrate temperature (T_s=90-150°C) variation of *a-Si:H*(*n*) thin films: In this series, structural and opto-electronic properties of *a-Si:H*(*n*) films were studied with variation in T_s (90-150^{o}C). Raman and *SE* results confirmed that all the deposited films are amorphous in nature irrespective of variation in T_s. The dark conductivity of *a-Si:H*(*n*) films showed more than 6 orders of magnitude increase as compared to that of intrinsic *a-Si:H* films. These results suggest that films are doped efficiently by adding phosphine during deposition. The activation energy of the T_s=150^{o}C film was 0.33eV, suggesting that Fermi level is closer to conduction band for these phosphorus doped films.

4.4 References

[1] Y. Yuan, W. Zhao, J. Ma, Z. Yang, W. Li, K. Zhang, Structural evolution of nanocrystalline silicon in hydrogenated nanocrystalline silicon solar cells, *Surface and Coatings Technology*, **320** (2017) 362-365.

[2] J. Robertson, The electronic and atomic structure of hydrogenated amorphous Si—C alloys, *Philosophical Magazine Part B*, **66** (1992) 615-638.

[3] C.H. Lee, K.S. Lim, Boron-doped amorphous diamondlike carbon as a new p-type window material in amorphous silicon p-i-n solar cells, *Applied Physics Letters*, **72** (1998) 106-108.

[4] K. Shrestha, V.C. Lopes, A.J. Syllaios, C.L. Littler, Raman spectroscopic investigation of boron doped hydrogenated amorphous silicon thin films, *Journal of Non-Crystalline Solids*, **403** (2014) 80-83.

[5] D. Beeman, R. Tsu, M. Thorpe, Structural information from the Raman spectrum of amorphous silicon, *Physical Review B*, **32** (1985) 874-878.

[6] S.Y. Lee, J.H. Shim, D.J. You, S.W. Ahn, H.M. Lee, The novel usage of spectroscopic ellipsometry for the development of amorphous Si solar cells, *Solar Energy Materials and Solar Cells*, **95** (2011) 142-145.

[7] X. Li, L. Li, Z. Ma, J. Lu, A.A. Volinsky, F. Ren, Boron doping effects on microcrystalline silicon film roughness studied by spectroscopic ellipsometry, *Journal of Alloys and Compounds*, **684** (2016) 582-586.

[8] D.K. Basa, G. Abbate, G. Ambrosone, U. Coscia, A. Marino, Spectroscopic ellipsometry study of hydrogenated amorphous silicon carbon alloy films deposited by plasma enhanced chemical vapor deposition, *Journal of Applied Physics*, **107** (2010) 023502.

[9] R. Swanepoel, Determination of the thickness and optical constants of amorphous silicon, *J. Phys. E: Sci. Instrum.*, **16** (1983) 1214.

[10] G.R. Tauc J, Vancu A, Optical properties and electronic structure of amorphous germanium, *Phys Status Solidi*, **15** (1966) 627.

[11] J. L. Andujar, J. Kasaneva, J Serra, A. Canlllas, C. Roth, J. L. Morenza, E. Bertran, Effects of r.f. power on optical and electrical properties of plasma-deposited hydrogenated amorphous silicon thin films, *Sensors and Actuators A*, **37-38** (1993) 733-736.

[12] A.M. Funde, N.A. Bakr, D.K. Kamble, R.R. Hawaldar, D.P. Amalnerkar, S.R. Jadkar, Influence of hydrogen dilution on structural, electrical and optical properties of hydrogenated nanocrystalline silicon (nc-Si:H) thin films prepared by plasma enhanced chemical vapour deposition (PE-CVD), *Solar Energy Materials and Solar Cells*, **92** (2008) 1217-1223.

[13] T. Anutgan, S. Uysal, Low temperature plasma production of hydrogenated nanocrystalline silicon thin films, *Current Applied Physics*, **13** (2013) 181-188.

[14] C.J. Fang, K.J. Gruntz, L. Ley, M. Cardona, The hydrogen content of a-Ge:H and a-Si:H as determined by IR spectroscopy, gas evolution and nuclear reaction techniques, *Journal of Non-Crystalline Solids*, **35 & 36** (1980) 255-260.

[15] W. Du, X. Yang, H. Povolny, X. Liao, X. Deng, Impact of hydrogen dilution on microstructure and optoelectronic properties of silicon films deposited using trisilane, *Journal of Physics D: Applied Physics*, **38** (2005) 838-842.

[16] H.-J. Lin, S.-H. Chen, Effect of the hydrogen concentration on the growth mechanism of sputtered hydrogenated silicon thin films, *Optical Materials Express*, **3** (2013) 1215.

[17] R.J. Prado, M.C.A. Fantini, M.H. Tabacniks, C.A.V. Cardoso, I. Pereyra, A.M. Flank, Improvements on the local order of amorphous hydrogenated silicon carbide films, *Journal of Non-Crystalline Solids*, **283** (2001) 1-10.

[18] S. Ray, P. Chaudhuri, A.K. Batabyal, A.K. Barua, Electronic and Optical-Properties of Boron Doped Hydrogenated Amorphous-Silicon Thin-Films, *Sol Energ Mater*, **10** (1984) 335-347.

[19] P. Sanchez, O. Lorenzo, A. Menendez, J.L. Menendez, D. Gomez, R. Pereiro, B. Fernandez, Characterization of doped amorphous silicon thin films through the investigation of dopant elements by glow discharge spectrometry: a correlation of conductivity and

bandgap energy measurements, *International journal of molecular sciences*, **12** (2011) 2200-2215.

[20] S. Hamma, P.R.I. Cabarrocas, Low-temperature growth of thick intrinsic and ultrathin phosphorous or boron-doped microcrystalline silicon films: Optimum crystalline fractions for solar cell applications, *Solar Energy Materials and Solar Cells*, **69** (2001) 217-239.

[21] C. Jeong, Y.-B. Kim, S.-H. Lee, J.H. Kim, Preparation of Born-Doped a-SiC:H Thin Films by ICP-CVD Method and to the Application of Large-Area Heterojunction Solar Cells, *Journal of Nanoscience and Nanotechnology*, **10** (2010) 3321-3325.

[22] H.S. Jha, A. Yadav, M. Singh, S. Kumar, P. Agarwal, Growth of Wide-Bandgap Nanocrystalline Silicon Carbide Films by HWCVD: Influence of Filament Temperature on Structural and Optoelectronic Properties, *Journal of Electronic Materials*, **44** (2015) 922-928.

[23] C.-D. Sen, J.-I. Son, H.-H. Kim, H.-S. Yun, N.-H. Cho, Variation of the nanostructural feature of nc-SiC:H thin films with post-deposition thermal annealing, *Thin Solid Films*, **571** (2014) 238-244.

[24] S.W. King, M. French, J. Bielefeld, W.A. Lanford, Fourier transform infrared spectroscopy investigation of chemical bonding in low-k a-SiC:H thin films, *Journal of Non-Crystalline Solids*, **357** (2011) 2970-2983.

[25] V.A. Volodin, D.I. Koshelev, Quantitative analysis of hydrogen in amorphous silicon using Raman scattering spectroscopy, *Journal of Raman Spectroscopy*, **44** (2013) 1760-1764.

[26] S. Kageyama, M. Akagawa, H. Fujiwara, Dielectric function ofa-Si:H based on local network structures, *Physical Review B*, **83** (2011).

[27] V. Kanneboina, R. Madaka, P. Agarwal, Spectroscopic ellipsometry studies on microstructure evolution of a-Si:H to nc-Si:H films by H 2 plasma exposure, *Materials Today Communications*, **15** (2018) 18-29.

[28] M. Sato, S.W. King, W.A. Lanford, P. Henry, T. Fujiseki, H. Fujiwara, Network structure of a-SiO:H layers fabricated by plasma-enhanced chemical vapor deposition: Comparison with a-SiC:H layers, *Journal of Non-Crystalline Solids*, **440** (2016) 49-58.

[29] E. Pascual, J.L. Andujar, J.L. Fernandez, E. Bertran, Spectral Ellipsometric and Compositional Characterization of Hydrogenated Amorphous-Silicon Carbide Thin-Films, *Diam Relat Mater*, **4** (1995) 702-705.

[30] M.N.P. Carreno, I. Pereyra, p-type doping in a-Si1-xCx : H obtained by PECVD, *Journal of Non-Crystalline Solids*, **266** (2000) 699-703.

[31] T. Kaneko, D. Nemoto, A. Horiguchi, N. Miyakawa, FTIR analysis of a-SiC:H films grown by plasma enhanced CVD, *Journal of Crystal Growth*, **275** (2005) e1097-e1101.

[32] J. Podder, M. Rusop, T. Soga, T. Jimbo, Boron doped amorphous carbon thin films grown by r.f. PECVD under different partial pressure, *Diamond and Related Materials*, **14** (2005) 1799-1804.

[33] A.R. Oliveira, M.N.P. Carreño, N and p-type doping of PECVD a-SiC:H obtained under "silane starving plasma" condition with and without hydrogen dilution, *Materials Science and Engineering: B*, **128** (2006) 44-49.

[34] Y. Zhang, P. Du, R. Zhang, G. Han, W. Weng, Structure and properties of hydrogenated amorphous silicon carbide thin films deposited by PECVD, *Journal of Non-Crystalline Solids*, **354** (2008) 1435–1439.

[35] A. Matsuda, Microcrystalline silicon. Growth and device application, *Journal of Non-Crystalline Solids*, **338-340** (2004) 1-12.

[36] C. Song, J. Xu, G. Chen, H. Sun, Y. Liu, W. Li, L. Xu, Z. Ma, K. Chen, High-conductive nanocrystalline silicon with phosphorous and boron doping, *Applied Surface Science*, **257** (2010) 1337-1341.

[37] Y. Lu, H. Li, G. Yang, B. Jiang, Influence of doping and microstructure on electrical properties of doped silicon thin films, *Materials Technology*, **30** (2014) 28-32.

Chapter 5

Optimization of Indium Tin Oxide Films

The transparent conducting oxide (*TCO*) thin films are very useful as contact layers as well as anti-reflection coatings to improve the performance of the solar cells and many other optoelectronic devices such as flat panel displays etc. Thin film hydrogenated amorphous silicon (*a-Si:H*) solar cells require a wide bandgap transparent conductor as window electrode for efficient light transmission as well as extraction of photocurrent. The *TCO*s have good electrical conductivity and high transmission (>90%) in the visible spectrum. The most commonly used *TCO*s for front electrode are zinc oxide (*ZnO*) [1], Aluminum doped zinc oxide (*ZnO:Al*) [2-4], and indium tin oxide (*ITO*) [5, 6]. In addition to this, *TCO* is also used as a back electrode alone or in combination with metals (Ag or Al). Generally, *TCO* films are deposited at lower temperature and then annealed at high temperature to exhibit high transmission and electrical conductivity for *p-i-n* configuration of solar cells [4]. However, in case of *n-i-p* configuration, solar cell is first fabricated on opaque substrates followed by deposition of *TCO* layer. Normally, doped and intrinsic *a-Si:H* layers are deposited at low substrate temperature on flexible substrates, in order to avoid annealing effects on these films. Therefore for *n-i-p* configuration, *TCO* layers need to be deposited at relatively lower substrate temperature than that of *a-Si:H* layers. In this present chapter, the studies on two series of *ITO* thin films deposited at low substrate temperature (T_s=100^{o}C) by rf-sputtering technique are presented. The deposition parameters for each series are listed in Table 5.1.

5.1 Experimental details

In the present study, we have deposited two series of indium tin oxide (*ITO*) films on corning 1737 glass (Corning) substrate by rf-sputtering technique. **Series (I)**: Variation of process pressure and **Series (II)**: Variation of Ar flow rate during deposition of *ITO* films. The deposition parameters for *ITO* thin films are listed in Table 5.1

***Table 5.1**: Deposition parameters for ITO thin films using rf-sputtering technique.*

Deposition parameter	**Process pressure variation**	**Ar flow rate variation**
rf power (Watt)	80	80
Ar flow rate (sccm)	5	**5-9***
Process pressure (mbar)	**0.034-0.074***	0.054
Substrate temperature (°C)	100	100
Electrode distance (cm)	3.5	3.5
Deposition time (minute)	15	15

*variable parameter

5.2 Results and discussions

5.2.1 Series (I): Variation of process pressure

In this series, *ITO* thin films were deposited by varying process pressure in the range of 0.034 – 0.074 mbar, keeping other deposition parameters constant. The deposition parameters are listed in Table 5.1.

5.2.1.1 X-Ray diffraction

Figure 5.1 shows the XRD pattern of *ITO* thin films deposited at different process pressure. It is observed that diffraction from the (222) plane is most prominent in all films with $2\theta = 30.5°$ very close to that of the standard In_2O_3 crystal ($2\theta = 30.61°$) [7, 8]. This indicates preferential growth is along this direction regardless of process pressure. This observation is in agreement with those of Li-Jian *et al* and J-H Gu *et al* [7, 9].

In addition to peak corresponding to (222) plane, low intensity peaks at 2θ =21.4, 35.36, 45.54, 50.82 and 60.48°corresponding to (211), (400), (431), (440) and (622) planes respectively have also been observed in the XRD pattern. The presence of other planes in XRD spectra indicates that *ITO* films are polycrystalline in nature. The peak positions of (222) plane as well as other planes are found to be in good agreement with cubic structure of *ITO* (JCPDS card No: 06-0416). From Figure 5.1, one can clearly notice that at 0.034 mbar pressure, the peak intensities corresponding to (222) and (400) planes are almost equal. However, as the process pressure increases to 0.054 mbar, the intensity of the (400) plane decreases. With further increase in pressure from 0.054 to 0.074 mbar, the intensity of (400) plane again increases. The mean crystallite size was estimated using Debye Scherrer's formula [8] corresponding to for (222) plane as mentioned in Chapter 2. The full width at half

maxima (*FWHM*) of (222) plane and crystallite size values are listed in Table 5.2. The size of the crystallites is found to be largest for the films deposited at 0.054 mbar pressure, for which the intensity of peaks corresponding to the other planes is significantly low.

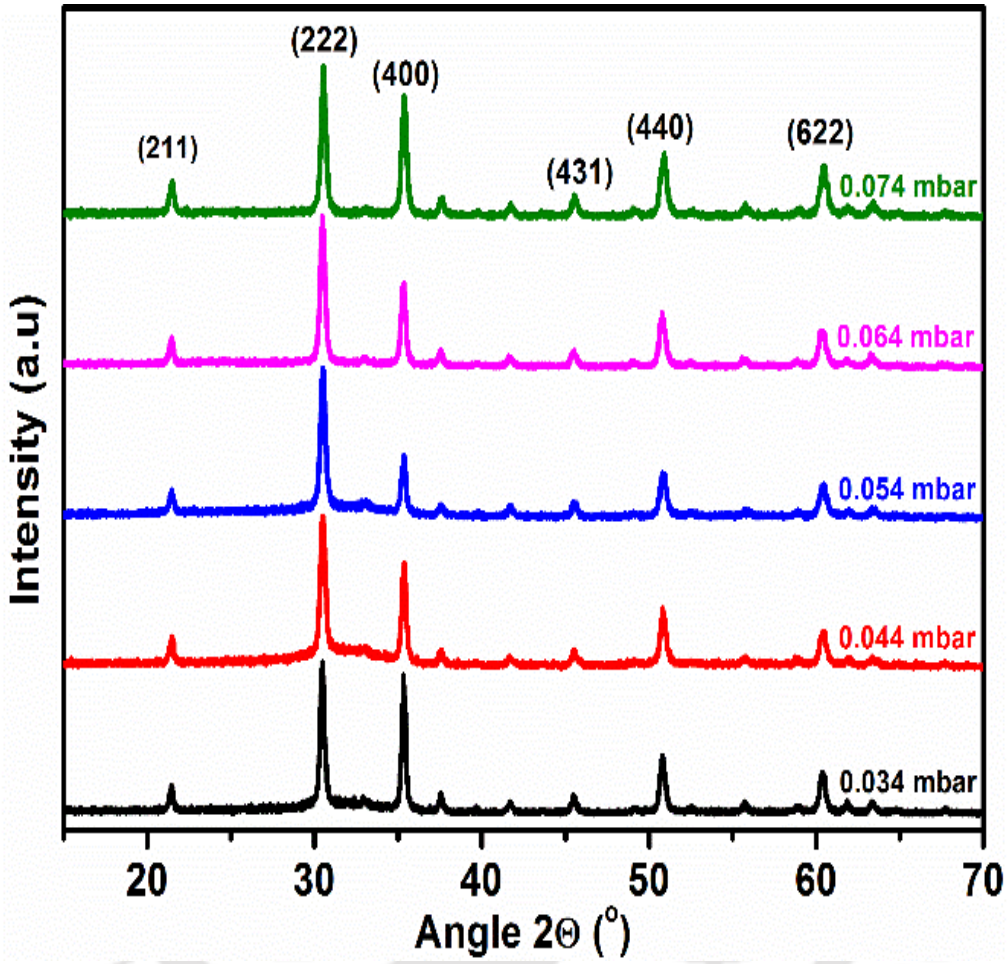

***Figure 5.1**: XRD spectra of ITO films deposited at different process pressure on Corning glass.*

5.2.1.2 UV-Vis-NIR

Figure 5.2 (a) show UV-Vis-NIR transmission spectra of *ITO* films on Corning substrate at different process pressure. All *ITO* films are highly transparent and maximum % transmission is close to that of bare Corning glass substrate. The blank Corning substrate transmission is also included in Figure 5.2(a).

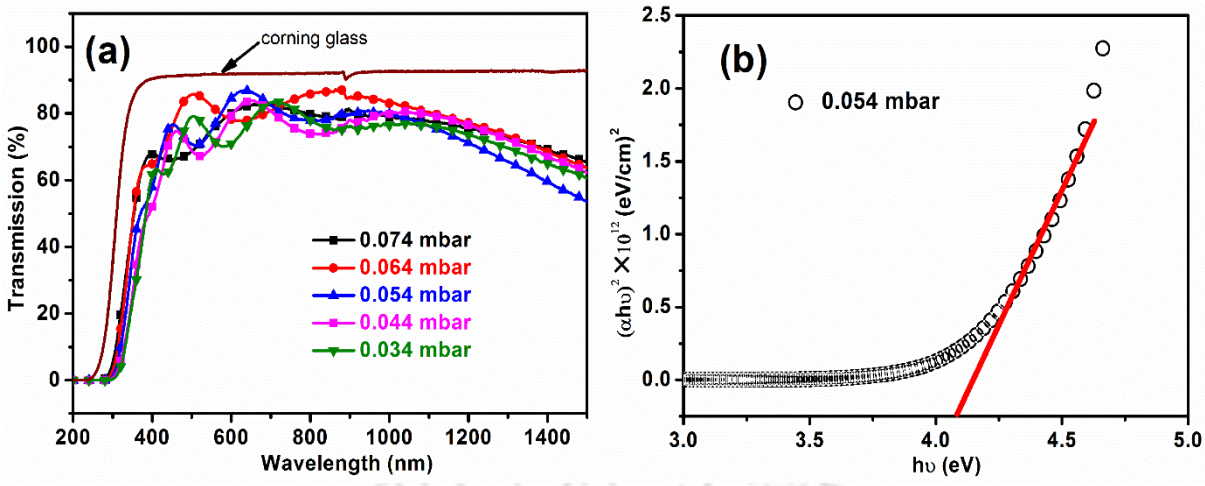

***Figure 5.2**: (a) UV-Vis-NIR transmission spectra of ITO films at different process pressures. (b) Plot of $(\alpha h\upsilon)^2$ vs $h\upsilon$ for ITO film at 0.054 mbar.*

The thickness of *ITO* films was calculated using swanepole's [10] method and was also estimated from surface profilometer. The thickness of the films at different process pressure is in the range of 186±10-379±09 nm and is listed in Table 5.2. It is observed that the thickness of the films decreases with increase in the process pressure. As the process pressure is increased, the mean free path of sputtered atoms from the target is diminished [11] resulting in the decrease in thickness of the films. The optical band gap (E_g) of the films is estimated using Tauc's plot [8]. For 0.054 mbar film, the plot of $(\alpha h\upsilon)^2$ versus $h\upsilon$ is shown in Figure 5.2 (b). The E_g values are in the range of 4.08±0.01 to 4.11±0.01 eV suggesting that E_g of these *ITO* films is not affected by the process pressure. The E_g values are listed in the Table 5.2.

***Table 5.2**: The full width at half maxima of (222) plane, $I_{(222)}/I_{(400)}$, crystallite size (nm), thickness (nm) and band gap (eV) of ITO thin films at different process pressure.*

Process pressure (mbar)	*FWHM* of (222) plane	$I_{(222)}/I_{(400)}$	Crystallite size (nm)	Thickness(nm)		Band gap (eV)
				UV-Vis-NIR	Profilometry	
0.034	0.346	1.09	31	362±06	379±09	4.08±0.01
0.044	0.303	1.43	35	315±11	327±10	4.09±0.01
0.054	0.262	2.32	41	321±09	310±08	4.11±0.01
0.064	0.294	1.79	37	245±12	260±11	4.09±0.01
0.074	0.302	1.25	36	186±10	200±11	4.11±0.01

5.2.1.3 Resistivity

Figure 5.3 shows the room temperature sheet resistance and electrical resistivity of *ITO* films as a function of process pressure. The calculation procedure of sheet resistance and resistivity is discussed in Chapter 2. There is not much variation in sheet resistance of the films; however, its value is least for the films deposited at 0.054 mbar pressure, which is likely to be related to the larger crystallite size and lesser grain boundaries in films deposited at this pressure. This film (at 0.054mbar) is also found to be preferably oriented along (222) direction with least *FWHM* and highest ratio of the intensity ($I_{(222)}/I_{(400)}$) of (222) and (400) planes in XRD pattern, which correspond to the larger crystallite size and reduction in grain boundaries in these otherwise polycrystalline films. A decrease in resistivity with increase in pressure is more likely to be related to the thickness of the films, which decreases with increase in pressure. These observations suggest that a pressure of 0.054mbar is more suitable to deposit the *ITO* films for solar cell application.

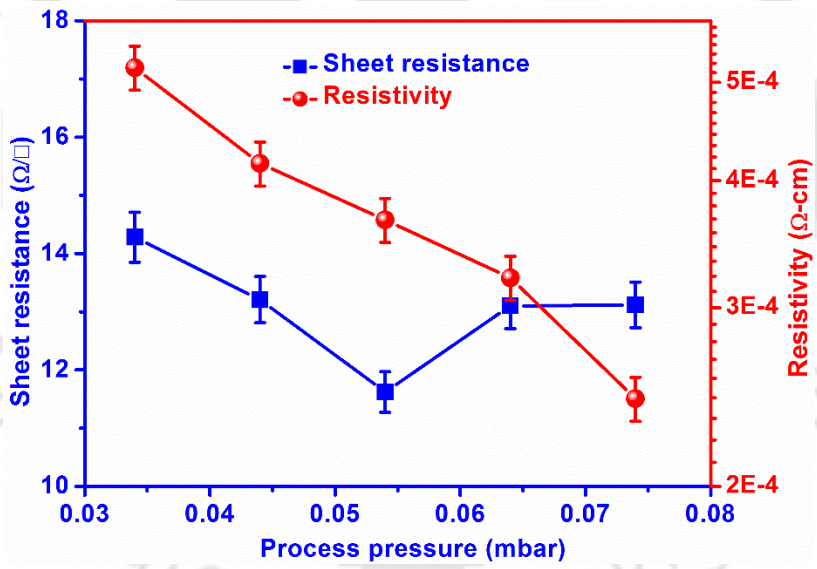

***Figure 5.3**: Sheet resistance and resistivity of ITO films at different process pressure.*

5.2.2 Series (II): Variation of Ar flow rate on *ITO* films

In previous series, we have observed that, *ITO* films deposited at process pressure 0.054 mbar show better structural and electronic properties. To further optimize the deposition parameters, another series of *ITO* films was made by varying the Ar flow rate in the range of 5-9 sccm, keeping the process pressure fixed at 0.054 mbar and other deposition parameters same as that for series I. The deposition parameters for this series are also listed in Table 5.1.

5.2.2.1 X-ray diffraction

Figure 5.4 shows the XRD pattern of *ITO* films deposited at different argon flow rate (5-9 sccm). A strong peak at 2θ = 30.5° corresponding to (222) plane indicates this as preferred growth direction regardless of Ar flow rate. Relatively very low intensity peaks of (211), (400), (431), (440) and (622) crystal planes have also been observed in XRD pattern, indicating a polycrystalline structure of the films. The crystallite size was calculated from Debye Scherrer's formula [8] using *FWHM* of (222) plane. The relative intensity ratio ($I_{(222)}/I_{(400)}$) is found to be highest for film deposited at 7 sccm Ar flow rate. The *FWHM* of (222) plane, relative intensity ratio ($I_{(222)}/I_{(400)}$) and crystallite size values are listed in Table 5.3.

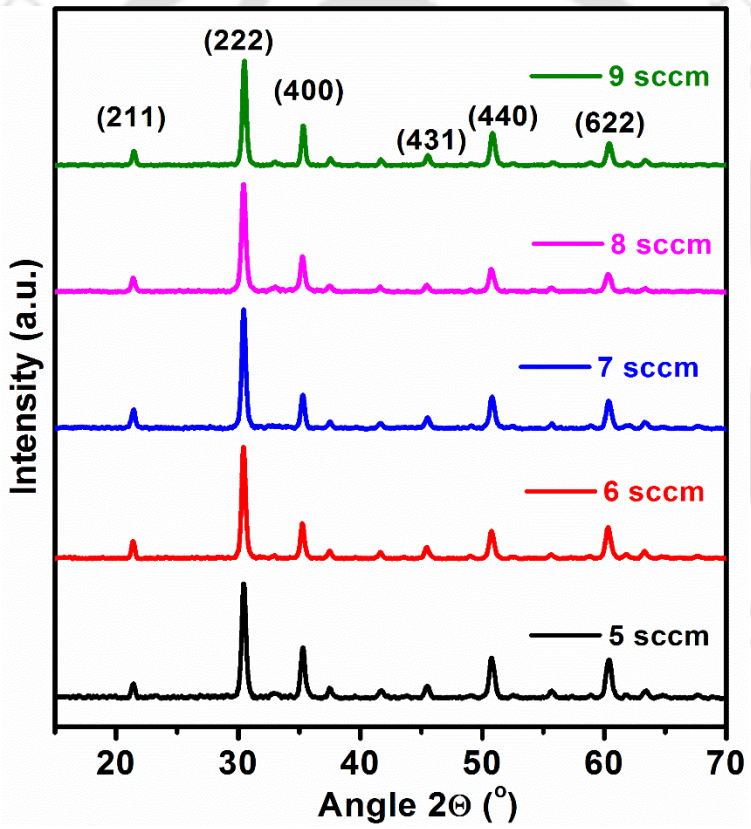

***Figure 5.4**: XRD spectra of ITO films deposited at different Ar flow rate on Corning glass.*

5.2.2.2 UV-Vis-NIR

Figure 5.5 (a) shows the transmission spectra of *ITO* thin films measured with respect to air on Corning substrate at different Ar flow rate. These films shows high transmission (>85%) and the maximum % transmission is close to blank Corning glass transmission.

The thickness of the films was calculated from swanepole's [10] method and was also estimated from surface profilometer. Thickness of these films is found to be in the range of 321±09 to 415 ±07 nm. The thickness of the film is found to be highest at Ar flow rate of 7 sccm, though not much change in crystallite size is observed for different Ar flow rate.

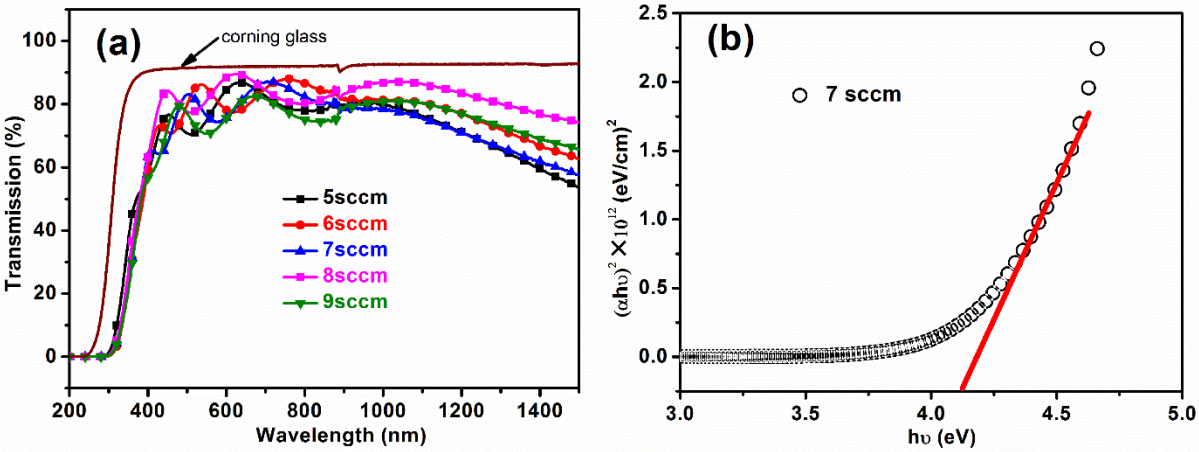

***Figure 5.5**: (a) UV-Vis-NIR transmission spectra of ITO deposited at different Ar flow rate (b) plot of $(\alpha h\upsilon)^2$ vs $h\upsilon$ for ITO film at 7 sccm Ar flow rate.*

***Table 5.3**: The full width at half maxima of (222) plane, crystallite size (nm), thickness (nm) and band gap (eV) of ITO thin films at different Ar flow rate.*

Ar flow rate (sccm)	*FWHM* of (222) plane	$I_{(222)}/I_{(400)}$	Crystallite size (nm)	Thickness(nm)		Band gap (eV)
				UV-Vis-NIR	Profilometry	
5	0.262	2.32	41	321±09	310±08	4.11±0.01
6	0.289	3.16	37	412±07	396±12	4.03±0.01
7	0.276	3.55	39	415±07	398±08	4.09±0.01
8	0.292	3.01	37	330±10	343±07	4.08±0.01
9	0.310	2.62	35	342±09	337±10	4.04±0.01

The E_g of the films was calculated using Tauc's plot. The plot of $(\alpha h\upsilon)^2$ versus $h\upsilon$ for Ar flow rate at 7 sccm film is shown in Figure 5.5 (b). The E_g values at different Ar flow rate are in the range of 4.03±0.01 to 4.11±0.01eV. The Ar flow rate did not have a significant influence on E_g values, however a small variation in E_g, around ±0.1 eV, was observed. The thickness and E_g values at different Ar flow rate are listed in Table 5.3.

5.2.2.3 Resistivity

Figure 5.6 shows the variation of the sheet resistance and resistivity of the films deposited at different argon flow rate. It is observed that both sheet resistance and resistivity decrease with increase of Ar flow rate and reach a minimum value of ~9.75 Ω/□ and 3×10^{-4} Ω-cm respectively at Ar flow rate of 7 sccm. Further increase of Ar flow rate to 9 sccm results in an increase in values of both. From XRD results also, the intensity ratio of $I_{(222)}/I_{(400)}$ is found to be highest at argon flow rate of 7 sccm. These results suggest that Ar flow rate of 7 sccm at a process pressure of 0.054 mbar is more suitable for growth of *ITO* films for solar cell applications.

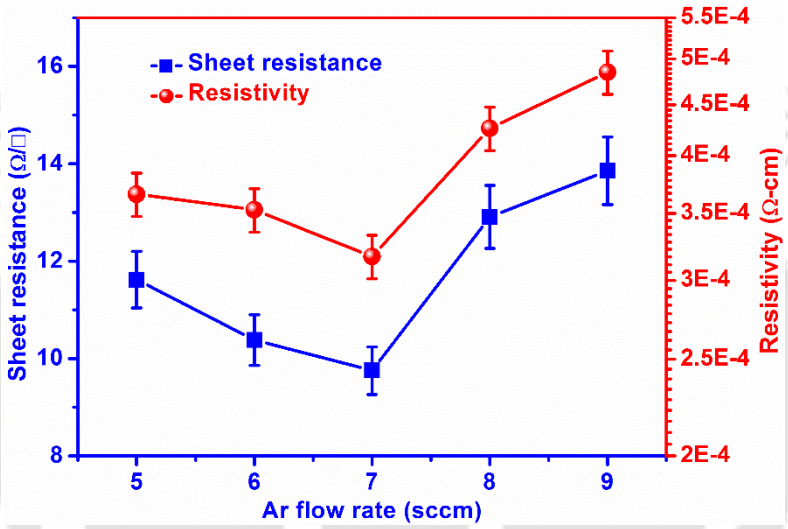

***Figure 5.6**: Sheet resistance and resistivity of ITO films at different Ar flow rate.*

5.3 Conclusion: In this chapter, influence of process pressure and Ar flow rate on microstructure and opto-electronic properties of *ITO* films is reported. The observations for each series are summarized below:

Series (I): Variation of process pressure on *ITO* films: In this series, influence of process pressure on microstructure and optoelectronic properties of the *ITO* films is studied. The XRD results show that (222) plane is most preferred orientation, though other planes are also present in the film indicating polycrystalline structure. UV-Vis-NIR show all *ITO* films are highly transparent (>85%) and maximum % transmission is very close to bare Corning glass substrate. Thicknesses of the films decreases with increase in the process pressure due to the decrease in mean free path of sputtered atoms. The resistivity decreases with increase in the pressure and lowest sheet resistance (~11.6 Ω/□) was found for the film deposited at 0.054 mbar.

Series (II): Variation of Ar flow rate on *ITO* films: In this series, influence of Ar flow rate variation on microstructure and optoelectronic properties of the *ITO* films is studied. The XRD results show that (222) plane is most preferred orientation though other planes are also present in the film indicating polycrystalline structure. UV-Vis-NIR show all *ITO* films are highly transparent (>85%) and maximum % transmission is not influenced by variation in Ar flow rate. The E_g values do not change with Ar flow rate. The lowest values of resistivity (3×10^{-4} Ω-cm) and sheet resistance (~9.75 Ω/□)) are found to be for film deposited at 7 sccm.

5.4 References

[1] P. Mondal, D. Das, Transparent and conducting intrinsic ZnO thin films prepared at high growth-rate with c-axis orientation and pyramidal surface texture, *Applied Surface Science*, **286** (2013) 397-404.

[2] Q. Jiang, J. Lu, Z. Ye, Plasma-induced surface textures of ZnO:Al transparent conductive films, *Vacuum*, **111** (2015) 42-47.

[3] X. Yan, W. Li, A.G. Aberle, S. Venkataraj, Investigation of the thickness effect on material and surface texturing properties of sputtered ZnO:Al films for thin-film Si solar cell applications, *Vacuum*, **123** (2016) 151-159.

[4] A. Rayerfrancis, P.B. Bhargav, N. Ahmed, S. Bhattacharya, B. Chandra, S. Dhara, Sputtered AZO Thin Films for TCO and Back Reflector Applications in Improving the Efficiency of Thin Film a-Si:H Solar Cells, *Silicon*, **9** (2015) 31-38.

[5] N. Manavizadeh, F.A. Boroumand, E. Asl-Soleimani, F. Raissi, S. Bagherzadeh, A. Khodayari, M.A. Rasouli, Influence of substrates on the structural and morphological properties of RF sputtered ITO thin films for photovoltaic application, *Thin Solid Films*, **517** (2009) 2324-2327.

[6] Q.H. Fan, C. Chen, X. Liao, X. Xiang, X. Cao, W. Ingler, N. Adiga, X. Deng, Spectroscopic aspects of front transparent conductive films for a-Si thin film solar cells, *Journal of Applied Physics*, **107** (2010) 034505.

[7] Li-jian Meng, M.P.d. Santos, Properties of indium tin oxide (ITO) films prepared by r.f. reactive magnetron sputtering at different pressures, *Thin Solid Films*, **303** (1997) 151-155.

[8] G.D. Yüzüak, Ö.D. Coşkun, The effect of annealing on the structural, electrical, optical and electrochromic properties of indium-tin-oxide films deposited by RF magnetron sputtering technique, *Optik - International Journal for Light and Electron Optics*, **142** (2017) 320-326.

[9] J.-H. Gu, J.-L. Si, J.-X. Wang, Y.-Y. Feng, X.-Y. Gao, J.-X. Lu, Indium–tin oxide films obtained by DC magnetron sputtering for improved Si heterojunction solar cell applications, *Chinese Physics B*, **24** (2015) 117703.

[10] R. Swanepoel, Determination of the thickness and optical constants of amorphous silicon, *J. Phys. E: Sci. Instrum.*, **16** (1983) 1214.

[11] N. Yasrebi, B. Bagheri, P. Yazdanfar, B. Rashidian, P. Sasanpour, Optimization of Sputtering Parameters for the Deposition of Low Resistivity Indium Tin Oxide Thin Films, *Acta Metallurgica Sinica*, **27** (2014) 324-330.

Chapter 6

Fabrication of Solar Cells on Flexible Substrates at Low Temperature

Amorphous silicon based solar cells consist of several layers of different chemical composition and different optical and electronic properties. The main layers of a single junction device structure are: the transparent conductive layer, the sequence of *p*- doped, intrinsic, *n*- doped amorphous Si layers and the light reflecting back contact layer. For the proper device performance each layer has to be optimized for its thickness according to the desired optoelectronic properties. In addition, the interface between *n/i* and *i/p* layers also need to be optimized. In *n-i-p* or *p-i-n* based solar cells, intrinsic layer is the main absorber layer. In general, when thickness of this layer increases, more photons are absorbed resulting in generation of more electron-hole pair which in turn increase the current density (J_{sc}) and thus efficiency, provided the thickness of the absorber layer is less than the carrier drift length. The efficiency of solar cells also decreases due to Staebler-Wronsky (S-W) effect [1, 2], which depends upon the quality as well as thickness of *i*- layer [3]. In addition to *i*- layer, interface between *n/i* and *i/p* layers play a major role in performance of *n-i-p* or *p-i-n* solar cell. The interface defects at *n/i* and *i/p* layers limit electrical transport in the solar cell. Zhang *et al*. [4], Mews *et al*. [5], Agbo *et al*. [6], Bai *et al*. [7], and Xiao *et al*. [8] reported that these interface defects could be minimized by subjecting to H_2 plasma treatment (*HPT*) at interfaces. With the motivation of reducing the cost of solar cells, we have fabricated solar cells on low cost flexible and other substrates with the optimized deposition parameters of each layer. The chapter presents the studies on the influence of the intrinsic layer thickness, back reflector, *HPT* at *n/i* and *i/p* interfaces and *a-SiC:H*(*p*) as window layer on the solar cell efficiency.

6.1 Deposition parameters for solar cell fabrication

Solar cells were fabricated using individual layer deposition parameters corresponding device quality films for the intrinsic and doped amorphous silicon films. The structure of the cells, for *n-i-p* configuration, fabricated at 150^{o}C and 110^{o}C on flexible polyimide (PI), photo paper (PP) and rigid corning 1737 glass (Corning) substrates is *substrate/Ag/ITO/n(a-Si:H)/i(a-Si:H)/p(a-Si:H)/ITO*. In this configuration silver (*Ag*) acts as a back reflector as well as back

electrode. On the other hand, structure of the cells fabricated on commercially purchased *ITO* coated Corning (sigma Aldrich) and *ITO* coated polyethylene terephthalate (*PET*) (Technistro) was slightly different. The cell structure on these substrate is *substrate/ITO/n(a-Si:H)/i(a-Si:H)/p(a-Si:H)/ITO*. After cells were fabricated, *Ag* was deposited on the back side of the *ITO* coated corning and PET substrates to serve as back reflector for better performance. Doped *p-* & *n-* layer thicknesses were kept constant at 35 and 20 nm respectively. Doped layers and intrinsic layers were deposited in three different chambers in multi chamber RF-PECVD system in order to avoid the contamination during deposition. Prior to the fabrication of *n-, i-, & p-* layers, PI, PP and blank corning substrates were coated with ~100 nm thick *Ag* film (back reflector and electrode) followed by 20 nm thick *ITO* layer to avoid the diffusion of *Ag* in the active layer of solar cells. A thick *ITO* (~220 nm) was also deposited on top of *p-* layer of solar cells which act as top transparent electrode. Both *Ag* and *ITO* were deposited using rf-sputtering. The deposition parameters for *n-, i-,* & *p-* layers used for fabrication of solar cells at substrate temperature (T_s) of 150^{o}C and 110^{o}C are listed in Table 6.1 and Table 6.2 respectively.

The influence of intrinsic layer thickness, influence of back reflector, *HPT* at *n/i* and *i/p* interface layers on solar cell parameters with *a-SiC:H*(*p*) used as a window layer was investigated. Solar cell current density-voltage (*J-V*) and external quantum efficiency (*EQE*) measurements were performed at room temperature. The details of these measurements are discussed in Chapter 2.

Table 6.1*: Deposition parameter for each layer was used for the fabrication of solar cell (T_s=150^{o}C): HFR (hydrogen flow rate), SFR (silane flow rate), BFR (diborane B_2H_6 (2% in H_2) flow rate), MFR (methane flow rate), PFR (phosphine PH_3 (1% in H_2) flow rate), Proc. pressure (process pressure) and T_s (substrate temperature).*

layer	*SFR* (sccm)	*HRF* (sccm)	*BFR* (sccm)	*MFR* (sccm)	*PFR* (sccm)	Proc. pressure (mbar)	rf power (W)	T_s (^{o}C)
a-Si:H(n)	5	50	-		5	0.86	20	150
a-Si:H(i)	5	60	-		-	0.72	40	150
a-Si:H(p)	5	100	5		-	0.61	60	120
a-SiC:H(p)	5	100	5	1	-	0.61	60	120

***Table 6.2**: Deposition parameter for each layer was used for the fabrication of solar cell (T_s= 110°C): HFR (hydrogen flow rate), SFR (silane flow rate), BFR (diborane B_2H_6 (2% in H_2) flow rate), MFR (methane flow rate), PFR (phosphine PH_3 (1% in H_2) flow rate), Proc. pressure (process pressure) and T_s (substrate temperature).*

layer	*SFR* (sccm)	*HRF* (sccm)	*BFR* (sccm)	*MFR* (sccm)	*PFR* (sccm)	Proc. pressure (mbar)	rf power (W)		T_s (°C)
							Corning, PI, PET	PP	
a-Si:H(n)	5	50	-		5	0.86	20	20	110
a-Si:H(i)	5	60	-		-	0.72	50	40	110
a-Si:H(p)	5	100	5		-	0.61	60	60	110
a-SiC:H(p)	5	100	5	1	-	0.61	60	-	110

6.2 Results and discussion

6.2.1 Influence of *i*- layer thickness on solar cell (T_s: 150°C)

In order to find the optimum thickness of intrinsic *a-Si:H* layer for solar cell, thickness of the layer was varied from 200-700 nm. Figure 6.1(a) and Figure 6.1(b) show the current density-voltage (*J-V*) characteristics of single junction *n-i-p* solar cell on rigid Corning and flexible PI with different *i*- layer thickness.

The short circuit current density (J_{sc}) is found to increase from 8.16 to 11.22 mA/cm^2 for cells on Corning and 7.44 to 10.87 mA/cm^2 for cells on PI with the increase in *i*- layer thickness from 330 nm to 700 nm. A slight increase in open circuit voltage (V_{oc}), from 790 to 810 mV on Corning substrates and 770 to 787 mV on PI substrates, is also observed with increase in thickness of *i*- layer. The improvement in J_{sc} could be due to absorption of more number of photons within the cell with increase in *i*- layer thickness [9-11]. Further, the J_{sc} and V_{oc} values on Corning and PI substrates are comparable. The fill factor (*FF*) of the cells on Corning and PI substrates is found to be around 0.59, which is similar to the values reported in literature for amorphous silicon based solar cells [10, 12-14] fabricated at similar temperatures. Though the *FF* is found to decrease a little with increase in thickness of *i*- layer, the overall efficiency η(%) of solar cells, on these two substrates has increased due to more absorption of the photons. The photo-conversion efficiency of the cells on these substrates is similar to the reported values at this substrate temperature, though neither a buffer layer nor high band gap *p*- type SiC layer is used in our case [15].

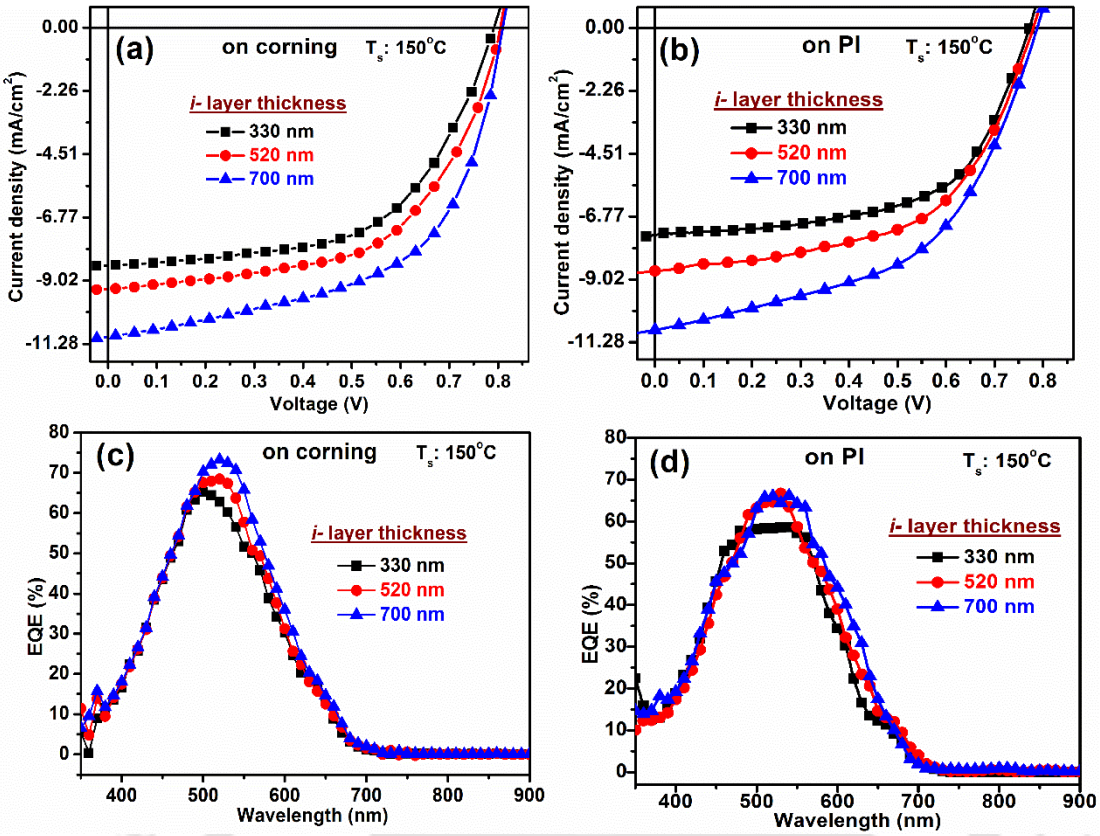

Figure 6.1*: Current density vs voltage characteristics of solar cell with different i- layer thickness on (a) Corning (b) polyimide substrate. External quantum efficiency of solar cells with different i- layer thickness is on (c) Corning (d) polyimide substrate.*

Table 6.3*: a-Si:H single junction solar cell parameters for different i-layer thickness on Corning, polyimide and photo paper substrates*

Thickness (nm)	V_{oc} (mV)			J_{sc} (mA/cm^2)			*FF*			Efficiency (%)		
	Corning	PI	PP	Corning	PI	PP	Corning	PI	PP	Corning	PI	PP
200	-	-	610	-	-	7.17	-	-	0.35	-	-	1.54
330	790	772	535	8.16	7.44	5.31	0.59	0.59	0.31	3.81	3.38	0.88
520	802	779	336	9.18	8.73	3.37	0.58	0.55	0.26	4.27	3.70	0.30
700	810	787	250	11.22	10.87	0.05	0.55	0.51	0.26	5.02	4.38	0.03

To further investigate the effect of *i*- layer thickness on solar cell properties, external quantum efficiency (*EQE*) was measured for all *a-Si:H* solar cells. Figure 6.1(c & d) show *EQE* spectra of the solar cells with different *i*- layer thickness on Corning and PI respectively. No change in *EQE* response is observed in the low wavelength region (λ<500 nm); however, the high wavelength response is enhanced with increasing thickness of *i*- layer, which also

indicates more absorption of photons due to higher thickness of the absorber layer. The V_{oc}, J_{sc}, *FF* and η(%) values for solar cells on different substrates are listed in Table 6.3.

The *J-V* characteristics for the cells fabricated on PP are shown in Figure 6.2(a). The best characteristics are obtained when the thickness of *i-* layer is reduced to 200 nm, with a photo conversion efficiency of 1.54%. The values of V_{oc}, J_{sc}, *FF* and η(%) for different *i-* layer thickness are listed in Table 6.3. As per our knowledge, for the first time we are reporting *a-Si:H* thin film based *n-i-p* solar cells on PP substrate. Both J_{sc} and V_{oc} values are found to be lower compared to cells on Corning and PI substrates. Also, for the cells fabricated on PP, the *J-V* characteristic deteriorates with increase in thickness of *i-* layer. The Spectroscopic Ellipsomery studies show that films on PP have lower amplitude factor *A* and higher broadening *C*, which corresponds to the relatively poor quality of these films (low density and high void fraction) as discussed in Chapter 3 (section 3.2.1.2). We have also observed that photocurrent decays much rapidly in case of films on PP as compared to those on Corning substrate (Appendix, Figure A2), which indicate that Steabler- Wronski (S-W) effect [1, 2] is more pronounced in these films on PP substrate. This could be the probable reason of decrease in efficiency of the cells (on PP) with increase in thickness of intrinsic (absorber) layer. S-W effect is more pronounced for *a-Si:H* films having higher concentration of weakly bonded Si-H_2 bonds and could also be a possible reason for lower J_{sc} and η values. These values may seem to be low at first glance; however, the results are encouraging as PP is a new substrate, which is not only cheap and flexible but also bio-compatible and eco-friendly.

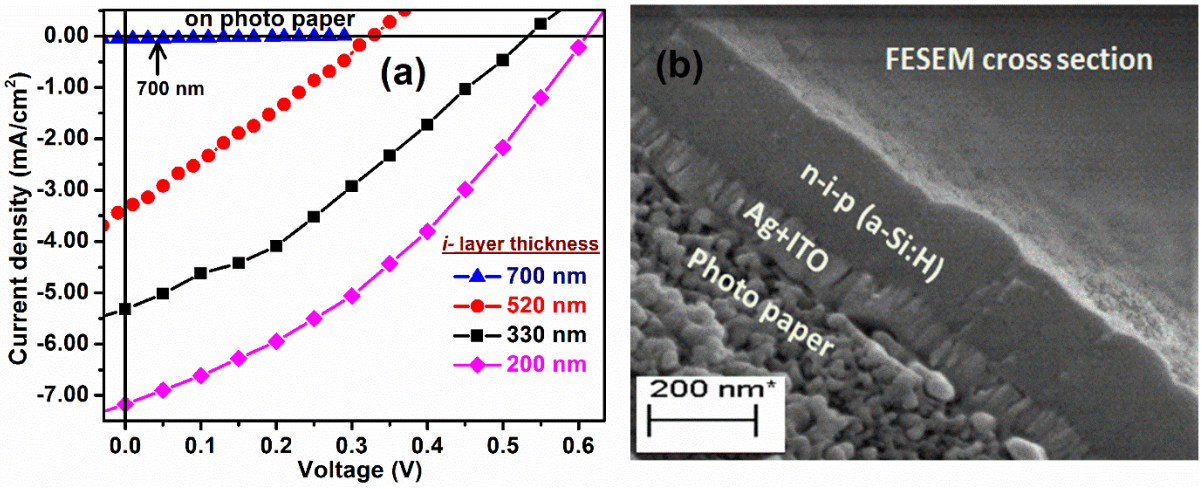

***Figure 6.2**: (a) Current density vs voltage characteristics of solar cell with different i- layer thickness on photo paper (b) FESEM cross section of i = 200 nm solar cell fabricated on photo paper.*

The FESEM cross section image of solar cell, with 200 nm thick *i*- layer, fabricated on PP is shown in Figure 6.2(b). From FESEM image, one can see that there are no pin-holes or crack in the solar cell.

The *FF* and thus the efficiency of the solar cells depend a lot on the series resistance (R_s) and shunt resistance (R_{sh}) of the device. In order to estimate the R_s and R_{sh} of the different cells, the slope of *J-V* curve near short circuit and open circuit points were calculated. The values of R_{sh} and R_s are listed in Table 6.4. It is clear from the Table 6.4 that R_s of the solar cells on PP is higher and shunt resistance is lower as compared to the corresponding values for the cells fabricated on Corning and PI substrates. The values are comparable for Corning and PI substrates. This also explains the relatively poor performance of the cells on PP substrates, whereas the performance of the cells on other two substrates is comparable.

Table 6.4*: Series and shunt resistances determined from J-V curve of solar cell for different i- layer thickness on Corning, polyimide and photo paper substrates*

Substrate	Thickness (nm)	Series resistance R_s (Ω-cm^2)	Shunt resistance R_{sh} (Ω-cm^2)
Corning	330	17.5	1113.63
	520	19.6	666.66
	700	18.14	375.47
PI	330	20.32	1032.78
	520	24.23	527.19
	700	19.6	267.75
PP	200	26.47	54.08
	330	28.26	45.27
	520	29.26	32.84
	700	1222.82	839.55

6.2.2 Influence of back reflector on solar cells (T_s: 110^{o}C)

In order to study the influence of back reflector on solar cells, ITO coated PET and ITO coated Corning transparent substrates are used to fabricate these cells. The deposition parameters used for fabrication of solar cells at T_s=110^{o}C are listed in Table 6.2. We have also used non transparent flexible PI and PP substrates for solar cell fabrication.

Figure 6.3(a) show the current density- voltage (*J-V*) characteristics of single junction *n-i-p* solar cells fabricated T_s at 110^{o}C on flexible PET, PI and rigid Corning substrate. The J_{sc} is found to be 6.94, 7.41, 7.82 mA/cm^2 for cells on PET, PI and Corning substrates respectively. A small increase in J_{sc} is observed when *Ag* is used as back reflector on PET and Corning

substrates. The V_{oc} is found to be 796, 782, 797 mV on PET, PI and Corning respectively. The V_{oc} for the solar cells are found to be nearly equal for all substrates. Fill factor (*FF*) of the cells on PET, PI, Corning substrates is found to be 0.58, 0.58 and 0.59 respectively and remain same with back reflector on PET and Corning substrates.

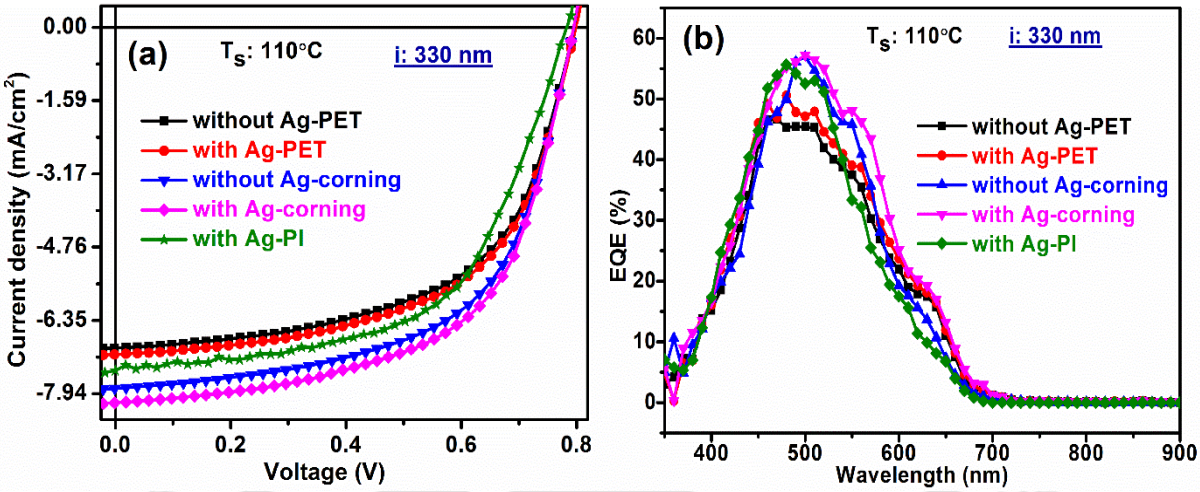

***Figure 6.3**: (a) Current density-voltage characteristics and (b) External quantum efficiency of solar cells deposited at 110 °C on PET, PI, and Corning substrates.*

Due to the back reflector, J_{sc} has slightly increased from 6.94 to 7.14 mA/cm^2 on PET, and from 7.82 to 7.94 mA/cm^2 on Corning resulting in an increase in efficiency (η) from 3.21 to 3.30% on PET and 3.70 to 3.82% on Corning respectively. Further, the J_{sc}, V_{oc}, *FF* and η (%) values on PET, PI and Corning substrates are comparable. Our solar cell results are comparable with other works reported at the same substrate temperature (110 °C) [16, 17]. The values of V_{oc}, J_{sc}, *FF* and η(%) for the cells fabricated on PET, PI and Corning substrates are listed in Table 6.5. In order to estimate the series resistance (R_s) and shunt resistance (R_{sh}) of these cells, the slope of *J-V* curve near short circuit and open circuit points were calculated. The values of R_s and R_{sh} are listed in Table 6.5. The values are comparable for cell on PET, Corning and PI substrates. Figure 6.3(b) shows *EQE* spectra of the solar cells on PET, Corning and PI respectively. The *EQE* for cells on PET and PI is slightly lower compared to cells on Corning substrates. Further, with back reflector, an increase in *EQE* is observed in the mid (450 - 550 nm) and long wavelength region (>550nm), which is also seen as an increase in J_{sc} for these cells with back reflector [18]. The increase is more for cells on PET as compared to that on Corning substrate. The *EQE* curve for different cells is well correlated with the corresponding *J-V* curve; higher *EQE* corresponds to higher J_{sc} value.

***Table 6.5**: The values of V_{oc}, J_{sc}, FF and efficiency of the cells fabricated on PET, PI, and Corning substrates (with and without (W/O) Ag)*

	Substrate	*i*-layer thickness (nm)	R_s (Ω-cm^2)	R_p (Ω-cm^2)	V_{oc} (mV)	J_{sc} (mA/cm^2)	*FF*	η (%)
W/O *Ag*	PET	330	19	1076	796	6.94	0.58	3.21
With *Ag*			19	1519	795	7.14	0.58	3.30
W/O *Ag*	Corning	330	17	989	797	7.82	0.59	3.70
With *Ag*			16	1058	794	7.94	0.59	3.82
With *Ag*	PI	330	25	984	782	7.41	0.58	3.36
With *Ag*	PP	330	27	46	533	5.63	0.31	0.96
		200	24	50	571	6.05	0.32	1.08

Figure 6.4 shows the *J-V* characteristics of the solar cells on PP substrates with two different *i*- layer thickness 330 and 200 nm. As per our knowledge, we are reporting for the first time *a-Si:H* thin film solar cells fabricated on PP at low T_s 110°C. The conversion efficiency of 0.96 and 1.08% correspond to 330 and 200 nm of *i*- layer thickness respectively. The values of V_{oc}, J_{sc}, *FF* and η (%) for these cells are listed in Table 6.5.

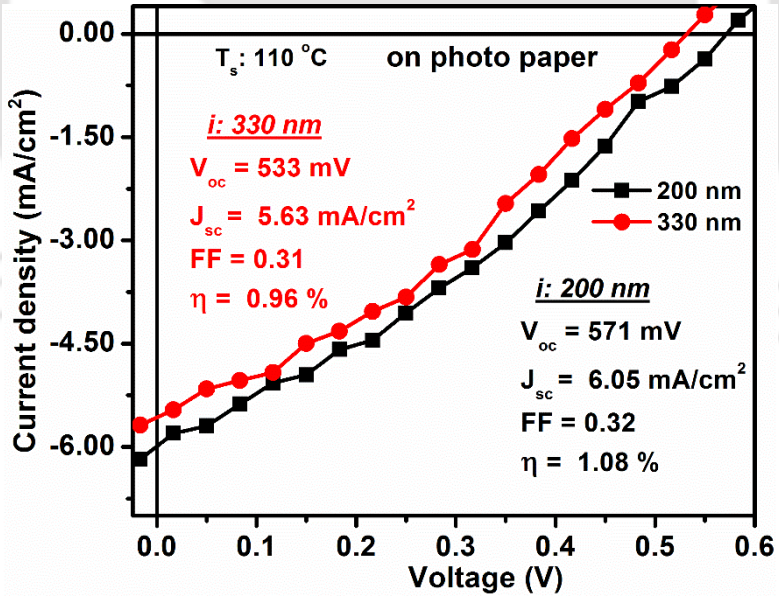

***Figure 6.4**: J-V characteristics of solar cell with different i-layer thickness (200nm, 330nm) on photo paper.*

The efficiency of these cells on PP substrates is lower than cells on PI, PET and Corning substrates due to significantly low shunt resistance and high series resistance (Table 6.5). This could be the possible reason for the lower value of J_{sc}, V_{oc} and *FF* for the cells on PP. It

is also observed that increase in *i*- layer thickness (200 to 330 nm) results in decrease in efficiency (1.08 to 0.96%) on photo paper substrate. There could be several reasons for the poor performance of the device with thick absorber layer, which include the S-W effect [2] and poor transport of photo-generated carriers to the respective electrodes due to drift and diffusion limited issues. It could also be a possible reason for lower J_{sc} and η values for solar cells on PP substrates.

6.2.3 Influence of H_2 plasma treatment (*HPT*) at interfaces and *a-SiC:H*(*p*) as window layer

We have fabricated *n-i-p* single junction solar cells at T_s ~ 150°C and110 °C under different conditions as follows; **case (i)**: *a-Si:H*(*p*) as a window layer without *HPT* at *n/i* and *i/p* interfaces; **case (ii)**: *a-Si:H*(*p*) as a window layer and with *HPT* at *n/i* and *i/p* interfaces; **case (iii)**: *a-SiC:H*(*p*) as a window layer along with *HPT* at *n/i* and *i/p* interfaces. The deposition parameters used for fabrication of solar cells are listed in Table 6.1 and Table 6.2.

Figure 6.5 (a & b) and Figure 6.6 (a-c) show the current density-voltage (*J-V*) characteristics of *n-i-p* solar cells fabricated on different substrates at T_s=150°C and T_s=110°C respectively. The parameters of the solar cells fabricated at T_s=150°C and T_s=110°C are listed in Table 6.6 and Table 6.7 respectively. It has been observed that, with the *HPT* treatment at *n/i* & *i/p* interface (Case (ii)) of the solar cell fabricated at 150°C and 110°C, the current density (J_{sc}) was slightly increased on PI and Corning substrate but there was no significant change in J_{sc} values in case of PET substrate (110°C). Further, in Case (iii), a small increase in J_{sc} was observed with *a-SiC:H*(*p*) as window layer along with *HPT* for solar cells on PET, PI and Corning substrates.

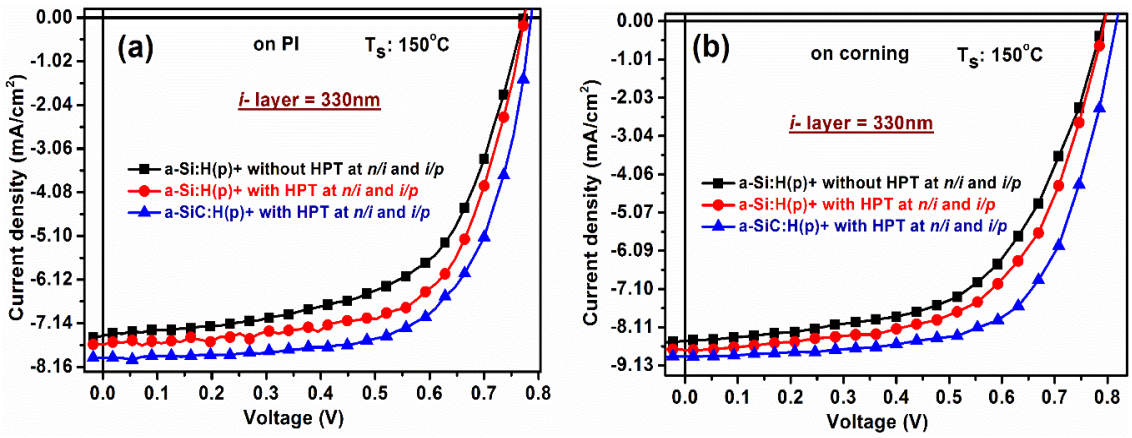

***Figure 6.5**: Current density vs voltage (J-V) characteristics of solar cells fabricated at T_s=150°C on (a) PI (b) Corning substrates.*

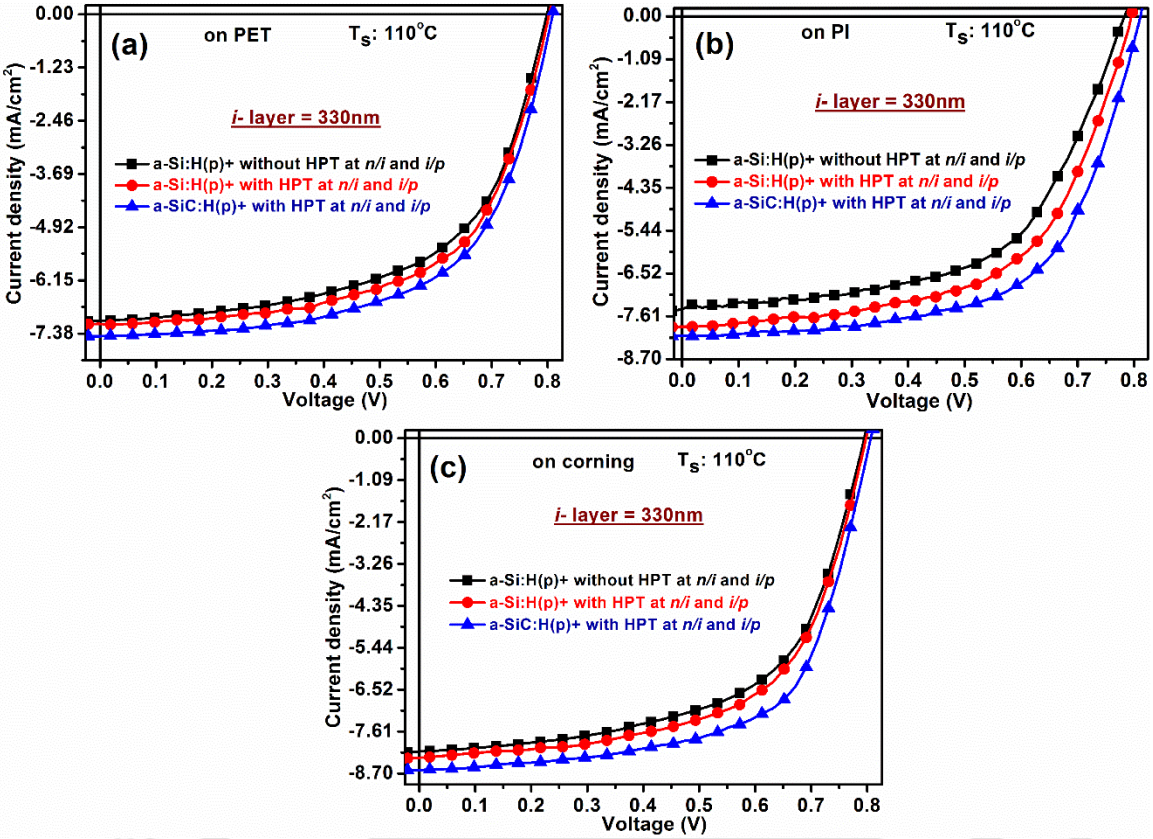

***Figure 6.6**: Current density vs voltage (J-V) characteristics of solar fabricated at T_s=110°C on (a) PET (b) PI (c) Corning substrates.*

The open circuit voltage (V_{oc}) for cell fabricated at T_s=150°C on PI and Corning and cells fabricated at T_s=110°C on PET and Corning substrate was not much influenced with *HPT* (case (ii)), whereas a significant improvement for solar cells at T_s=110°C on PI substrate was observed. The improvement in J_{sc} and V_{oc} with *HPT* at interfaces is due to surface passivation of unsaturated bonds with atomic hydrogen [19]. In case (iii), the V_{oc} of solar cells on PET, PI and Corning substrate has enhanced compared to V_{oc} of solar cells in case (i). The fill factor (*FF*) of the cells fabricated at 110°C on PET, PI and Corning are found to be equal and not affected by *HPT* at the interface, however a small increase in *FF* was observed for cells fabricated at 150°C on PI in case (ii). A small increase in *FF* was observed for cells fabricated at 150°C and 110°C in case (iii) for all the substrates. In order to estimate the R_s and R_{sh} of the solar cells, the slopes of *J-V* curve near short circuit and open circuit points were calculated. The R_{sh} and R_s were significantly improved in the solar cells on PI (T_s= 150°C and 110°C) and Corning (T_s=150°C) substrate with *HPT* at *n/i* and *i/p* interfaces. Whereas, no significant change in R_s value of solar cells were observed on PET and Corning substrates (T_s=110°C) after *HPT* (Case (ii)) though a slight increment in R_{sh} value was observed in this case. However, the R_s and R_{sh} values of solar cells on PET, PI and Corning

substrates had significantly improved in case (iii) as compared to case (i). Here, the efficiency of solar cells was clearly enhanced with *a-SiC:H*(*p*) as a window layer with *HPT* at interfaces. Our solar cell results are very close to the values reported in literature for amorphous silicon based solar cells fabricated at low T_s [12, 15, 17, 20-23].

***Table 6.6**: Single junction n-i-p solar cell parameters for T_s at 150^{o}C on PI and Corning substrates*

	Substrate	R_s (Ω-cm^2)	R_{sh} (Ω-cm^2)	V_{oc} (mV)	J_{sc} (mA/cm^2)	*FF*	η (%)
a-Si:H(*p*) as *p*-layer + without *HPT* at *n/i* & *i/p* interface	PI	20.32	1032.78	772	7.44	0.59	3.38
	Corning	17.50	1113.63	790	8.16	0.59	3.81
a-Si:H(*p*) as *p*-layer + with *HPT* at *n/i* & *i/p* interface	PI	14.43	2226.18	776	7.65	0.64	3.80
	Corning	16.69	2222.22	795	8.72	0.59	4.01
a-SiC:H(*p*) as *p*-layer + with *HPT* at *n/i* & *i/p* interface	PI	9.33	2520.00	795	7.94	0.66	4.15
	Corning	13.06	2921.01	818	8.93	0.65	4.76

***Table 6.7**: Single junction n-i-p solar cell parameters for T_s at 110^{o}C on PET, PI and Corning substrates*

	Substrate	R_s (Ω-cm^2)	R_{sh} (Ω-cm^2)	V_{oc} (mV)	J_{sc} (mA/cm^2)	*FF*	η (%)
a-Si:H(*p*) as *p*-layer + without *HPT* at *n/i* & *i/p* interface	PET	19.68	1519.9	795	7.14	0.58	3.30
	PI	25.35	984.37	782	7.41	0.58	3.36
	Corning	16.91	1058.82	794	7.94	0.59	3.82
*a-Si:*H(*p*) as *p*-layer + with *HPT* at *n/i* & *i/p* interface	PET	18.08	1344	801	7.16	0.6	3.48
	PI	19.78	1460.02	796	7.88	0.58	3.64
	Corning	16.32	1565.21	798	8.29	0.61	4.00
a-SiC:H(*p*) as *p*-layer + with *HPT* at *n/i* & *i/p* interface	PET	15.53	2183.71	809	7.44	0.61	3.66
	PI	18.86	1869.43	811	7.94	0.63	4.06
	Corning	15.54	2146.5	810	8.61	0.62	4.27

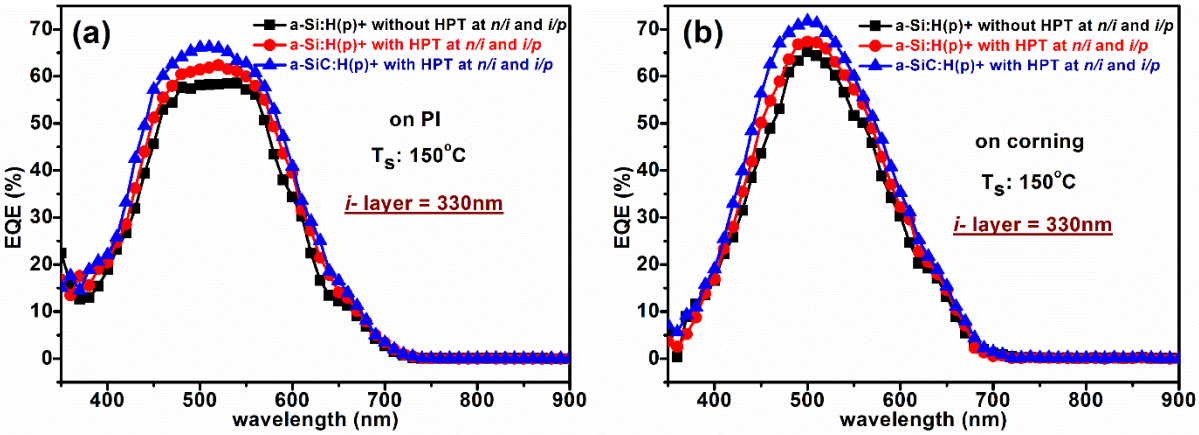

***Figure 6.7**: External quantum efficiency of solar cell fabricated at T_s=150°C on (a) PI (b) Corning substrates*

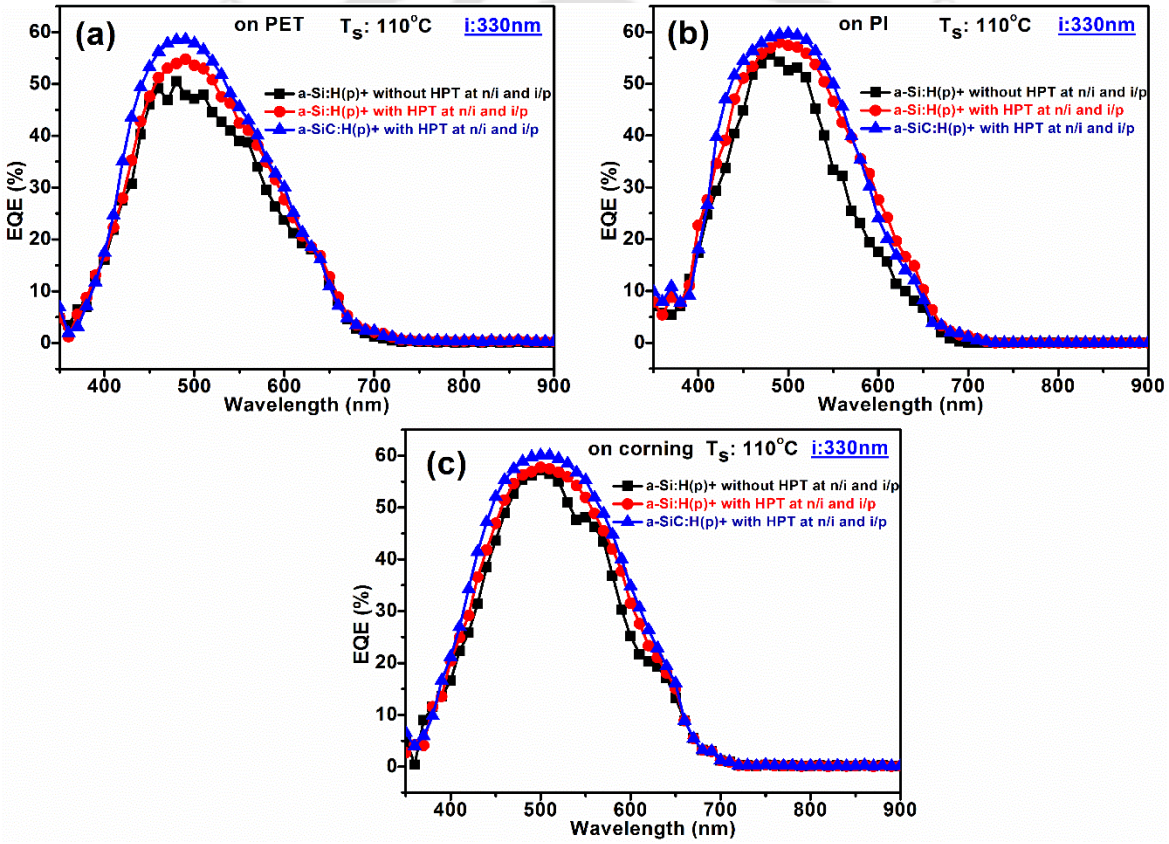

***Figure 6.8**: External quantum efficiency of solar cells fabricated at T_s=110°C on (a) PET (b) PI (c) Corning substrates.*

To further investigate the effect of *HPT* at interfaces and *a-SiC:H*(*p*) window layer on solar cell performance, external quantum efficiency (*EQE*) was measured for all *a-Si:H* solar cells. Figure 6.7 (a & b), Figure 6.8 (a-c) show *EQE* spectra of of *n-i-p* solar cells fabricated on different substrates at T_s=150°C and T_s=110°C respectively. It was observed that after *HPT*

treatment (Case (ii)), the *EQE* spectra of solar cells on PET, PI and Corning substrates remained identical in the low wavelength region 350-430 nm and long wavelength region (> 650 nm) however in the wavelength range of 450-640 nm, a gradual increase in *EQE* response was observed for all the substrates. The increase in *EQE* values in the wavelength range of 450-640 nm is attributed to the change in sub-layers after *HPT*, which results in improvement in performance of the cells on PET, PI and Corning substrates. The sub-layer formed with the *HPT* acts as a buffer layer, which has a lower defect density and improves the interface properties. In case (iii), with *a-SiC:H*(*p*) as window layer, additional improvement in *EQE* is observed in the wavelength region (430-550 nm) due to wider band gap of the window layer, which allows the transmission of photons through *p*- layer which are later absorbed in *i*- layer. In the wavelength region >600 nm, no change in *EQE* response was observed in cells on PET, PI and Corning substrates. The improvement in *EQE* is reflected as increase in J_{sc} of the solar cells.

6.3 Conclusion:

Influence of *i*- layer thickness on solar cell (T_s: 150°C): In this case, influence of *i*- layer thickness on solar cell efficiency was studied. The values of V_{oc}, J_{sc}, *FF* and η (%) for solar cells fabricated on flexible PI substrate are similar to those on conventional Corning substrate. We have observed that with increase in *i*- layer thickness, η (%) was increased due to more absorption of photons in the cells on Corning and PI substrates. Whereas for solar cells fabricated on PP, best cell efficiency (1.54 %) are obtained for lower thickness (200 nm) of *i*- layer, due to the S-W effect being dominant as compared to cells fabricated on PI and Corning substrates.

Influence of back reflector on solar cells (T_s: 110°C): In this study, solar cells (*n-i-p*) were fabricated on a number of substrates including Corning as well as flexible PET, PI and PP at low substrate temperature of 110°C. A small increase in J_{sc} was observed when *Ag* is used as back reflector on PET and Corning substrates, which was also observed as an improvement in in *EQE* in the mid and long wavelength region. The performances of solar cells on Corning, PI and PET substrates are comparable and show promising results with significant amount of cell efficiency. Whereas for solar cells fabricated on PP, best cell efficiency (1.08 %) are obtained for lower thickness (200 nm) of *i*- layer, due to the much lower carrier diffusion length as compared to those fabricated with higher thickness (330 nm) of *i*- layer. The study show that PP could also be a potential flexible substrate for the fabrication of

cheap silicon based solar cell. We believe that with further optimization of deposition parameters, it is possible to increase the efficiency of *a-Si:H* based solar cells on photo paper at a low substrate temperature.

Influence of H_2 plasma treatment at interfaces and *a-SiC:H*(*p*) as window layer: In this study, the influence *HPT* at *n/i* and *i/p* interface layers along with *a-SiC:H*(*p*) as window layer on performance of solar cells has been investigated. The performance of *n-i-p* solar cells on flexible PET, PI and rigid Corning substrate was slightly improved after *HPT*, before the deposition of *i*- layer and *a-Si:H*(*p*) layer due to improvement of *n/i* and *i/p* interface layer. The performance was further improved when *a-Si:H*(*p*) was replaced with *a-SiC:H*(*p*) layer which also acts as window layer. Our results point out the importance of wide band gap *a-SiC:H*(*p*) as window layer along with *HPT* at the interfaces for better performance of the solar cells.

6.4 References

[1] A. Kolodziej, Staebler-Wronski effect in amorphous silicon and its alloys, *Opto-Electron Rev*, **12** (2004) 21-32.

[2] D.L. Staebler, C.R. Wronski, Reversible conductivity changes in discharge-produced amorphous Si, *Applied Physics Letters*, **31** (1977) 292-294.

[3] P. Chaudhuri, S. Ray, A.K. Batabyal, A.K. Barua, Thickness dependence of light-induced effects in a-Si solar cells, *Solar Cells*, **31** (1991) 13-21.

[4] L. Zhang, W. Guo, W. Liu, J. Bao, J. Liu, J. Shi, F. Meng, Z. Liu, Investigation of positive roles of hydrogen plasma treatment for interface passivation based on silicon heterojunction solar cells, *Journal of Physics D: Applied Physics*, **49** (2016) 165305.

[5] M. Mews, T.F. Schulze, N. Mingirulli, L. Korte, Hydrogen plasma treatments for passivation of amorphous-crystalline silicon-heterojunctions on surfaces promoting epitaxy, *Applied Physics Letters*, **102** (2013) 122106.

[6] S.N. Agbo, J. Krč, R.A.C.M.M. van Swaaij, M. Zeman, Optimization of the p–i interface properties in thin film microcrystalline silicon solar cell, *Solar Energy Materials and Solar Cells*, **94** (2010) 1864-1868.

[7] L. Bai, B. Liu, J. Zhao, S. Suo, G. Hou, D. Zhang, J. Sun, C. Wei, Y. Zhao, X. Zhang, Mechanism insight into the effect of I/P buffer layer on the performance of NIP-type hydrogenated microcrystalline silicon solar cells, *Journal of Applied Physics*, **117** (2015) 175309.

[8] H. Xiao, X. Zeng, X. Xie, P. Yang, W. Peng, S. Liu, W. Yao, X. Liao, Y. Zuo, Q. Wang, Improvement of microcrystalline silicon N-I-P solar cell by hydrogen plasma treatment for n/i interface, 37th IEEE photovoltaic Specilists Conference DOI: 10.1109/pvsc.2011.6186048 (2011) 000693-000695.

[9] M.I. Kabir, S.A. Shahahmadi, V. Lim, S. Zaidi, K. Sopian, N. Amin, Amorphous Silicon Single-Junction Thin-Film Solar Cell Exceeding 10%Efficiency by Design Optimization, *International Journal of Photoenergy*, **2012** (2012) 1-7.

[10] B. Yan, G. Yue, J. Yang, A. Banerjee, S. Guha, Hydrogenated microcrystalline silicon single junction and multi junction solar cells, *Mat. Res. Soc. Symp. Proc.*, **762** (2003) A41.41-A44.41.12.

[11] C.-H. Hsu, I.-C. Hsieh, C.-C. Tsou, S.-Y. Lien, Simulation and Experimental Study of Photogeneration and Recombination in Amorphous-Like Silicon Thin Films Deposited by 27.12 MHz Plasma-Enhanced Chemical Vapor Deposition, *International Journal of Photoenergy*, **2013** (2013) 1-6.

[12] M. Brinza, J.K. Rath, R.E.I. Schropp, Thin film silicon n–i–p solar cells deposited by VHF PECVD at 100°C substrate temperature, *Solar Energy Materials and Solar Cells*, **93** (2009) 680-683.

[13] K.-H. Kim, S. Kasouit, E.V. Johnson, P. Roca i Cabarrocas, Substrate versus superstrate configuration for stable thin film silicon solar cells, *Solar Energy Materials and Solar Cells*, **119** (2013) 124-128.

[14] K. Tao, J. Wang, H. Cai, D. Zhang, Y. Sui, Y. Zhang, Y. Sun, Low-temperature preparation of flexible a-Si:H solar cells with hydrogenated nanocrystalline silicon p layer, *Vacuum*, **86** (2012) 1477-1481.

[15] J. Wang, K. Tao, H. Cai, D. Zhang, G. Li, A study of the i/p interface for flexible n–i–p a-Si:H thin film solar cells, *Materials Science in Semiconductor Processing*, **25** (2014) 186-189.

[16] Y. Ishikawa, M.B. Schubert, Flexible protocrystalline silicon solar cells with amorphous buffer layer, *Jpn J Appl Phys* 1, **45** (2006) 6812-6822.

[17] J. Ni, J. Zhang, Y. Cao, X. Wang, X. Chen, X. Geng, Y. Zhao, Low temperature deposition of high open-circuit voltage (>1.0V) p–i–n type amorphous silicon solar cells, *Solar Energy Materials and Solar Cells*, **95** (2011) 1922-1926.

[18] G. Tao, B.S. Girwar, G.E.N. Landweer, M. Zeman, J.W. Metselaar, Enhanced Light Absorption in a-Si:H Layers of Solar Cells by Applying Tco/Metal Back Contacts, *MRS Proceedings*, **297** (1993) 845.

[19] C. Shin, J. Park, J. Jung, S. Bong, S. Kim, Y.-J. Lee, J. Yi, Control of micro void fraction and optical band gap in intrinsic amorphous silicon thin films (VHF-PECVD) for thin film solar cell application, *Materials Research Bulletin*, **60** (2014) 895-899.

[20] T. Söderström, F.J. Haug, V. Terrazzoni-Daudrix, C. Ballif, Optimization of amorphous silicon thin film solar cells for flexible photovoltaics, *Journal of Applied Physics*, **103** (2008) 114509.

[21] S.A. Filonovich, P. Alpuim, L. Rebouta, J.E. Bourée, Y.M. Soro, Hydrogenated amorphous and nanocrystalline silicon solar cells deposited by HWCVD and RF-PECVD on plastic substrates at 150°C, *J Non-Cryst Solids*, **354** (2008) 2376-2380.

[22] H. Cai, D. Zhang, Y. Xue, K. Tao, Study on diffusion barrier layer of silicon-based thin-film solar cells on polyimide substrate, *Solar Energy Materials and Solar Cells*, **93** (2009) 1959-1962.

[23] Y. Vygranenko, E. Fathi, A. Sazonov, M. Vieira, A. Nathan, Nanocrystalline p-layer for a-Si:H p-i-n solar cells and photodiodes, *Solar Energy Materials and Solar Cells*, **94** (2010) 1860-1863.

Chapter 7

Conclusion and Future Scope

The aim of the work presented in this thesis was to fabricate amorphous silicon solar cells on flexible substrates. For the device fabrication, we have studied the influence of different deposition parameters on the microstructural and optoelectronic properties of each layer. Solar cells were fabricated on flexible (Polyimide, PET and photo paper) and rigid corning 1737 glass substrates using individual layer deposition parameters corresponding to device quality films for the intrinsic and doped amorphous silicon films. We have achieved a few new results, which are not reported in literature prior to this work. The overall conclusion of the thesis work and future research scopes are given in the following sections.

7.1 Thesis conclusion

- The effect of substrate temperature (T_s) on microstructure and optoelectronic properties of the intrinsic *a-Si:H* films deposited on rigid Corning, flexible PI and PP substrates is studied. The formation of nanocrystallites started in amorphous matrix at around T_s=130 ^{o}C and it was further increased with increase in T_s irrespective of the substrate. With increase in T_s, an improvement in the SRO and less broadening in $<\varepsilon_2>$ was observed from Raman and ellipsometry measurements. The films deposited at high T_s ($\geq$ 150 ^{o}C) exhibit a high photosensitivity (~ 6 orders of magnitude) at room temperature.
- Influence of variation in H_2 flow rate during SiH_4 plasma on microstructure and optoelectronic properties of the intrinsic *a-Si:H* films, deposited on Corning, and PP substrates at T_s = 150^{o}C, is studied. The formation of nanocrystallites took place in the amorphous film on both the substrates irrespective of HFR. The crystallite size calculated from Raman spectroscopy was found to increase with increase in HFR. SE studies showed that, $<\varepsilon_2>_{max}$ shifted towards high energy side with increase in HFR due to presence of nanocrystallites in the film. The thickness of the film has decreased at higher HFR as atomic H lead to excessive etching and breaking of weak Si–Si bonds. FTIR studies showed the hydrogen content is in the range of ~ 8.97±0.44-

10.78±0.53 atomic %. These films are found to possess good photo sensitivity (~6 orders of magnitude).

- Influence of variation of rf power during silane plasma on microstructure and optoelectronic properties of the intrinsic *a-Si:H* films, deposited on Corning, and PP substrates at T_s = 110 ^{o}C, is studied. Raman and spectroscopic ellipsometry show that films are purely amorphous irrespective of rf power. In FESEM images, a rough microstructure is seen for films on PP, whereas film on Corning seems to be very smooth. The films deposited at rf power of 50 W on Corning, and 40 W on PP possess device grade quality; improvement in the SRO, less broadening in $<\varepsilon_2>$, lesser Si-H_2 fraction and good photosensitivity (σ_{ph}/σ_d) ~ 4 orders of magnitude in these films.
- Influence of rf power on microstructure and optoelectronic properties of the *a-Si:H*(*p*) films deposited at T_s = 110 ^{o}C, is studied. Raman and spectroscopic ellipsometry results show that films are purely amorphous structure irrespective of rf power. The films deposited at rf power of 60 W possess device grade quality; improvement in the SRO, less broadening in $<\varepsilon_2>$, lesser Si-H_2 fraction. The dark conductivity of *a-Si:H*(*p*) films show more than 4 orders of magnitude increase from that of intrinsic *a-Si:H* films. These results suggest that films are doped efficiently by adding diborane during deposition.
- Effect of *MFR* on structural and optoelectronic properties of *a-SiC:H*(*p*) films is studied. Thin films deposited at different *MFR* are amorphous in nature as confirmed by Raman spectroscopy measurements and also supported by the SE measurements. The mass density of film decreases with increase in the carbon content due to increase in void density at higher *MFR*. The FTIR results show hydrogen bonded to Si decreases due to etching of hydrogen atoms and replacement of weak Si-H bonds with Si-C. The bond densities Si-C and C-H ($N_{Si\text{-}C}$ and $N_{C\text{-}H}$), increase steadily with the increase in CH_4 flow rate. Films deposited at *MFR*=1 sccm was found to be suitable for solar cell fabrication due to its less broadening in $<\varepsilon_2>$, low SRO, MRO and lower densities of Si-C and C-H bonds.
- Structural and optoelectronic properties of *a-Si:H*(*n*) films were studied with variation in T_s (90-150^{o}C). Raman and SE results confirmed that all the deposited films are amorphous in nature irrespective of variation in T_s. The dark conductivity of *a-Si:H*(*n*) films showed more than 6 orders of magnitude increase as compared to that of intrinsic *a-Si:H* films. These results suggest that films are doped efficiently by adding

phosphine during deposition. The activation energy of the T_s=150^{o}C film was 0.33eV, suggesting that Fermi level is closer to conduction band for these phosphorus doped films.

- Influence of process pressure on microstructure and optoelectronic properties of the *ITO* films studied. The XRD results show that (222) plane is most preferred orientation, though other planes are also present in the film indicating polycrystalline structure. UV-Vis-NIR show all *ITO* films are highly transparent (>85%) and maximum % transmission is very close to bare Corning glass substrate. Thicknesses of the films decreases with increase in the process pressure due to the decrease in mean free path of sputtered atoms. The resistivity decreases with increase in the pressure and lowest sheet resistance (~11.6 Ω/□) was found for the film deposited at 0.054 mbar.
- Influence of Ar flow rate variation on microstructure and optoelectronic properties of the *ITO* films is studied. The XRD results show that (222) plane is most preferred orientation though other planes are also present in the film indicating polycrystalline structure. UV-Vis-NIR show all *ITO* films are highly transparent (>85%) and maximum % transmission is not influenced by variation in Ar flow rate. The lowest values of resistivity (3×10^{-4} Ω-cm) and sheet resistance (~9.75 Ω/□)) are found to be for film deposited at 7 sccm.
- Influence of *i*- layer thickness on solar cell efficiency was studied. The values of V_{oc}, J_{sc}, *FF* and η (%) fabricated solar cells on flexible PI substrate are similar to those on conventional Corning substrate. We have observed that with increase in *i*- layer thickness, η (%) was increased due to more absorption of photons in the cells on Corning and PI substrates. Whereas in the solar cells fabricated on PP, best cell efficiency (1.54 %) are obtained for lower thickness (200 nm) of *i*- layer due to the S-W effect being dominant as compared to cells fabricated on PI and Corning substrates.
- Solar cells (*n*-*i*-*p*) were fabricated on a number of substrates including Corning as well as flexible PET, PI and PP at low substrate temperature of 110^{o}C. A small increase in J_{sc} was observed when *Ag* is used as back reflector on PET and Corning substrates, which was also observed as an improvement in in *EQE* in the mid and long wavelength region. The performances of solar cells on Corning, PI and PET substrates are comparable and show promising results with significant amount of cell efficiency.

Whereas for solar cells fabricated on PP, best cell efficiency (1.08 %) are obtained for lower thickness (200 nm) of *i*- layer, due to the much lower carrier diffusion length as compared to those fabricated with higher thickness (330 nm) of *i*- layer. The study show that PP could also be a potential flexible substrate for the fabrication of cheap silicon based solar cell. We believe that with further optimization of deposition parameters, it is possible to increase the efficiency of *a-Si:H* based solar cells on photo paper at a low substrate temperature.

- The influence *HPT* at *n/i* and *i/p* interface layers along with *a-SiC:H*(*p*) as window layer on performance of solar cells has been investigated. The performance of *n-i-p* solar cells on flexible PET, PI and rigid Corning substrate was slightly improved after *HPT*, before the deposition of *i*- layer and *a-Si:H*(*p*) layer due to improvement of *n/i* and *i/p* interface layer. The performance was further improved when *a-Si:H*(*p*) was replaced with *a-SiC:H*(*p*) layer which also acts as window layer. Our results point out the importance of wide band gap *a-SiC:H*(*p*) as window layer along with *HPT* at the interfaces for better performance of the solar cells.

7.2 Scope for future work

Some of the future research scopes based on the present thesis could be followings:

- Since we are not able to deposit nanocrystallites embedded *a-Si:H* films at $T_s \leq 110^oC$, a few additional changes in deposition parameters such as H_2 dilution, process pressure etc. could also be tried to see their effect on structural and optoelectronic properties of *a-Si:H* films at low T_s.
- Solar cells fabricated on photo paper show low efficiency in comparison to those fabricated on PET, PI and Corning substrates. However, a deep instigation is required to find out the actual cause of this behavior.
- Texturing of the ITO can improve the light travelling path in with the solar cell to increase the efficiency of the cell.
- The ultimate aim is to fabricate multi junction solar cells on flexible substrates to achieve better device performance.

Appendix

Atomic force microscopy (AFM):

The AFM measurements were performed on bare Corning 1737 glass (corning), polyimide (PI) and photo paper (PP) substrates. Figure A1 (a-c) show the 2D images of bare corning, PI and PP substrates respectively. The root mean square (RMS) roughness values are estimated to be 0.28 nm, 0.83 nm and 6.56 nm for corning, PI and PP substrates respectively.

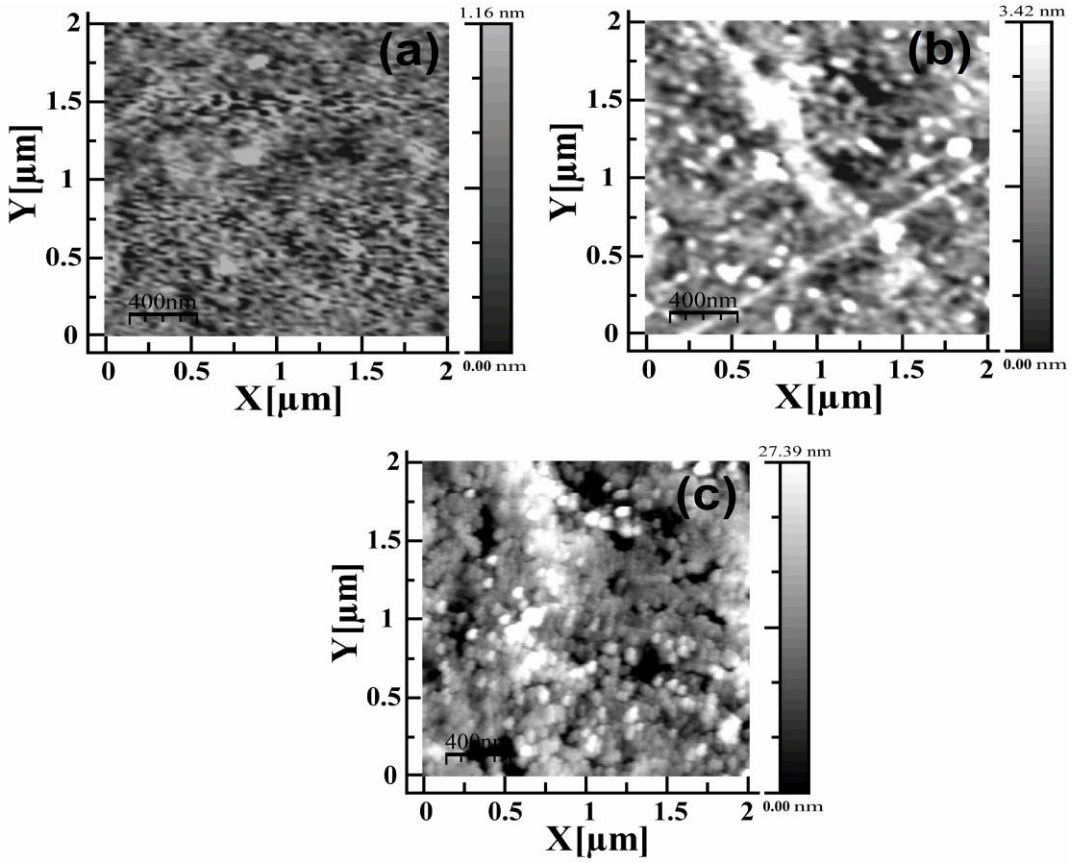

Figure 1A: *2- dimensional AFM surface morphologies of bare (a) corning 1737 glass (b) polyimide and (c) photo paper substrates respectively.*

Photocurrent decay:

The photo current decay of *a-Si:H* thin film (T_s=150^{o}C) on corning, PI and PP is shown in Figure A2. The photocurrent decays much rapidly in case of films on PP (for films on Corning, the decay is very slow), which indicate that S-W effect [1] is more pronounced on these films.

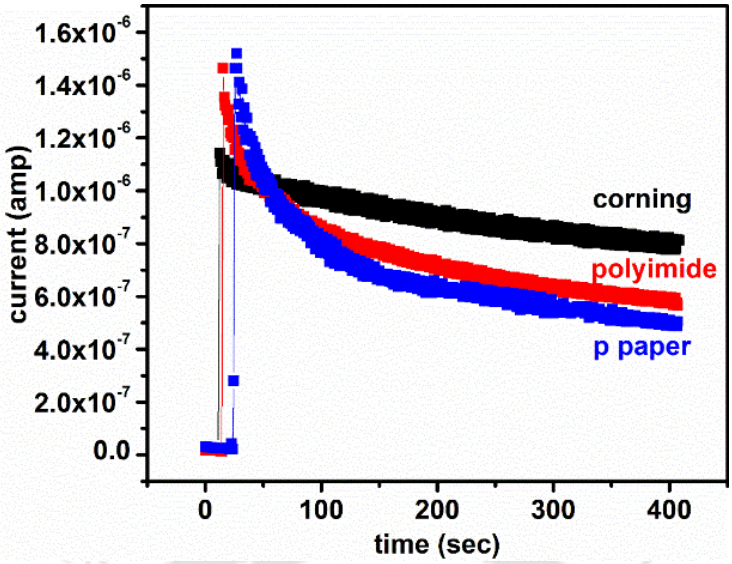

***Figure A2**: photo current decay of a-Si:H thin film (T_s = 150^{o}C) on Corning, polyimide and photo paper substrates.*

Reference

[1] Staebler. D. L, Wronski C. R. Reversible conductivity changes in discharge produced amorphous Si, *Applied Physics Letters* **31** (1977) 292.

List of publications

*1 **Ramakrishna Madaka**, Venkanna Kanneboina, Pratima Agarwal, "Exploring the photo paper as flexible substrate for fabrication of a-Si:H based thin film solar cells at low temperature (110°C) and influence of rf-power on opto-electronic properties" ***Thin Solid Films*** 662 (2018) 154-165.

*2 **Ramakrishna Madaka**, Venkanna Kanneboina, Pratima Agarwal, "Enhancement in performance of amorphous silicon solar cells (110°C) on flexible substrates with p-a-SiC:H window layer and H_2 plasma treatment at n/i and i/p interface" ***Semiconductor Science and Technology*** 33 (2018) 085009.

*3 **Ramakrishna Madaka**, Venkanna Kanneboina, Pratima Agarwal, "Low temperature growth of amorphous silicon films and direct fabrication of solar cells on flexible polyimide and photo paper substrate" ***Journal of electronic materials*** 47 (2018) 4710-4720.

*4 **Ramakrishna Madaka**, Venkanna Kanneboina, Pratima Agarwal, "Evolution of nanostructure in hydrogenated amorphous silicon thin films with substrate temperature studied by Raman mapping, Ramanscattering and spectroscopic ellipsometry" ***Journal of material science: materials in electronics*** (2017) 28:8885-8894.

*5 **Ramakrishna Madaka**, Juhi Kumari, Venkanna Kanneboina, Pratima Agarwal, "Hydrogenated amorphous silicon solar cells fabricated at low substrate temperature 110ºC on flexible PET substrate" ***AIP Conf. proc.*** **1953** (2018) 100040.

*6 **Ramakrishna Madaka**, Venkanna Kanneboina, Pratima Agarwal, "Raman and spectroscopic ellipsometry studies of a-Si:H thin films on low-cost photo paper substrate" ***Materials Today: Proceedings*** **4** (2017) 12666–12670.

*7 **Ramakrishna Madaka**, Pilik Basumatary, Venkanna Kanneboina, Pratima Agarwal, "Amorphous silicon thin film solar cells fabricated on different substrates", ***Springer journal Conf. Proc***. (Accepted)

*8 **Ramakrishna Madaka**, Venkanna Kanneboina, Pilik Basumatary, Pratima Agarwal, "Influence of radio frequency power on opto-electronic properties of boron doped hydrogenated amorphous silicon films at low substrate temperature 110^{o}C". ***Springer journal Conf. Proc***. (Accepted)

9 **Ramakrishna Madaka**, Juhi K, Venkanna K, H S Jha, Pratima Agarwal "Role of chamber pressure on crystallinity and composition of silicon films using silane and methane as precursors in HWCVD technique. ***Thin Solid Films*** (Submitted)

10 **Ramakrishna Madaka**, Juhi kumari, Pilik Basumatary, Pratima Agarwal "Annealing effects on hydrogenated amorphous silicon based thin film transistors (Manuscript under preparation)

11 Venkanna Kanneboina, **Ramakrishna Madaka**, Pratima Agarwal, "High open circuit voltage c-Si/a-Si:H hetrojunction solar cells: Influence of hydrogen plasma treatment studied by spectroscopic ellipsometry" ***Solar energy*** **166** (2018) 255–266.

12 Venkanna Kanneboina, **Ramakrishna Madaka**, Pratima Agarwal, "Spectroscopic ellipsometry studies on microstructure evolution of a-Si:H to nc-Si:H films by H_2 plasma exposure" ***Materials Today Communication*** **15** (2018) 18–29.

13 Venkanna Kanneboina, **Ramakrishna Madaka**, Pratima Agarwal, "Influence of hydrogen plasma treatment of intrinsic a-Si:H layer on the performance of the c-Si/a-Si:H hetro junction solar cells" ***Materials Today: Proceedings*** **4** (2017) 12726–12729.

14 Venkanna Kanneboina, **Ramakrishna Madaka** and Pratima Agarwal "Spectroscopic Ellipsometry Investigation of Optical and Structural Properties of a-Si:H Thin Films" ***Springer Conf. Proc.*** (Accepted).

15 Venkanna Kanneboina, **Ramakrishna Madaka** and Pratima Agarwal "Single side c-Si/a-Si:H heterojunction solar cells with high open circuit voltage of 705 mV and 17.3% efficiency: Role of a-Si:H (p) layer doping and thickness" ***Solar Energy.*** (Under review).

16 Lalhriat Zuala**, Ramakrishna** and PratimaAgarwal, "Structural, optical and electrical characterization of CdSe nanorods synthesized by solvothermal process, ***Conference papers in Energy***, Volume 2013 (2013), DOI: 10.1155/2013/257359.

17 Lalhriat Zuala**, Ramakrishna** and PratimaAgarwal , " Effect of substrate temperature on the thermal and optical properties of CdTe films prepared by thermal evaporation", ***17th International workshop in the Physics of semiconductor devices***, DOI: 10.1007/978-3-319-03002-9.

* related to this thesis work

List of papers presented in International/National conferences

1. **Ramakrishna Madaka**, AshaYadav, Venkanna Kanneboina and Pratima Agarwal, "Comparison of electrical conductivity of a-Si:H films deposited on flexible

polyimide and corning glass substrate", TransLES 2014, IASST Guwahati, 11-13th December 2014. Abstract book pp: 102.

2. **Ramakrishna Madaka**, AshaYadav, Venkanna Kanneboina and PratimaAgarwal, "Electrical and structural properties of a-Si:H on flexible substrates", Reflux 2015-annual symposium , IIT Guwahati, 27-29th March 2015. Abstract book pp: 56.

3. **Ramakrishna Madaka,** V. Kanneboina, Pratima Agarwal, "Hydrogenated amorphous and nanocrystalline silicon thin films deposited on paper substrate by rf-PECVD technique" 4thInternational Conference on Advanced nanomaterials and Nanotechnology (ICANN-2015), IIT Guwahati, 8-12th December 2015. Abstract book pp: 32.

4. **Ramakrishna Madaka,** Venkanna Kanneboina, Pratima Agarwal, "Hydrogenated amorphous silicon based thin film solar cells on flexible solar cells", Departmental Annual Day, Department of Physics, IIT Guwahati , 12th March 2016.

5. **Ramakrishna Madaka,** V. Kanneboina, Pratima Agarwal, "Hydrogenated amorphous silicon based thin film solar cells on flexible substrate", Research Conclave'16, IIT Guwahati, 17-20th March 2016.

6. **Ramakrishna Madaka**, V.Kanneboina, Pratima Agarwal**, "**Hydrogenated amorphous silicon solar cells on low cost photo paper" 2nd International conference on solar energy photovoltaic (ICSEP-2016), KIIT university, Odisha, India 17-19th Dec 2016. Abstract book pp:19.

7. **Ramakrishna Madaka**, V.Kanneboina, Pratima Agarwal**,"** Hydrogenated amorphous silicon solar cells on low cost photo paper and flexible substrates" Annual Physics meet, 2nd department day physics, IIT Guwahati, 28th January 2017.

8. **Ramakrishna Madaka**, Pilik Basumatary, Pratima Agarwal**,"** Study of Morphological Evolution In Hydrogenated Amorphous Silicon (a-Si:H) Thin Films By Atomic Force Microscopy", UGC-SAP (DRS II) sponsored national conference on hard and soft condensed matter physics, Tezpur university, Tezpur, Assam, India, 2-4th March 2017. Abstract book pp: 79.

9. **Ramakrishna Madaka**, V.Kanneboina, Pratima Agarwal,"Hydrogenated amorphous silicon (a-Si:H) thin film solar cells on flexible substrates" Research conclave, IIT

Guwahati, Guwahati, India, 16-19th March 2017. Abstract book pp: 216. **(Awarded for Best poster)**

10. **Ramakrishna Madaka**, Asha.Y, V.Kanneboina, Pilik Basumatary, Pratima Agarwal, "Evolution of nanostructure in hydrogenated amorphous silicon thin films with substrate temperature studied by Raman mapping, Ramanscattering and spectroscopic ellipsometry" UGC-SAP(DRSIII) sponsored national seminar on advanced materials science, Guwahati, India 24-25th March 2017. Abstract book pp: 36.

11. **Ramakrishna Madaka**, V.Kanneboina, Pratima Agarwal, "Raman mapping and Raman scattering studies to understand the Evolution of nanostructure in a-Si:H films deposited at different temperature" International Conference on Sophisticated Instruments in Modern Research (ICSIMR-2017)", Central instrument facility, IIT Guwahati, Guwahati, India, 30th June -1st July 2017. Abstract book pp: 129-130. **(Awarded for Best poster)**

12. **Ramakrishna Madaka**, V.Kanneboina, Pratima Agarwal, "Hydrogenated amorphous silicon solar cells deposited at 150 ºC low-cost photo paper substrate" 17th International conference on Thin Films (ICTF-2017), CSIR- National Physical Laboratory, New Delhi, India, 13-17th November 2017. Abstract book pp: 79.

13. **Ramakrishna Madaka**, Juhi Kumari, V.Kanneboina, Pratima Agarwal, "Hydrogenated amorphous silicon solar cells fabricated at low substrate temperature 110ºC on flexible PET substrate" 2nd International conference on Condensed matter and applied Physics (ICC-2017), Bikaner, Rajasthan, India, 24-25th November 2017. Abstract book pp: 871.

14. **Ramakrishna Madaka**, Pilik Basumatary, V.Kanneboina, Pratima Agarwal, "Amorphous silicon thin film solar cells fabricated on different substrates" 19th International workshop in the Physics of semiconductor devices (IWPSD-2017), IIT Delhi, Delhi, India, 11-15th December 2017. Abstract book pp: 1-3. **(Awarded for Best poster)**

15. **Ramakrishna Madaka**, V.Kanneboina, Pratima Agarwal, "Nanostructure in a-Si:H films: Raman mapping and Raman scattering studies, National work shop on Fluorescence and Raman spectroscopy (FCS-2017), IIT Guwahati, Assam, India 17-21st December 2017. ID: Abstract book pp: 100.

16. **Ramakrishna Madaka**, V.Kanneboina, Pratima Agarwal,"Hydrogenated amorphous silicon based thin film solar cells on low cost photo paper and polyimide sheets" Research conclave, IIT Guwahati, Guwahati, India, 8-11th March 2018.

17. **Ramakrishna Madaka**, V.Kanneboina, Pratima Agarwal,"Hydrogenated amorphous silicon based solar cells on flexible substratess" Three minute thesis presentation, Research conclave, IIT Guwahati, Guwahati, India, 8-11th March 2018.

List of workshops attended

1. **Ramakrishna Madaka, INUP Familiarization Workshop** on "Nanofabrication Technologies". IIT Guwahati, Guwahati, 28-29th September 2012.
2. **Ramakrishna Madaka,** National workshop on advanced probing techniques in TEM (APTTEM-2016), IIT Guwahati, 15-17th February 2016.
3. **Ramakrishna Madaka**, "One day workshop on Vacuum Technology and its Application in Optical Science" 19th August 2017, IIT Guwahati, India.
4. **Ramakrishna Madaka,** 4th national workshop on NEMS/MEMS & Theranostic Devices (NWNTD-2018), Centre for Nanotechnology, IIT Guwahati, India, 26-28th February 2018.